# High-precision mass spectrometry of nobelium, lawrencium and rutherfordium isotopes and studies of long-lived isomers with SHIPTRAP

## Dissertation

zur Erlangung des Grades
*Doktor der Naturwissenschaften*
(Dr. rer. nat.)
im Promotionsfach Chemie

am Fachbereich Chemie, Pharmazie, Geographie und Geowissenschaften
der Johannes Gutenberg-Universität Mainz

**Oliver T. Kaleja**

geb. in Kassel

Mainz, 2020

1. Berichterstatter: Professor Dr. Michael Block
2. Berichterstatter: Professor Dr. Klaus Blaum

Tag der mündlichen Prüfung: Montag, 17.08.2020

*For your continuous support and your bottomless love throughout the last twelve years I want to deeply thank you, Julia. In the vastness of space and the immensity of time, it is my pleasure and my joy to share a planet and an epoch with you.*

# Contents

# Declaration

Hiermit erkläre ich, dass ich diese Arbeit selbstständig verfasst und keine anderen, als die darin angegebenen Hilfsmittel und Hilfen benutzt habe. Diese Arbeit wurde weder als Ganzes, noch in Teilen als Prüfungsarbeit für eine staatliche oder andere wissenschaftliche Prüfung eingereicht. Insbesondere nicht als Dissertation bei einer anderen Fakultät oder einem anderen Fachbereich.

Bensheim, den 25.05.2020

# List of Figures

# List of Tables

# Abstract

In this work, the first successful application of the recently developed Phase-Imaging Ion-Cyclotron Resonance (PI-ICR) technique in the region of the heaviest elements is presented. For the first time, the atomic masses of several nobelium (No, $Z = 102$), lawrencium (Lr, $Z = 103$) and rutherfordium (Rf, $Z = 104$) isotopes and isomers have been measured directly, reaching uncertainties on the order of few keV/c$^2$ using the Penning-trap mass spectrometer SHIPTRAP. These heavy radionuclides were produced in fusion-evaporation reactions and separated from the primary beam by the velocity filter SHIP located at the GSI Helmholtz Centre for Heavy Ion Research in Darmstadt, Germany. The mass measurements were carried out at production rates of few ions per second down to few ions per minute. To improve the overall efficiency on stopped and thermalized ions, the recently developed cryogenic gas-stopping cell was implemented into the existing beam line. Its performance with respect to purity and efficiency has been characterized and improved. The overall efficiency of SHIPTRAP is increased by about one order of magnitude with respect to previous measurements on heavy ions. The atomic masses are determined by measuring the cyclotron frequency of the ion of interest in the strong magnetic field of a 7 T superconducting magnet. The atomic masses of $^{251}$No, $^{254}$Lr and $^{257}$Rf were measured directly for the first time, reaching high precision. The latter marks the very first direct high-precision mass spectrometry of a superheavy element with a detection rate of one detected ion per day and only five ions in total. In addition, the uncertainties of the atomic masses of $^{254}$No and $^{255,256}$Lr have been reduced by up to two orders of magnitude with respect to previous experiments at SHIPTRAP. The precise determination of binding energies is key in nuclear physics as it is a model-independent quantity comprising all interactions that are present within the atomic nucleus. This allows studying, e.g., quantum-mechanical shell effects, which are elementary for the existence of (super-)heavy elements. The results of this work are used to benchmark atomic mass models in the vicinity of the deformed neutron shell closure at $N = 152$. Furthermore, these measurements will provide additional anchor points of very heavy odd-$N$ and odd-$Z$ as well as odd-$A$ nuclides, affecting the masses up to darmstadtium ($Z = 110$). With the enhanced mass resolving power of up to 11 000 000, the isomeric states $^{251m}$No, $^{254m}$Lr and $^{255m}$Lr were resolved from their respective ground states despite low excitation energies of tens of keV. Their masses and the corresponding excitation energies were measured directly for the first time. Up to now, only tentative level energies were derived from previous $\alpha$-decay spectroscopy experiments. This work proves the feasibility of PI-ICR in the region of the heaviest elements at lowest yields and particle integrals. It paves the way to precisely study exotic superheavy species with very long half-lives which becomes inevitable when progressing towards the island of stability.

# Zusammenfassung

Diese Arbeit präsentiert die erste erfolgreiche Anwendung der phasenabbildenden Ionen-Zyklotron-Resonanz Methode (engl. *Phase-Imaging Ion-Cyclotron-Resonance*, kurz PI-ICR) in der Region der schwersten Elemente. Mit Hilfe des Penningfallen-Massenspektrometers SHIPTRAP wurden erstmalig die atomaren Massen mehrerer Nobelium- (No, $Z = 102$), Lawrencium- (Lr, $Z = 103$) und Rutherfordium- (Rf, $Z = 104$) Isotope und Nobelium- und Lawrencium-Isomere direkt bestimmt und experimentelle Messunsicherheiten von wenigen keV/c$^2$ erzielt. Dazu wurden die Radionuklide in Fusions-Evaporations-Reaktionen erzeugt und mittels des Geschwindigkeitsfilters SHIP an dem GSI Helmholtzzentrum für Schwerionenforschung in Darmstadt, Deutschland, vom Primärstrahl getrennt. Die Massenmessungen wurden mit Produktionsraten von wenigen Ionen pro Sekunde bis hin zu wenigen Ionen pro Minute durchgeführt. Um die Gesamteffizienz des Abbremsens der Ionen zu steigern, wurde die kürzlich entwickelte kryogene Gaszelle in das bestehende System integriert. Ihre Effizienz und Reinheit wurde charakterisiert und optimiert, sodass die Gesamteffizienz des Systems, verglichen zu vorherigen Massenmessungen von SHIPTRAP an schweren Ionen, um etwa eine Größenordnung gesteigert werden konnte. Die atomaren Massen wurden über die Messung der Zyklotronfrequenz der Ionen im starken Magnetfeld eines 7 T starken, supraleitenden Magneten bestimmt. Erstmalig wurden die atomaren Massen von $^{251}$No, $^{254}$Lr und $^{257}$Rf direkt und mit hoher Präzision gemessen. Mit einer Detektionsrate von etwa einem Ion pro Tag und insgesamt nur fünf Ionen stellt die Messung an $^{257}$Rf die erste direkte präzise Massenmessung eines superschweren Elements dar. Zusätzlich wurden die experimentellen Unsicherheiten der atomaren Massen von $^{254}$No und $^{255,256}$Lr verglichen zu früheren Massenmessungen an SHIPTRAP um bis zu zwei Größenordnungen reduziert. Die präzise Bestimmung von Bindungsenergien ist von fundamentaler Bedeutung in der Kernphysik, da sie eine modellunabhängige Größe darstellt, die alle Wechselwirkungen des atomaren Kerns enthält. Sie erlaubt es beispielsweise die quantenmechanischen Schaleneffekte zu studieren, die für die Existenz von (super-)schweren Elementen verantwortlich sind. Die Ergebnisse dieser Arbeit werden mit atomaren Massenmodellen in der Nähe des deformierten Neutronen-Schalenabschlusses bei $N = 152$ verglichen. Diese Messungen liefern zusätzliche Ankerpunkte für sehr schwere ungerade-$N$ und ungerade-$Z$, sowie ungerade-$A$ Nuklide und beeinflussen die atomaren Massen von Elementen bis zu Darmstadtium ($Z = 110$). Die hohe Massenauflösung von bis zu 11 000 000 ermöglichte es, die isomeren Zustände $^{251m}$No, $^{254m}$Lr und $^{255m}$Lr trotz niedriger Anregungsenergien von wenigen zehn keV von ihren Grundzuständen zu separieren. Ihre Massen und die damit verbundenen Anregungsenergien konnten dadurch erstmals direkt bestimmt werden. Bisher waren die Anregungsenergien nur indirekt über Kernspektroskopie-Experimente bestimmt. Diese Arbeit bestätigt die Anwendbarkeit von PI-ICR im Bereich der schwersten Elemente, bei niedrigsten Detektionsraten mit wenigen detektierten Ionen insgesamt. Sie ebnet den Weg, noch exotischere superschwere Spezies mit langen Halbwertszeiten zu untersuchen, wodurch theoretische Vorhersagen zur Insel der Stabilität verbessert werden können.

# Chapter 1

# Introduction

The question of the origin and composition of matter has fascinated mankind for hundreds of years. Nowadays we know that any matter we experience in daily life consists of atoms which are composed out of an atomic nucleus accompanied by electrons. The nucleus itself consists of protons and neutrons. An element is defined by the number of protons in its atomic nucleus. Ever since more and more elements have been discovered, the question of the heaviest element that can exist arose. As any element requires a bound atomic nucleus for its very existence, this question translates into the question of a bound nucleus with the most possible number of protons. Today, about 3300 different compositions of protons and neutrons (so-called *isotopes*) have been found to exist, out of which about 250 are stable. The major variety does not occur on earth and has to be produced artificially at accelerator-based facilities. As elements get heavier and heavier in proton number, the repulsive Coulomb force increases. In simple nuclear models such as the liquid drop model this results in the disappearance of the fission barrier for $Z \approx 106$. Thus, such models cannot explain the existence of superheavy elements (SHE) with proton numbers $\geq 104$. However, elements with up to 118 protons have been discovered [1]. Their very existence is linked to quantum-mechanical shell effects that enhance their stability. The maximum amount of protons that - in combination with neutrons - form a bound nucleus still remains a key question in the field of nuclear physics. In addition, an *island of stability* was predicted in the region of the superheavy elements. An expanded region of isotopes in which the quantum-mechanical shell effects result into a maximum in binding energy, possibly resulting in extraordinary long half-lives. Therefore, the presence of superheavy elements in microscopic crystalline monazite inclusions (asteroids or fossil finds) [2] have been investigated with no distinct evidence so far [3]. Some of these superheavy elements exist in long-lived excited states (so-called *isomeric states* or *isomers*) in which their binding energy is reduced by the excitation energy. Isomers, as for instance in $^{270}$Ds ($Z = 110$), have been found that live longer than their corresponding ground state [4].

The stability of a nucleus is expressed in its *binding energy*, which is directly connected to its experimental mass. This is a consequence of Einstein's mass-energy equivalence principle $E = mc^2$ [5]. Therefore, measuring atomic masses with high precision enables to quantify stability, which is crucial to constraint the boundaries of nuclear existence. The precise determination of atomic masses and binding energies in the region of the heaviest elements is of particular interest. Far away from stability, located at the top right end of the nuclear chart at the border of nuclear existence, SHE with atomic numbers $Z \geq 104$ exhibit unique atomic and nuclear properties [6, 7].

Penning traps are state-of-the-art for high-precision mass measurements. Based on the precise determi-

nation of the cyclotron frequency in a strong magnetic field, these measurements only require few ions in total to pin down the mass of an ion species with highest accuracy. In addition, the time to perform a measurement can be well below one second, giving access to many exotic nuclides far away from stability. With the recent development of the Phase-Imaging Ion-Cyclotron-Resonance (PI-ICR) technique at the Penning-trap mass spectrometer SHIPTRAP [8, 9] its mass resolving power, precision and sensitivity has been greatly improved. The additional phase information of the ion's motion eludes the Fourier limit, which naturally occurs in frequency measurements. It thus outperforms and replaces the well-established Time-Of-Flight Ion-Cyclotron-Resonance technique (ToF-ICR) [10].

This work presents the first successful application of the PI-ICR technique in the region of transfermium elements. In a beam time campaign in summer 2018, the atomic masses of $^{251,254}$No and $^{254-256}$Lr isotopes were measured and their uncertainties improved by up to two orders of magnitude. The masses of $^{251}$No and $^{254}$Lr were measured directly and with high-precision for the first time. In addition, this work presents the first direct high-precision mass spectrometry of a superheavy element: $^{257}$Rf. The high mass resolving power of PI-ICR allowed separating the isomeric states $^{251m}$No and $^{254m,255m}$Lr from their respective ground states. For the first time, the excitation energies of these isomers have been determined directly. This work proves the feasibility of PI-ICR in the region of the heaviest elements at lowest detection rates and particle integrals and as a complementary tool to decay-spectroscopy investigations.

The following chapter 2 introduces the theoretical aspects of atomic masses and nuclear isomerism with an emphasis on the heaviest elements. In chapter 3 the experimental setup is introduced. Such challenging measurements would not have been possible without the implementation of the cryogenic gas-stopping cell at SHIPTRAP and its improvements with respect to efficiency and purity, which is described in chapter 4. The beam time campaign in 2018 is summarized and evaluated with respect to the overall performance in chapter 5. The data analysis is explained in chapter 6, while the results are presented in chapter 7. Finally, future perspectives are discussed in chapter 8, followed by a summary in chapter 9.

# Chapter 2

# Theory

The derivation of theories from observation and their benchmark to experimental data, respectively, is of fundamental importance to any science. In the case of nuclear physics, theories are mandatory to understand the behaviour and properties of nuclear matter. This has been and still is of practical relevance for mankind. As examples, a variety of modern medical diagnostics and treatments rely on nuclear properties, like the Magnetic Resonance Imaging (MRI) and the Positron-Emission Tomography (PET) therapy. Nuclear power is accounting for 10 % of global electricity generation and the second-largest low-carbon power source in the world today [11]. In theory, nuclear fusion is capable of producing large amounts of energy in an environmentally friendly way. In addition, exploiting nuclear isomers can allow for much more compact and lightweight energy storages [12]. The development of a nuclear clock can improve satellite-based navigation and data transfer [13]. With respect to fundamental research, nuclear theories are inevitable to study the origin of elements and the boundaries of nuclear and atomic existence.

The theoretical description of a nucleus and its properties is non-trivial. First, the nuclear force between nucleons cannot be derived from fundamental principles as it results from the residual strong interaction of the quarks confined within the nucleons. Second, the number of nucleons in an atomic nucleus range from one (in the case of hydrogen) to few hundreds in the case of the heaviest elements. In quantum mechanics, already few-body systems cannot be solved analytically, let alone nuclei with dozens or even hundreds of nucleons. On the other hand, the latter are still way too few from being well described by purely statistical approaches.

There are several global mass models of various kinds that try to describe the experimentally known masses with good accuracy. Their goal is to deliver accurate predictions for yet unknown masses to estimate the boundaries of nuclear existence and for the calculation of the pathway of nucleosynthesis processes. Global models are based on parameters that are fitted to nuclei across the entire nuclear chart. Their performance is usually benchmarked by their root-mean-square (rms) deviation to experimental data. There are several successful and promising approaches for global mass formulas for nuclei with $N, Z \geq 8$, e.g. purely microscopic (self-consistent) approaches based on the Hartree–Fock–Bogolyubov method like HFB21 [14] and the GHFB [15], macroscopic-microscopic formulas like the finite-range (liquid) droplet model FRDM (FRLDM) [16], the Thomas–Fermi (TF) model [17] and the Lublin–Strasbourg (LSD) model [18]. Whereas microscopic models approximate the solution of the Hamilton equations using, e.g., the Ritz variation principle [19], macroscopic-microscopic methods add microscopic solutions to macroscopic models, e.g. by adding shell effects to liquid-drop models. Other approaches have been

performed by J. Duflo and A. P. Zuker (DZ) [20], by H. Koura et al. (KTUY) [21], and recently by means of the Weizsäcker-Skyrme formula by N. Wang *et al.* (WS3.3 [22] and WS4 [23]) and by M. Liu *et al.* (WS3.6) [24]. Recent studies show that the obtained root-mean-square values differ, depending on the region within nuclear chart [25, 26]. The semi-empirical Liran-Marinov-Zeldes (LMZ) formula [27] and the macroscopic-microscopic heavy nuclei model (HN) [28] are of local type, adapted to describe nuclei above the proton and neutron shell closures $Z = 82$ and $N = 126$, respectively. The accuracies reached are at the border of 300 keV/$c^2$ for known masses, but the accuracy on extrapolated values may be much lower.

This chapter briefly addresses theoretical aspects of nuclear mass models. For this reason, section 2.1 gives a general introduction on atomic binding energies. One of the first approaches to theoretically describe binding energies has been the liquid-drop model (LDM), which is presented in section 2.2, followed by the spherical and deformed shell model in sections 2.3 and 2.4, respectively. General aspects of macroscopic-microscopic approaches are discussed in section 2.5. As representatives of a purely microscopic approach, section 2.6 introduces the Skyrme-Hartree-Fock method. The chapter ends with a brief introduction on nuclear isomers in the context of high-precision mass spectrometry in section 2.7.

## 2.1 Binding Energies in the Context of Nuclear Masses

First advanced mass spectrometry with mass resolving powers of about 1 in 600 and accuracies in the order of 1 in 10 000 in the early 1920s by F. W. Aston established that the mass of the atom was about 1 % smaller than the sum of the masses of its constituents [29][1]. It was shown that this *mass defect* changes for different atomic species and emphasized that for this reason measurements of this quantity are of fundamental importance to learn about the actual structure of the nucleus [29, 30]. The mass defect's origin was correctly interpreted by A. Eddington [31] as an example of Einstein's mass-energy equivalence $E = mc^2$ [5], which - in this context - connects the mass of a bound system to its associated binding energy. Still, the precise determination of binding energies is key as it is a model-independent quantity comprising all interactions that are present within the atomic nucleus. It is directly connected to the stability of nuclei and thus to the very existence of atoms and elements.

In 1869 the Russian chemist D. Mendeleev started to develop what is now known as the periodic table[2], by arranging chemical elements with respect to their atomic mass [32]. Around 56 elements were known to him at that time. Due to open spaces in his arrangement, he predicted the existence of other elements at certain atomic weights and estimated their chemical properties.

It was also thanks to F. W. Aston's mass spectrometry on atmospheric neon in the 1920s that elements with different atomic masses were determined[3], where the difference in atomic mass approximately equals multiple integers of the atomic mass of the hydrogen atom [34]. We now know that the chemical properties of an element are dictated by the shell structure of its valence electron(s) and that the total number of electrons of an atom equals the number of its protons in the nucleus. It was only after the discovery of the neutron in 1932 by J. Chadwick [35] that different atomic weights are understood as *isotopes* of this element, differing in neutron number at a constant number of protons in the nucleus. With the discovery of the element oganesson (Og) with 118 protons [1] the $\mathbf{7^{th}}$ period of the Periodic Table is filled. However, the periodic table is most likely not complete and the discovery of elements with even more protons is

[1] Note that the neutron had not yet been discovered.

[2] The year 2019 was proclaimed by the UN General Assembly and the UNESCO as the *International Year of the Periodic Table*, celebrating its $150^{\text{th}}$ birthday.

[3] F. W. Aston had first identified the isotopes $^{20}$Ne and $^{22}$Ne.

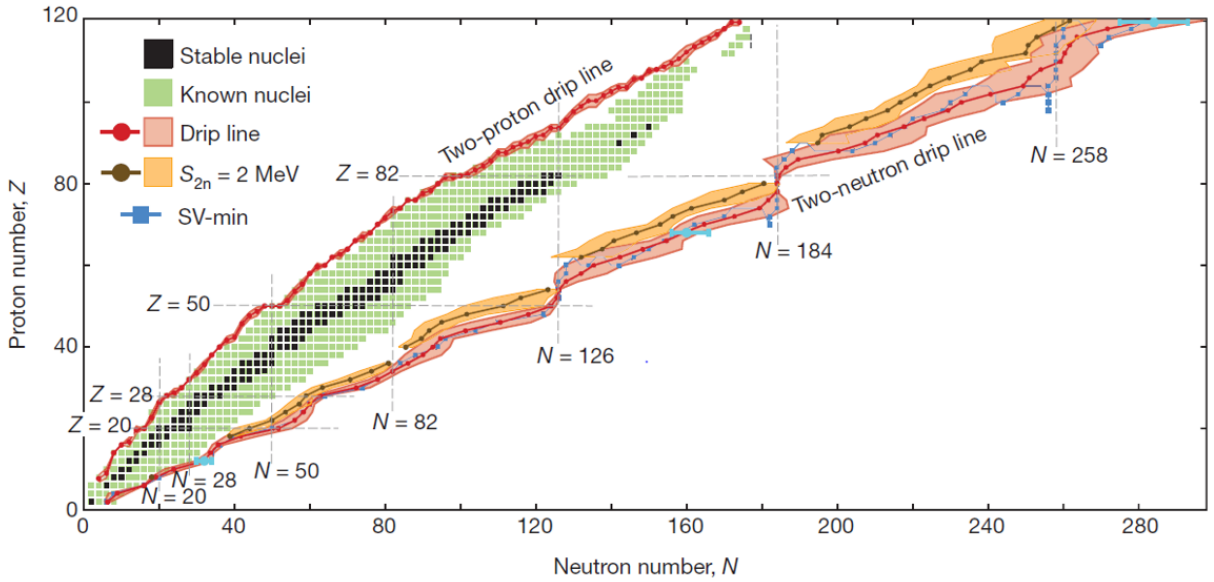


Figure 2.1: Landscape of even-even nuclei as of 2012. Fig. modified from [33].

still an ongoing process. In fact, atomic theories expanded calculations for elements with up to 172 and 173 protons [36, 37, 38].[4] Sorting and plotting all identified isotopes with respect to their neutron (as the abscissa) and proton number (as the ordinate), the *table of nuclides* is obtained (figure 2.1). This iconic figure represents the playground of nuclear physics. Besides the quest for the heaviest element, the question arises how many isotopes of each element can exist. As an arbitrary combination of protons and neutrons does not necessarily yield to a bound nucleus, it is decisive to theoretically understand the origin and limits of stability, which is connected to the binding energy

$$BE(N,Z) = (N \times m_n + Z \times (m_p + m_e) - m(N,Z))c^2 \tag{2.1}$$

of an atom with proton number $Z$ and neutron number $N$. Here, $m_n$, $m_p$ and $m_e$ correspond to the neutron, proton and electron rest mass, respectively. The atomic mass of this atom is represented by $m(N,Z)$ with $c$ being the speed of light in vacuum. The binding energy of an atom comprises the nuclear binding of the nucleons and the electromagnetic binding of the electrons. Nuclear mass models (see sections 2.2 to 2.6) are used to calculate nuclear binding energies. Figure 2.2(a) shows the binding energies for all isotopes with proton numbers $Z \geq 90$ as a function of their neutron number $N$, based on the current Atomic Mass Evaluation (AME) from 2016 [39]. The boundaries of nuclear existence are best studied using nucleon separation energies. Following equation 2.1 the neutron and proton separation energies are given by

$$S_n(N,Z) = BE(N,Z) - BE(N-1,Z) \tag{2.2}$$

and

$$S_p(N,Z) = BE(N,Z) - BE(N,Z-1), \tag{2.3}$$

respectively. If these separation energies are negative, it is energetically favourable for the nucleus to separate itself from the corresponding nucleon. In other words, for negative separation energies it becomes energetically unfavourable for a nucleus to accept and bind an additional nucleon, which, in case, would just *drip* out. The resulting borders are referred to as proton and neutron drip lines. Whereas the proton drip line is in general well established for all elements that are naturally occurring on earth, the neutron

[4] Nuclear theories, however, exclude the existence of nuclei with that many protons.

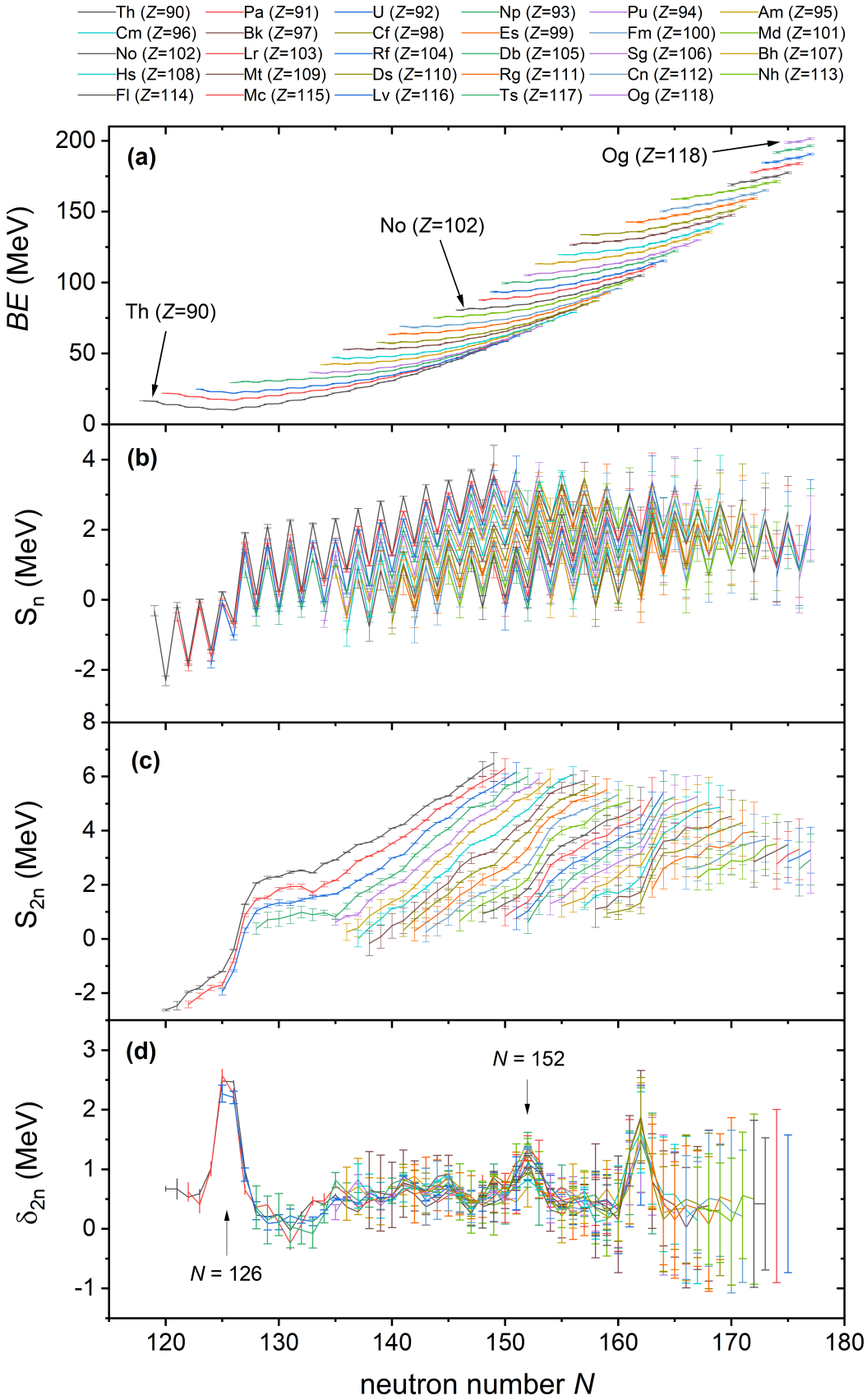


Figure 2.2: Binding energies $BE$ (a), neutron separation energies $S_{\mathrm{n}}$ (b), two-neutron separation energies $S_{2\mathrm{n}}$ (c) and two-neutron shell gap parameters $\delta_{2\mathrm{n}}$ (d) for all known isotopes with proton numbers $Z \geq 90$ as a function of their neutron number $N$. The data is based on the most recent Atomic Mass Evaluation (AME) from 2016 [39].

drip line is only established for the first ten elements up to neon [39]. Due to the Coulomb repulsion in between protons, the proton drip compared to the neutron drip line runs closer to the valley of stability, which in general makes these isotopes more accessible.

Paired nucleon configurations enhance binding energy. The addition or removal of one single nucleon to a nucleus can thus lead to a relatively large change in binding energy in the order of few MeV as seen in figure 2.2(b). Therefore, it is often more useful to evaluate the two-neutron separation energy

$$S_{2n}(N,Z) = BE(N,Z) - BE(N-2,Z) = (m(N-2,Z) + 2m_n - m(N,Z))\,c^2 \tag{2.4}$$

to identify signatures of nuclear structure features like shell effects. The two-proton separation energy is obtained similarly. The associated two-nucleon drip lines are shown in figure 2.1. Figure 2.2(c) shows the two-neutron separation energy $S_{2\mathrm{n}}$ for all known isotopes with proton numbers $Z \geq 90$ as a function of their neutron number $N$. The sudden and relatively steep increase of the two-neutron separation energies of thorium, protactinium and uranium isotopes at neutron number $N = 126$ indicates a nuclear shell gap, which is less pronounced in the (single-)neutron separation energy. Compared to the neutron separation $S_n$ energy from equation (2.2), the two-neutron separation energy $S_{2n}$ eludes the contribution of the pairing effect to the binding energy. The shell structure and the associated *magic numbers* (proton and/or neutron number at shell gaps) of nuclei is one of the key findings of nuclear physics and will be discussed in section 2.3. For an even better evaluation of shell gaps, the neutron shell gap parameter

$$\delta_{2n}(N,Z) = S_{2n}(N,Z) - S_{2n}(N+2,Z) = (m(N-2,Z) - 2m(N,Z) + m(N+2,Z))\,c^2 \tag{2.5}$$

is evaluated and shown in figure 2.2(d) (a proton shell gap parameter can be obtained similarly). The neutron shell gaps now correspond to well-pronounced peaks in the plot. For the heaviest isotopes, the nuclear binding energies are obtained from nuclear mass models which result in relatively large uncertainties in the order of several MeV. The two-neutron separation energy also indicates less pronounced shell gaps at neutron numbers $N = 152, 162$. In the case of $N = 162$ the experimental uncertainties are still too large to unambiguously pin down the strength of the shell gap.

## 2.2 Liquid-Drop Model

A first attempt to describe the binding energy of a nucleus was performed by C. F. von Weizsäcker in 1935 by treating the nucleus as an incompressible homogeneous liquid kept together by the nuclear force [40]. In this so-called *liquid-drop model*, the binding energy is described by the semi-empirical Bethe-Weizsäcker formula

$$BE^{\mathrm{LDM}}(N,Z) = a_{\mathrm{vol}}A - a_{\mathrm{surf}}A^{\frac{2}{3}} - a_{\mathrm{coul}}\frac{Z^2}{A^{\frac{1}{3}}} - a_{\mathrm{asym}}\frac{(N-Z)^2}{A} \pm \delta_{\mathrm{pair}}. \tag{2.6}$$

The first and second terms are proportional to the volume and the surface of the nucleus.[5] The second term reduces the binding energy, as the outer lying nucleons on average are less attracted by the nuclear force. The third and fourth term consider the Coulomb repulsion of the protons within the nucleus and the Pauli principle which favours less asymmetric nuclei, respectively. The last term includes the pairing effect

[5]The nucleon density for most of the nuclei is to first order constant. Thus, the radius of any nucleus is approximated to be proportional to $A^{\frac{1}{3}}$. Therefore, $A$ and $A^{\frac{2}{3}}$ are proportional to the volume and the surface of any nucleus, respectively.

between the nucleons to minimise their spin[6]. It is positive if $Z$ and $N$ are even, negative if both are odd and zero in any other case. Depending on the parametrization, this term used to be $\delta_{\text{pair}} = a_{\text{pair}} A^{-\frac{3}{4}}$ [40, 41]. However, it is found that a scaling of $\delta_{\text{pair}} \propto A^{-\frac{1}{2}}$ gives a better representation of the experimental data [42]. The prefactors $a_{\text{vol}} \approx 16\,\text{MeV}$, $a_{\text{surf}} \approx 18\,\text{MeV}$, $a_{\text{coul}} \approx 0.7\,\text{MeV}$, $a_{\text{asym}} \approx 93\,\text{MeV}$ and $a_{\text{pair}} \approx 11\,\text{MeV}$ are chosen such that the experimentally measured binding energies are best represented. The liquid-drop model neglects any shell effects on the binding energies, which are seen in comparison with experimental data in figure 2.3. However, it still describes the binding energies of most nuclei better than a few percent and serves as the basis for many other mass models.

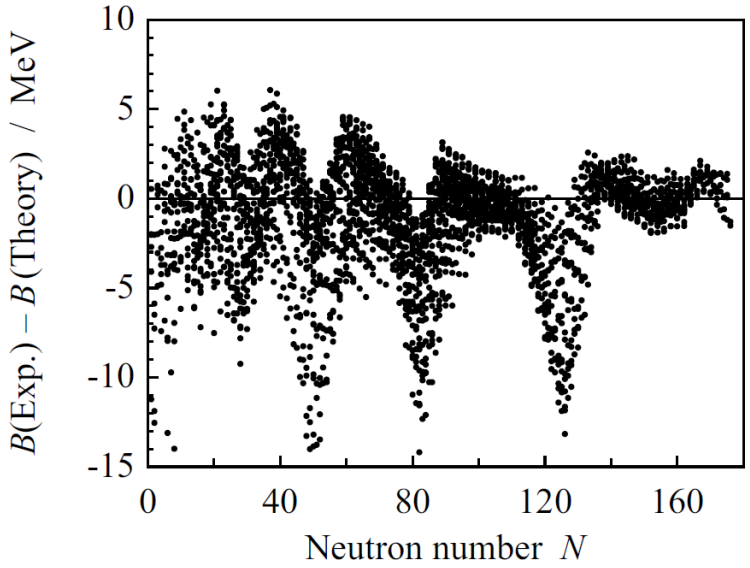


Figure 2.3: Deviation of the liquid-drop model from experimental data for all known isotopes based on the Atomic Mass Evaluation from 2003 [43]. Figure taken from [44].

## 2.3 Shell Model

Nuclei with proton and/or neutron numbers equal to one of the magic numbers are particularly stable. Although the existence of shell structure in nuclei had already been noticed in the 1930s, it took almost two decades before the correct description was found [45, 46]. It is of fundamental importance for the understanding of nuclear stability and has been confirmed in a vast number of experiments. As a consequence, in 1963, for their theoretical developments, the Nobel Prize in Physics was awarded to E. P. Wigner[7] together with M. Goeppert-Mayer and J. H. D. Jensen[8] [47]. The model presumes that a given nucleon moves in an effective three-dimensional potential formed by all the other nucleons. First descriptions of this potential had the form of a square-well and spherical-symmetric harmonic oscillators, respectively [42]. A better approximation for the analytic form of the effective potential is the Woods-Saxon potential [48] as it describes quite well the density distribution of nucleons within a nucleus [42].

As a consequence of quantum mechanics, only discrete energy levels can be occupied by the nucleons. In addition, in order to reproduce the experimentally observed magic numbers 2, 8, 20, 28, 50, 82 for protons and neutrons and additionally 126 for neutrons, further interactions have to be taken into account, e.g. the spin-orbit coupling [42]. The resulting energy levels are described by three distinct quantum numbers ${}^{n}l_{j}$, with the principal quantum number $n$, the orbital angular momentum $l$ and the total angular momentum $j$. Instead of the numerical integer value of the angular momentum, shells are named $s$-,$p$-,$d$-,... shell for

[6] Nucleons, being fermions, prefer to occupy energy levels in pairs in which their spin couples to zero.
[7] *For his contributions to the theory of the atomic nucleus.*
[8] *For their discoveries concerning nuclear shell structure.*

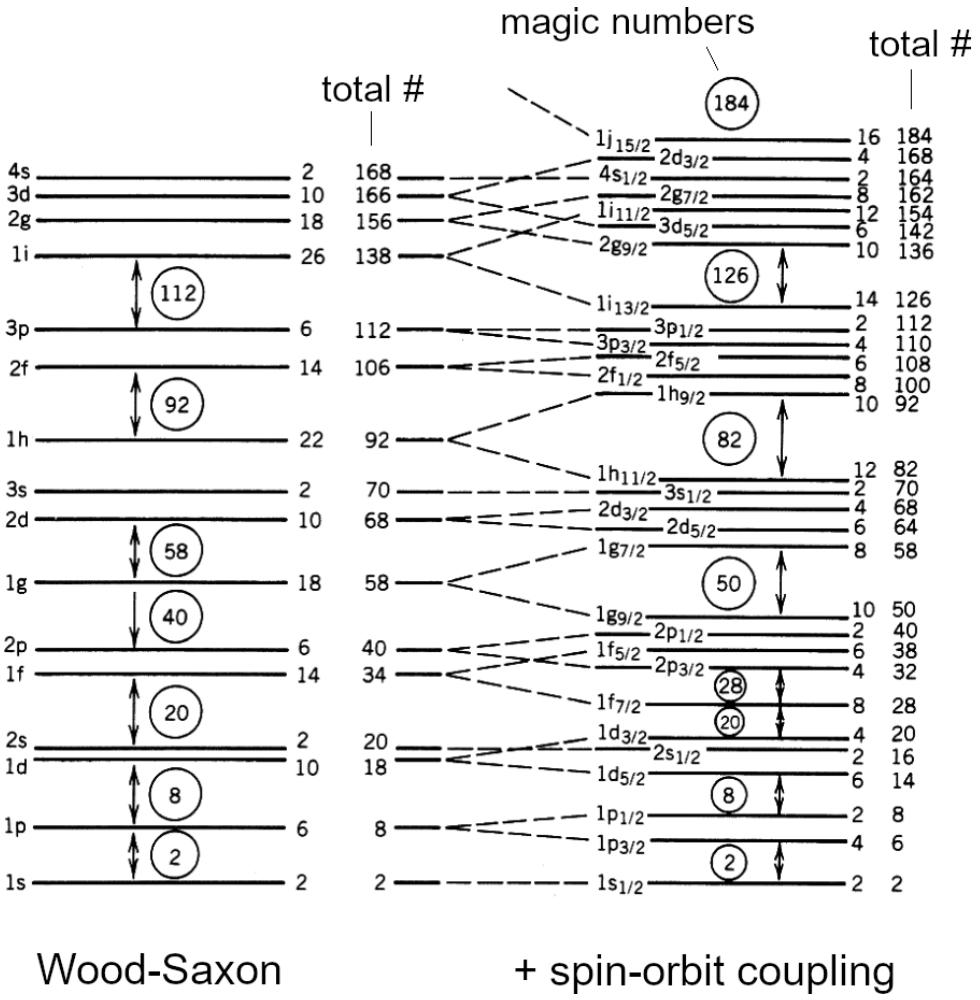


Figure 2.4: Calculated shell model energy levels for neutrons from a Wood-Saxon potential (left) and the same Wood-Saxon potential with the consideration of a spin-orbit coupling of the nucleon (right). In addition, the multiplicities and their sums are given. Figure taken and modified from [49].

$l = 0, 1, 2, \ldots$. The *multiplicity* of any energy level (number of nucleons that can share one energy level) is given by $2j + 1$. The nucleons therein will differ by their sub-state $m_j$ of the total angular momentum ranging from $-j$ to $+j$ in integer steps. As nucleons are fermions with spin 1/2, they obey the Pauli exclusion principle and cannot share the same quantum numbers, thus consecutively filling the discrete energy levels. The energy levels for protons and neutrons are slightly different due to their difference in charge (the energy levels of the protons are modified due to the additional Coulomb repulsion). To give an example: the lowest energy level has $n = 1$, $l = 0$ and therefore $j = 1/2$. Thus, the state is referred to as $^1s_{1/2}$ and can be filled with up to two nucleons (one with spin up and the other one with spin down). The energy levels, associated multiplicities and magic numbers calculated from a Wood-Saxon potential including a spin-orbit coupling are shown in figure 2.4.

## 2.4 Nilsson Model

In 1935 quadrupole moments of nuclei were discovered by H. Schüler and Th. Schmidt [50] which revealed the existence of deformed nuclei. In fact, the majority of today's known nuclei are deformed and only very few are spherical. In the following decades, the presence of rotational bands in nuclei were observed, that follow the same $J(J + 1)$ pattern of energies as known from rotating molecules[42]. The (spherical) shell model (see section 2.3) is not capable of explaining this phenomenon, as it is impossible for any quantum

mechanical and spherical system to rotate collectively. Therefore, A. Bohr, B. Mottelson and S. G. Nilsson extended the shell model to deformed nuclei by using a deformed (elliptic) harmonic oscillator potential as a basis. In this so-called *Nilsson model* the motion of the nucleons is described by independent oscillators along the symmetry axis ($z$) and perpendicular to it ($\perp$). The eigenvalues of the energy

$$E(n_z, n_\perp) = \hbar\omega_z(n_z + \frac{1}{2}) + \hbar\omega_\perp(n_\perp + 1) \; + \text{corrections} \tag{2.7}$$

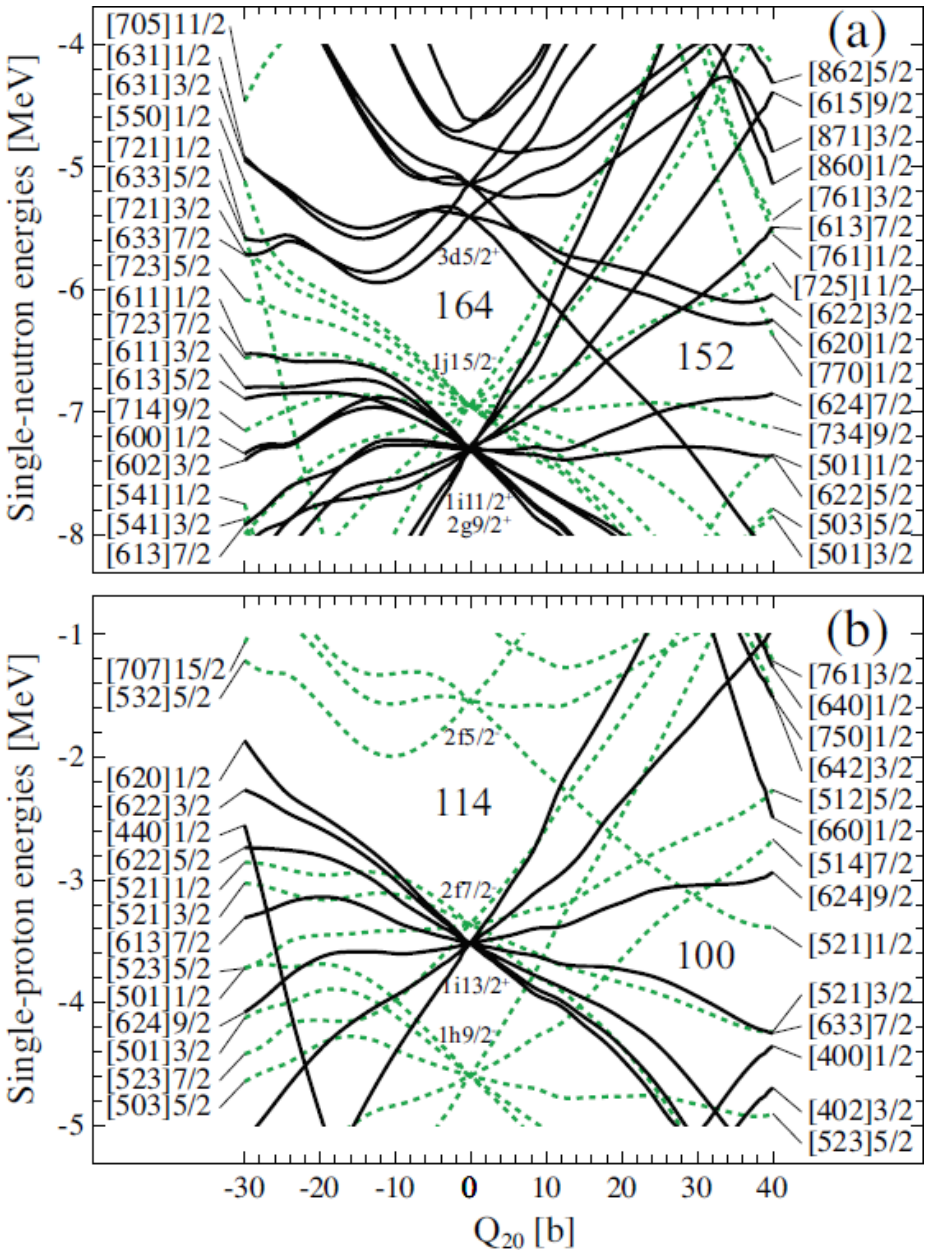


Figure 2.5: Nilsson orbitals for neutrons (a) and protons (b) calculated in $^{254}$No. The solid and dashed lines represent even- and odd-parity levels, respectively. The quadrupole deformation $Q_{20}$ is proportional to the deformation parameter $\delta$, introduced in the text. Figure taken from [51].

depend upon the number of oscillator quanta along the symmetry axis $n_z$ and perpendicular to it $n_\perp = n_x + n_y$.[9] Due to the deformation $n$, $l$ and $j$ from the spherical shell model are no longer good quantum numbers. Instead, the notation $[N, n_z, \Lambda]\Omega^\pi$ (also $\Omega^\pi[N, n_z, \Lambda]$) is used, where $\Omega$ corresponds to the projection of the total angular momentum onto the symmetry axis, $N = n_z + n_\perp$ to the total number of oscillator

[9] Here a Cartesian coordinate system is assumed.

quanta and $\Lambda$ to the projection of the angular momentum onto the symmetry axis. The correction terms in equation (2.7) are identical to the ones used in the shell model, e.g. a spin-orbit coupling. The level of deformation is described by a deformation parameter $\delta = (3/2)(\bar{R}^2 - 1)/(2\bar{R}^2 + 1)$ with the axis ratio $\bar{R} = \omega_\perp/\omega_z$ [42].

Any deformation $\delta$ results in a shift in energy for the associated energy levels as seen in the Nilsson diagram shown in figure 2.5. This has two interesting consequences. First, due to a different response of the energy levels, shell gaps can change with respect to deformation up to a point where existing shell gaps vanish and new gaps occur.[10] Second, as the energy difference between energy levels varies with respect to deformation, spherical (ground-state) levels of much heavier isotopes can be occupied in lighter nuclei by means of single-particle excitations at a given deformation.

## 2.5 The Macroscopic-Microscopic Approach

The liquid-drop model (see section 2.2) is able to reproduce the general trend of the binding energy for the majority of the known isotopes but does not include shell structure. In contrast, the shell model (see section 2.3) very well explains the occurrence of magic numbers but is not feasible to calculate the absolute energy of the nucleus, i.e. its binding energy. For this reason, in 1966, W. D. Myers and W. J. Swiatecki attempted to combine both theories and extended the liquid-drop model by additional contributions to the binding energy, including shell corrections [52]. As both, the microscopic assumptions of single-particle energy levels and the macroscopic assumptions of the liquid-drop model are included, these kind of approaches are referred to as macroscopic-microscopic approaches.[11]

Only one year after, V. M. Strutinsky presented yet another ansatz, which is still of relevance for many macroscopic-microscopic models [53, 54], where shell corrections ($\delta S$) and pairing corrections ($\delta P$) of the individual protons ($p$) and neutrons ($n$) contribute to the binding energy

$$BE^{\mathrm{MM}}(N,Z) = BE^{\mathrm{LDM}} + \sum_{\mathrm{p,n}} (\delta S + \delta P) \tag{2.8}$$

of the nucleus. $BE^{\mathrm{LDM}}$ corresponds to the binding energy calculated using the liquid-drop model (see equation (2.6)). The shell corrections are determined by evaluating the energy difference between a non-uniformly distributed level spacing $S$ and a uniformly distributed one $\tilde{S}$, where

$$S = \sum_i n_i \epsilon_i \quad \text{and} \quad \tilde{S} = \int_{-\infty}^{\infty} \epsilon g(\epsilon) d\epsilon. \tag{2.9}$$

Here, $\epsilon_i$ are energy eigenvalues of the protons and neutrons, respectively and $n_i$ is the occupation number of the given energy level. The distribution function

$$g(\epsilon) = \frac{1}{\gamma\sqrt{\pi}} \sum_i n_i e^{-\frac{(\epsilon-\epsilon_i)^2}{\gamma^2}} \tag{2.10}$$

[10] The multiplicity as discussed in section 2.3 of each energy level is unaffected by the deformation.

[11] The *macroscopic* part describes the *global* properties of the nucleus including its deformation, whereas the *microscopic* part comprises the corrections in binding energy due to (nuclear) shell effects.

makes use of a smearing parameter $\gamma$ which is part of the parametrization. Similarly, the pairing corrections $\delta P$ are obtained using the Bardeen-Cooper-Schrieffer theory [54]. Over the past decades additional corrections and assumptions have been added to this ansatz. As an example, the modern microscopic-macroscopic finite-range droplet model (FRDM) also allows for a compression of the liquid drop [16].

## 2.6 The Skyrme-Hartree-Fock Method

Besides macroscopic-microscopic approaches, purely microscopic methods have been developed to approximate the quantum-mechanical many-body problem. In the Hartree-Fock approximation [14], the interaction between single nucleons is reduced to the interaction of any nucleon with a mean field $V_i^{\mathrm{HF}}$ generated by all the other nucleons. The resulting Hamiltonian is given by

$$\hat{H}^{\mathrm{HF}} = -\frac{\hbar^2}{2m}\sum_i \nabla_i^2 + \sum_i \hat{V}_i^{\mathrm{HF}}. \tag{2.11}$$

The binding energy

$$BE^{\mathrm{SHF}} = E_{\mathrm{kin}} + E_{\mathrm{coul}} + E_{\mathrm{skyrme}} + E_{\mathrm{pair}} + E_{\mathrm{corr}} \tag{2.12}$$

is evaluated as the sum of energy functionals that are solved using the Ritz variation method [19]. Except for additional energy correction terms (corr), the main contributions originate from the kinetic (kin), the Coulomb (coul) and the pairing (pair) energy functional of the nucleons. Even though the Hartree-Fock method makes use of a mean-field interaction for any nucleon within the nucleus, nucleon-nucleon interactions cannot be neglected. One of the most commonly used phenomenological nucleon-nucleon interaction is the so-called Skyrme force which is a zero-range interaction composed of three terms [55, 56, 57]

$$\hat{V}_{\mathrm{Skyrme}} = \hat{V}_{12} + \hat{V}_{\mathrm{DD}} + \hat{V}_{\mathrm{LS}} \tag{2.13}$$

that depends upon the spins and the relative momenta of the nucleons as well as the nucleon density. The first addend corresponds to a spin-dependent two-body interaction

$$\hat{V}_{12} = t_0(1 + x_0\hat{P}_\sigma)\delta(\hat{\vec{r}}_1 - \hat{\vec{r}}_2) + \frac{t_1}{2}(1 + x_1\hat{P}_\sigma)\{\hat{\vec{k}}^2, \delta(\hat{\vec{r}}_1 - \hat{\vec{r}}_2)\} \tag{2.14}$$

$$+ t_2(1 + x_2\hat{P}_\sigma)\hat{\vec{k}}\delta(\hat{\vec{r}}_1 - \hat{\vec{r}}_2)\hat{\vec{k}} \tag{2.15}$$

with the spin-exchange operator $\hat{P}_\sigma = \frac{1}{2}(1 + \hat{\sigma}_1\hat{\sigma}_2)$ and the relative momentum operator $\hat{\vec{k}} = -i(\vec{\nabla}_1 - \vec{\nabla}_2)$. $\{\hat{A}, \hat{B}\} = \hat{A}\hat{B} + \hat{B}\hat{A}$ is the anti-commutator. The second term corresponds to a three-body interaction, approximated by a two-body density-dependent interaction

$$\hat{V}_{\mathrm{DD}} = \frac{t_3}{6}(1 + x_3\hat{P}_\sigma)\hat{\rho}^\alpha((\hat{\vec{r}}_1 + \hat{\vec{r}}_2)/2)\delta(\hat{\vec{r}}_1 - \hat{\vec{r}}_2), \tag{2.16}$$

where $\hat{\rho}^\alpha((\hat{\vec{r}}_1 + \hat{\vec{r}}_2)/2)$ corresponds to the nucleon density operator with $\alpha$ determining the incompressibility

of nuclear matter [56]. The last term equals a spin-orbit interaction

$$\hat{V}_{\mathrm{LS}} = i\frac{t_4}{2}\{\delta(\hat{\vec{r}}_1 - \hat{\vec{r}}_2)\hat{\vec{k}}, (\hat{\vec{\sigma}}_1 + \hat{\vec{\sigma}}_2) \times \hat{\vec{k}}\}. \tag{2.17}$$

The 10 parameters $x_i$, $t_i$, $t_4$ and $\alpha$ ($i \in \{0, 1, 2, 3\}$) are fitted to experimental data. To compare the magnitude of the shell correction energy from the Skyrme-Hartree-Fock (SHF) model with respect to, e.g., macroscopic-microscopic approaches (see equation (2.8)), the binding energy in the SHF mean field approach from equation (2.12)

$$BE^{\mathrm{SHF}} \approx \widetilde{BE} + E_{\mathrm{shell}} \tag{2.18}$$

is decomposed into an average energy that changes smoothly with particle number $\widetilde{BE}$ and a shell correction energy $E_{\mathrm{shell}}$ [58]. The evaluation of the shell correction energy is of fundamental importance to understand the stability of superheavy elements. The associated magic numbers of superheavy elements vary, depending upon the underlying model and its parametrization. Whereas SHF models prefer magic numbers at $N = 172$ and $Z = 120$, other models like the relativistic mean-field theory (RMF) suggest $N = 184$ and $Z = 124, 126$ [58]. Figure 2.6 presents calculated shell-correction energies in the region of superheavy elements for both SHF and RMF models using different parametrizations.

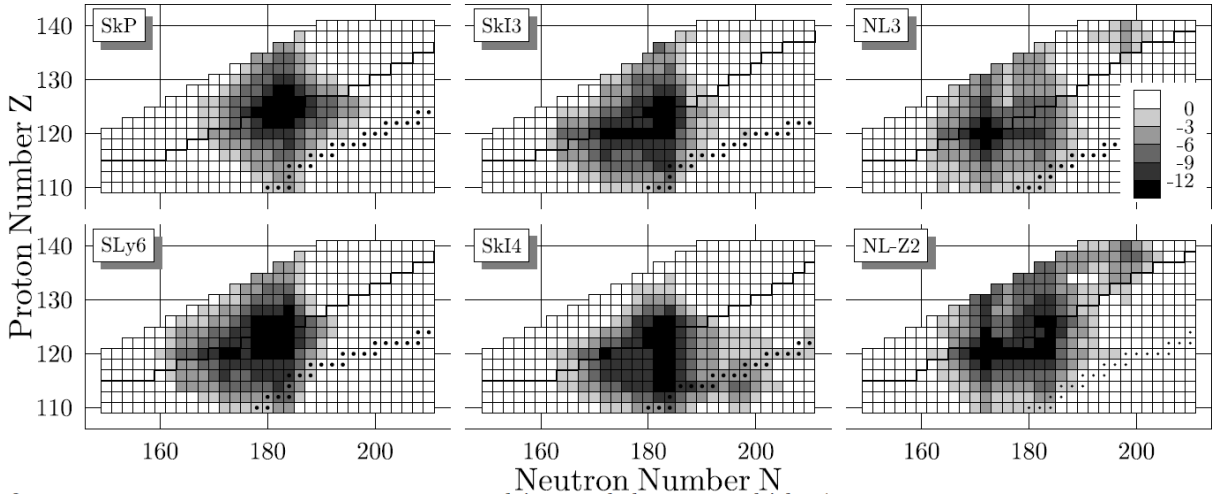


Figure 2.6: Calculated shell-correction energies (in MeV) using the Skyrme-Hartree-Fock model (SHF) and the relativistic mean-field theory (RMF) using different parametrizations. SkP [59], SLy6 [60], SkI3 [61] and SkI4 [61] in the case of SHF and NL3 [62] and NL-Z2 [63] in the case of RMF. Figure taken from [58].

## 2.7 Nuclear Isomers

Atomic nuclei are complex quantum systems that nonetheless often exhibit simple structural patterns. Investigations of excited nuclear states that differ from the ground state by the orbital configuration of their nucleons are key to reveal this structure and to benchmark nuclear models [12]. The excitation energy is usually released in prompt successive changes of the orbital configuration by emission of $\gamma$-ray radiation with half-lives often on the order of picoseconds. However, the decay probability of certain configurations is diminished by high angular momentum differences to lower-lying states requiring large multipolarities of the radiation. Such states are of particular interest as they may exhibit very long half-lives making them attractive for practical applications. Prominent examples are concepts for realizing a nuclear clock using

$^{229m}$Th [13] or energy storage using $^{178m}$Hf and attempts to build gamma ray lasers using $^{180m}$Ta[12]. Isomers may also play an important role in the formation of elements in stellar environments [64].

We distinguish three different classes of nuclear isomers: Spin-isomers occur for large spin differences between the isomeric and the ground state inhibiting electromagnetic decays based on angular momentum selection rules for high-multipole transitions. As an example, the isotope $^{180}$Ta naturally only occurs in its isomeric state. Resulting from the large difference in angular momentum, the decay of $^{180m}$Ta ($9^-$) into its ground state ($1^+$) has never been observed with an estimated half-life of $> 10^{16}$ years [65], exceeding the age of the universe by far. A large difference in shape between the initial (deformed) and final (less deformed) states also results in high-multipole transitions, leading to shape-isomers. In a deformed nucleus the energy of an orbit depends on its orientation with respect to the nucleus symmetry axis. For example, in axially-symmetric deformed nuclei, the energy depends upon the magnitude and projection of the total intrinsic angular momentum $K$ onto the symmetry axis. As a result, $K$-isomers can occur if the difference in orientation of the angular momentum between initial and final states requires high multipolarity of the electromagnetic radiation. Whereas spin-isomers are typically found near nuclear shell closures, $K$-isomers predominantly occur in between. This distinction becomes blurred in the region of the superheavy nuclei (SHN) with proton numbers $Z \geq 104$, where deformed shell closures are present (see figure 2.2). The study of nuclear structure in this region has been in the focus due to its proximity to the long-predicted island of stability. Experimental data in this region is still scarce as these exotic species must be produced artificially in complete fusion-evaporation reactions using particle accelerators providing high-intensity mid-heavy beams at Coulomb barrier energies. The achievable production rates rapidly drop from few ions per minute ($Z = 104$) down to about one ion per week ($Z = 118$). Despite this challenge, several isomeric states were identified by nuclear spectroscopy showing that isomerism in this region is a key feature [64].

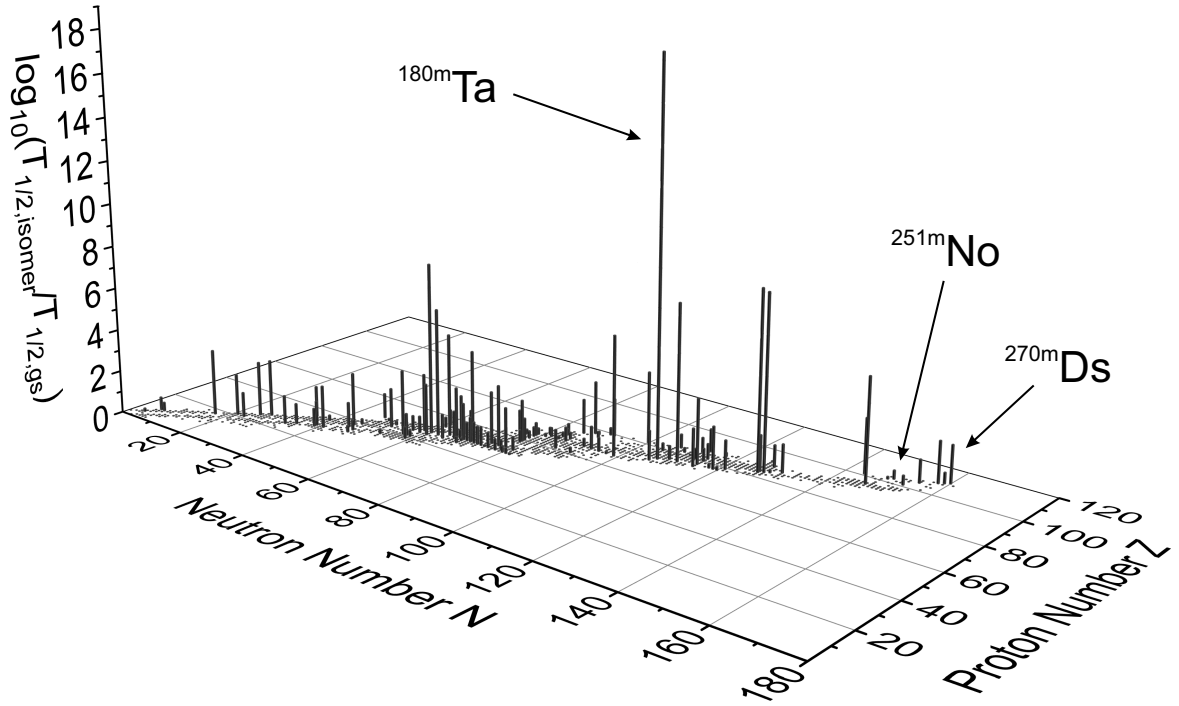


Figure 2.7: Logarithmic ratio of isomer to ground state half-life throughout the nuclear chart.

More than three decades after first experimental hints the isomeric state $^{254m}$No ($Z = 102$) at an excitation energy of 1.3 MeV was finally established [66]. Its underlying structure as a $K$-isomer at the deformed shell closure $N = 152$ demonstrates the high stability of these configurations against spontaneous fission. This can also be seen in the $K$-Isomer $^{270m}$Ds that exceeds the half-life of its ground state by about a factor of 60 [4] as seen in figure 2.7. Up to now, research in this area was restricted to the detection of decay products by means of decay spectroscopy. These measurements are inhibited by energy thresholds and background radiation and often require the derivation of complicated excitation level schemes. As stability enhances and half-lives increase, decay spectroscopy may become more difficult. An independent way to identify isomers in the region of SHN is offered by high-resolution mass spectrometry.

High-resolution mass spectrometry allows distinguishing nuclear states and measuring their excitation energies. However, the required mass resolving power in combination with the low incoming ion rate and small overall particle numbers demands a fast and efficient measurement scheme. This includes ion thermalization, preparation and measurement. First pioneering experiments with the mass spectrometer SHIPTRAP demonstrated that direct high-precision Penning-trap mass spectrometry (PTMS) in this region is indeed feasible [67, 68]. The precise determination of ground-state masses of nobelium ($Z = 102$) and lawrencium ($Z = 103$) ions with uncertainties down to 10 keV/c$^2$ pinned down the deformed neutron shell closure at $N = 152$ [69]. Although having been state-of-the-art at the time, the limitation in mass resolving power of the time-of-flight ion-cyclotron-resonance (ToF-ICR) technique (ultimately limited by the half-life) inhibited the measurement of any low-lying isomeric state in this region. In this work, this restriction is surpassed by applying the enhanced mass resolving power of the PI-ICR method. Throughout this work, ground states of the isotope $^{A}$X are denoted as $^{A}$X and $^{Ag}$X, respectively, whereas isomeric states are represented by $^{Am}$X.

# Chapter 3

# High-Precision Penning-Trap Mass Spectrometry at SHIPTRAP

SHIPTRAP is a double Penning-trap mass spectrometer located behind the Separator for Heavy Ion reaction Products (SHIP) [70] at the end of the UNIversal Linear ACcelerator (UNILAC) [71] at the GSI Helmholtz Centre for Heavy Ion Research, Darmstadt, Germany. It is dedicated to direct high-precision mass measurements of the heaviest elements, produced in fusion-evaporation reactions. The production cross sections for these type of reactions rapidly drop from micro-barn in the case of $^{254}$No (Z=102) down to the order of pico-barn in the case of the heaviest elements, resulting in production rates of few ions per second down to single ions per week [1]. In addition, direct high-precision PTMS requires a proper ion stopping, thermalization and preparation. Therefore, the cryogenic gas-stopping cell plays a crucial role during measurements. It is introduced in section 3.2 and described in more detail in section 4. Accounting unpreventable ion losses in these fundamental steps make these measurements challenging as detection rates and particle integrals are sparse. The ion production and separation is presented in section 3.1 while an overview of the setup is given in section 3.2. A more detailed description of the Penning-trap system is presented in section 3.3.

With the recent development of the PI-ICR technique (see section 3.6), the sensitivity of direct mass measurements has been improved. Compared to the ToF-ICR method, the mass resolving power and precision of PI-ICR for similar experimental conditions has been increased by up to a factor of 40 and 5, respectively [8, 9]. In addition, it can perform approximately 25 times faster compared to the ToF-ICR method as less ions are required to obtain a given statistical precision. Since its development at SHIPTRAP, the PI-ICR technique has proven itself in various off-line measurements at SHIPTRAP [72, 73, 74] to become state-of-the-art with respect to off-line high-precision mass spectrometry. Meanwhile, PI-ICR has been implemented at the Canadian Penning Trap (CPT) [75], ISOLTRAP [76] and JYFLTRAP [77] and first on-line experiments on light and mid-heavy elements have been performed using PI-ICR, including the simultaneous detection of ground and isomeric states [78, 79]. In these experiments detection rates and particle integrals were not limiting due to the relatively high production rates. This work represents the first successful application of PI-ICR in the region of the transfermium elements and proves the feasibility for this technique even at lowest detection rates and for only few detected ions in total.

## 3.1 Production and Separation of Heavy Ions at SHIP

The artificial production of transuranium elements with proton numbers $Z > 92$ requires complete fusion reactions using high-intensity heavy-ion beams at Coulomb barrier energies of about 5 MeV/u. The formation of a compound nucleus is very rare. In most cases the incident beam scatters elastically within the target. The compound system can fission depending on its excitation energy and fission barrier. For transfermium isotopes around neutron number $N = 152$, the evaporation of few neutrons from the compound is the most probable de-excitation channel. As an example, figure 3.1 shows the excitation functions for the production of $^{253-255}$No isotopes via the fusion-evaporation reactions $^{208}$Pb($^{48}$Ca,$x$n).

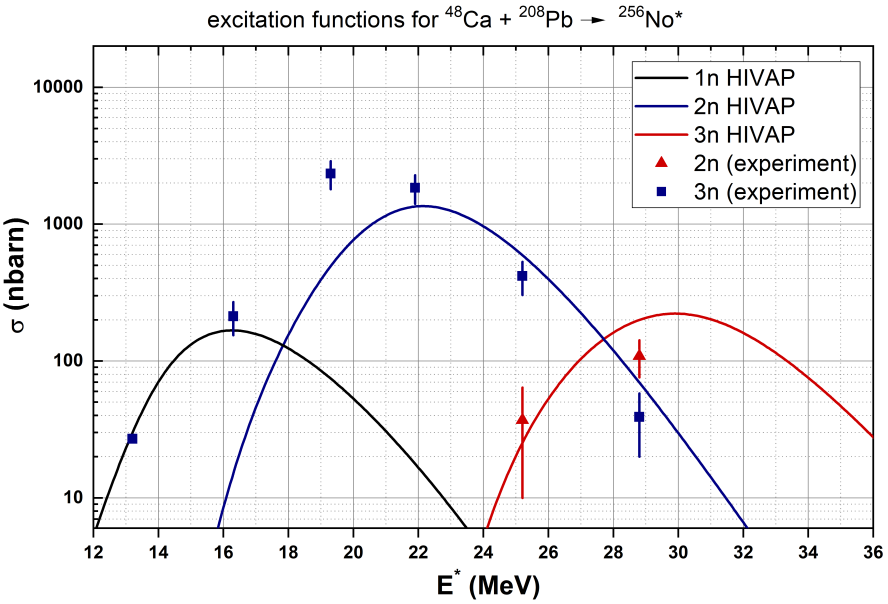


Figure 3.1: Excitation functions for the fusion-evaporation reactions $^{208}$Pb($^{48}$Ca,$x$n). The 1n-, 2n- and 3n-channel correspond to the production of $^{255}$No, $^{254}$No and $^{253}$No, respectively. The experimental data has been measured at SHIP [80] and compared to calculations using the HIVAP code [81, 82].

The cross section of $\approx 2\,\mu$b for the production of $^{254}$No is the highest amongst the transfermium elements. Therefore, this isotope is often targeted first by experimental techniques employed to explore the region of nuclei above fermium, e.g. by direct Penning-trap mass spectrometry in 2010 [67], laser spectroscopy in 2016 [83] and by multi-reflection time-of-flight mass spectrometry in 2018 [84]. The cross sections for these so-called fusion-evaporation reactions rapidly drop from micro-barn in the case of $^{254}$No (Z=102) down to the order of pico-barn in the case of the heaviest elements, resulting in production rates of few ions per second down to single ions per week [1]. For this, the SHIPTRAP facility is located at the GSI, in Darmstadt, Germany, behind its universal linear accelerator (UNILAC), which provides high-intensity $^{48}$Ca and $^{50}$Ti beams in the order of 1 particle $\mu$A that are used for the production of (super-)heavy elements. Table 3.1 gives an overview of the fusion-evaporation reaction products (EVRs) which are presented within the scope of this work.

The primary beam with beam intensities of 1 particle $\mu$A hits a rotating[1] target wheel. The EVRs have characteristic recoil energies in the order of several dozens MeV and are separated in-flight from the primary beam by the velocity filter SHIP shown in figure 3.2. Its transmission efficiency ranges from about 20 % to 50 %, depending on the fusion-evaporation reaction [89].

[1] To enlarge the beam-on-target surface and allow for a passive or active cooling of the target.

Table 3.1: Primary beam energies, fusion-evaporation reactions and production cross sections for the EVRs $^{251,254}$No, $^{254-256}$Lr and $^{257}$Rf. The cross sections comprise long-lived isomeric states.

| isotope | reaction | primary beam energy | cross section $\sigma$ |
|---|---|---|---|
| $^{251}$No | $^{206}$Pb($^{48}$Ca,3$n$) | 4.8 MeV/u | ≈15 nb [85] |
| $^{254}$No | $^{208}$Pb($^{48}$Ca,2$n$) | 4.56 MeV/u | ≈2000 nb [68] |
| $^{254}$Lr | $^{209}$Bi($^{48}$Ca,3$n$) | 4.81 MeV/u | ≈22 nb [86] |
| $^{255}$Lr | $^{209}$Bi($^{48}$Ca,2$n$) | 4.56 MeV/u | ≈250 nb [87] |
| $^{256}$Lr | $^{209}$Bi($^{48}$Ca,$n$) | 4.5 MeV/u | ≈60 nb [86] |
| $^{257}$Rf | $^{208}$Pb($^{50}$Ti,$n$) | 4.65 MeV/u | ≈15 nb [88] |

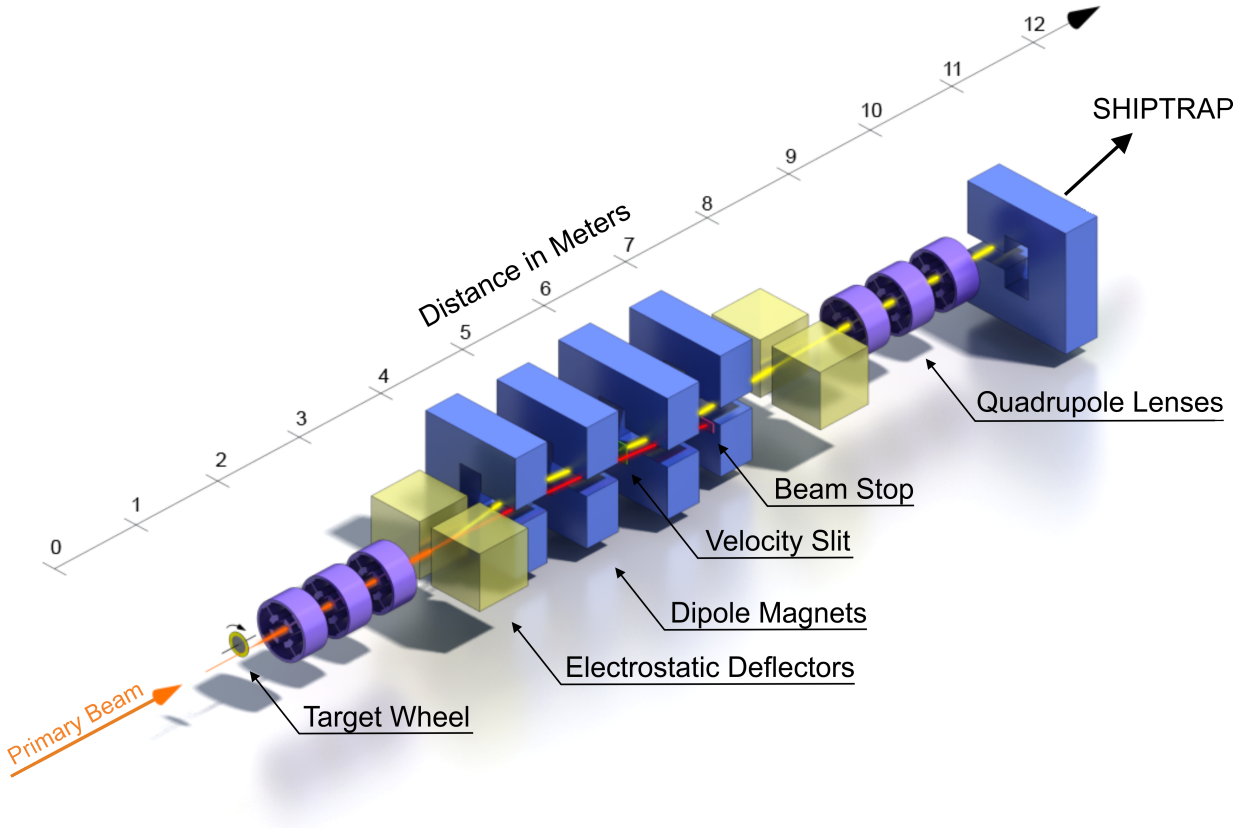


Figure 3.2: Schematic view of the separator for heavy ion reaction products (SHIP) located at the GSI Helmholtz Centre for Heavy Ion Research in Darmstadt, Germany. The primary beam (orange) hits a rotating target wheel. The recoiling fusion-evaporation reaction products (yellow) are separated in flight from the remaining primary beam and other unwanted ion species (red) by means of electrostatic and magnetic fields. Quadrupole lenses are used for proper beam focussing. Figure modified from [90].

## 3.2 The SHIPTRAP Setup

The SHIPTRAP setup is schematically depicted in 3.3. After their in-flight separation at SHIP, the ions are stopped in the active volume of the cryogenic buffer-gas stopping cell (CGC) which they accessed passing through optional degrader foils (typical thicknesses between 0.5 µm and 4.5 µm) and a titanium entrance window (typical thickness of 3.5 µm) [91]. Typical operation temperatures and pressures are 40 K and 7 mbar, respectively. The density corresponds to a room-temperature equivalent pressure of ≈ 50 mbar. Due to collisions between the ions and the residual helium buffer-gas atoms, charge exchange takes place. In the absence of any gas-impurities the resulting charge state of the ions, usually singly or doubly charged, is determined by the ionization potentials of the ion and the buffer gas atoms.

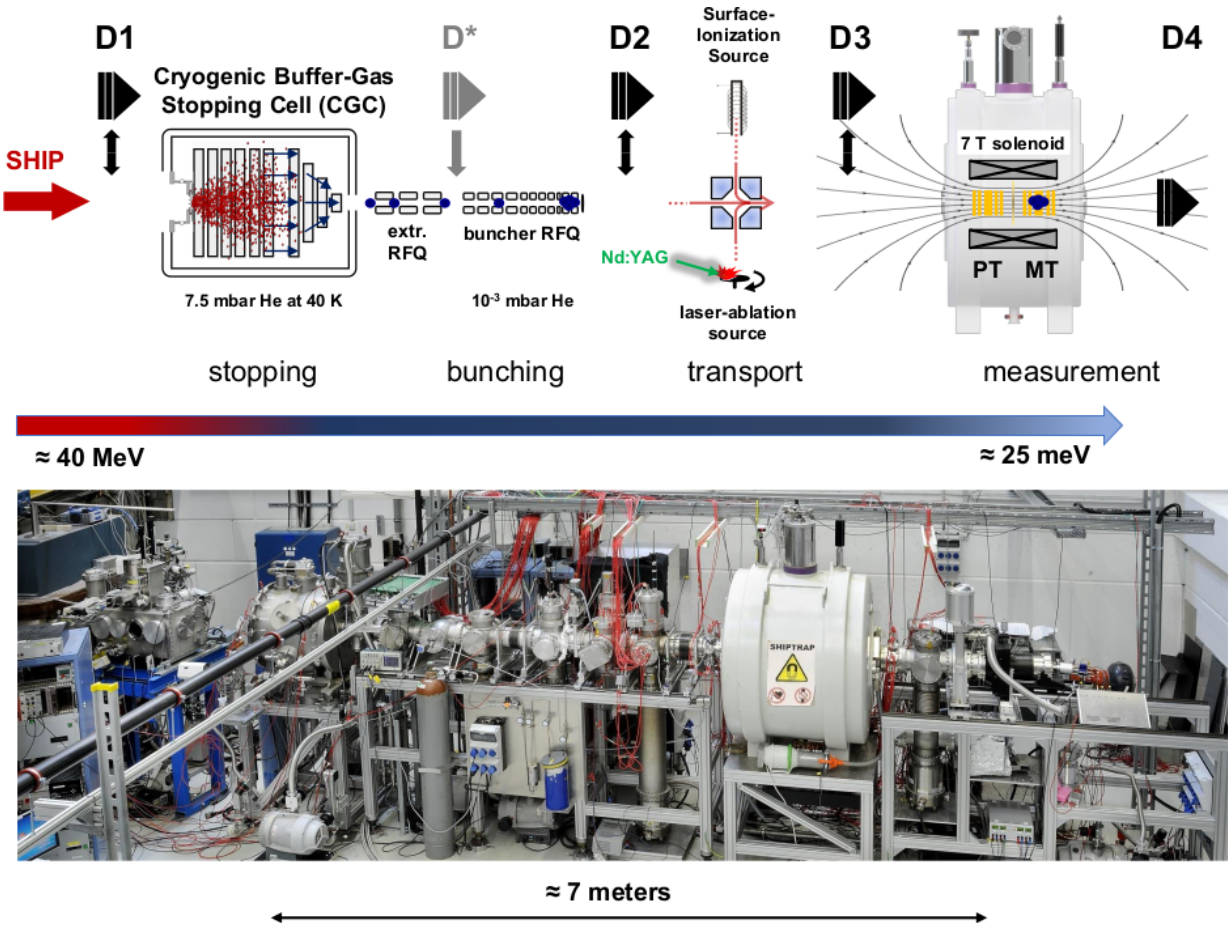


Figure 3.3: (Top figure) Schematic view of the SHIPTRAP setup. The fusion-evaporation reaction products are stopped and thermalized in the cryogenic buffer-gas stopping cell (CGC) and afterwards extracted using electric dc and rf fields. This is followed by ion guiding (extraction RFQ), ion bunching (buncher RFQ), ion preparation (preparation trap) and the high-precision mass measurement (measurement trap) using the position-sensitive detector at detector position D4. D1, D2 and D3 indicate additional detector positions (comprising $\alpha$ and time-of-flight detectors). Temporarily, an $\alpha$ detector at D$^*$ is used to test the CGC when de-assembled from the beam line. For further details see text. (Bottom figure) Photograph of the SHIPTRAP setup (vertically mirrored; credits G. Otto/GSI).

Hence, the ions are guided by the means of electric dc and rf fields towards an extraction nozzle of *de Laval type*, where ion guidance is undertaken by a gas-jet formation, followed by an rf quadrupole (extraction RFQ) ion guide. In this region the carrier gas is pumped away and the ions enter a low-vacuum regime at a pressure of $\approx 10^{-2}$ mbar. In a subsequent rf quadrupole buncher the ions are cooled and bunched using helium buffer gas at a pressure of $\approx 10^{-3}$ mbar. The section is followed by ion optics to ensure an efficient injection into the double Penning-trap system located inside the bore of a 7 T superconducting solenoid.

Within the scope of this work, several improvements and investigations of the CGC have been performed. They are presented in section 4. The double-Penning-trap system is explained in more detail in the following section 3.3.

## 3.3 The Double Penning-Trap System

SHIPTRAP makes use of two subsequent Penning traps located inside the bore of a 7 T superconducting magnet (figure 3.4). Penning traps are introduced in section 3.4 and in more detail in the appendix 10.1.

Both traps are separated via a diaphragm with a diameter of 1.5 mm acting as a pumping barrier. The first trap (Preparation Trap (PT)) is used for ion preparation which is discussed in more detail in section 3.5.3. The second trap (Measurement Trap (MT)) in combination with a position-sensitive detector is used to determine the cyclotron frequency of an ion. The detector is placed downstream, at the end of the beam line after the superconducting magnet, at a distance of about 80 cm with respect to the MT trap center. The high-precision mass spectrometry is carried out by means of the PI-ICR method, recently developed at SHIPTRAP [8, 9]. It is described in section 3.6. The determination of the atomic mass is presented in section 3.7.

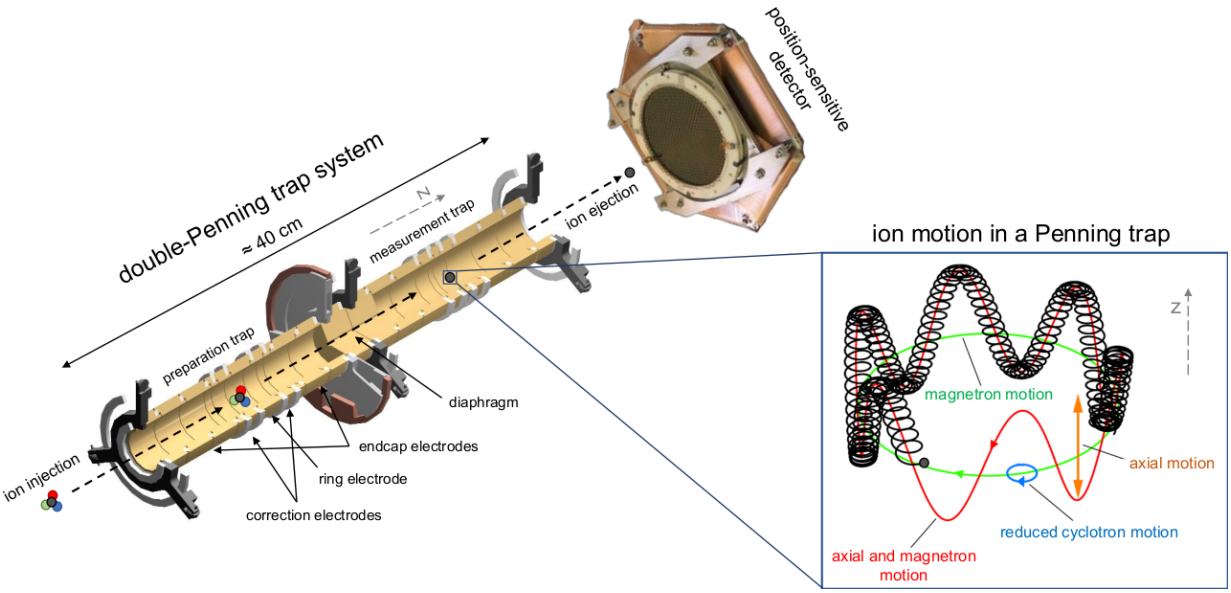


Figure 3.4: Sketch of the cylindrical double Penning-trap system used at SHIPTRAP. The traps are located inside the bore of a 7 T superconducting magnet. The magnetic field lines are oriented along the z-axis. The preparation trap is used for ion purification and preparation. The radial motion of the ion of interest is enhanced in the measurement trap and its frequency is determined according to the final position projected onto a position-sensitive detector placed downstream at the exit of the superconducting magnet. For this the ion is ejected out of the measurement trap. The distance between the detector and the traps is not to scale. The inlet figure shows the ion motion in a Penning trap (figure modified from [44]). Note the different orientation of the z-axis of the inlet figure with respect to the schematic depiction. For further details see text.

## 3.4 Ion Motion in a Penning Trap

An ion with charge-to-mass ratio $q/m$ exposed to a dipolar magnetic field pointing along the z axis (A10.5) oscillates with its so-called *true cyclotron frequency*

$$\omega_c = \frac{q}{m}|\vec{B}| \tag{3.1}$$

in the $x$-$y$-plane, perpendicular to the magnetic field axis. By superimposing the magnetic field with the electrostatic quadrupole field of the Penning trap (A10.6), the equations of motion in radial direction are modified. In general, the force $\vec{F}$ acting on an ion with the charge-to-mass ratio $q/m$ and the velocity $\vec{v}$ is then given by

$$\vec{F}(r,z) = m\frac{d^2}{dt^2}\vec{v}(r,z) = q\left(\vec{E}(r,z) + \frac{\vec{v}(r,z)}{c} \times B_0\vec{e}_z\right), \tag{3.2}$$

with the electric field $\vec{E}(r,z) = -\vec{\nabla}\phi(r,z)$. Due to its axial symmetry, the axial motion is decoupled from the radial motion. The equation of motion is solved by a harmonic oscillation in the axial direction using

the ansatz $z(t) = z_0 e^{-i\omega_z t}$ with the so-called *axial frequency*

$$\omega_z = \sqrt{\frac{q\tilde{C}_2 U_0}{md^2}} \tag{3.3}$$

and is independent of the magnetic field strength. To determine the radial motions in the $x$-$y$-plane the complex variable $u = x + iy$ is introduced [92]. The ansatz $u(t) = u_0 e^{-i\omega t}$ leads to

$$\omega^2 - \omega_c \omega + \frac{1}{2}\omega_z^2 = 0 \tag{3.4}$$

where equations (3.1) and (3.3) have been used. The eigenfrequencies

$$\omega_\pm = \frac{1}{2}\left(\omega_c \pm \sqrt{\omega_c^2 - 2\omega_z}\right) \tag{3.5}$$

correspond to two independent eigenmotions in the radial plane. The so-called *modified cyclotron motion* ($\omega_+$) originates from the true cyclotron motion of a free ion that is modified by the repulsive radial field component of the electrostatic potential reducing the centrifugal force.[2] The so-called *magnetron frequency* corresponds to a new mode of motion, which originates from an azimuthal $\vec{E} \times \vec{B}$ drift. The inlet of figure 3.4 illustrates the ion motion in a Penning trap. In addition to the stability criteria (A10.7), equation (3.5) requires its radical to be real for stable ion trajectories. This results in another stability criteria

$$\omega_c > \sqrt{2}\omega_z \Leftrightarrow B_0 > \sqrt{2\frac{m}{q}\frac{\tilde{C}_2 U_0}{d^2}}. \tag{3.6}$$

A Taylor expansion of equation (3.5) shows that the magnetron frequency to first order is ion independent

$$\omega_- \approx \frac{\tilde{C}_2 U_0}{2d^2 B_0}. \tag{3.7}$$

Note that equations (3.3) and (3.5) imply a hierarchy

$$\omega_c > \omega_+ \gg \omega_z \gg \omega_-. \tag{3.8}$$

In the context of mass spectrometry, the relation

$$\omega_c = \omega_+ + \omega_- \tag{3.9}$$

originating from the equation (3.5) is of great importance, as it directly connects the charge-to-mass ratio of an ion with the radial frequencies by means of equation (3.1). However, in the presence of magnetic and electric field imperfections, this relation is weakened and only serves as an approximation. These field imperfections are unavoidable due to e.g. an imperfect machining of the trap electrodes[3], patch potentials and electric field fluctuations [93]. Despite that, previous direct mass-measurements on stable ions have shown that this approximation is still valid to reach relative uncertainties in the order of $10^{-10}$. To reach lower uncertainties, the so-called *invariance theorem* [93]

$$\omega_c^2 = \omega_+^2 + \omega_-^2 + \omega_z^2 \tag{3.10}$$

can be used as it is less affected by field imperfections [93]. However, it requires to additionally measure the axial frequency $\omega_z$.

[2] The corresponding eigenfrequency is also referred to as the *reduced* cyclotron frequency.

[3] Hyperbolical Penning traps in addition suffer from imperfections originating from the in- and ejection hole in both endcaps.

## 3.5 Ion Manipulation and Preparation in a Penning Trap

When a stored ion is exposed to external rf fields, the ion motion can be manipulated in various ways. The extent of such manipulation depends upon several parameters like the applied frequency and amplitude, the excitation time and phase differences (see, e.g., [94]). The manipulation of an ion's motion equals the transfer or removal of energy in or from one of the ion's eigenmotion, respectively, and results into the change of the corresponding eigenmode's radius. Especially the removal of energy is of practical importance as it allows the ions to be cooled to low kinetic energies and energy spread. Whereas dipolar rf fields allow addressing and manipulating eigenmotions individually, quadrupolar fields enable the coupling and conversion between two eigenmodes. Both types are of importance for high-precision PTMS and are explained in more detail in sections 3.5.1 and 3.5.2. To address the radial eigenmodes, the external rf fields are applied via the (segmented) trap electrode (see figure 3.4). The following sections make use of the quantum mechanical framework provided by M. Kretzschmar [92, 95]. Here, the radial ion motions are described as complex amplitudes

$$\alpha_{\pm}(t) = |\alpha_{\pm}(t)| \cdot e^{+i(\varphi_{\pm}(t)+\chi_{\pm})} \tag{3.11}$$

with $\chi_{\pm} \equiv \phi_{\pm}(0)$ representing an initial phase [95]. The subscripts denote the magnetron ($-$) and modified cyclotron ion motion ($+$). The direction of motion (clockwise or anticlockwise) can be chosen arbitrarily. The axial motion is similarly described. The ion's absolute radius $R_{\pm}(t)$ and phase $\varphi_{\pm}(t)$ for any given time are obtained by

$$R_{\pm}(t) = \sqrt{\frac{\hbar}{m\pi(\nu_+ - \nu_-)}}|\alpha_{\pm}(t)| \quad \text{and} \tag{3.12}$$

$$\varphi_{\pm}(t) = \mathrm{Arg}(\alpha_{\pm}(t)) = \arctan\left(\frac{\mathrm{Im}(\alpha_{\pm}(t))}{\mathrm{Re}(\alpha_{\pm}(t))}\right), \tag{3.13}$$

with $|\alpha_{\pm}(t)| = \sqrt{\alpha_{\pm}(t)\alpha_{\pm}(t)^{\dagger}}$ being the absolute of the complex function $\alpha_{\pm}(t)$ [95]. Here, the superscript $\dagger$ corresponds to the complex conjugate. $\mathrm{Arg}(z)$, $\mathrm{Im}(z)$ and $\mathrm{Re}(z)$ are the complex argument, imaginary part and real part of a complex number $z$, respectively. Without any excitation we obtain

$$\alpha_{\pm}(t) = |\alpha_{\pm}(0)| \cdot e^{+i(\omega_{\pm}t+\chi_{\pm})}, \tag{3.14}$$

with the eigenfrequencies defined in equations (3.3) and (3.5). Note that $\alpha_{\pm}(0) = |\alpha_{\pm}(0)| \cdot e^{+i\chi_{\pm}}$ defines the initial phase.

### 3.5.1 Dipolar Excitation

Assume a dipolar excitation of the ion (mass $m$ and charge $q$) with angular frequency $\omega_d$, initial phase $\chi_d$ and amplitude $V_d$. The general solution for the resulting equations of motion is presented in equations (41) and (42) of [96] and the complex amplitudes evolve as

$$\alpha_{\pm}(t) = \alpha_{\pm}(0)e^{\mp i\omega_{\pm}t} \mp \frac{De^{\mp i(\chi_d-\phi_{\pm})}}{\omega_d-\omega_{\pm}}\left(e^{\mp i\omega_d t} - e^{\mp i\omega_{\pm}t}\right) \pm \frac{De^{\pm i(\chi_d+\phi_{\pm})}}{\omega_d+\omega_{\pm}}\left(e^{\pm i\omega_d t} - e^{\mp i\omega_{\pm}t}\right), \tag{3.15}$$

where $D = qV_d/(2\sqrt{2m\hbar\omega_1})$ with $\omega_1 \equiv \sqrt{\omega_c^2 - 2\omega_z^2}$ is proportional to the excitation amplitude. $\phi_{\pm}$ corresponds to the initial phase difference between the applied radio-frequency field and the ion motion. This alters the initial phase of the excitation $\chi_d$. The phase difference $\Delta_{\pm} \equiv \chi_d - \chi_{\pm} - \phi_{\pm}$ is of relevance. Note that the excitation affects both modes independently from each other. The last part, the so-called

*counter-rotating* term, can be omitted for a small detuning $\delta_{\pm}^{\mathrm{d}} \equiv \omega_d - \omega_{\pm}$ (*rotating wave approximation*). The superscript $d$ reflects a detuning with respect to a dipolar excitation and is used to distinguish it from a detuning $\delta^{\mathrm{q}}$ with respect to a quadrupolar excitation that is discussed in section 3.5.2. Within the rotating wave approximation and for $\alpha_{\pm}(0) = |\alpha_{\pm}(0)|e^{\mp i\chi_{\pm}}$ equation (3.12) leads to the ion radii

$$R_{\pm}(t) = |R_{\pm}(0) - \frac{qV_{\mathrm{d}}}{2m\omega_1} \cdot t \cdot \mathrm{sinc}(\delta_{\pm} t) \cdot e^{\mp i(\Delta_{\pm} - (\delta_{\pm}/2)t)}|. \tag{3.16}$$

Dipolar excitations allow increasing and decreasing the energy of the ion's eigenmotions if close to resonance, depending on the initial phase difference between the excitation and the ion (see figure 3.5).

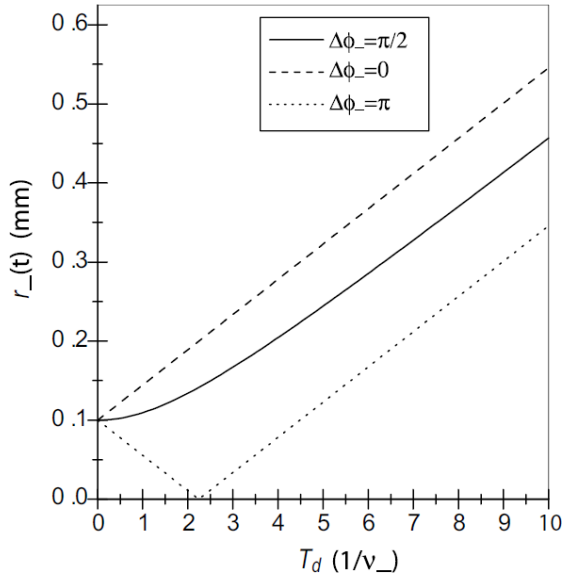


Figure 3.5: Temporal evolution of the magnetron radius exposed to a dipolar excitation at resonance as a function of the excitation time for different initial phase differences $\Delta_- = \phi_- = 0°$, 90° and 180°. The initial ion radius is arbitrary set to $R_-(0) = 0.1\,\mathrm{mm}$. Figure taken from [97].

### 3.5.2 Quadrupolar Excitation

Suppose a quadrupolar excitation in the radial plane of the ion at a frequency $\omega_{\mathrm{q}}$, initial phase $\chi_{\mathrm{q}}$ and amplitude $V_{\mathrm{q}}$ starting at time $t = 0$. For small detunings from the true cyclotron frequency of the ion $\delta^{\mathrm{q}} \equiv \omega_{\mathrm{q}} - \omega_c$ the complex amplitudes of the magnetron and modified cyclotron motion are given by [95]

$$\alpha_+(t) = e^{-i(\omega_+ + \delta^{\mathrm{q}}/2)t}\left[\left(\cos\left(\frac{\omega_{\mathrm{R}}t}{2}\right) + i\frac{\delta^{\mathrm{q}}}{\omega_{\mathrm{R}}}\sin\left(\frac{\omega_{\mathrm{R}}t}{2}\right)\right)\alpha_+(0) - i\frac{2g}{\omega_{\mathrm{R}}}\sin\left(\frac{\omega_{\mathrm{R}}t}{2}\right)e^{-i\chi_q}\alpha_-(0)\right], \tag{3.17}$$

$$\alpha_-(t) = e^{+i(\omega_- + \delta^{\mathrm{q}}/2)t}\left[-i\frac{2g}{\omega_{\mathrm{R}}}\sin\left(\frac{\omega_{\mathrm{R}}t}{2}\right)e^{+i\chi_q}\alpha_+(0) + \left(\cos\left(\frac{\omega_{\mathrm{R}}t}{2}\right) - i\frac{\delta^{\mathrm{q}}}{\omega_{\mathrm{R}}}\sin\left(\frac{\omega_{\mathrm{R}}t}{2}\right)\right)\alpha_-(0)\right], \tag{3.18}$$

with the *Rabi frequency* $\omega_{\mathrm{R}} = \sqrt{4g^2 - (\delta^{\mathrm{q}})^2}$ and the coupling parameter

$$g = \frac{q}{2m(\omega_+ - \omega_-)}\frac{\tilde{C}_{2\mathrm{q}}}{d^2} = \frac{\omega_c}{2(\omega_+ - \omega_-)}\frac{\tilde{C}_{2\mathrm{q}}}{d^2 B}, \tag{3.19}$$

respectively [95]. Here, $\tilde{C}_2 \approx 0.5$ and $d = 0.025\,\mathrm{mm}$ are the dimensionless scaling factors and the characteristic trap dimension, respectively, as used in equation (A10.6). The equality in equation (3.19) makes use of the true cyclotron frequency of the ion $\omega_c = (q/m)B$. Note that the Rabi frequency defines the pace at which the interconversion between modes happen. For a pure initial ion motion, e.g. either $\alpha_+(0) = 0$ or $\alpha_-(0) = 0$ at resonance ($\delta^{\mathrm{q}} = 0$) a full interconversion occures if $\omega_{\mathrm{R}}t/2 = \pi/2 + 2\pi p$ with $p$ being an

integer value. This leads to a minimum conversion time of $t_{\mathrm{conv}} = \pi/\omega_{\mathrm{R}} = (2\nu_{\mathrm{R}})^{-1}$ where $\omega_{\mathrm{R}} \equiv 2\pi\nu_{\mathrm{R}}$. For an ion mass-to-charge-ratio $m/q = 125$, a magnetic field strength of 7 T and an excitation amplitude of 9.5 V $\omega_{\mathrm{R}} \approx 1060\,\mathrm{rad/s}$ and $t_{\mathrm{conv}} \approx 3\,\mathrm{ms}$. Figure 3.7 visualizes the interconversion of the radial modes.

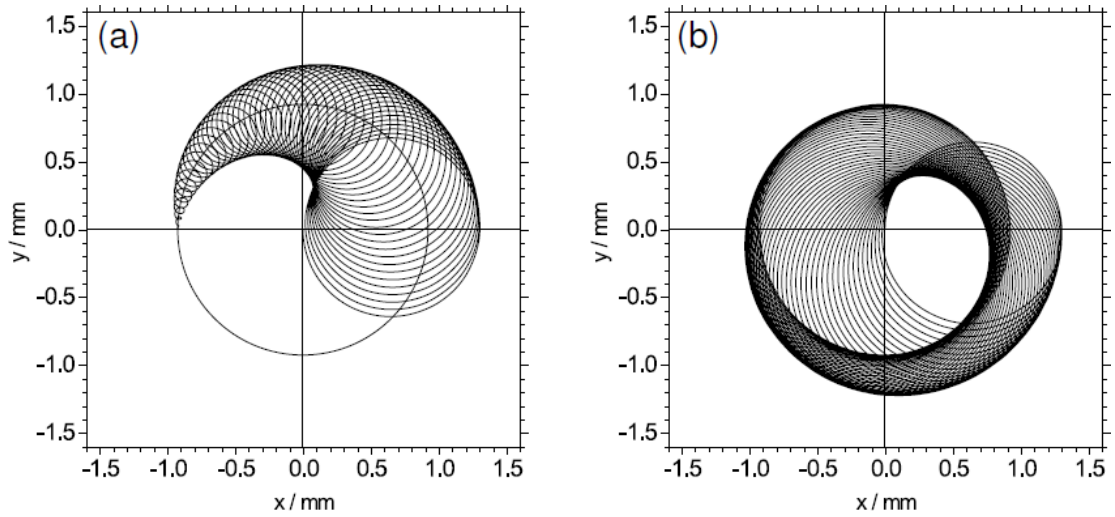


Figure 3.6: The interconversion from the magnetron into the modified cyclotron motion by applying a quadrupolar excitation at resonance ($\nu_{\mathrm{rf}} = \nu_- + \nu_+$). At start the ion performs a pure magnetron motion which corresponds to the circle drawn around the origin. During the quadrupolar excitation the magnetron radius is reduced, while the modified cyclotron radius increases. After one full conversion time the modified cyclotron radius corresponds to the initial magnetron radius. (a) and (b) show the first and second half of the conversion, respectively. Figure taken from [44].

### 3.5.3 Mass-selective Buffer-Gas Cooling in the Preparation Trap

When exposed to a residual buffer gas in the Penning trap the ion with mass $m$ and charge $q$ experiences a damping force [98] proportional to its velocity $v$

$$\vec{F}_{\mathrm{d}} = -\delta m\vec{v} \quad \text{with} \quad \delta = \frac{q}{m}\frac{1}{K_0}\frac{p/p_0}{T/T_0}. \tag{3.20}$$

It depends upon the reduced ion mobility $K_0$ and the buffer-gas pressure $p$ and $T$ with respect to standard conditions at $p_0 = 1013.25\,\mathrm{bar}$ and $T_0 = 273.15\,\mathrm{K}$, respectively. The damping force originates from collisions between the ion and the buffer-gas atoms. As a result any eigenmode will exponentially lose energy. The radial eigenmotions of an ion in a Penning trap are then characterized by initial radii $R_\pm(0)$ which evolves in time according to [98]

$$R_\pm(t) = R_\pm(0)e^{\mp\delta\frac{\omega_\pm}{\omega_+-\omega_-}t}. \tag{3.21}$$

The energy loss decreases the radius of the modified cyclotron mode (+) but increases the radius of the magnetron mode (−). In addition, due to $\omega_+ >> \omega_-$ the decrease is much faster than the increase. Thus, sooner or later, any ion exposed to buffer gas is lost due to its constantly increasing magnetron radius. This is exploited in buffer-gas cooling techniques [98]. Here, the ion's magnetron radius is reduced by applying a quadrupolar excitation at the true cyclotron frequency as discussed in section 3.5.2 which effectively leads to a centering of the ion in the Penning trap. As this strongly depends on the mass-to-charge ratio of the ion, the buffer-gas cooling is mass-selective. Currently, the buffer-gas technique is used in the preparation trap of SHIPTRAP reaching mass resolving powers in the order of 100 000 which is sufficient to remove

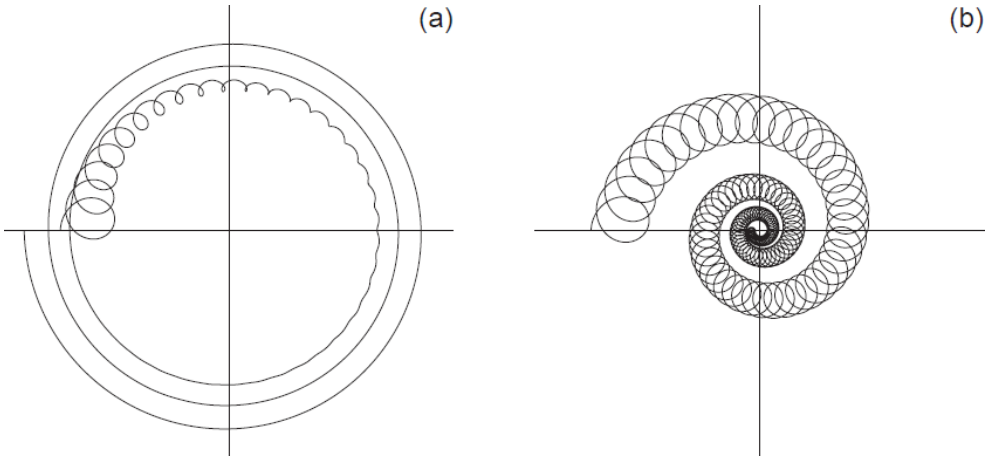


Figure 3.7: Schematic visualization of the buffer-gas cooling. (a) No rf fields applied. Without any excitations the buffer-gas rapidly dampens the modified cyclotron motion and reduces its radius. The dampening of the magnetron motion results in a slow increase of the magnetron radius. (b) By coupling both radial modes via a quadrupolar excitation at $\nu_{\mathrm{rf}} = \nu_c = \nu_+ + \nu_-$ the radii of the magnetron and modified cyclotron motion are successively reduced and the ion is centred in the preparation trap. For further details see text. Figure taken from [99].

isobaric contaminations. After cooling, the ions are in thermal equilibrium with the atoms of the buffer gas. As SHIPTRAP operates at room temperature, the kinetic energy of the ions after buffer-gas cooling corresponds to about 25 meV.[4]

## 3.6 Phase-Imaging Ion-Cyclotron-Resonance Technique

The Phase-Imaging Ion-Cyclotron-Resonance (PI-ICR) technique makes use of a position-sensitive detector (type DLD40 from RoentDek GmbH) with an active diameter of 42 mm and a position resolution of 70 µm. Is is positioned on-axis with respect to the symmetry axis of the Penning traps at a distance of about 80 cm from the center of the measurement trap outside of the superconducting magnet.[5] The basic idea of PI-ICR originates from the definition of frequency itself. Frequency is defined as the amount of accumulated phase, e.g. a full circle, per unit time. The projection of the radial eigenmotion of an ion onto the position-sensitive detector for two different storage times in the Penning trap allows obtaining the frequency value by measuring the accumulated phase difference [100].

### Single-Pattern Scheme

As illustrated in figure 3.8, the projection is performed by ejecting the ion from the measurement trap onto the detector.[6] Suppose an ion to be prepared in a pure magnetron state at a well-defined radius with respect to the trap center and without residual energy in the modified cyclotron and axial mode. In this state the ion's trajectory is solely given by a circular orbit around the trap axis with the magnetron frequency $\omega_-$. If the ion is ejected from the measurement trap at the time $t_0$ it hits the detector at a given radius and phase $\phi_-^{\mathrm{ref}}$ (*reference phase*). Suppose that the same procedure is performed on another ion of identical species. This time, prior to ejection, the ion spends an additional *accumulation time* $t_{\mathrm{acc}}$ in the

[4] Resulting from $k_B T$, where $k_B = 8.6 \times 10^{-5}$ eV/K represents the Boltzman constant.

[5] Due to limitations in the maximal ambient magnetic field strength of $< 100$ mT, it cannot be positioned closer to the measurement trap.

[6] Thus, PI-ICR is a *destructive* measurement technique in the sense that an ion, after being detected, is no longer available for additional measurements.

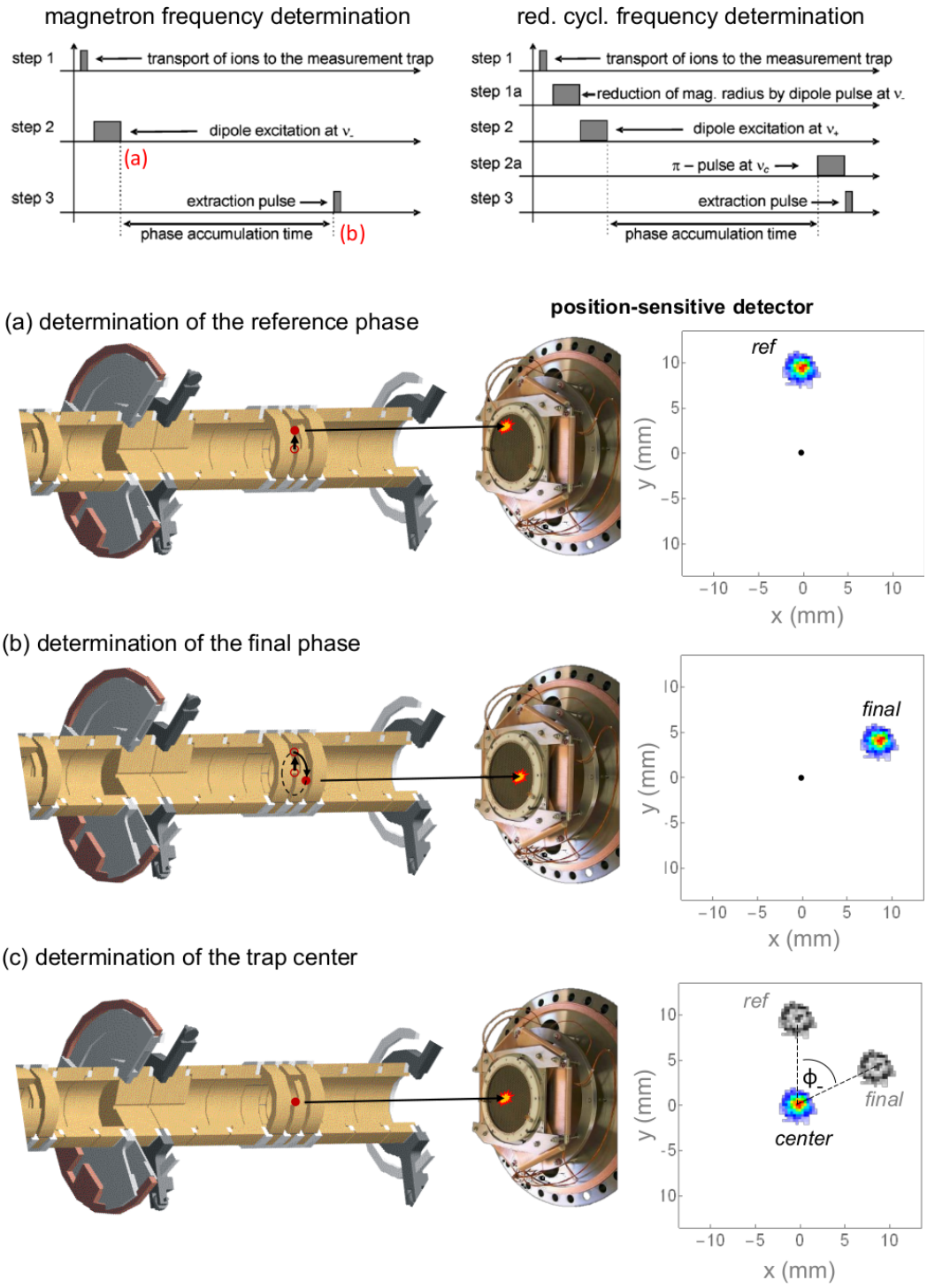


Figure 3.8: Schematic depiction of the *single-pattern* PI-ICR measurement scheme used to determine the magnetron and modified cyclotron frequency of an ion at SHIPTRAP. (Upper panel) The patterns used to obtain the frequencies are presented (modified from [9]). (Lower panel) Exemplary, figures (a) to (c) show the determination of the magnetron frequency $\nu_-$. (a) The ion is transported to the measurement trap and its magnetron eigenmotion is excited using a dipolar excitation at $\nu_{\mathrm{rf}} = \nu_-$. Immediately afterwards the ion is ejected out of the trap onto the position-sensitive detector. (b) The ion is transported into the measurement trap and excited as in (a). After its excitation an additional phase accumulation time $t_{\mathrm{acc}}$ is waited prior to its ejection out of the trap. During this time, the ion accumulates a phase given by $\nu_- t_{\mathrm{acc}}$. (c) The center position of the measurement trap is obtained according to (b) but without any excitation. The magnetron frequency is determined by the accumulated phase difference $\phi_- \equiv \phi_-^{\mathrm{final}} - \phi_-^{\mathrm{ref}}$ between the *reference* and *final* phase image. For this the center position need to be measured.

measurement trap and the phase $\phi_-^{\text{final}}$ (*final phase*) is detected. The difference between the final and the reference phase directly gives access to the magnetron frequency

$$\nu_- = \frac{(\phi_-^{\text{final}} - \phi_-^{\text{ref}}) + 2\pi \times n_-}{2\pi \times t_{\text{acc}}} \tag{3.22}$$

with which the ion orbited during the accumulation time $t_{\text{acc}}$.[7] The integer value $n_-$ accounts for full magnetron ion evolutions. The cyclotron frequency

$$\nu_+ = \frac{(\phi_+^{\text{final}} - \phi_+^{\text{ref}}) + 2\pi \times n_+}{2\pi \times t_{\text{acc}}} \tag{3.23}$$

is obtained similarly with a slight modification (see figure 3.8 - upper panel). In this case the number of full modified cyclotron evolutions is given by $n_+$. In practice the axial motion cannot be damped entirely. Thus, the ions in addition to their radial motion oscillate in axial direction due to the residual axial amplitude. As this motion is uncorrelated to the radial motions, the ions will be ejected from different axial positions which results into a time-of-flight distribution at the detector with a typical FWHM of about 1 µs. During this time span an ion with a modified cyclotron frequency of about 845 kHz (corresponding to a mass-to-charge ratio of $m/q = 125$ at a magnetic field of 7 T) accumulates a phase of about 300 °. Prior to the ejection, the modified cyclotron mode is converted into the slower magnetron motion. The additional change in phase introduced by the interconversion is equal for the reference and final phase measurement if the same quadrupole excitation is used in both cases. The phase between the reference and final phase of the modified cyclotron frequency stays unaffected. Using equations (3.22) and (3.23) in combination with equation (3.9) immediately gives access to the true cyclotron frequency

$$\nu_c = \frac{\omega_c}{2\pi} = \frac{\left((\phi_+^{\text{final}} - \phi_+^{\text{ref}}) + (\phi_-^{\text{final}} - \phi_-^{\text{ref}})\right) + 2\pi \times (n+m)}{2\pi \times t_{\text{acc}}} \tag{3.24}$$

of the ion. Note that equation (3.24) only holds if the accumulation time is equal for the measurement of the magnetron and modified cyclotron frequency, respectively. Thus, a measurement of the four phases $\phi_\pm^{\text{ref}}$ and $\phi_\pm^{\text{final}}$ is sufficient for a mass measurement. As a phase in theory can be measured with one single ion event, a minimum of four ions are required. In practice, mainly due to residual radii in the opposing radial mode, several ions are required to ensure a correct phase assignment.[8]

### Double-Pattern Scheme

As discussed in [8] the ion's phase after a quadrupolar excitation is mirrored, resulting in a change of sign. This is exploited in the so-called *double-pattern* scheme in which only the final phases of both radial motions are measured to directly obtain the true cyclotron frequency via

$$\nu_c = \frac{\omega_c}{2\pi} = \frac{\phi + 2\pi(n+m)}{2\pi \times t_{\text{acc}}} \tag{3.25}$$

with the phase difference between the final phases $\phi \equiv \phi_-^{\text{final}} - \phi_+^{\text{final}}$. Compared to equation (3.24) the statistics required to perform a mass measurement is reduced by a factor of two. Since $\nu_+ \gg \nu_-$ the statistical uncertainty for the determination of $\nu_c$ is dominated by the determination of $\phi_+$final. Therefore, in low-rate experiments where detected ion events are sparse, $\phi_+^{\text{final}}$ is measured more often with respect to $\phi_-^{\text{final}}$.

[7] As every ion passes the same (magnetic) field gradient, the unknown accumulated phase throughout the ejection $\phi_0$ is the same for both cases. Therefore, the phase difference between the reference and the final phase is unaffected.

[8] For this, the opposing radial mode is *scanned*, i.e. the accumulation time is increased up to one period of the opposing radial mode.

The PI-ICR double-pattern scheme used within the scope of this work is presented in figure 3.9. It relies on a dipolar excitation at $\nu_{\mathrm{rf}} \approx \nu_+$ and a quadrupolar excitation at the true cyclotron frequency of the ion of interest $\nu_{\mathrm{rf}} \approx \nu_c$. Both frequencies are mass-dependent. The fact that the ion's mass itself is measured by PI-ICR sounds counter-intuitive. However, it can be shown that these excitations do not need to be in resonance up to a certain extent. In fact, any systematic error introduced due to non-resonant excitations cancel out if only one single ion species is measured and the excitations are the same in the magnetron and modified cyclotron pattern of the PI-ICR double-pattern scheme presented in figure 3.9.

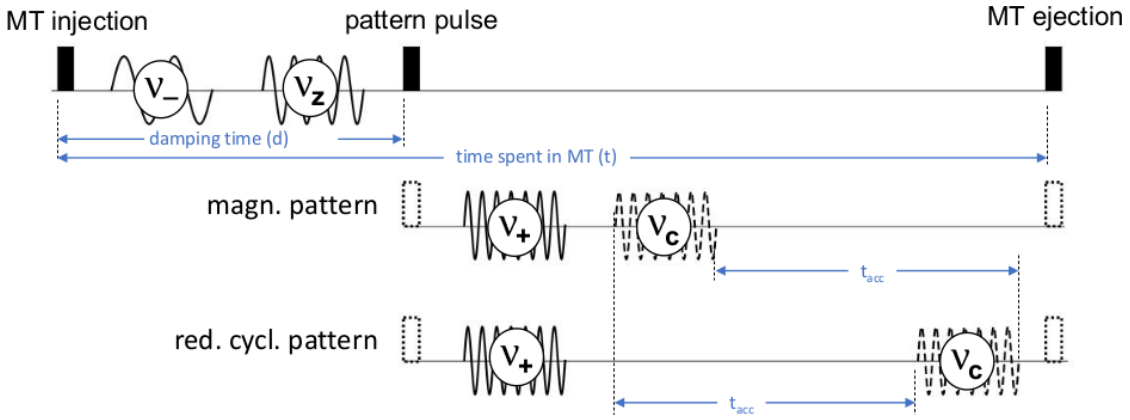


Figure 3.9: PI-ICR double-pattern scheme of this work. The dipolar excitations at $\approx \nu_-$ and $\approx \nu_z$ within the *dampening time d* are used to dampen the magnetron and axial mode of the ions after the transport from the preparation into the measurement trap. The PI-ICR cycle starts with the dipolar excitation at $\nu_+$, followed by a quadrupolar excitation at $\approx \nu_c$. The final phases of the magnetron and modified cyclotron mode after a given accumulation time $t_{\mathrm{acc}}$ are obtained by a rearrangement of the quadrupolar excitation. Note that any ion is either measured in the magnetron or the modified cyclotron pattern. For further details see text.

## 3.7 High-Precision Penning-Trap Mass Spectrometry

The atomic mass of an atom with proton number $Z$ and neutron number $N$ is given by

$$m(N,Z) = Z \times (m_p + m_e) + N \times m_n - \left( E_{\mathrm{nucl}}/c^2 + \sum_{i=1}^{Z} E_{e,i}/c^2 \right), \tag{3.26}$$

where $m_p, m_n$ and $m_e$ are the proton, neutron and electron masses, respectively. $E_{\mathrm{nucl}}$ corresponds to the total binding energy of the nucleons and $E_{\mathrm{e,i}}$ to the individual binding energy of the $i^{\mathrm{th}}$ bound electron[9], respectively. The mass of an ion with charge state $0 \leq q \leq Z$ is therefore given by

$$m(N,Z,q) = Z \times (m_p + (1-q)m_e) + N \times m_n - \left( E_{\mathrm{nucl}}/c^2 + \sum_{i=1}^{Z-q} E_{\mathrm{e,i}}/c^2 \right). \tag{3.27}$$

Compared to equation (3.26) the mass of the ion is reduced by $q$ times the electron mass and the missing binding energies of the $q$ weakest bound electrons. In direct high-precision PTMS of the heaviest elements at SHIPTRAP, the charge states are typically limited to singly- or doubly-charged ions[10] and the reached mass uncertainties are in the order of few keV/$c^2$. In this case the binding of energy of the missing electrons in the order of few tens of eV can be neglected. Since the proton, neutron and electron masses from

[9] For simplicity we assume that the electrons are in their ground state.

[10] Even though the EVRs are produced in higher charge states, the EVRs are subjected to charge-exchange with the buffer-gas atoms during their slow down in the CGC, which reduce their final charge state typically to $1^+$ or $2^+$.

equation (3.27) are known with high precision, the direct mass spectrometry of an ion also corresponds to a direct measurement of its nuclear binding energy.

According to the expression $2\pi\nu = (q/m)B$ (see equation (3.1)), an accurate determination of the ion mass requires the measurement of its true cyclotron frequency with high accuracy, as well as an equally precise measurement of the magnetic field strength $B$. The latter is achieved by measuring the true cyclotron frequency of a reference ion of well-known atomic mass $m_{\mathrm{ref}}$ and charge $q_{\mathrm{ref}}$. To minimize systematic uncertainties, a similar charge-to-mass ratio of the reference ion with respect to the ion of interest is favoured, preferably isobars [101]. The systematic uncertainty due to a difference in the charge-to-mass ratio is evaluated in section 6.5.3. For doubly-charged transfermium ions at SHIPTRAP, single-charged $^{133}Cs^{+}$ ions from a surface ion source are used. In the case of singly-charged transfermium ions, either carbon clusters $[^{12}C_n]^{+}$, $[^{123}Sb_2]^{+}$ and $[^{124}Sn_2]^{+}$ clusters from a laser-ablation source are available [102, 101]. Both ion sources are positioned upstream with respect to the Penning traps (see figure 3.3). The magnetic field strength is then represented by $B_{\mathrm{ref}} = (m_{\mathrm{ref}}/q_{\mathrm{ref}})2\pi\nu_{\mathrm{ref}}$. It is therefore convenient to state the result of a high-precision PTMS by means of the true cyclotron frequency ratio

$$R = \frac{\nu_{\mathrm{ref}}}{\nu}. \tag{3.28}$$

The experimentally obtained atomic mass of the ion of interest is then obtained by

$$m_{\mathrm{exp}} = \frac{q}{q_{\mathrm{ref}}} R\,(m_{\mathrm{ref}} - q_{\mathrm{ref}} m_e) + q m_e. \tag{3.29}$$

## 3.8 Mass Resolving Power and Isobaric Separation

Besides low production rates and sparse particle integrals, direct high-precision mass spectrometry in the region of the heaviest elements faces yet another challenge. In this region several long-lived isomers have already been identified (see e.g. [64]). They are often populated throughout the same production reactions as the corresponding ground state. Therefore, any direct mass measurement that aims at determining the atomic (ground-state) mass of an isotope needs to ensure that no isomeric state contributes to the measurement. This becomes in particular challenging if the isomeric state has a half-life comparable with the measurement time. A possible solution is to use a sufficient mass resolving power to disentangle any isomeric state from the respective ground state. In the region of the heaviest elements this is not trivial given the fact that transfermium ions are currently only available in low charge states, typically singly or doubly charged. In fact, multireflection time-of-flight mass spectrometry (mass resolving powers of several 100 000) and even ToF-ICR MS (mass resolving powers of up to 1 000 000) are often insufficient to resolve low-lying isomeric states in this region, as illustrated for ToF-ICR in the case of $^{255}$Lr (see figure 7.5). The enhanced mass resolving power of PI-ICR on the other hand is sufficient to resolve low-lying isomeric states down to excitation energies of several tens of keV for doubly-charged transfermium ions with a half-life in excess of one second. A comparison between ToF-ICR and PI-ICR in the context of the direct high-precision PTMS of $^{255}$Lr is given in section 7.2.6.

The $\beta$ decays within the decay chain of the recoil-ion sources $^{223}$Ra and $^{225}$Ac (see figures 4.2) result in isobar doublets that can be accessed by PI-ICR measurements off-line. They may be used to quantify the

mass resolving power

$$\mathbb{R} \approx \frac{\pi \nu_+ t_{\mathrm{acc}} R_+}{\Delta R_+} \tag{3.30}$$

of SHIPTRAP for given experimental conditions. $R_+$ corresponds to the radius of the modified cyclotron phase image and $\Delta R_+$ its FWHM. Depending on their $Q(\beta^-)$ value, the mass difference can be on the order of the mass differences between isomeric and ground states, e.g., the value for the $\beta^-$ decay of $^{207}\mathrm{Tl}^+$ into $^{207}\mathrm{Pb}^+$ is given by $Q(\beta^-) = 1.4\,\mathrm{MeV}$ [103] which is very close to the excitation energy of $^{254m}$No of $\approx 1.3\,\mathrm{MeV}$ [104]. Figure 3.10 shows the isobaric separation of $^{207}\mathrm{Pb}^+$ with respect to $^{207}\mathrm{Tl}^+$ and $^{209}\mathrm{Tl}^+$ with respect to $^{209}\mathrm{Pb}^+$.

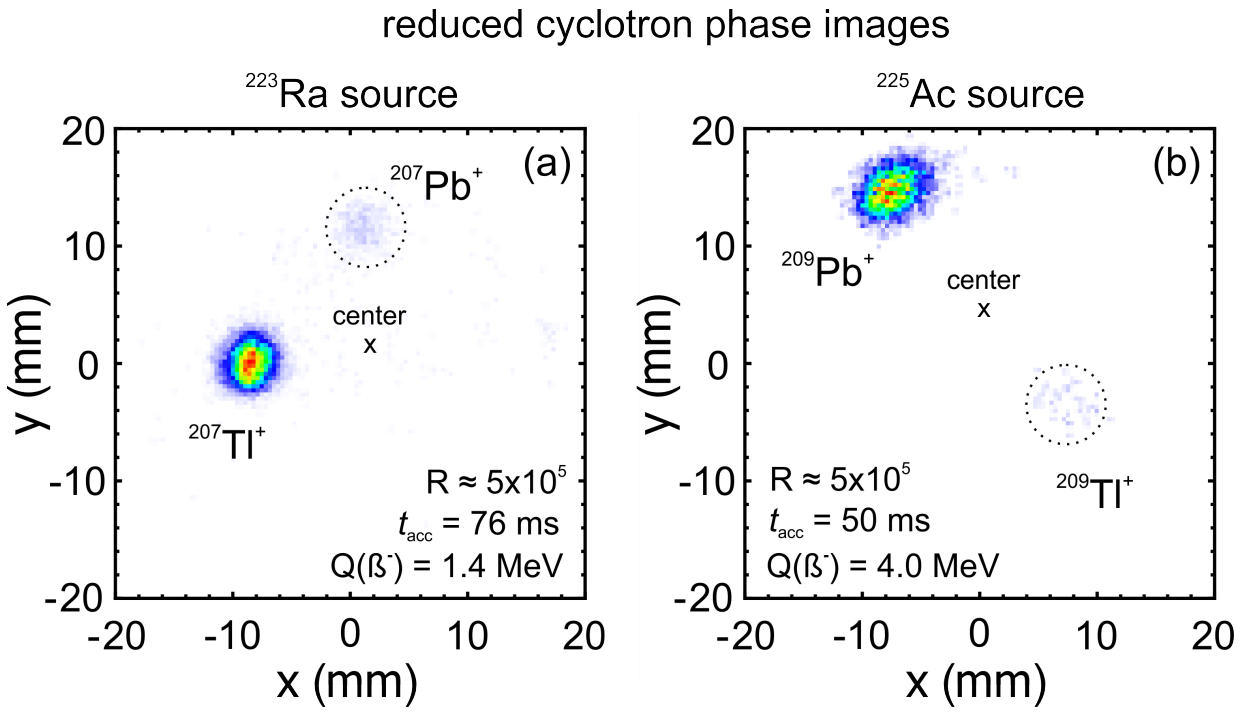


Figure 3.10: Isobaric separation of singly-charged lead and tellurium ions originating from the recoil-ion sources $^{223}$Ra (a) and $^{225}$Ac (b). The final modified cyclotron phases after a given accumulation time $t_{\mathrm{acc}}$ are shown. The isobars are connected via a $\beta^-$ decay. The corresponding $Q(\beta^-)$ values as well as the achieved mass resolving powers $R$ are given. For further details see text.

The modified cyclotron phase images of both species are very well separated at an accumulation time of 76 ms. The angle difference correspond to $\approx 90\,^\circ$. In this measurement the final phase images are obtained by performing a PI-ICR double-pattern measurement with a dipole excitation at 518 346.414 Hz with $3.5\,\mathrm{V_{pp}}$ for 1.0 ms and a conversion pulse at 519 688.315 Hz with $9.5\,\mathrm{V_{pp}}$ for 3.1 ms. The data was taken for $\approx 22$ hours. In the case of the isobaric separation between $^{209}\mathrm{Tl}^+$ and $^{209}\mathrm{Pb}^+$ the corresponding $Q(\beta^-)$ value corresponds to 4.0 MeV [103]. Thus, at an accumulation time of 50 ms a phase difference of $\approx 180\,^\circ$ is obtained. Here, a dipole excitation at 513 368.727 Hz with $1.5\,\mathrm{V_{pp}}$ for 1.6 ms and a conversion pulse at 514 697.14 Hz with $4.3\,\mathrm{V_{pp}}$ for 6.4 ms is used. The measurement time is 1.5 hours. The center positions of the trap are measured using both ion species without any excitation.[11] In both cases the mass resolving power, given by the FWHM of the fitted phase images divided by their radius, has a similar value of $\mathbb{R} = 5 \times 10^5$. The mass resolving power is proportional to the accumulation time $t_{\mathrm{acc}}$ (see equation

[11] The smaller phase spot radii for the $A = 207$ mass doublet with respect to the other is explained by a *weaker* dipole excitation (the energy transfer to the ion is approximately proportional to the excitation amplitude and excitation time, see section 3.5.1). In addition, the center spot position between both figures is shifted by several millimetres. This is due to a lateral translation of the detector with respect to the trap axis.

(3.30)). Thus, based on figure 3.10 a mass resolving power of

$$\mathbb{R} \approx 6\,\text{million} \times q[e] \times t_{\text{acc}}[s] \tag{3.31}$$

is obtained at SHIPTRAP for the given experimental conditions. The obtained mass resolving power is scaled by the charge of the ion $q$. For the interesting case of the low-lying isomeric state $^{255m}$Lr with an excitation energy of $\approx 37\,\text{keV}$ [105], an accumulation time of about 1.2 s results into a phase difference of $\approx 50\,^\circ$ if both, the isomeric and the ground state, are measured as doubly-charged ions.

# Chapter 4

# The Cryogenic Gas-Stopping Cell

The production of transfermium nuclei in fusion-evaporation reactions requires primary beam energies in the order of 5 MeV/u to overcome the Coulomb repulsion, which results in recoil energies with tens of MeV. As an example, the recoiling $^{254}$No ions from the fusion-evaporation reaction $^{208}$Pb($^{48}$Ca,2n) at SHIP have a recoil energy of ≈35 MeV when leaving the target material. On the other hand, high-precision mass measurements are typically performed at low particle energies. High-precision PTMS requires a proper ion preparation and ion cooling down to about 0.025 eV, as discussed in section 3.6. Although the energy acceptance of the Penning-trap system is on the order of tens of eV[1], it exceeds the recoil energies of the fusion-evaporation residuals (EVR) by ≈6 orders of magnitude. Thus, it is inevitable to slow down the recoiling ions after their production and separation. In addition, the fusion-evaporation reaction products are highly charged with broad charge-state distributions when they leave the target [89]. As discussed in section 3.2, SHIPTRAP is limited to measurements on ions with low charge states of up to few elementary charges.

Gas-stopping cells (also referred to as gas catchers) are ideal to stop and thermalize fast ions. The ions are slowed down in a pure inert gas volume by inelastic collision which results in charge exchange processes. This method was first applied at the Ion-Guide Isotope-Separator On-Line (IGISOL) facility in 1985 [106] on fusion-evaporation reaction products. Meanwhile, this technique has been implemented in various experiments involving different nuclear reaction products, e.g at the FRagment Separator (FRS) experiment at GSI [107], the RIKEN Projectile Fragment Separator (RIPS) [108], the Low Energy Beam and Ion Trap experiment (LEBIT) at the National Superconducting Cyclotron Laboratory (NSCL) [109], the Canadian Penning Trap (CPT) mass spectrometer [110] and at SHIPTRAP [111, 112]. To avoid chemical reactions to occur, inert gases are used as their ionization potentials are relatively large and thus allow the colliding ions to stay charged. The final charge-state distribution of the stopped ions depends upon the involved ionization potentials and is influenced by the presence of contaminants in the inert gas.

In order to improve the gas purity and thus moderate the charge state distribution to ideally a single charge state, a second-generation gas-stopping cell, the so-called Cryogenic Gas-stopping Cell (CGC) or CryoCell, has been developed at SHIPTRAP that can operate at cryogenic temperatures [113, 91]. This effectively reduces the amount of contaminants in the buffer-gas volume, as impurities freeze out at the surfaces. The highest possible charge state that can survive the subsequent room-temperature buffer-gas in the buncher section and the preparation trap, respectively, is favoured to maximize the mass resolving

[1] This is mainly given by the depth of the electrostatic potential of the preparation trap of ≈ 40 V.

power and precision of SHIPTRAP (see section 3.7). For most of the cases this corresponds to a doubly-charged state. In addition, charge-state mixtures have to be avoided as mass measurements are performed for one fixed charge-to-mass ratio and cannot make use of any other occurring charge states. The CGC has been implemented at the SHIPTRAP facility [114], requiring the rearrangement of the entire beamline from a perpendicular [115] to a close-to-zero-degree position with respect to SHIP [116].

The CGC is a crucial part of the SHIPTRAP setup to allow mass measurements in the region of the heaviest elements. As the production rates for these elements are low and the overall particle integral is limited, the CGC has to operate as efficiently as possible. In addition, the stopping and extraction from the CGC has to be fast enough to avoid any additional ion losses due to the finite half-lives of the EVRs. At SHIPTRAP, a proper ion preparation in the preparation trap and the subsequent measurement in the measurement trap can be as fast as $\approx 200\,\mathrm{ms}$ for EVRs. As the CGC in general reaches extraction times in the order of tens of milliseconds at cryogenic temperatures [91], the upcoming discussions are focussed on optimizing the extraction efficiency on EVRs.

## 4.1 Setup

Figure 4.1 shows a schematic view of the CGC. For a more detailed description of the setup the reader is referred to the articles of Droese *et al.* [91] and Kaleja *et al.* [114]. First extraction measurements and optimizations have been presented in the PhD thesis of Droese [117] using recoil-ion sources. In the MSc thesis of Kaleja [118] the CGC has been tested on the fusion-evaporation reaction products $^{254}$No and $^{154-156}$Yb. This work concentrates on the optimization and performance with respect to the high-precision PTMS beam time in summer 2018. For the upcoming discussions its key components and features are summarized.

The CGC consists of two vacuum chambers. The inner chamber which is filled with ultra-pure helium buffer gas at densities that correspond to room-temperature pressures of about 50 mbar. For thermal isolation, the inner chamber is embedded into an outer chamber which is kept under vacuum and, in addition, contains multilayer insulation foils to further reduce the heat load from thermal radiation. To minimize the thermal conductivity the inner chamber is supported only by thin titanium rods. The gas volume of the CGC is separated from the high-vacuum regime of SHIP (typically $10^{-6}$ mbar) by a titanium entrance window foil with typical thicknesses of 3 to 4 µm. The inner chamber is connected to the cold head of a cryo cooler (type SUMITOMO RDK-400, capacity of 54 W at 40 K) via stranded copper wires. Usually, operation temperatures of about 40 K are reached after 40 hours of cooling starting from room temperature. The warming up process takes approximately 100 hours which may be sped up to about 60 hours if the outer chamber is vented once the temperature exceeds the boiling point of liquid nitrogen at about 77 K.

The gas inlet line is equipped with a heated getter purifier (type MonoTorr S4-MT3, SAES pure gas) to further reduce reactive contaminations from the injected buffer gas (typically helium 5.6 or 6.0), in particular water ($H_2O$), methane ($CH_4$), nitrogen ($N_2$) and oxygen ($O_2$). In addition, the buffer gas passes an elongated copper tubing installed in between the cold head and the inner chamber. This acts as an additional purification step as contaminants of the buffer gas with freezing points above 40 K are frozen out at the copper surface before the insertion into the active buffer-gas volume.

An EVR with a kinetic energy of $\approx 35\,\mathrm{MeV}$ looses about 90 %[2] of its kinetic energy by passing through

[2] Which can be simulated using the SRIM software (see section 10.4.3).

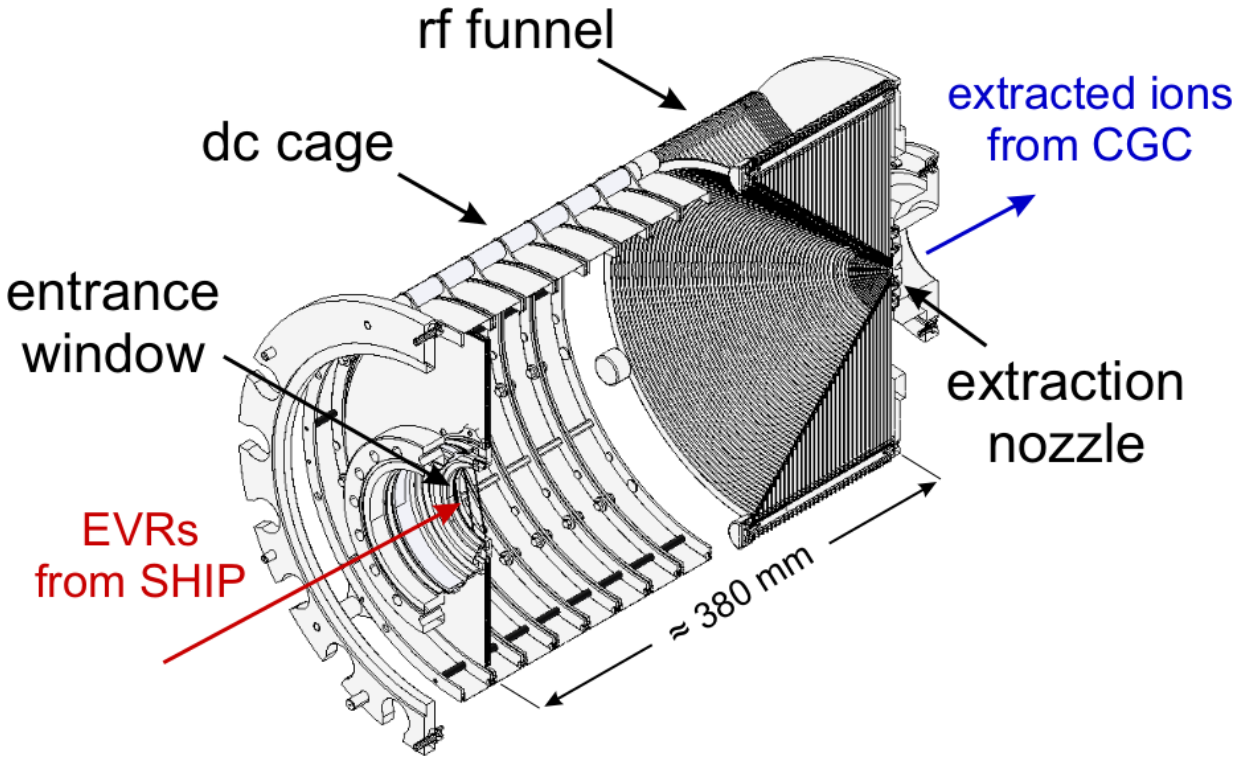


Figure 4.1: Schematic view of the inner chamber from the cryogenic gas-stopping cell (CGC) at SHIPTRAP. The active buffer-gas volume has an axial extension of about 380 mm. The geometric extensions of the inner chamber are given in more detail in table 10.2 in Appendix 10.4. More detailed views on applied potentials, potential curves and ion trajectories are given in [91, 117, 118].

a 3 to 4 µm thin titanium entrance window foil. The residual kinetic energy is lost throughout inelastic collisions with the buffer-gas atoms in the subsequent buffer-gas volume. For extraction the ions are guided by means of electrical dc field gradients applied to the 8 cylindrical electrodes of the dc cage and the rf funnel ring electrodes. As the ions have to be transported towards the nozzle of *de-Laval*-type, the 76 electrodes of the rf funnel are successively reduced in diameter. For the dimensions, i.e. lengths, distances and diameters, the reader is referred to table 10.2. To prevent the ions from colliding with the rf funnel electrodes, an rf field is superimposed with the dc field gradient. The rf field's phase is shifted by 180 ° with respect to neighbouring electrodes resulting in a repulsive force [108].

## 4.2 Recoil-Ion Sources

Recoil-ion sources offer a great opportunity to characterize and optimize gas-stopping cells. They are based on isotopes that undergo $\alpha$ decay. The $\alpha$ decay is a two-body process and, according to momentum and energy conservation, the $\alpha$ particle and the daughter nucleus are emitted in opposite direction when the mother nucleus is at rest. In the region of $A \approx 200$ with $Q_\alpha \approx 6$ MeV the kinetic energy of the recoiling daughter ion is on the order of 75 keV. As a consequence, the recoil ion is ejected out of the source holder material. If positioned in the buffer-gas environment of the CGC, the recoiling ions are stopped and thermalized by gas collisions. As an example, the recoil ion $^{219}$Rn following the decay of $^{223}$Ra has a range of about 1 cm in helium gas at a room-temperature gas density of 50 mbar (simulated using the SRIM code [119]). Therefore, these recoil-ion sources can be considered point-like sources. In addition, the characteristic $\alpha$-decay energies of emitted daughter isotopes are used as a fingerprint, allowing to identify and count extracted ions from the CGC, down to single-ion sensitivity. From practical considerations with respect to the introduced activity, the half-lives and the chemical properties, only few isotopes are suitable

to be used for the CGC. Appendix 10.2 explains in more detail the requirements for a suitable recoil-ion source at SHIPTRAP.

Within the scope of this work the recoil-ion sources $^{225}$Ac ($t_{1/2}$=10 d) and $^{223}$Ra (11.4 d) have been commonly used. The corresponding recoil daughters are $^{221}$Fr (4.9 m) and $^{219}$Rn (4.0 s), respectively. Due to its shorter half-life the latter is preferred. These recoil-ion sources are obtained by molecular plating and collecting the decay daughters in the gas phase, using $^{229}$Th (7900 y) and $^{227}$Ac (21.7 y) sources, respectively. For fast optimizations, the $^{223}$Ra source is favoured as the half-life of its daughter $^{219}$Rn of $t_{1/2}$ =3.9 s allows for fast repetitive measurements (compared to 4.9 m for $^{221}$Fr recoiling from $^{225}$Ac). The half-lives are taken from [103]. If the absolute efficiency is not of interest and the recoil-ion source activity is sufficiently high, Channeltron detectors are used at the cost of ion selectivity. This allows for even faster repetitive measurements and optimizations.

### 4.2.1 Calibration of the Recoil-Ion Sources $^{223}$Ra and $^{225}$Ac

Figures 4.2a and 4.2b show the decay-chains of the $^{223}$Ra and $^{225}$Ac recoil-ion sources, respectively.

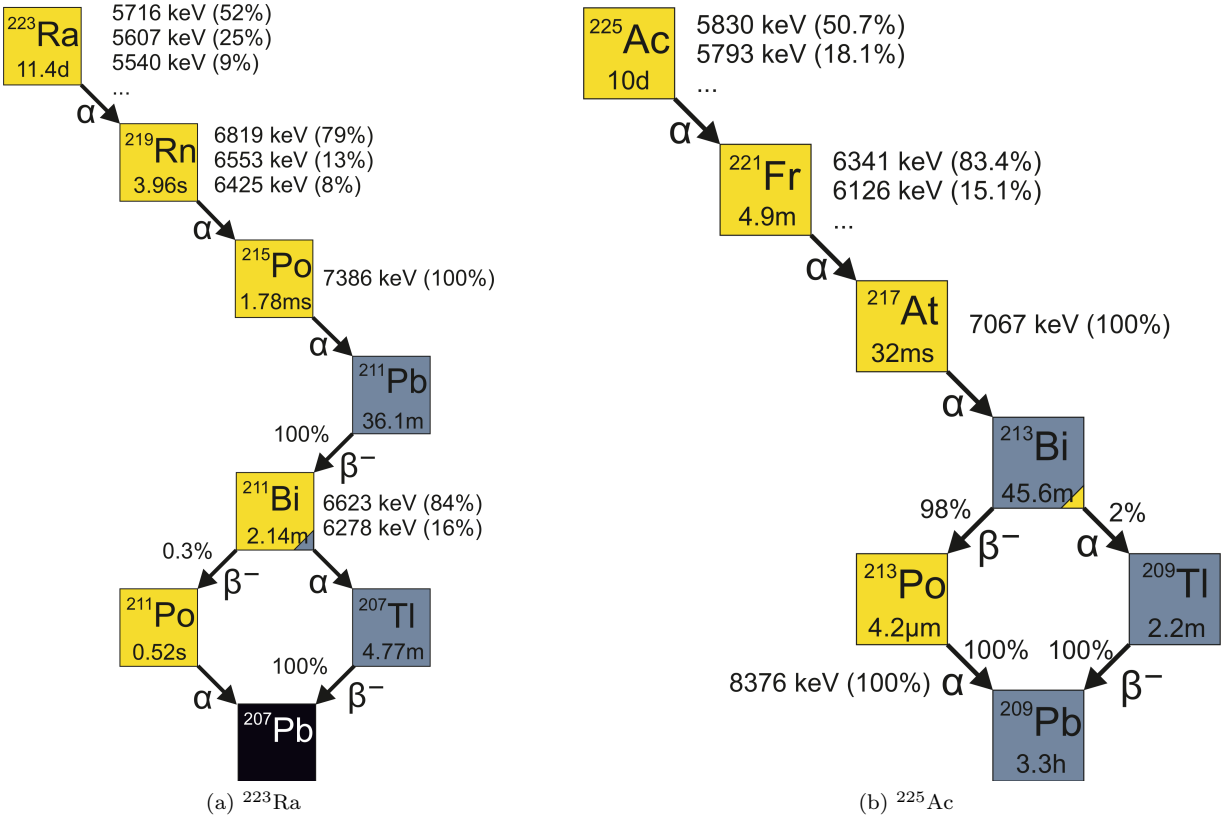


(a) $^{223}$Ra (b) $^{225}$Ac

Figure 4.2: Decay scheme of the recoil ion sources (a) $^{223}$Ra and (b) $^{225}$Ac. Data taken from [103].

Every $\alpha$ decay results into a recoiling daughter nucleus. Considering a flat surface, half of these recoil ions, recoil off the source holder. However, especially in the case of molecular plating, organic impurities can also be deposited onto the source holder which leads to the formation of a dead-layer (for more details the reader is referred to [120, 121, 122] and appendix B in [123]). The recoil ion sources were partly obtained from the University of Groningen (collected in gas phase) and more recently from the Institute for Nuclear Chemistry Mainz (by molecular plating as well as collected in gas-phase). The recoil release rate of any

recoil-ion source at a given time $t$

$$\dot{n}_{\mathrm{recoil}}(t) = \frac{1}{2}\eta_{\mathrm{rrf}} \times \dot{\alpha}_{\mathrm{source}}(t) = \frac{1}{2}\eta_{\mathrm{rrf}} \times \dot{\alpha}_{\mathrm{source}}(t_0) e^{-\frac{(t-t_0)\ln(2)}{t_{1/2}}} \tag{4.1}$$

has therefore to consider the *recoil release factor* $\eta_{\mathrm{rrf}}$ that corresponds to the fraction of recoil ions that leave the source material. The factor of two accounts for half a hemisphere as discussed before. The mother activity at a given time $t_0$

$$\dot{\alpha}_{\mathrm{source}}(t_0) = \frac{\alpha_{\mathrm{mother}}/t_{\mathrm{meas}}}{\Omega \mu_{\mathrm{branch}}} \quad \text{with} \quad \Omega = \frac{\pi(d_{\mathrm{det}}/2)^2}{4\pi R_{\mathrm{d}}^2} \tag{4.2}$$

is determined by placing the recoil-ion source at a distance $R_{\mathrm{d}}$ in front of an $\alpha$ detector (Ortec TU-016-150-100) in (pre-)vacuum conditions. The activity of the mother $\alpha_{\mathrm{mother}}/t_{\mathrm{meas}}$ is measured taking into account the $\alpha$-branching ratio $\mu_{\mathrm{branch}}$. In practise the $\alpha$ lines of $^{223}$Ra and $^{225}$Ac are well separated within the obtained $\alpha$ spectrum, such that $\mu_{\mathrm{branch}} = 100\,\%$ in both cases. As the measurement time $t_{\mathrm{meas}}$ for calibration is typically less than an hour, which is small compared to the half-life of the mother in the range of several days, the change in activity during the calibration measurement can be neglected. The geometric factor $\Omega$ corresponds to the solid angle coverage between the source and the $\alpha$ detector with an active surface diameter $d_{\mathrm{det}}$. As the detector surface is flat and the source activity is distributed over a finite size, this is only an approximation. However, for the used distances of $R_{\mathrm{d}} \approx 10\,\mathrm{cm}$ this approximation is valid. Source activities are typically measured with relative uncertainties in the order of 10 %, limited by the relative precision of $R_{\mathrm{d}}$. This distance is typically measured with a precision of 1 mm. However, the limited space within the calibration setup restricts the maximal distance to about this distance. Figure 4.3 shows typically obtained calibration spectra for both ion sources. The energy resolution of the $\alpha$ detector is typically in the order of 30 keV to 100 keV and mainly limited by background noise during detection due to operational radiofrequency sources in the experimental hall. Thus, the resolution of these spectra can vary, depending on the day and time of measurement.

To measure the extraction efficiencies with sufficient precision, a precise knowledge of the recoil rates from the sources, which depends on the activity of the source as well as on the recoil release factor, is crucial. In fact, the main contribution to the uncertainty of measured extraction efficiencies originates from the uncertainty of the recoil ion source activity. However, due to the production mechanism of the recoil ion sources, radioactive contamination can be present. In the process of molecular plating, the recoil ion sources $^{223}$Ra and $^{225}$Ac themselves originate as recoiling ions from actinium and thorium sources, respectively. $^{223}$Ra is produced via an $\alpha$-decay from $^{227}$Th ($t_{1/2} = 18.7\,\mathrm{d}$) that is populated via an $\beta^-$-decay from a $^{227}$Ac ($t_{1/2} = 21.8\,\mathrm{y}$) source. In the case of $^{225}$Ac a $^{229}$Th ($t_{1/2} = 7932\,\mathrm{y}$) source recoils $^{225}$Ra ($t_{1/2} = 14.9\,\mathrm{d}$) ions that decay via a $\beta^-$-decay into $^{225}$Ac. Some $^{229}$Th sources are contaminated with $^{228}$Th ($t_{1/2} = 1.9\,\mathrm{y}$) such that the resulting $^{225}$Ac source consists of isotopes of both decay chains. This is seen in figure 4.3 where two different $^{225}$Ac sources are shown out of which one is contaminated with isotopes of the $^{224}$Ra decay chain that originates from $^{228}$Th. This exacerbates the source calibration and extraction efficiency measurements.

### 4.2.2 Determination of the Recoil Release Factor

Due to clean and controllable conditions, recoil-ion sources produced in gas phase are expected to have no considerable deadlayer and thus a recoil release factor of $\approx 100\,\%$. For sources produced by molecular plating factors of $< 100\,\%$ are expected. To deduce the recoil release factor $\eta_{\mathrm{rrf}}$ of a recoil-ion source, it is positioned in front of a movable $\alpha$ detector (see figure 4.5). As $\eta_{\mathrm{rrf}}$ corresponds to a ratio of rates as defined in equation 4.1, the source is positioned as close as possible to the detector to maximize the solid

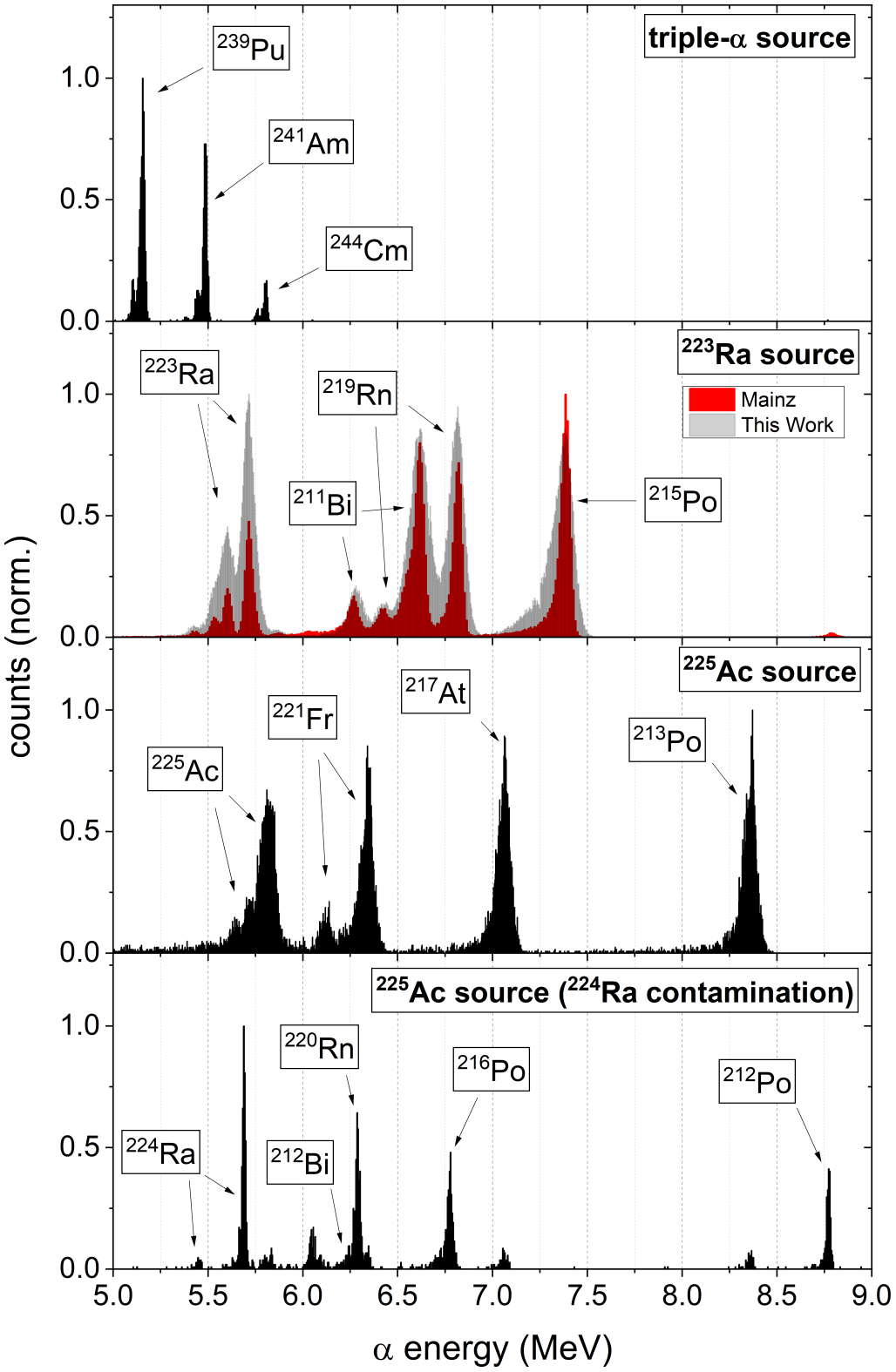


Figure 4.3: Normalized calibration spectra for the recoil-ion sources $^{223}$Ra and $^{225}$Ac. A triple-$\alpha$ source containing $^{239}$Pu, $^{241}$Am and $^{244}$Cm can only be used as a rough calibration due to its low $\alpha$ energies in comparison with the recoil ion sources. In practice, prominent $\alpha$ lines of the spectra are used for calibration. As a comparison, the energy calibrated spectra obtained from the Institute for Nuclear Chemistry Mainz is shown for the case of $^{223}$Ra. In the case of $^{225}$Ac one of the provided recoil ion sources showed a strong contamination of $\alpha$ energies from the $^{224}$Ra decay chain (bottom figure). A small contamination seems to be also present for the $^{223}$Ra recoil ion source as the $^{212}$Po $\alpha$ line also appears in this spectrum. For more details see text.

angle coverage. As the detector efficiency cancels out in the determination, the precise knowledge of the distance between the source and detector surface as well as any misalignments are irrelevant. In order to determine $\eta_{\mathrm{rrf}}$ the source has to be blocked at a given time $t_b$ and the decaying $\alpha$ activity of the implanted recoil ions is measured. For this, the time required to move the detector out of line-of-sight from the source has to be much shorter compared to the half-life of the decaying recoil ion. This procedure takes approximately 5 s to 10 s. Thus, only the release rate factor of the $^{225}$Ac recoil ion source was determined within the scope of this work as its recoiling daughter $^{221}$Fr lives for about 4.9 m. Since the $^{223}$Ra recoil-ion sources were solely produced in clean gas-phase environments, $\eta_{\mathrm{rrf}}^{\mathrm{Ra}} = 100\,\%$ is expected, which agrees well with experimental observation. A setup consisting of a mechanical shutter to block the source (instead of moving the detector) will allow measuring the recoil release factor of $^{223}$Ra experimentally. Regardless of how, due to the low half-life of $^{219}$Rn of few seconds, a relatively high mother activity is required to perform this measurement.

For the experimental determination of the recoil release factor, the $^{225}$Ac source is positioned in front of the detector in vacuum conditions. Due to the low half-life of the recoiling daughter compared to its mother (see also figure 4.2b), the emitted $\alpha$-line rates from both species are in a equilibrium, i.e. the ratio between both rates does not change over time. This is described by the Bateman equation [124]

$$\lambda_n N_n(t) = \lambda_n \prod_{j=1}^{n-1} \lambda_j \sum_{i=1}^{n} \sum_{j=i}^{n} \left( \frac{N_i(0) e^{-\lambda_j t}}{\prod_{p=i,p\neq j}^{n} (\lambda_p - \lambda_j)} \right). \tag{4.3}$$

that represents an analytical solution for the activity of an isotope within a decay chain. Here, $N_i(t)$ and $\lambda_i$ are the activities and the decay constant of the $i^{\mathrm{th}}$ isotope within the decay chain, respectively, where the decay always happens from $i$ into $i+1$. Thus, $\lambda_n N_n(t)$ resembles the activity of the $n^{\mathrm{th}}$ isotope within a chain. Due to the implantation of recoiling nuclei from the source on the detector surface, the measured activity of $^{221}$Fr increases over time. Their $\alpha$ rate will add up to the $\alpha$ rate that originates directly from the source. Thus, it is essential for the measurement to reach the state in which the decaying rate of the implanted recoil ions $^{221}$Fr is equal to their implantation rate (secular equilibrium). The amount of recoil ions implanted into the detector surface at a given time $t$ can be expressed as

$$\frac{dN_{\mathrm{Fr}}(t)}{dt} = \underbrace{\Omega \eta_{\mathrm{rrf}}^{\mathrm{Ac}} \lambda_{\mathrm{Ac}} N_{\mathrm{Ac}}(t)}_{\text{implantation}} - \underbrace{\lambda_{\mathrm{Fr}} N_{\mathrm{Fr}}(t)}_{\text{decay}}, \tag{4.4}$$

where $\lambda_{\mathrm{Ac}} = 8.023 \times 10^{-7}\,\mathrm{s}^{-1}$ and $\lambda_{\mathrm{Fr}} = 0.00238\,\mathrm{s}^{-1}$ are the decay constants of $^{225}$Ac and $^{221}$Fr, respectively (calculated using the half-lives from [103]). The required secular equilibrium is reached for $dN_{\mathrm{Fr}}(t)/dt = 0$ in which the implantation and decay rate cancel out. Using the Bateman equation (4.3) we obtain

$$N_{\mathrm{Fr}}(t) = \frac{\Omega \eta_{\mathrm{rrf}}^{\mathrm{Ac}} \lambda_{\mathrm{Ac}} N_{\mathrm{Ac}}(0)}{\lambda_{\mathrm{Fr}} - \Omega \eta_{\mathrm{rrf}}^{\mathrm{Ac}} \lambda_{\mathrm{Ac}}} \left( e^{-\Omega \eta_{\mathrm{rrf}}^{\mathrm{Ac}} \lambda_{\mathrm{Ac}} t} - e^{-\lambda_{\mathrm{Fr}} t} \right), \tag{4.5}$$

which represents the number of $^{221}$Fr atoms implanted into the detector surface at a given time $t$. The decaying rate of the recoils at the surface of the detector $\lambda_{\mathrm{Fr}} N_{\mathrm{Fr}}(t)$ exponentially approaches the implantation rate $\Omega \eta_{\mathrm{rrf}}^{\mathrm{Ac}} \lambda_{\mathrm{Ac}} N_{\mathrm{Ac}}(t)$ as shown in figure 4.4 for the case of a $^{225}$Ac recoil ion source. After about 1500 s both rates are equal within 3 %, which is below typical statistical uncertainties of 10 % to 20 % for these measurements. Thus, waiting for approximately 25 minutes is sufficient and the detector can be moved out.[3] Now, as no further recoil ions are implanted into the detector surface, the differential equation (4.4)

[3] Note that equation 4.5 in principle allows to directly determine the recoil release factor $\eta_{\mathrm{rrf}}^{\mathrm{Ac}}$ if the solid angle $\Omega$ is known. However, there is a third contribution to the detected $\alpha$ activity from $^{221}$Fr. These are events from recoiled $^{221}$Fr implanted in the surfaces of the vacuum chamber. This contribution cannot be quantified directly as the integrated solid angle is

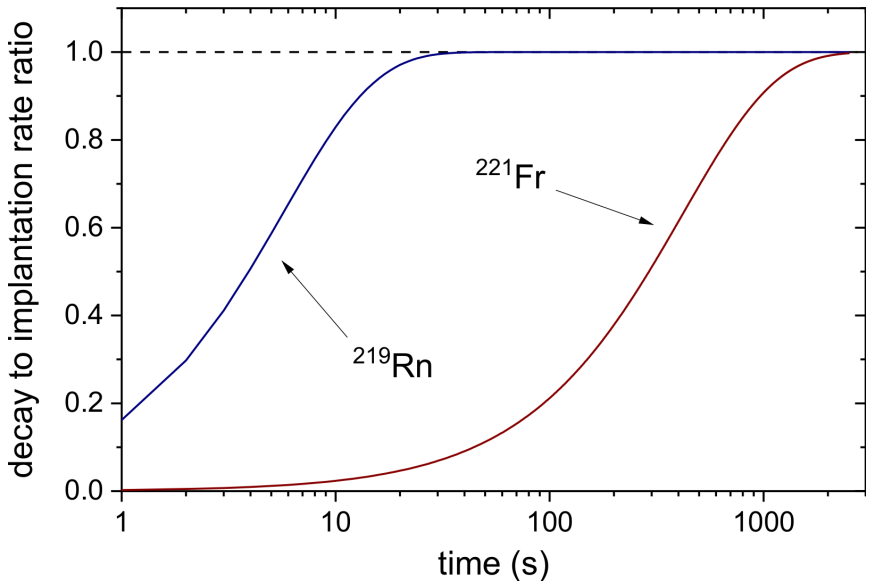


Figure 4.4: The ratio of the decay rate to the implantation rate of $^{221}$Fr ions into the $\alpha$ detector. For comparison the case of a $^{219}$Rn source is also shown. Due to its substantial lower half-life the equilibrium state is already reached within 30 s. Note that the ratio is independent of the absolute source activity. For further details see text.

reduces to

$$\frac{dN_{\mathrm{Fr}}(t)}{dt} = -\underbrace{\lambda_{\mathrm{Fr}} N_{\mathrm{Fr}}(t_b)}_{\text{decay}}, \tag{4.6}$$

while the starting conditions are given from the secular equilibrium. The lack of any time dependence in equation (4.6) corresponds to the free decay of the implanted $^{221}$Fr ions at the time $t_b$. Because finite measurement times are required (typically 30 seconds) to obtain $\alpha$ rates with sufficient statistics, the activity $\lambda_{\mathrm{Fr}} N_{\mathrm{Fr}}(t_b)$ is extrapolated back in time to $t = t_b$. For this, successive measurements are taken and an exponential fit is performed using the decay constant $\lambda_{\mathrm{Fr}}$. Figure 4.5 shows successive $\alpha$-rate measurements for a $^{225}$Ac recoil ion source as a function of the absolute time after pre-vacuum conditions were reached. The source was provided by the Institute for Nuclear Chemistry in Mainz. The figure shows the equilibrium condition, i.e. a constant ratio between the rates of $^{225}$Ac and $^{221}$Fr until the detector has been moved out of line-of-sight. The $^{221}$Fr $\alpha$ rate is slightly higher than the rate of $^{225}$Ac due to the secular equilibrium in addition to events originating from implanted ions (both from the detector surface and the surfaces of the vacuum chamber). At the time $t_b$ the source was blocked and the $^{225}$Ac activity immediately drops to zero as there is no more line of sight between source and detector. The drop in activity of $^{221}$Fr can be seen. The recoil release factor is then obtained via

$$\eta_{\mathrm{rrf}}^{\mathrm{Ac}} = 2 \times \frac{\dot{\alpha}_{\mathrm{Fr}}(t_b)}{\dot{\alpha}_{\mathrm{Ac}}(t_b)}. \tag{4.7}$$

As the $\alpha$ decay is isotropic and the recoil ions are implanted at the beginning of the detector surface, only half of the $\alpha$ decays of the implanted $^{221}$Fr recoils are measured in practice. Thus, a factor of two is taken into account. At the detector an $\alpha$ rate of $\dot{\alpha}_{\mathrm{Ac}}(t_b) = 4.5(7)\,\mathrm{s}^{-1}$ is obtained. The extrapolated value of the implanted recoil rate is $\dot{\alpha}_{\mathrm{Ac}}(t_b) = 0.56(4)\,\mathrm{s}^{-1}$. Using equation 4.7 a recoil release factor of $\eta_{\mathrm{rrf}}^{\mathrm{Ac}}$ =25(4) % is obtained for this particular $^{225}$Ac source, which is a relatively high value. The $^{225}$Ac ion sources that were molecular plated in liquid phase from the Institute for Nuclear Chemistry Mainz have typically release factors of only a few %.

unknown.

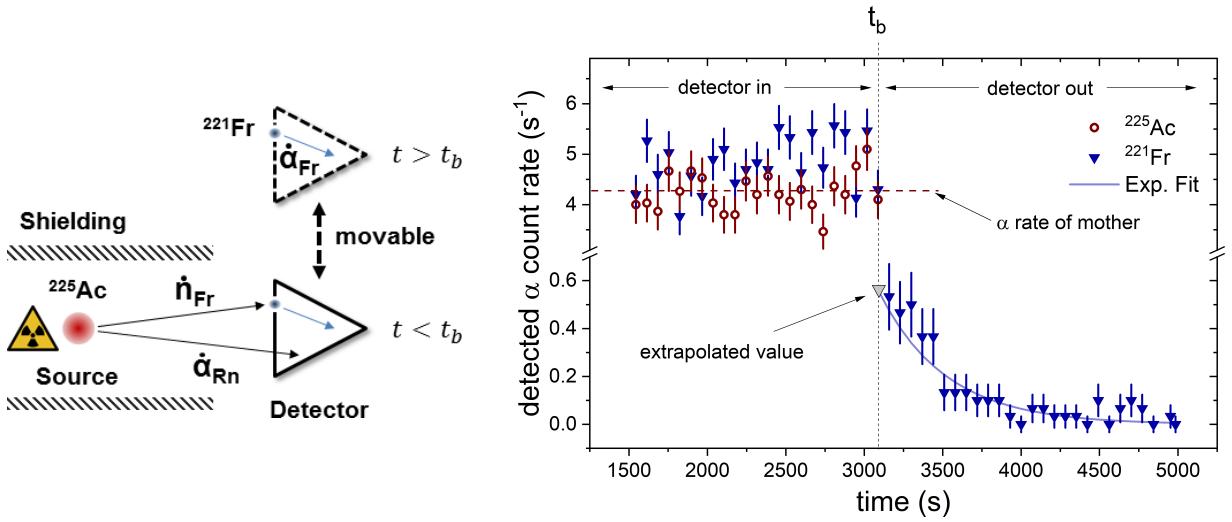


Figure 4.5: (Left figure) Schematic illustration of the recoil release factor determination for $^{221}$Fr. First, the $\alpha$ activity $\dot{\alpha}_{\mathrm{Rn}}$ of the mother $^{225}$Ac is measured using a silicon detector while the recoil ions $n_{\mathrm{Fr}}$ are implanted and accumulated at the detector surface. At a time $t_b$ the detector is moved out and the remaining $\alpha$ activity of the implanted recoil ions $\dot{\alpha}_{\mathrm{Fr}}$ is measured as a function of time (right figure). A fitted exponential decay allows the extrapolation of the activity to the time $t_b$. The rates are determined by successive measurements with measurement times of 30 seconds.

## 4.3 Improving the Performance of the CGC

### 4.3.1 General Procedure

To measure and optimize the performance of the CGC, e.g. its extraction efficiency, extraction time and purity, a point-like recoil-ion source (see section 4.2) is installed inside its buffer-gas volume. In a standard configuration the source is positioned axially $\approx 10\,\mathrm{cm}$ in front of the rf funnel. In the work of C. Droese [91] no considerable loss in extraction efficiency has been observed for off-axial source positions. Thus, all the upcoming off-line measurements were performed using on-axis source positions. In order to quantify the performance of the CGC the extracted ions are detected using two types of detectors which is explained in the following.

#### Absolute Extraction Efficiency Measurements

One of the most important parameters for the gas cell is the extraction efficiency, which is defined as the ratio between extracted ion rate $\dot{n}_{\mathrm{extr}}^{\mathrm{DX}}$ and emitted recoil ions $\dot{n}_{\mathrm{recoil}}$

$$\epsilon_{\mathrm{extr}} \equiv \frac{\dot{n}_{\mathrm{extr}}^{\mathrm{DX}}}{\dot{n}_{\mathrm{recoil}}} = \frac{\dot{\alpha}^{\mathrm{DX}}/(\mu_{\mathrm{branch}}\Omega_{\mathrm{det}})}{\dot{n}_{\mathrm{recoil}}}. \tag{4.8}$$

It is obtained by measuring the $\alpha$ activity of the extracted ions $\dot{\alpha}^{\mathrm{DX}}$ using an $\alpha$ detector. The $\alpha$ detectors are identical to the ones used for calibration as discussed in 4.2. Here, DX denotes the detector position as defined in figure 3.3. In most cases the extraction efficiency is measured using detector D2 subsequent to the buncher as it does not interfere with off-line Penning-trap measurements. The rate of emitted recoil ions $\dot{n}_{\mathrm{recoil}}$ (see equation 4.1) is determined as discussed in section 4.2. The extracted ions cannot be implanted directly into the $\alpha$-detector surface, due to the fact that the ions are extracted at approximately ground potential while the $\alpha$ detectors have a bias of $+80\,\mathrm{V}$. Thus, a $0.8\,\mu\mathrm{m}$ thin aluminium foil biased to

about -1.7 kV[4] is positioned 9(1) mm in front of the detector (this is identical to the foil-detector assembly used in [91] and [114]). For this reason, the geometric solid angle between the foil and the detector $\Omega_{\mathrm{det}} = 16(1)\,\%$ is taken into account. This assumes a point-like distribution of the implanted ions in the foil at a distance of 9(1) mm to the detector with an active diameter of 18 mm. In practise, the ions are distributed within the foil which lowers the geometrical efficiency. Thus, by taking $\Omega_{\mathrm{det}} = 16(1)\,\%$ as an upper limit, the calculated extraction efficiencies using equation (4.8) are underestimated. However, for the upcoming discussions a value of 16 % is used to be congruent to the measurements performed by C. Droese *et al.* [91, 117] and O. Kaleja *et al.* [118, 114]. As the obtained extracted ion rate and thus the extraction efficiency directly depends upon $\Omega$ one has to note that beam line optimizations, e.g. maximizing the extraction efficiency with respect to dc voltages of ion optics in front of the foil-detector assembly, have to be performed with care, as these changes also change the ion distribution of the implanted ions within the foil and not necessarily correspond to an increase in the efficiency.

To deduce the extraction efficiency, the extracted $\alpha$ activity of the first recoiling daughter, i.e. $^{219}$Rn and $^{221}$Fr in the case of the recoil ion sources $^{223}$Ra and $^{225}$Ac, respectively, has to be taken into account. This is due to the fact that any other (grand) daughter of these isotopes can either be extracted directly from the source or be produced from the decays of $^{219}$Rn and $^{221}$Fr within the foil. However, in the case of the $^{223}$Ra recoil ion source the first grand daughter $^{215}$Po can also be used for a rough estimate of the extraction efficiencies. Due to its low half-life of about 2 ms [103] $^{215}$Po ions are most likely not extracted directly from the CGC given the fact that extraction times are typically tens of milliseconds [91]. Thus, the detected $\alpha$ activity of $^{215}$Po predominantly originates from the decay of $^{219}$Rn within the foil. A good assumption is that the measured $^{215}$Po $\alpha$ rate corresponds to approximately half the rate of the extracted $^{219}$Rn ions. The factor of two accounts for half the hemisphere in which the recoiling $^{215}$Po ion (from the $\alpha$ decay of $^{219}$Rn) is implanted deeper into the aluminium foil rather than being ejected out of it. This is of practical importance as the energy resolution of $\alpha$ detectors can exceed 200 keV for given experimental conditions which prevents resolving the $\alpha$ lines of $^{219}$Rn from $^{211}$Bi (see also figure 4.2a). A similar discussion is not valid in case of the $^{225}$Ac recoil-ion source as the half-life of $^{217}$At ($t_{1/2} \approx$ 32 ms [103]) is on the order of typical extraction times from the CGC. In addition, due to the relative long half-life of $^{221}$Fr of about 5 min, a measurement of the extraction efficiency can only be performed if the radioactive equilibrium between the implantation rate of $^{221}$Fr into the aluminium foil and its decaying rate is reached. The differential equations are similar to the one stated in equation 4.4. The number of $^{221}$Fr implanted atoms at a given time $t$ is described by

$$\frac{dN_{\mathrm{Fr}}(t)}{dt} = \underbrace{\epsilon_{\mathrm{extr}}\dot{n}_{\mathrm{recoil}}(t)}_{\text{implantation}} - \underbrace{\lambda_{\mathrm{Fr}}N_{\mathrm{Fr}}(t)}_{\text{decay}}\,. \tag{4.9}$$

As discussed in 4.2 the time it takes to approach a rate equilibrium is independent on the implantation rate. Thus, as in figure 4.4, a time of approximately 1500 s is required to reach this condition. In addition, a finite measurement time to determine the extracted ion rate is mandatory. Depending on the strength of the source this measurement time can vary between tens of seconds down to tens of minutes. Usually a statistical uncertainty of less than 5 % is mandatory. This requires the number of detected $\alpha$ signals $N$ to be $\sqrt{N}/N < 0.05$ which results in $N > 400$. Given a typical recoil ion source activity of $^{225}$Ac of 200 Bq, a typical extraction efficiency of about 35 % at the detector position D2 and taking into account $\Omega_{\mathrm{det}} = 16\,\%$ with $\mu_{\mathrm{branch}} = 100\,\%$ this translates into a measurement time of approximately 70 s for a sufficient rate measurement. Thus, using $^{225}$Ac as a recoil ion source is impractical for efficiency optimizations using radiation detection. If any parameter that affects the extraction efficiency, e.g. voltages, gas pressures and

[4] Relatively high voltages are required in order to avoid volatile atoms to leave the foil surface, e.g. the noble-gas atom $^{219}$Rn.

the axial source position, is changed, a minimum waiting time of 1500 s is required to obtain reliable values for the extraction efficiency. Following this discussion, $^{223}$Ra recoil ion sources are preferred for extraction efficiency measurements, as the half-life of $^{219}$Rn of about 4 s allows for faster optimizations and successive measurements. This practical dependency on the half-life of the recoil ion becomes unimportant if, instead of the extracted $\alpha$ activity, the time of flight of the ions is measured. For this, a Channeltron detector is used. This will be discussed in more detail in the following section. Nevertheless, the $^{225}$Ac source allows testing for different ion species which are non-volatile and have a different ionization potential compared to the isotopes present in the $^{223}$Ra decay chain.

**Charge State Distribution and Extraction Time Measurements**

When installed at the SHIPTRAP beam line the CGC is followed by a buncher section for cooling, storing and bunching of the extracted ions, as mass measurements are performed in cycles with a (small) finite number of ions trapped in the Penning traps at the same time The continuous stream of slowed ions extracted from the CGC has to be properly chopped prior their guidance to the trap system. Following the buncher section Channeltron detectors are mounted at the positions D2 and D3, respectively, to get access to the time-of-flight distribution of the extracted ions. A stored and bunched ion with charge $q$ and mass $m$ that passes a potential difference $\Delta U$ after an extraction pulse will obtain the kinetic energy $E_{\mathrm{kin}} = 1/2mv^2 = q\Delta U$. Here, it was assumed that the obtained kinetic energy is much smaller than the ion's rest mass energy $mc^2$ which allows for a non-relativistic treatment. This is fulfilled at SHIPTRAP since voltage differences do not exceed few keV. For a given kinetic energy, the ion will traverse a path of length $L$ in a time of flight (ToF)

$$t_{\mathrm{ToF}} = \frac{L}{v} = \sqrt{\frac{m}{q}\frac{L^2}{2\Delta U}} \propto \sqrt{\frac{m}{q}}, \tag{4.10}$$

where $v = \sqrt{(q/m)2\Delta U}$ denotes the ion's velocity. The mass resolving power

$$R = \frac{m/q}{\delta(m/q)} = \frac{t_{\mathrm{ToF}}}{2\delta t_{\mathrm{ToF}}} \tag{4.11}$$

is of practical relevance as the ToF spectra allow determining $m/q$ ratios, giving insight into charge-state distributions, impurities and molecule formation. Here, $\delta t_{\mathrm{ToF}}$ denotes the peak width of the time-of-flight distribution. As these are approximately Gaussian-shaped peaks, the Full-With-at-Half-Maximum (FWHM) is taken. To measure the charge-state distribution, the time-of-flight peaks of interest need to be resolved. As $\alpha$-decaying recoil ion sources around mass number 220 are used, the mass resolving power needs to exceed approximately $220/4 \approx 50$. This will allow resolving the $\alpha$-emitting isotopes. The detector positions D2 and D3 contain a Channeltron (type SJUTS KBL25RS) and MCP plates in chevron configuration (type TOPAG MCP-MA25/2), respectively. The time-of-flight peak widths (FWHM) are on the order of 0.5 µs, respectively, which translates into mass resolving powers of 100 (D2) and 200 (D3), thus allowing to obtain charge-state distributions of isotopes. To resolve the isobars that are present due to $\beta$ decays in the decay chains resolving powers in the order of 100 000 are required, the Penning traps are used instead.

In addition, the ToF detectors at D2 and D3, respectively, are used to measure extraction times. For this, the dc voltage of the recoil-ion source is pulsed[5] and the rf voltage of the extraction RFQ is switched off after a well-defined time delay. This procedure is identical to the one described by C. Droese *et al.* [91].

[5]Pulsed between a more attractive and more repulsive source holder which enables and prohibits ion extraction.

**Parameter Optimizations**

The ToF detectors are also used to optimize the system with respect to its extraction efficiency as they allow for fast successive measurements, independently of any decay mode.[6] Usually their detection efficiencies are difficult to be measured accurately which makes them less suitable for absolute efficiency measurements. However, as the time of flight is detected on the ion impact it is independent on any half-life as long as the ion's half-life exceeds the measurement time. The minimum half-life is on the order of the extraction time of the CGC of tens of ms. The ToF detection requires the extracted ions to be cooled and bunched using the buncher section. The cooling time at typical helium-gas pressures of $10^{-2}$ mbar are $\approx 10$ ms, about the same order of magnitude than the extraction time from the CGC [91]. Therefore, successive measurements can be as fast as tens of milliseconds, allowing for fast parameter optimization.

### 4.3.2 Improving the Purity of the CGC

Up to now, the extraction efficiency of the CGC by means of extracted $\alpha$ activity has been investigated [91, 118]. In this work the CGC has been assessed with respect to its purity for the first time. For this, the charge-state distribution of extracted ions are investigated by means of their ToF. This only became available after the implementation of the CGC in the SHIPTRAP beam line (see figure 3.3) [116].

Due to cryogenic conditions in the helium buffer-gas volume of the CGC, molecular formation and ion neutralization is expected to be supressed. Figure 4.6(a)(1) shows a typical ToF spectrum that has been obtained after the implementation of the CGC at SHIPTRAP. The operation temperature and a room-temperature equivalent pressure corresponds to 40 K and 50 mbar, respectively. Even at cryogenic temperatures, molecular formation is found, predominantly for the doubly-charged ion species. In fact, no doubly-charged ions are seen, whereas $^{219}$Rn is solely extracted as singly-charged ion. As only doubly-charged species are affected, it is assumed that the molecular bond corresponds to a rather weak van der Waals bond. Indeed, by applying an increased dc field gradient between the extraction nozzle and the first electrode of the extraction rfq (figures (1) to (5)), the bonds start to break up and the doubly-charged species become visible. The ToF spectra (1), (2), (3), (4) and (5) have been obtained for voltage differences of 5 V, 10 V, 45 V, 60 V and 80 V, respectively. The bonds are breaking up due to collisions with residual buffer-gas atoms in the low-vacuum regime of $\approx 10^{-2}$ mbar between the extraction nozzle and the extraction rfq. This so-called *collision-induced dissociation* (CID) is a common technique in analytical chemistry and investigations of CID with respect to beam purification have been performed, e.g. at LEBIT [125], the JGU-Gießen [126] and more recently at TITAN [127].

Although the CID technique is effective, it reduces the extraction efficiency of the CGC, depending on the pressures in the CGC and the extraction RFQ. The impure conditions at cryogenic temperatures are attributed to the evaporation of contaminations from locally heated regions within the funnel ac/dc mixing board. The components of the originally used board has been soldered to a printed circuit board [91]. Therefore, to further improve the purity of the CGC, a second-generation ac/dc mixing board has been developed, which is shown in figure 4.7. All components have been either crimped or plugged together to avoid any impurities due to soldering and to prevent the use of the printed circuit board. Therefore, after the replacement with the new ac/dc mixing board, clean conditions at cryogenic temperatures have been reached. Figure 4.6(b) shows a ToF spectrum obtained without applying the CID, at the same operational temperature and pressure conditions as in (a)(1). With the upgrade of the ac/dc mixing circuit, the bismuth and lead ions are predominantly extracted as doubly-charged ions. Even the charge-state distribution of $^{219}$Rn, being a noble-gas, is in the order of 60 % doubly charged and 40 % singly charged. This is explained

[6] By definition $\alpha$ detectors rely on $\alpha$ decays.

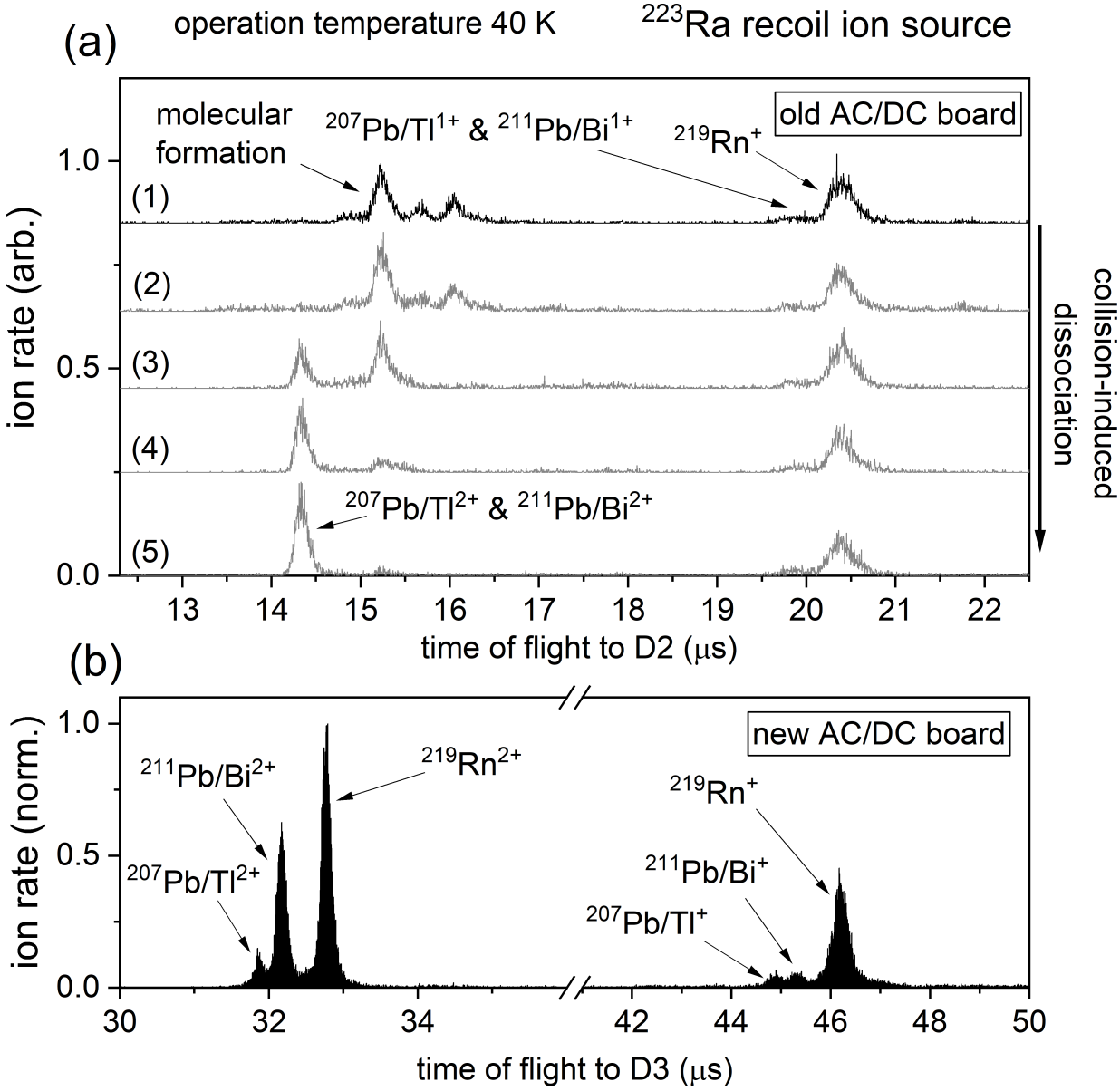


Figure 4.6: Time-of-flight (ToF) spectra of extracted ions from a $^{223}$Ra recoil-ion source positioned $\approx 15$ cm in front of the funnel rf inside the CGC. The operation temperature is 40 K. The room-temperature equivalent pressure is 50 mbar. The bunching frequency is 25 Hz. (a)(1) Typical ToF spectrum obtained after the implementation of the CGC at SHIPTRAP. Figures (2) to (5) show the impact of the collision-induced dissociation. (b) Obtained ToF spectrum after the replacement of the AC/DC mixing board. Figure (b) modified from [114]. The difference in the ToF between both figures is due to the usage of D2 and D3 in the cases of (a) and (b), respectively. For further details see text.

by the low second ionization potentials for bismuth and lead of 16.7 eV [128, 129] and 15.0 eV [130], respectively, compared to 21.4 eV [131] for radon [114]. If the distance between the recoil-ion source and the extraction nozzle is increased from $\approx$ 15 cm to $\approx$ 45 cm radon gets predominantly extracted as singly-charged ion while the charge-state distribution of lead is less affected than for bismuth. This is attributed to the presence of atomic or molecular impurities in the CGC with ionization potentials in the range of 15 eV to 16 eV, e.g. Ar (15.8 eV [132]), $N_2$ (15.6 eV [133]) and $H_2$ (15.4 eV [134]), respectively [114]. However, Ar and $N_2$ should not be present at cryogenic temperatures around 40 K. To further improve the purity of the CGC the installation of a non-evaporable getter pump is foreseen in near future.

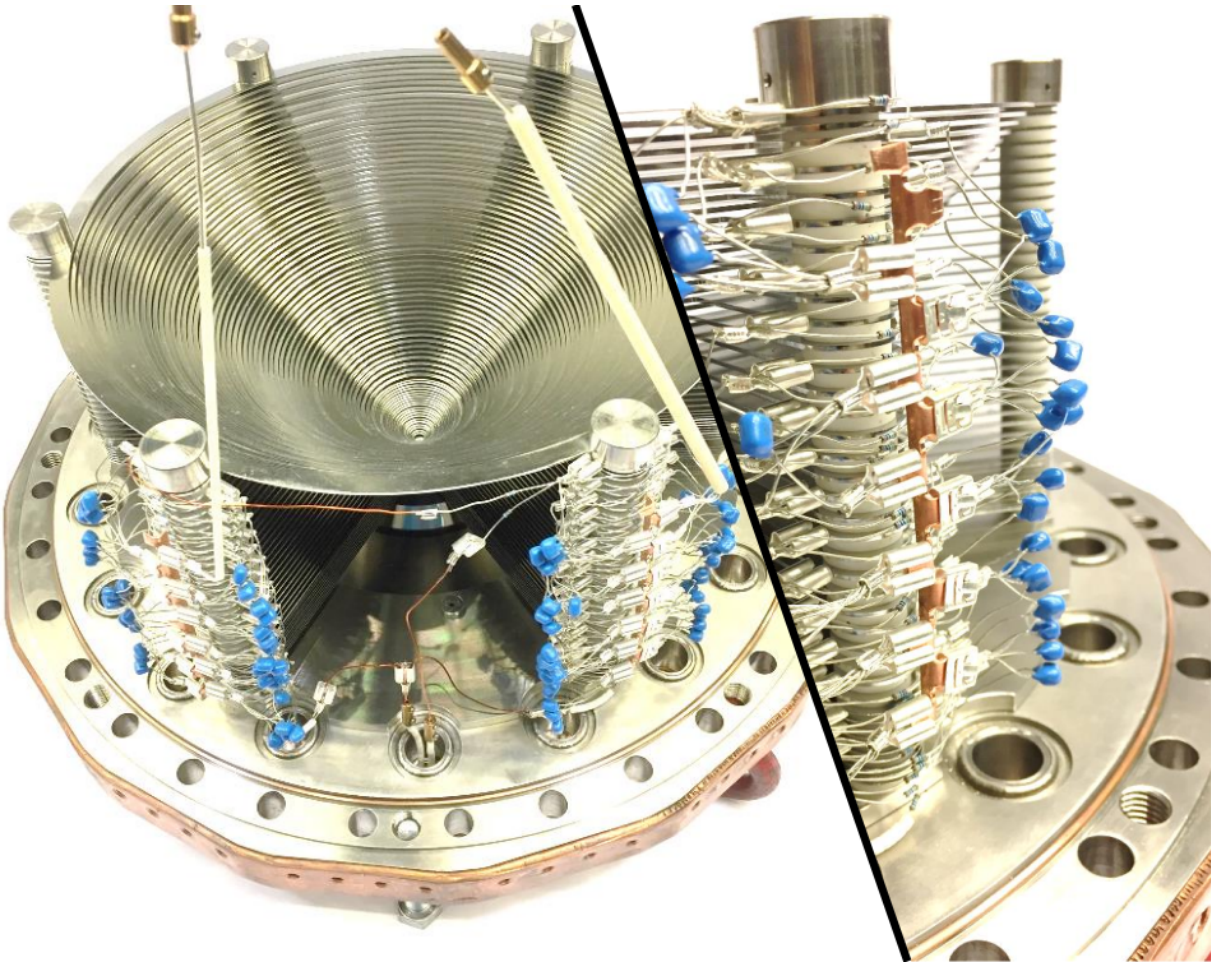

Figure 4.7: Photograph of the new funnel rf ac/dc mixing board. For further details see text.

### 4.3.3 Adjusting the Buffer-Gas Density

The buffer-gas density inside the CGC is adjusted by a mass flow controller. In equilibrium, the stagnation pressure

$$p = \frac{Q_{\text{flow}}}{C_{\text{noz}}} \tag{4.12}$$

in the buffer-gas volume is specified by the mass flow rate of the buffer-gas $Q_{\text{flow}}$ through the extraction nozzle with conductivity $C_{\text{noz}}$ (see e.g. [135]). For a monoatomic ideal gas the latter can be approximated by (see e.g. [136])

$$C_{\text{noz}} = 1.42 \times 10^4 \frac{d_0[\text{mm}]}{\sqrt{A[\text{u}]T[\text{K}]}}[\text{cm}^3/\text{s}], \tag{4.13}$$

where $A$ and $T$ correspond to the atomic mass number and temperature of the buffer-gas, respectively, and $d_0$ describes the throat diameter of the extraction nozzle. The change in mass flow originates from a change in the speed of sound[136]. Equation (4.13) does not account for gas viscosity effects that lead to a reduction of the conductivity of a few percent [136] and neglects the fact that the nozzle material shrinks during cooling. Following the ideal gas law $pV = nRT$ (see e.g. [137]) the gas density $n/V$ is proportional to $p/T$ ($n$ being the amount of substance in moles). However, as the nozzle conductivity itself depends upon the buffer-gas temperature, the stagnation pressure and thus the gas density for a fixed mass flow will change as a function of the buffer-gas temperature. This is of importance, as parameters like the stopping and extraction efficiencies depend upon the prevalent gas density. As an example, figure 4.8 shows the extraction efficiency of the CGC as a function of the buffer-gas temperature. Cooling down the buffer-gas improves its purity and an increase in extraction efficiency is expected. However, a sudden decrease of

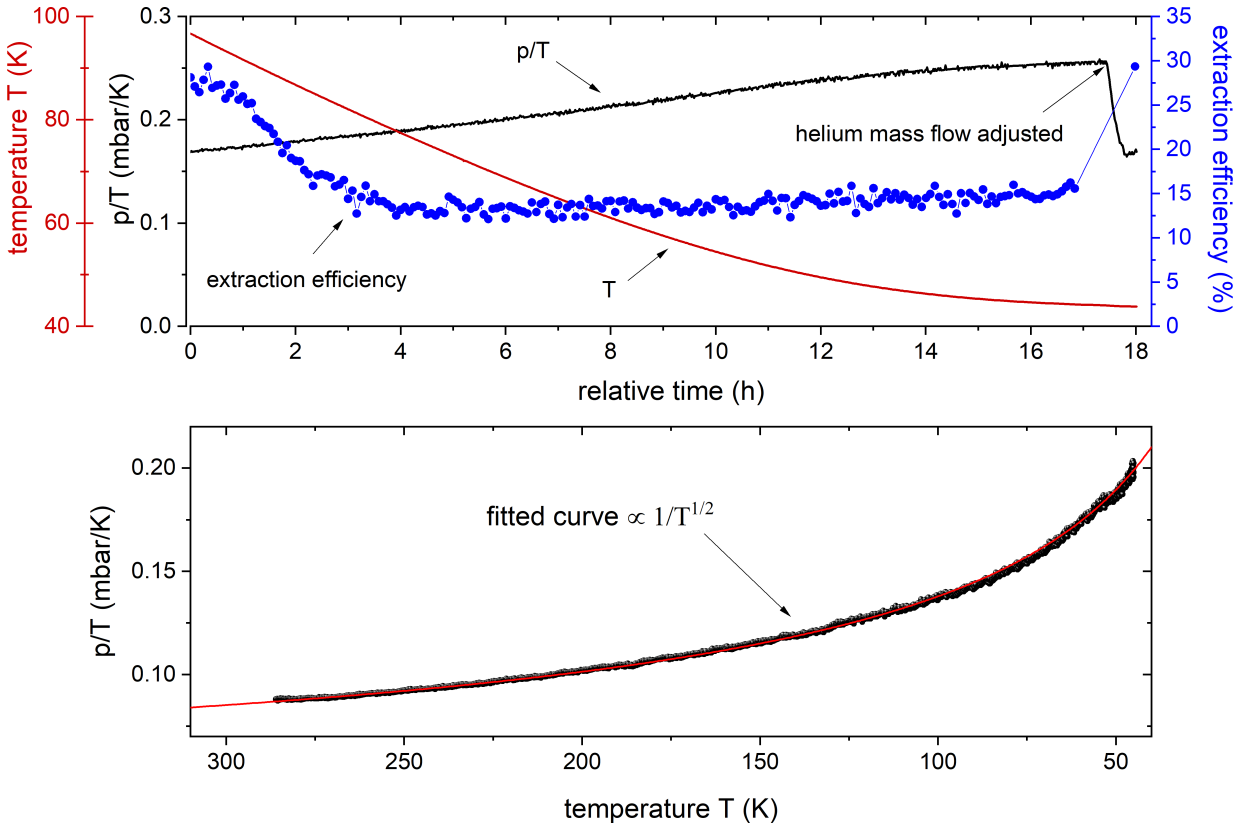


Figure 4.8: (Top figure) Extraction efficiency, operating temperature and pressure to temperature ratio as a function of the relative time during the cooling down of the CGC. After about 17 hours the mass flow was adjusted to match the buffer-gas density with its initial value. This restores the initially obtained extraction efficiency. (Bottom figure) Buffer-gas density, represented as the ratio between the buffer-gas pressure and its temperature, as a function of the buffer-gas temperature at a constant mass flow. The data is well described by a fit function proportional to $1/T^{1/2}$ which agrees well with equation (4.13).

the extraction efficiency is seen. This is due to the fact that the gas density, represented as the pressure to temperature ratio $p/T$, increases during the cooling process up until it reaches a point at which the repulsive force from the radio-frequency field at the funnel is not able to efficiently guide the ions. Once the inserted buffer-gas mass flow is corrected for the change in nozzle conductivity and the initial buffer-gas density is reached, the extraction efficiency is restored. Note that the extraction efficiencies at about 100 K and 50 K, respectively, are similar. At these temperatures most of the gas impurities are already frozen out. In addition, figure 4.8 shows that the temperature dependency of the buffer-gas density is well described by a $1/T^{1/2}$ proportionality as indicated by equations (4.12) and (4.13).

### 4.3.4 Optimizing the RF Funnel

In the funnel region the ion is subject to the dc and rf fields applied to the funnel electrodes. The resulting force on the ion is balanced by friction with the buffer gas, which depends upon the ion mobility $K$. For the case of an electric dc field gradient in axial direction, the resulting axial force on the ion is given by

$$\vec{F}_{\mathrm{dc}} = q(\vec{E} - \frac{\vec{v}}{K}). \tag{4.14}$$

where $\vec{v}$ corresponds to the steady-state velocity of the ion in the buffer gas. To first order the ion mobility scales linear with the inverse of the gas density. Thus, it is more convenient to make use of the reduced ion mobility $K_0$ which is defined as the ion mobility at standard temperature $T_0 = 273.15$ K and standard

pressure $p_0 = 1013\,\mathrm{mbar}$ $K = K_0(p_0/T_0)/(p/T)$. Here, $K_0$ is referred to as the reduced ion mobility and is subordinate to the buffer-gas type and the ion's electronic configuration including its charge state. Indeed, this dependencies are used in modern high-resolution ion mobility spectrometers to separate different ion species due to their difference in ion mobility (see e.g. [138]). In the case of singly-charged radon ions in helium gas the reduced ion mobility corresponds to about $K_0 = 17.4\,\mathrm{cm}^2/(\mathrm{V\,s})$ [139]. In order to extract the ions, the repulsive force induced by the applied radio frequency field at the funnel electrodes, given by (see e.g. [108])

$$F_{\mathrm{rf}} = -\left(\frac{m}{q}\right) K^2 \frac{V_{\mathrm{rf}}^2}{r_0^4} r \propto -\left(\frac{m}{q}\right)\left(\frac{T}{p}\right)^2 V_{\mathrm{rf}}^2, \tag{4.15}$$

needs to counter the axial force acting on the ion. Here, $2r_0$ is the local distance between two funnel electrodes and $r$ is the distance of the ion in the locally created quadrupole field. Combining equations (4.14) and (4.15) it is shown that for a fixed funnel geometry the minimum required rf voltage is determined by the charge $q$ and the mass $m$ of the ion as well as its ion mobility. As seen in figure 4.9, doubly-charged radon and lead ions require a higher radio-frequency amplitude for an efficient ion extraction compared to their singly-charged equivalent (about $90\,\mathrm{V_{pp}}$ compared to $70\,\mathrm{V_{pp}}$ which is a bit less then a factor of $\sqrt{2}$). In contrast to the charge state, no element-specific dependences among distinct elements are observed. This is of particular interest for the beam time operation of the CGC. Depending upon the ionization potentials of the fusion-evaporation reaction products it is conceivable for different charge states to be present in the CGC. Following the trend from figure 4.9 it has to be ensured that the radio-frequency amplitude of the funnel is sufficiently strong to efficiently transport these species if mass measurements on this species is foreseen. Typically, the radio-frequeny amplitude is set to about 120 V during beam times to ensure an efficient transport of singly- and doubly-charged ions. Equation (4.15) indicates the repulsive force of the funnel to be inversely proportional to the square of the gas density $\delta \propto p/T$. Figure 4.10 shows measured extraction efficiencies as a function of the radio-frequency amplitude at the funnel for different gas densities. The gas densities in terms of the ratio between buffer gas pressure and its temperature is plotted against the amplitude required to reach 50 % of the maximum extraction efficiency. The data is well described by a square-root function which verifies that for ion guiding in the funnel the rf voltage - for a given dc gradient along the funnel structure - is proportional to the square root of the gas density.

Figure 4.10 also shows that the increase in extraction efficiency gets steeper the lower the gas density. In the case of gas densities equivalent to 50 mbar at room temperature, the extraction efficiency increases from about 10 to 90 % within $20\,\mathrm{V_{pp}}$ ($30\,\mathrm{V_{pp}}$ in the case of gas densities equivalent to 84 mbar at room temperature (14 mbar at 50 K)). To ensure an efficient ion transport for any occurring charge state the funnel rf amplitude is typically set to $120\,\mathrm{V_{pp}}$ at cryogenic temperatures.

### 4.3.5 Optimizing the Nozzle Transition

The extraction efficiency is very sensitive to the dc field gradient at the extraction nozzle [91]. Whereas the ion guidance within the CGC is predominantly given by the electrical dc and rf fields of the electrodes, the ions are finally extracted from the CGC by means of a gas jet formed by the extraction nozzle of *de-Laval* type [140]. The transition from electrical to gas jet guidance needs to be matched in order to achieve efficient transitions into the gas jet and thus an efficient ion extraction. This transition is tuned by the dc field gradient applied between the last funnel electrode and the extraction nozzle. This allows to (de-)accelerate the ions prior to their transition into the gas jet. In the previous work of [91] an attractive voltage difference of about -5 V between the last funnel electrode $V_{\mathrm{fun}}^{\mathrm{min}}$ and the nozzle voltage $V_{\mathrm{noz}}$ was measured to be most efficient at room and cryogenic temperatures. These measurements were solely based on the extracted $\alpha$ activity from $^{219}$Rn ions. Radon as a noble gas has a relatively high first ionization potential compared to the first and even second ionization potentials of fusion-evaporation reaction products. It is therefore

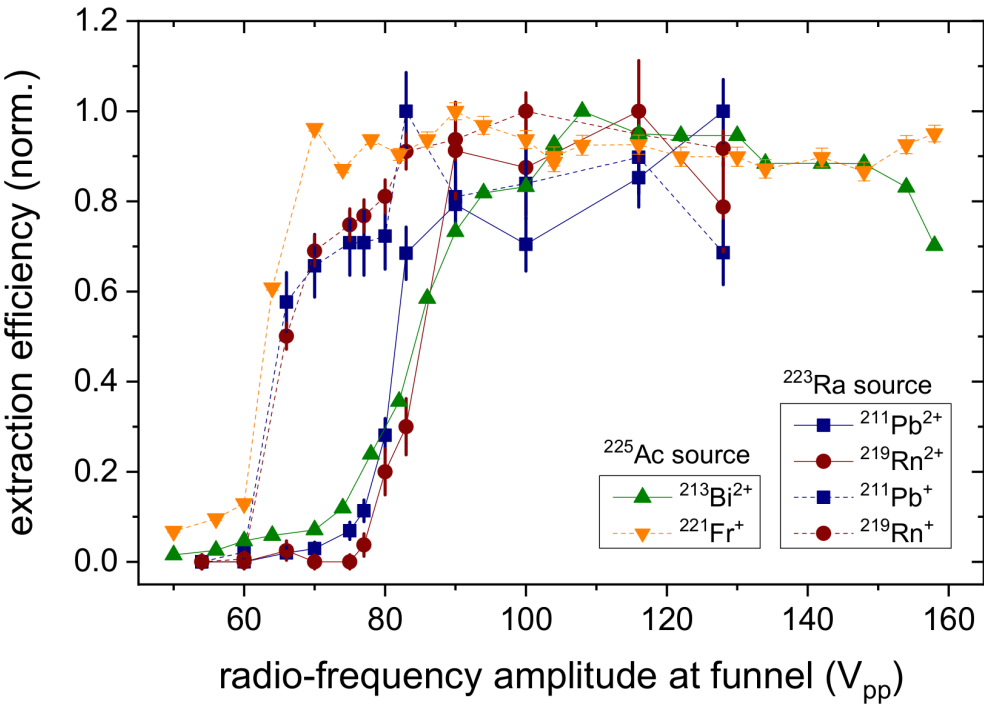


Figure 4.9: Normalized extraction efficiencies for singly- and doubly-charged ions extracted from $^{223}$Ra and $^{225}$Ac recoil-ion sources as a function of the applied rf voltage to the funnel electrodes. In the cases of bismuth and francium the normalized extraction efficiency is obtained using the $\alpha$ detector at D2 (bismuth and francium were solely extracted as doubly and singly charged ions, respectively, which was confirmed by measurements using the Penning traps). For lead and radon the normalized efficiency is obtained by ToF measurements using the Channeltron detector at D2. The sources were placed axially 10 cm in front of the funnel. A dc voltage gradient of 3 V/cm along the funnel electrodes has been applied (corresponding to a voltage difference of 40 V between the first and last funnel electrode). The operating temperatures and helium gas pressures were 40 K and 7.2 mbar in the case of $^{223}$Ra and 165 K and 30 mbar in the case of $^{225}$Ac (gas density equivalent to about 54 mbar at room temperature), respectively. The experimental uncertainty of the radio-frequency is on the order of $\pm$2 V in all cases.

of great importance to validate these measurements with respect to different charge states, especially for non-noble gas isotopes. For this, the extracted charge-state distributions as a function of the dc voltage difference between the last funnel and extraction nozzle electrode were measured using a Channel Electron Multiplier (CEM) detector at the detector position D2 [114]. As seen in figure 4.11, the obtained curves for the extraction efficiency of singly-charged ions have an increased FWHM when compared to their doubly-charged pendants. However, as all curves peak around a voltage difference of about $-1$ V to $-0.5$ V a simultaneous optimum voltage difference for all cases is found. These measurements are performed for two different gas pressures, namely 6.6 mbar and 7.7 mbar, at an operating temperature of 42 K (corresponding to room temperature equivalent gas pressures of 46 mbar and 55 mbar, respectively). This is consistent to a difference in gas density of about 15 % which is a typical range in which pressures are changed. Within this change in pressure no pressure dependency is oberserved. Thus, in standard operation where the extraction efficiency is maximized, a voltage difference of $(V_{\mathrm{noz}} - V_{\mathrm{fun}}^{\mathrm{min}}) = -0.5$ V is used. Note that compared to the value of -5 V from [91] the optimal voltage has shifted by several volts. This is due to the fact that in the measurements of [91] an radial misplacement was present. The radial center point of the funnel ring electrodes did not match the radial center point of the extraction nozzle by about 1 mm. As the ions arrived radially displaced with respect to the extraction nozzle a larger attractive dc field gradient was required to efficiently transition the ions into the gas jet. Due to vibrations of the cold head of the CGC, mechanical misalignments of electrodes, e.g. the funnel electrodes, cannot be excluded in long-term operation. However, a scan of the voltage difference as in figure 4.11 immediately reveals a mechanical displacement for the case of the funnel.

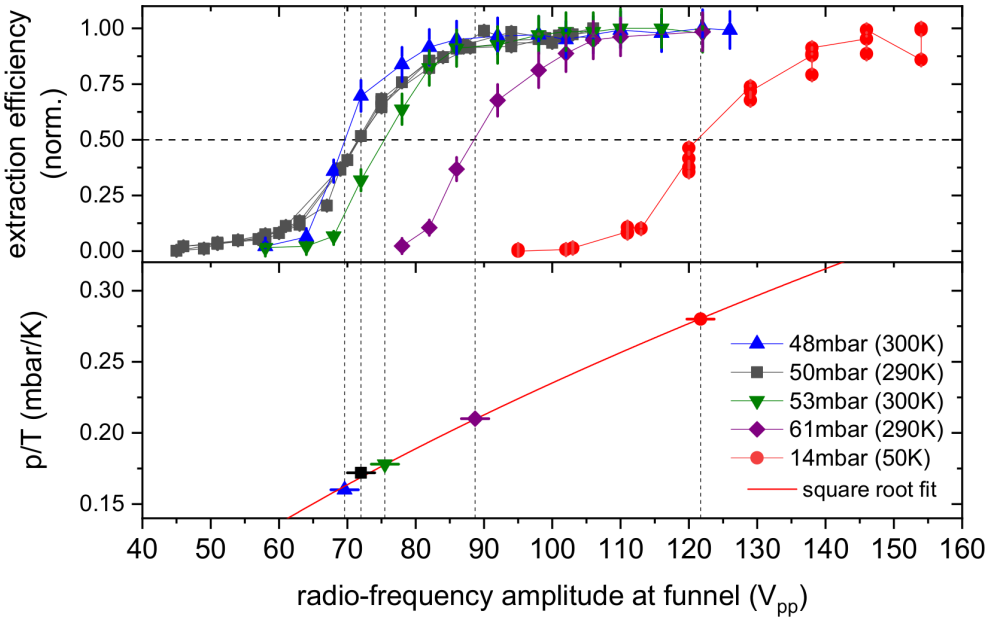


Figure 4.10: (Top) Normalized extraction efficiencies of $^{219}Rn^{+}$ ions as a function of the radio-frequency amplitude at the funnel for different buffer gas pressures and temperatures. The pressure to temperature ratio $p/T$ is proportional to the buffer-gas density. For these measurements a $^{223}$Ra recoil ion source was placed about 10 cm in front of the funnel and the $\alpha$ detector was used at position D2. (Bottom) The gas density is proportional to the square-root of the radio-frequency amplitude at the funnel as indicated by equation (4.15).

### 4.3.6 Trade-off between Extraction Efficiency and Extraction Time

In standard operation the CGC settings maximize the extraction efficiency. Following the discussion of figure 4.11 a slightly attractive extraction nozzle voltage with respect to the last funnel electrode is favoured to maximize the extraction efficiency. For more attractive voltages, the extraction efficiency decreases. However, a more attractive voltage leads to a higher dc field gradient which results into a faster extraction time. This is shown in figure 4.12. Here, the measured extraction times for different voltage differences between the extraction nozzle and the last funnel electrode is compared to the obtained extraction efficiency with the same settings. It is found that there is indeed a trade-off between the fastest possible extraction and the maximum extraction efficiency [114]. For a voltage difference of -0.4 V the extraction efficiency for $^{219}Rn^{+}$ ions is at its maximum. Using these settings, the extraction time for the ions are about 65 ms for a dc field gradient along the funnel of 1.6 V/cm. In order to speed up the ion extraction, a more attractive potential can be applied to the extraction nozzle. As an example, being 2.5 V more attractive at a voltage difference of -2.9 V between the extraction nozzle and the last funnel electrode, the extraction time decreases to about 30 ms. However, for these settings, the extraction efficiency for the $^{219}Rn^{+}$ ions drops by about 30 %. As previously discussed, doubly-charged ions are more sensitive to voltage changes of the nozzle. The drop in efficiency for $^{219}Rn^{2+}$ for this setting corresponds to 60 %. To further decrease the extraction time, higher dc field gradients can be applied. Figure 4.12 shows the extraction time for a voltage difference of -2.9 V with a higher dc field gradient along the funnel of 3.5 V/cm instead of 1.6 V/cm. In on-line experiments it is inevitable to find a compromise between fast extraction and highest efficiency to maximize the extracted ion rate. Currently, mass measurements on fusion-evaporation reaction products including potential isomers with half-lives of $\gtrapprox 200$ ms are feasible.

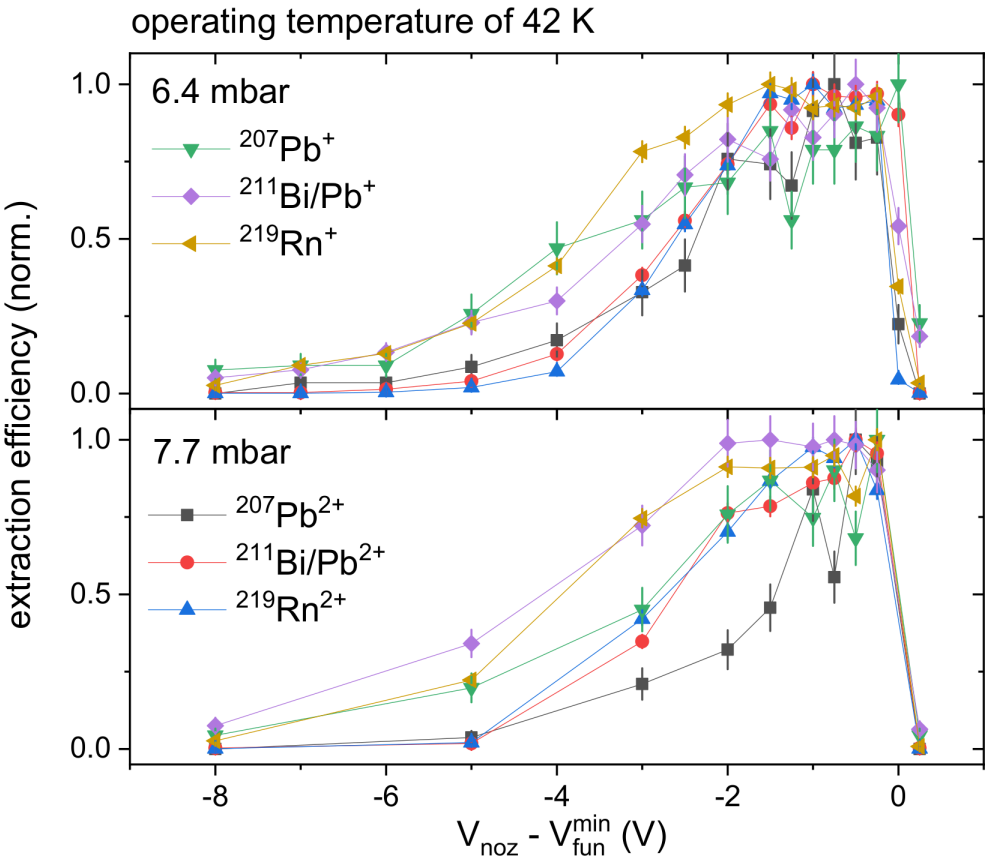


Figure 4.11: Normalized extraction efficiencies obtained from a $^{223}$Ra recoil-ion source as a function of the voltage difference between the last funnel electrode and the extraction nozzle for two different helium buffer-gas pressures at an operation temperature of 42 K. The gas pressures correspond to the room-temperature equivalent pressures of 46 mbar (top) and 55 mbar (bottom). The source was positioned axially 10 cm in front of the funnel. The pressure in the extraction RFQ region was fixed to $\cdot 5 \times 10^{-2}$ mbar. The dc-field gradient along the funnel and its rf amplitude were 1.6 V/cm and 118 $V_{pp}$, respectively. Here, $V_{fun}^{min} = 44$ V was fixed and the nozzle voltage was varied. The voltage difference to the first extraction RFQ electrode was fixed at 10 V. For further details see text.

### 4.3.7 Nozzle Bunching

As seen in figure 4.12 the ions can be slowed down inside the CGC by applying a more repulsive voltage to the extraction nozzle with respect to the last funnel electrode. If the repulsive voltage is strong enough to counter the axial drift force of the ions, the ions are stopped in front of the extraction nozzle. If a stable trapping is realized depends upon the ion parameters and the rf field generated by the funnel. The stability criteria are linked to those of a radio-frequency quadrupole [108]. Trapping ions in the high-pressure regime of the CGC can be of advantage. Charge-state distributions are manipulated towards lower-charged states by increasing the duration the ions are exposed to the buffer-gas. Figure 4.13 shows the extracted ion signal of a $^{223}$Ra source for two different voltage differences between the extraction nozzle (left) and the last funnel electrode as well as for different storage times (right). Note that at an operation temperature of 130 K, molecular compounds are still visible in the ToF spectra, even if the ions are extracted directly. It can be seen that an increase in the storage time results into a disappearance of the doubly-charged ion peaks and a simultaneous increase of the single-charged peaks. At the same time the molecular side bands increase. Note that for storage times longer than 100 ms an overall drop in extraction efficiency is observed.

Although these conditions are not directly applied to the measurements at SHIPTRAP they help to understand the purity level inside the gas cell and to estimate losses in the transport time inside the gas

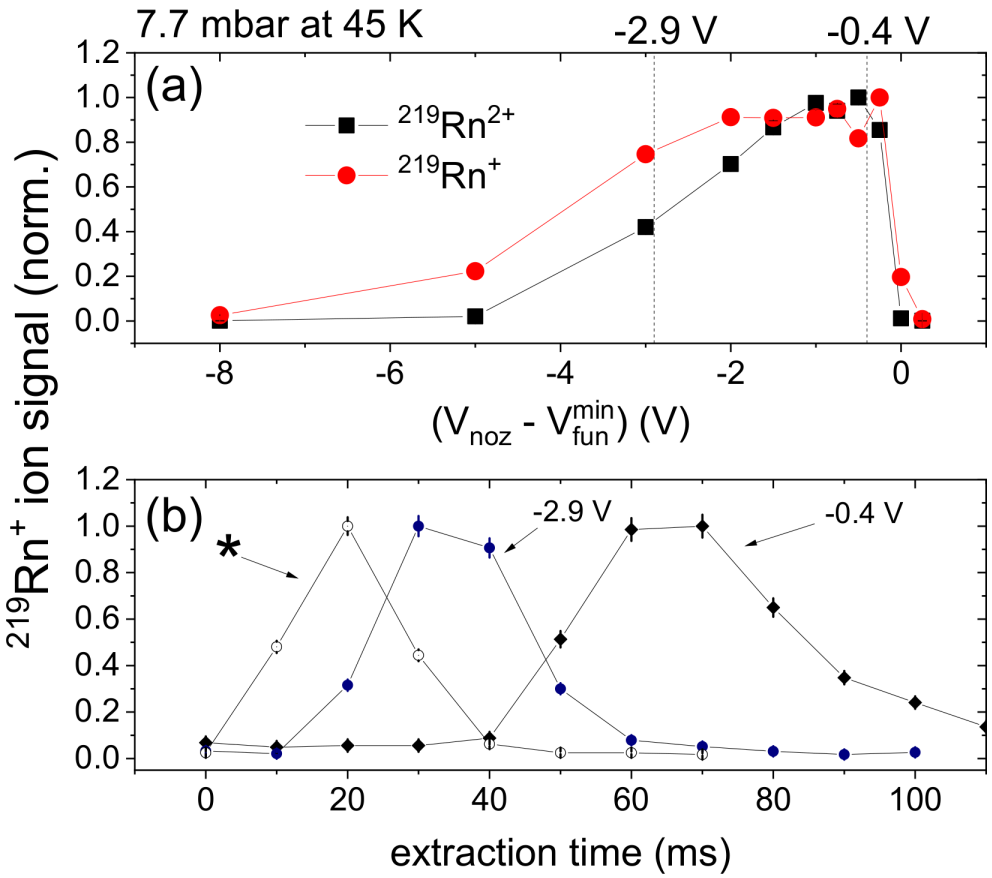


Figure 4.12: Extracted ion signal at D2 from a $^{223}$Ra recoil-ion source as a function of the voltage difference between the extraction nozzle and the closest funnel electrode (a) and as a function of the extraction time (b). The source is axially positioned 20 cm in front of the funnel with a dc gradient of 1.6 V/cm. The helium buffer-gas pressure is 7.7 mbar at an operating temperature of 45 K. The extraction times are measured for different voltage difference between the extraction nozzle and the closest funnel electrode of -0.4 V and -2.9 V, respectively. The distribution marked as * corresponds to -2.9 V with a higher funnel dc gradient of 3.5 V/cm along the funnel. To obtain the extraction time in (b) a pulsed source voltage in combination with a delay-pulsed extraction RFQ was used as described in [91]. Figure modified from [114].

cell and in addition might allow for investigations of gas-phase chemistry in the gas cell.

### 4.3.8 Optimizing the Extraction RFQ

The extraction nozzle is directly followed by a radio-frequency quadrupole (*extraction RFQ*). In this region the residual buffer-gas is drawn out by a turbomolecular pump (type Edwards STPH1203, 1200 l/s) and background pressures of about $10^{-2}$ mbar are reached when the CGC operates at a nominal gas density corresponding to a room-temperature equivalent pressure of 50 mbar. An applied radio-frequency field to the extraction RFQ with frequency $\nu_{\mathrm{rfq}}^{\mathrm{extr}} = 940$ kHz and amplitude $V_{\mathrm{pp}}^{\mathrm{extr}}$, with a phase shift of 180 ° with respect to neighbouring rods, allows for a radial confinement of the ions if certain stability criteria are fulfilled [141, 142]. A dc field gradient along the axial direction of the extraction RFQ is superimposed with the rf field to guide the ions towards the subsequent buncher section. The stability criterion for an ion transport is given by [141, 142]

$$0 < \frac{qeV_{\mathrm{pp}}^{\mathrm{extr}}}{2mr_0^2\pi^2(\nu_{\mathrm{rfq}}^{\mathrm{extr}})^2} < 0.92. \tag{4.16}$$

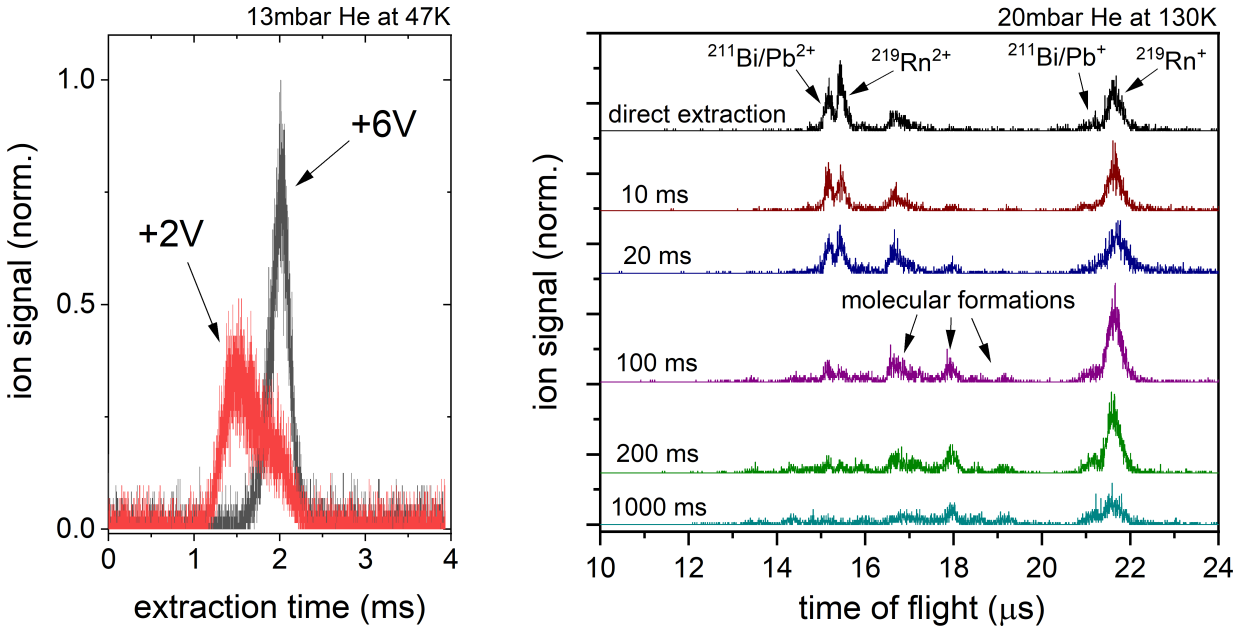


Figure 4.13: (Left) Extracted ion signal at D2 of a $^{223}$Ra source as a function of the extraction time. Ions are extracted in pulses by switching the potential at the extraction nozzle between +44 V (+50 V) and +42,V. The voltage of the last funnel electrode is 44 V which leads to the voltage differences between the extraction nozzle and last funnel electrode of +2 V and +6 V, respectively. The source was pulsed at 10 Hz with a pulse width of 1.4 ms. The CGC was operated at 13 mbar and 47 K. The source was axially positioned 10 cm in front of the funnel with a dc gradient of 3 V/cm along the funnel. Note that no distinct ion peaks are observed. (Right) Extracted time-of-flight spectra for different storage times ranging from zero (direct extraction) to 1000 ms. The extraction nozzle was pulsed from a voltage difference of +4 V to -1 V with respect to the last funnel electrode using a pulse width of 1 ms.

Here, $2r_0 = 10$ mm corresponds to the distance between the surface of opposing rods. For a given ion with the mass-to-charge ratio $m/q$ equation (4.16) indicates a cut-off voltage for which ions do not experience stable ion trajectories and thus are lost. In practise an rf amplitude of $V_{\mathrm{pp}}^{\mathrm{extr}} = 200$ V is used, which allows for a stable ion transport of any ion for which $m/q > 49$. The extraction RFQ section is followed

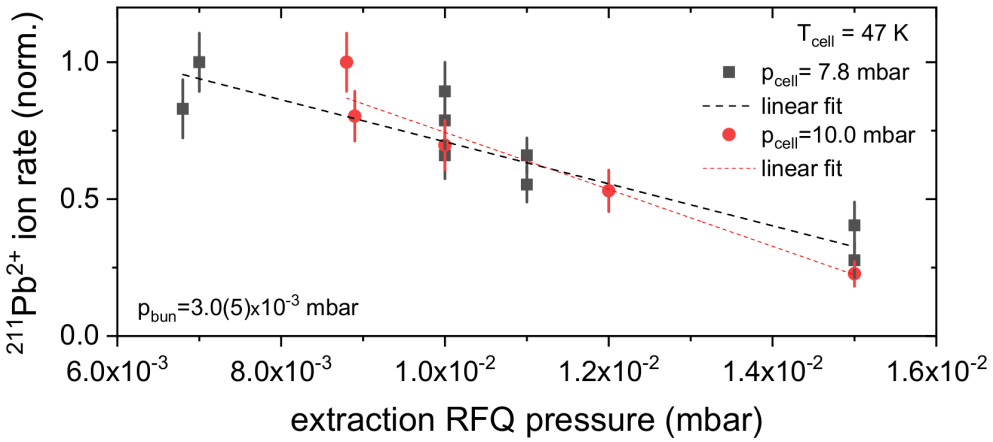


Figure 4.14: Normalized extracted ion rates of $^{211}$Pb$^{2+}$ ions as a function of the helium buffer-gas pressure of the buncher (top figure) and the extraction RFQ pressure (bottom figure) for different working conditions. For details see text.

by a buncher section, which again consists of a radio-frequency quadrupole. For an efficient transport of the ions from the extraction nozzle into the buncher the background pressures of both, the extraction rfq region and the buncher region has to be matched. This has been investigated in figure 4.14, where the normalized count rates of $^{211}$Pb$^{2+}$ ions for different pressures of the CGC and the extraction RFQ

are presented. The ions need to be cooled by collisions with the helium buffer-gas. Typically, buffer-gas pressures of $10^{-3}$ mbar are required to efficiently cool the ions. In practise, a helium buffer-gas pressure of $7 \times 10^{-3}$ mbar is used. In this region the extracted ion rate is least dependent upon pressure changes in the extraction RFQ region. However, this parameter is influenced by changes in the spatial distance between, e.g. the extraction nozzle and the extraction RFQ or the extraction RFQ and the buncher section, respectively. Thus, it is recommended to check these dependencies after any realignment of the CGC.

## 4.4 Optimization of the Stopping Efficiency

The stopping and thermalization of the incoming fusion-evaporation residuals (EVRs) is a key step in the PTMS of the heaviest elements. Due to the typically low incoming ion rates and low particle integrals this has to be as efficient as possible. As PTMS requires at least a few ions for a measurement, any loss should be avoided. The stopping efficiency

$$\epsilon_{\mathrm{stop}} \equiv \frac{n_{\mathrm{stopped}}}{n_{\mathrm{inc}} \epsilon_{\mathrm{geom}}} \tag{4.17}$$

is defined as the fraction of the incoming ions ($n_{\mathrm{inc}}$) that lost their entire kinetic energy within the active gas volume of the CGC ($n_{\mathrm{stopped}}$). The term *active* denotes the volume out of which ions can in principle be extracted from the CGC. A circular entrance window foil separates the gas volume of the CGC from the high-vacuum regime of SHIP. Its diameter of 56 mm does not necessarily cover the entire transversal profile of the incoming ion beam and, in addition, the support grid of the window further reduces its effective area. Thus, the fraction of ions which do not hit the entrance window $\eta_{\mathrm{geom}}$ has to be taken into account, resulting in an additional contribution to ion losses which is expressed as a geometrical efficiency $\epsilon_{\mathrm{geom}} = (1 - \eta_{\mathrm{geom}})$.

Based on the discussions in 3.2, the stopping efficiency is conditioned by the kinetic energy of the incident EVR, the entrance window foil type and thickness as well as the buffer-gas type and density of the CGC. Only the ions that are stopped within the active gas volume of the CGC can be extracted. Thus, a rather thin entrance window foil is favourable. On the other hand, the energy loss throughout the entrance window foil needs to be high such that the buffer-gas density suffices for the stopping. The gas density however is restricted by the maximum rf voltage that can be applied at the funnel structure as it was already shown in previous works (see for instance [118]). Therefore, a good compromise in ion losses due to both, the entrance window foil thickness and gas density, has to be achieved. These investigations were extended for the EVRs $^{251,254}$No, $^{254-256}$Lr and $^{257}$Rf which have been measured within the scope of this work. As an outlook, simulation results on $^{258}$Db are given.

The stopping efficiencies for EVRs at SHIPTRAP cannot be tested off-line and have to rely on simulations. For this the Stopping and Range of Ions in Matter (SRIM) software package is consulted [119]. It makes use of a semi-empirical Monte Carlo code based on a binary collision model which has been parametrized using experimental data. After several improvements over the last decades, SRIM is able to reproduce the stopping powers of about 25 000 experimental data points with an overall accuracy of better than 4 % [119]. However, experimental data is only available for isotopes with proton numbers up to $Z = 92$ and thus the simulations have to be scaled accordingly to reflect the behaviour of heavier elements. More detailed information on the simulations, their evaluation and the basics of ion stopping is given in Appendix 10.4. Here, only the results are presented.

### 4.4.1 Simulated Stopping Efficiencies

To simulate the stopping efficiency, specific energy distributions for the incoming fusion-evaporation reaction products are assumed. In this work, uranium isotopes are used and scaled in their incident kinetic energy (*energy-corrected* simulations) to reassemble the properties of heavier elements, as SRIM only allows to simulate isotopes with up to 92 protons. In a second approach, instead of scaling their incident kinetic energy, the density of both, the titanium entrance window foil and the buffer gas is scaled accordingly (*density-corrected* simulations). This section focusses on the results of the simulations. A detailed description of the procedure is given in the appendix 10.4.

The simulated stopping efficiencies for $^{251,254}$No, $^{254-256}$Lr and $^{257}$Rf are shown in figure 4.15. As an outlook, the simulated stopping efficiency for the next heavier element $^{258}$Db is also presented. Generally speaking, the stopping efficiencies the *density corrected* and the *energy corrected* simulations are in good agreement with each other which strengthens the discussion based on equation (A10.13). However, the curves for the *energy corrected* cases are shifted by about 0.1 µm towards higher entrance window thicknesses with respect to the *density corrected* curves. This is considered as a model dependent uncertainty in the calculation and matches the production uncertainty and the inhomogeneity of typical window entrance foils.

### 4.4.2 Optimized Entrance Window Foil Thickness

To obtain the optimal entrance window foil thickness for every reaction, figure 4.15 is evaluated. From recent experiments it is known that for the case of $^{254}$No ions, a titanium window foil thickness of 3.8 µm is too thick, resulting in an approximated stopping efficiency of 60 % [118]. For the on-line measurements of $^{254}$No presented in the following in this work, a titanium foil thickness of 3.4 µm resulted in a relatively good stopping efficiency. This is congruent with the SRIM simulations for $^{254}$No at 30 mbar. Note that, as discussed in section 10.4.1, the stopping power of (heavy) ions in gaseous materials is overestimated by SRIM by about a factor of 1.5 [143]. The optimal entrance window foil thickness is obtained by averaging the maximum values simulated for the energy-corrected and the density-corrected cases. The resulting optimal titanium entrance window foil thicknesses are summarized in table 4.1. The simulations suggest a change in the entrance window foil thickness of 0.2 µm with respect to its optimial value which results into a drop in the stopping efficiency of about 20 % (absolute). A too thin foil is countered by an increase in the buffer-gas density whereas a too thick foil results in inevitable ion losses. Thus, in practice, a *safety margin* of -0.1 µm is reasonable. In addition, optional degrader foils can be used to decrease the incident particles energy and help to counter a too thin entrance window foil. This is of practical relevance since in most of the on-line experiments a variety of different EVRs are addressed. The impact of additional degrader foils is therefore discussed in the following section.

Table 4.1: Obtained titanium entrance window foil thicknesses for the CGC on EVRs at SHIPTRAP. A *safety margin* of -0.1 µm to the optimal value is reasonable.

| | $^{251}$No | $^{254}$No | $^{254}$Lr | $^{255}$Lr | $^{256}$Lr | $^{257}$Rf | $^{258}$Db |
|---|---|---|---|---|---|---|---|
| Ti thickness (µm) | 3.7 | 3.5 | 3.7 | 3.4-3.5 | 3.4-3.5 | 3.7 | 3.8 |

### 4.4.3 Impact of Degrader Foils

When several EVRs of interest are addressed in an on-line experiment campaign the thickness of the titanium entrance window foil needs to be chosen in an appropriate way. Ions that are stopped within the

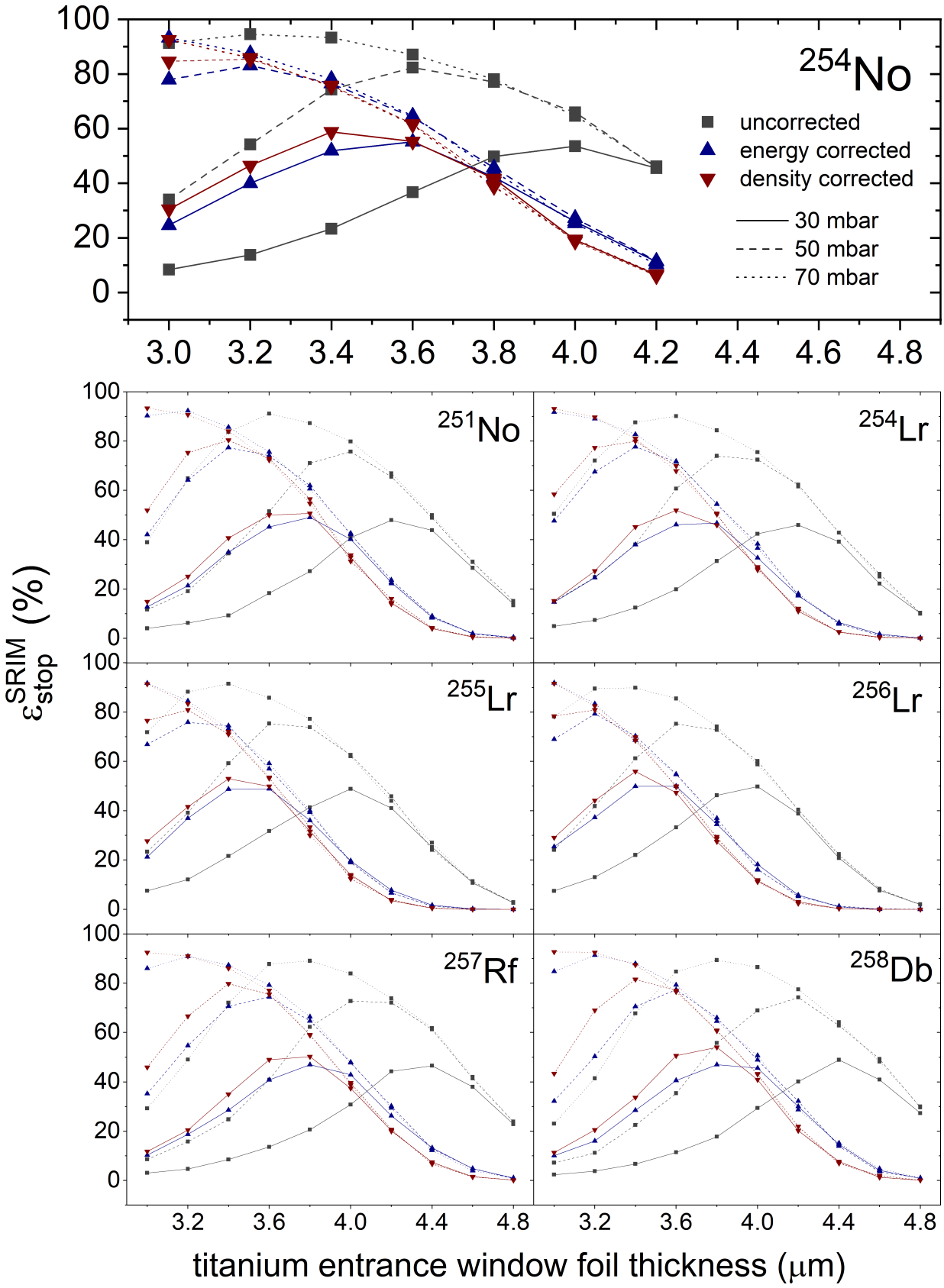


Figure 4.15: Simulated stopping efficiencies for the EVRs of interest as a function of the titanium entrance window foil thickness in steps of 0.2 µm for different gas pressures at room temperature. The EVRs are resembled by $^{238}$U ions for defined incident kinetic energies given in table 10.4. For further details see text.

entrance window foil are inevitable lost for extraction. Thus, the EVR with the slowest recoiling energy determines the entrance window thickness. If this entrance window foil is too thin to stop faster recoiling

EVRs, the buffer-gas density can be increased, up to a certain extent, to counterbalance.[7] Therefore,

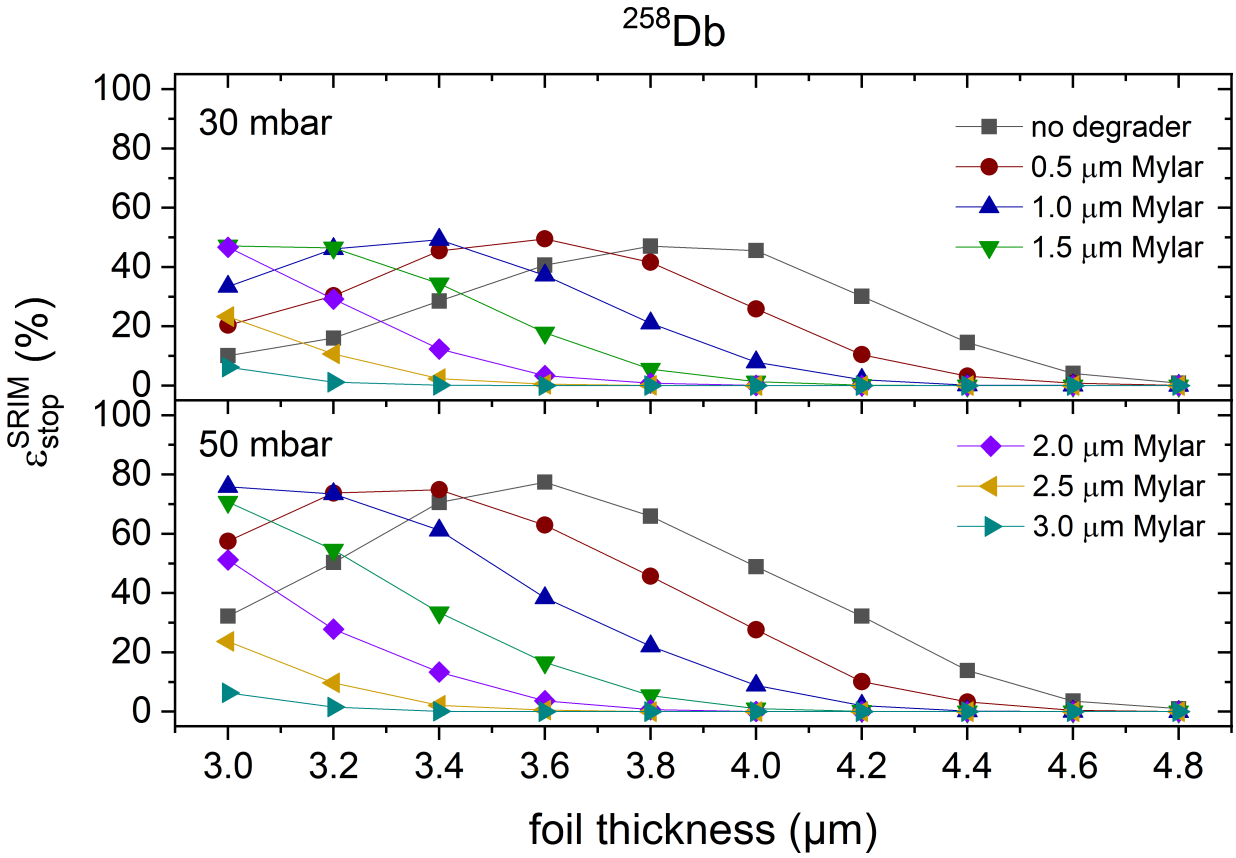


Figure 4.16: Simulated stopping efficiencies for $^{258}$Db ions as a function of the titantium entrance window foil thickness for various degrader foil thicknesses at room-temperature buffer-gas pressures of 30 mbar (top figure) and 50 mbar (bottom figure), respectively. For further details see text.

optional degrader foils (Polyethylene Terphtalate (PET, also known as Mylar), $H_8C_{10}O_4$) of various (combined) thicknesses ranging from 0.5 µm to 4.5 µm can be inserted *in-situ* into the beam line. The foils are positioned about 30 cm in front of the entrance window foil. To quantify the impact of degrader foils on the stopping efficiency, additional SRIM simulations have been performed. The evaluation is identical to the one presented in the previous sections. However, the additional thickness of the degrader foil $d_{\mathrm{deg}}$ has to be taken into account. This is done by the substitution $d_{\mathrm{foil}} \rightarrow d_{\mathrm{deg}} + d_{\mathrm{foil}}$ in equations (A10.14)-(A10.16). Note that in the SRIM simulations the degrader foil is positioned directly in front of the entrance window foil as SRIM does not allow to set up vacuum conditions below $10^{-2}$ mbar. Thus, the simulations do not account for additional losses due to straggling of the ions passing through the degrader foil.[8] Figure 4.16 shows the simulated stopping efficiencies for $^{258}$Db as a function of the titanium entrance window foil thickness for various degrader foil thicknesses at room temperature gas pressures of 30 mbar and 50 mbar, respectively. As seen, adding 0.5 µm of mylar foil in front of the entrance window foil is approximately equal to an increase in the entrance window foil thickness of 0.2 µm to 0.3 µm. Thus the stopping power for $^{258}$Db in mylar is simulated to be approximately half the value of the stopping in titanium. Comparing the tabulated stopping powers for $^{238}$U at an energy of 35 MeV for mylar (approx. 5 MeV/µm) and titanium (approx. 10 MeV/µm) [119] gives congruent results.

[7] However, this is only applicable to certain extent, as the repulsive force from the funnel rf is limited due to a limitation in the obtain radio-frequency amplitude as discussed in section 4.3.4.

[8] However, simulations have shown that additional losses can be neglected for the present distances.

# Chapter 5

# Experimental Campaign in 2018

## 5.1 Overview

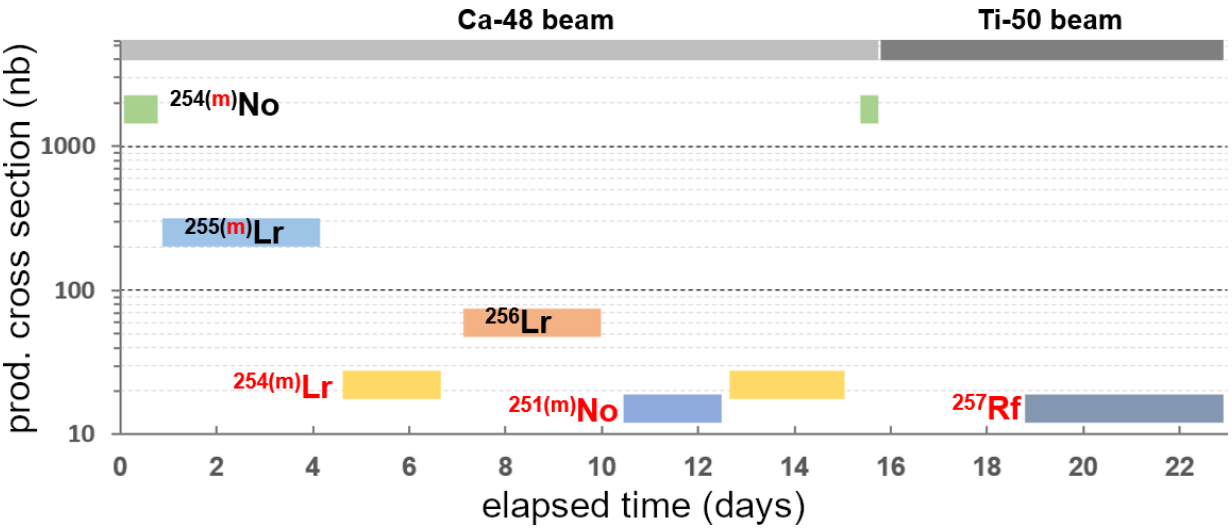


Figure 5.1: Overview of the SHIPTRAP beam time campaign in summer 2018, dedicated to perform high-precision PTMS in the region of the heaviest elements by means of the PI-ICR technique. In total, two beam time blocks of approximately 16 days of $^{48}Ca^{10+}$ and 7 days of $^{50}Ti^{12+}$ primary beam were covered to measure the atomic ground-state masses of $^{251,254}$No and $^{254-256}$Lr with uncertainties down to 1 keV/c$^2$. In addition, the first direct high-precision mass spectrometry of a superheavy element $^{257}$Rf has been performed. Furthermore, for the first time, the isomeric states $^{251m,254m}$No and $^{254m,255m}$Lr have been measured with excitation energies down to 30 keV. Red labels correspond to states which were measured for the first time with respect to direct high-precision PTMS.

For the first time the PI-ICR technique was successfully applied to transfermium elements. Due to the outstanding performance of the CGC all ion species are solely measured as doubly-charged state. The ground-state masses of $^{251,254}$No and $^{254-256}$Lr have been measured with yet unreached absolute uncertainties of down to 1 keV/c$^2$ with respect to mass spectrometry in this region. Out of these, the masses of $^{251}$No and $^{254}$Lr were measured directly for the first time. In all cases the mass uncertainty was increased by at least one order of magnitude with respect to previously performed mass measurements or the mass values extracted from $\alpha$-decay spectroscopy. In addition, the isomeric states $^{251m,254m}$No and $^{254m,255m}$Lr were measured directly for the first time using mass spectrometry. Except for $^{254m}$No these isomeric states are of low-lying nature with excitation energies in the region of 30 keV to 100 keV. Their spatial separation from their respective ground-state demands highest resolving powers in the order of more than 10 000 000.

In the case of $^{255}$Lr, the isomeric state with an excitation energy of about 30 keV required accumulation times of over one second which reflects the current limit with respect to background gas collision. This, in combination with the electric and magnetic field stability that need to be stabilized for several hours in order to acquire enough statistics, was challenging.

The shortest-lived species measured was the isomeric state $^{254m}$No with a half-life of about 250 ms. The highest obtained detection rate was approximately one count every ten seconds in the case of $^{254g}$No with a cross section of 1.8µb. The isotopes $^{251}$No and $^{257}$Rf shared the lowest cross section of 15 nb. However, due to a reduced overall efficiency of the SHIPTRAP setup in the case of rutherfordium, its detection rate of approximately one detected ion every 8 hours with only 5 ions in total proves the feasibility of PI-ICR for lowest production rates and particle integrates. The evaluation of the isomer $^{254m}$No is still under evaluation and will not be presented within this work.

## 5.2 Efficiency Determination

### 5.2.1 Overview

To perform high-precision PTMS of the heaviest elements, efficiency and sensitivity is key. In the upcoming discussion the detector positions defined in figure 3.2 are used. The overall efficiency of SHIPTRAP

$$\epsilon_{\mathrm{SHIPTRAP}} \equiv \frac{\dot{n}_{\mathrm{det}}^{\mathrm{D4}}}{\dot{n}_{\mathrm{inc}}} \tag{5.1}$$

is defined as the ratio of detected ion signal at the position-sensitive detector $\dot{n}_{\mathrm{det}}^{\mathrm{D4}}$ to the incoming particle rate $\dot{n}_{\mathrm{inc}}$. The latter is measured in front of the CGC using a 16-strip detector at position D1 ($\dot{n}_{\mathrm{inc}} \equiv \dot{n}_{\mathrm{det}}^{\mathrm{D1}}$), which in addition allows a mapping of the beam profile. Following the path of the incoming particles, the first ion losses occur due to the finite size of the titanium entrance window foil of the CGC with respect to the spatial distribution of the incoming particles and the supporting grid structure of the entrance window foil. For the first, a value of 4(1) % is obtained for typical beam profiles of EVRs[1] whereas the latter corresponds to about 7(3) % [118, 114]. This translates into a transmission efficiency at the entrance window of $\epsilon_{\mathrm{geom}} = 89(3)$ %. Next, the ions need to be stopped inside the buffer-gas volume of the CGC. Based on simulations (see section 4.4), the corresponding stopping efficiency $\epsilon_{\mathrm{stop}}$ strongly depends upon the kinetic energy of the incoming ion, the entrance window foil thickness and the buffer-gas density. The stopping efficiency typically ranges from 40 % to 80 %. Following the stopping, the ions are thermalized and extracted from the CGC, mainly by electric dc and radio-frequency fields, passing through an extraction nozzle and an extraction RFQ ion guide. The extraction efficiency $\epsilon_{\mathrm{extr}}$ in this section is strongly related to the gas purity (typical pressures of 7 mbar at 40 K) and the applied electric fields. The extraction efficiency is investigated in [91] where a value of $\epsilon_{\mathrm{extr}} = 74(3)$ % is obtained at cryogenic temperatures. However, this value is determined using point-like recoil ion sources (see section 4.2), in contrast to the on-line operation mode of the CGC, in which ions are spatially separated within the buffer-gas volume of the CGC after their stopping [118]. The ions enter a buncher RFQ section in which they are cooled, stored and bunched. The corresponding efficiency $\epsilon_{\mathrm{bunch}}$ is altered by impurities of the helium buffer-gas at typical room-temperature pressures of $1 \times 10^{-3}$ mbar. Following this, $\epsilon_{\mathrm{opt}}$ describes the transmission efficiency throughout the downstream ion optics. The efficiencies concerning the injection into the Penning-trap system, their cooling and preparation and the measurement is summarized in $\epsilon_{\mathrm{trap}}$. Last, $\epsilon_{\mathrm{det}}^{\mathrm{D4}}$ accounts

[1] The beam profiles for nobelium and lawrencium ions have been measured during beam time and no deviation to the ones presented in, e.g., the work of Lautenschläger *et al.* [144] is found.

for the detection efficiency of the position-sensitive detector. Therefore, the overall efficiency of equation (5.1) is given by

$$\epsilon_{\mathrm{SHIPTRAP}} = \frac{\dot{n}_{\mathrm{det}}^{\mathrm{D4}}}{\dot{n}_{\mathrm{inc}}} = \epsilon_{\mathrm{geom}}\epsilon_{\mathrm{stop}}\epsilon_{\mathrm{extr}}\epsilon_{\mathrm{bun}}\epsilon_{\mathrm{opt}}\epsilon_{\mathrm{trap}}\epsilon_{\mathrm{det}}^{\mathrm{D4}}. \tag{5.2}$$

Some of the partial efficiencies are measured using one of the removable detectors all along the SHIPTRAP setup (see figure 3.3). The combined stopping and extraction efficiency of the CGC

$$\epsilon_{\mathrm{CGC}} \equiv \frac{\dot{n}_{\mathrm{det}}^{\mathrm{D*}}}{\dot{n}_{\mathrm{det}}^{\mathrm{D1}}} = \epsilon_{\mathrm{geom}}\epsilon_{\mathrm{stop}}\epsilon_{\mathrm{extr}} = 35(5)\,\%, \tag{5.3}$$

has been investigated in an on-line beam time in 2015 using $^{254}$No ions [118]. Combining this measured value with results on the extraction efficiency [91]

$$\epsilon_{\mathrm{extr}} \equiv \frac{\dot{n}_{\mathrm{det}}^{\mathrm{D^*}}}{\dot{n}_{\mathrm{recoil}}} = 74(3)\,\% \tag{5.4}$$

and the geometrical losses [118] as listed above allows obtaining a stopping efficiency value of about 50 % which is congruent with simulations presented in section 4.4. Here, $\dot{n}_{\mathrm{recoil}}$ corresponds to the emitted ion rate of a recoil-ion source positioned inside the buffer-gas volume of the CGC (see section 4.2). The off-line efficiency of SHIPTRAP

$$\epsilon_{\mathrm{offline}} \equiv \epsilon_{\mathrm{extr}}\epsilon_{\mathrm{bun}}\epsilon_{\mathrm{opt}}\epsilon_{\mathrm{trap}}\epsilon_{\mathrm{det}}^{\mathrm{D4}}. \tag{5.5}$$

is extensively optimized prior to the on-line measurements. The expression

$$\epsilon_{\mathrm{SHIPTRAP}} = \epsilon_{\mathrm{geom}}\epsilon_{\mathrm{stop}}\epsilon_{\mathrm{offline}} \tag{5.6}$$

immediately follows from equations (5.2) and (5.5). Thus, in section 5.2.2, $\epsilon_{\mathrm{offline}}$ is evaluated in more detail. Moreover, $\epsilon_{\mathrm{extr}}\epsilon_{\mathrm{bun}} = \dot{n}_{\mathrm{det}}^{\mathrm{D2}}/\dot{n}_{\mathrm{recoil}}$ and $\epsilon_{\mathrm{opt}} = \dot{n}_{\mathrm{det}}^{\mathrm{D2}}/\dot{n}_{\mathrm{det}}^{\mathrm{D3}}$ allow a further disentanglement.

### 5.2.2 Off-line Efficiency

The off-line efficiency of SHIPTRAP $\epsilon_{\mathrm{offline}}$ defined in equation (5.5) is evaluated using the recoil-ion sources $^{223}$Ra and $^{225}$Ac positioned inside the buffer-gas volume of the CGC. Their attributed recoil ion rate $\dot{n}_{\mathrm{recoil}}$ is measured according to section 4.2.1. The results are presented in table 5.1.

Table 5.1: Obtained off-line efficiencies for $^{219}$Rn$^+$ and $^{221}$Fr$^+$ ions originating from the recoil-ion sources $^{223}$Ra and $^{219}$Ac. The sources are positioned inside the CGC at a helium buffer-gas pressure of 7.6 mbar at an operating temperature of 40 K about 20 cm in front of the funnel. The detected ions at D4 are subject to a full mass measurement cycle, including ion bunching, cooling and preparation in the preparation trap (about 200 ms) and a PI-ICR double-pattern with an accumulation time of 200 ms (without any excitation in the measurement trap). The detected rate of $^{219}$Rn$^+$ has been corrected due to its relatively short half-life of $\approx$ 4 s (see figure 4.2). $\bar{\epsilon}_{\mathrm{offline}}$ represents to the arithmetic mean value of the obtained individual uncertainties (uncertainty-weighted). This data has also been presented in the article of O. Kaleja *et al.* [114].

| recoil-ion | source | $\dot{n}_{\mathrm{recoil}}$ | $\dot{n}_{\mathrm{det}}^{D4}$ | $\epsilon_{\mathrm{offline}}$ | $\bar{\epsilon}_{\mathrm{offline}}$ |
|---|---|---|---|---|---|
| $^{219}$Rn$^+$ | $^{223}$Ra | 82(2) s$^{-1}$ | 7.0(2) s$^{-1}$ | 9.1(3) % | 9.3(3) % |
| $^{221}$Fr$^+$ | $^{225}$Ac | 17(2) s$^{-1}$ | 1.80(5) s$^{-1}$ | 10.4(11) % | |

The obtained off-line efficiencies for $^{219}$Rn$^+$ and $^{221}$Fr$^+$ are 9.1(3) % and 10.4 (11) %. Both values differ by about one standard deviation. This is explained by an overestimation of the release factor for $^{219}$Rn$^+$

(assumed to be 100 % as discussed in section 4.2) and changes in the optimized voltages and the alignment of ion optics, respectively. The error-weighted arithmetic mean value results in $\epsilon_{\mathrm{SHIPTRAP}} = 9.3(3)\,\%$.[2]

Typically, a combined efficiency around $\epsilon_{\mathrm{extr}}\epsilon_{\mathrm{bun}} = 45(5)\,\%$ is obtained at the detector position D2 [114] which in combination with $\epsilon_{\mathrm{extr}} = 74(3)\,\%$ results in a bunching efficiency of $\epsilon_{\mathrm{bunch}} = 61(7)\,\%$. Main losses in this section are due to an inefficient transition from the extraction RFQ into the buncher RFQ section or due to ion losses in the helium buffer-gas. Note that $\dot{n}_{\mathrm{det}}^{\mathrm{D4}}$ corresponds to the detected ion signal rate at the position-sensitive detector and not to the ion rate at this position since the detection efficiency $\epsilon_{\mathrm{det}}^{\mathrm{D4}} < 1$. Assuming $\epsilon_{\mathrm{det}}^{\mathrm{D4}} \approx 30\,\%$ [100] gives a combined transmission and trap-related efficiency of $\epsilon_{\mathrm{opt}}\epsilon_{\mathrm{det}}^{\mathrm{D4}} \approx 70\,\%$. On the other hand, $\dot{n}_{\mathrm{inc}}$ (which equals $\dot{n}_{\mathrm{det}}^{\mathrm{D1}}$), $\dot{n}_{\mathrm{det}}^{\mathrm{D}^*}$, $\dot{n}_{\mathrm{det}}^{\mathrm{D2}}$ and $\dot{n}_{\mathrm{det}}^{\mathrm{D3}}$ need to represent the ion rates at the respective positions. For the first case, the ion rate

$$\dot{n}_{\mathrm{inc}} = 2\dot{\alpha}_{\mathrm{det}}^{\mathrm{D1}}/\mu_{\mathrm{branch}} \tag{5.7}$$

is obtained by an $\alpha$-rate measurement of the 16-strip detector with the respective $\alpha$ branching ration. As the ions are implanted into this detector, a factor of two is attributed for the solid angle. The ion rates for $\dot{n}_{\mathrm{det}}^{\mathrm{D1}}$, $\dot{n}_{\mathrm{det}}^{\mathrm{D}^*}$, $\dot{n}_{\mathrm{det}}^{\mathrm{D2}}$ and $\dot{n}_{\mathrm{det}}^{\mathrm{D3}}$ are obtained in the same way using $\alpha$-rate measurements as explained in section 4.3.1.

### 5.2.3 Position-Dependent Detector Efficiency

The MCP plates of the position-sensitive detector experiences a degeneration in their detector efficiency $\epsilon_{\mathrm{det}}^{\mathrm{D4}}$ with respect to integrated ion counts on a given spots. Main causes of this effect are damages due to radiation of the implanted ions or the ion impacts themselves. Therefore, a position-dependent detector efficiency is expected. Figure 5.2 shows the evaluation of the detector efficiency for different phase image positions by using $^{133}Cs^{+}$ ions. In this case, the number of detected ion events per phase image is compared, e.g. by normalizing to the phase image with the highest intensity. Note that this only provides relative changes in the detector efficiency, the absolute detector efficiency is still unknown but approximated by about 30 % [100]. [3] A maximum deviation of 22(4) % between the phase images is found. Any loss in efficiency is tried to be prevented. However, this deviation is tolerated as the precise knowledge of the final phase image is often not known. In addition, in the case of the modified cyclotron phase image, the phase spots of the isomeric and the ground state would have to be considered.

## 5.3 Overall Efficiency of SHIPTRAP

With respect to the direct high-precision PTMS of the heaviest elements, the overall efficiency of the setup

$$\epsilon_{\mathrm{SHIPTRAP}} \equiv \frac{\dot{n}_{\mathrm{det}}}{\dot{n}_{\mathrm{inc}} \times \eta(t_{1/2}, T_{\mathrm{cycle}}) \times e^{-\ln(2)T_{\mathrm{cycle}}/t_{1/2}}} \tag{5.8}$$

is of primary importance. It is defined as the ratio of detected $\dot{n}_{\mathrm{det}}$ to incoming ions $\dot{n}_{\mathrm{inc}}$. The incoming ion rate is corrected for ion losses due to a finite half-life of the ion $t_{1/2}$ with respect to a measurement

[2] Note that in the article of O. Kaleja *et al.* [114] the efficiency of $^{219}Rn^{+}$ is stated as 8.6(3) % instead of 9.1(3) % because it has not been corrected for its finite half-life. Therefore the stated attributed error-weighted arithmetic mean value of 8.7(3) % also differs from this work's value of 9.3(3) %.

[3] For PI-ICR measurements, the ions of interest are measured at a similar and well-defined radius as $^{133}Cs^{2+}$ such that this is representative for any other ion species.

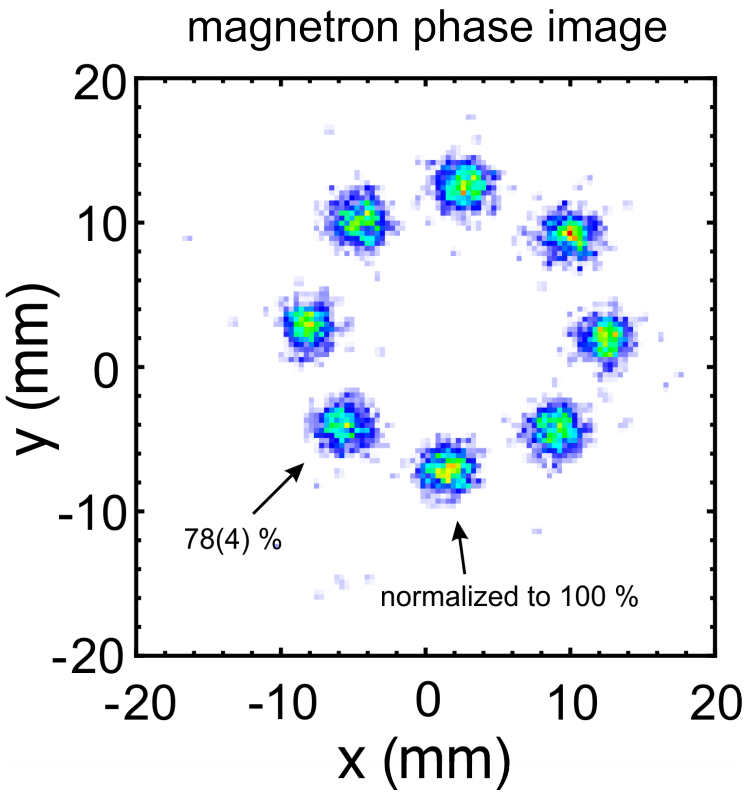


Figure 5.2: Relative detector efficiencies of the delay-line detector at D4 for standard PI-ICR ion radii. For this, the intensities of individual phases of the magnetron mode for $^{133}Cs^{+}$ ions are compared to the phase image with highest intensity.

cycle time $T_{\mathrm{cycle}}$ using

$$\eta(t_{1/2}, T_{\mathrm{cycle}}) = T_{\mathrm{cycle}}^{-1} \int_0^{T_{\mathrm{cycle}}} e^{-\frac{\ln(2)}{t_{1/2}} t} dt = T_{\mathrm{cycle}}^{-1} \frac{t_{1/2}}{\ln(2)} \left[ 1 - e^{-\frac{\ln(2)}{t_{1/2}} T_{\mathrm{cycle}}} \right], \tag{5.9}$$

due to a continuous ion loading into the buncher during the times 0 and $T_{\mathrm{cycle}}$. The factor $e^{-\ln(2) T_{\mathrm{cycle}}/t_{1/2}}$ accounts for the decay loss during the measurement. The cycle time is approximated as the sum of buffer-gas cooling in the preparation trap (about 300 ms) and the accumulation time in the measurement trap ($t_{\mathrm{acc}}$) which typically ranges from 40 ms to 1200 ms depending on the desired mass resolving power and precision, respectively.[4] Note that for $t_{1/2} >> T_{\mathrm{cycle}}$ equation (5.9) yields $\eta(T_{\mathrm{cycle}}) \approx 1$. To proceed to heavier and more exotic ion species it is inevitable to investigate the overall efficiency with respect to different experimental conditions to understand the general behaviour of the setup and allow for further improvements. The overall efficiency

$$\epsilon_{\mathrm{SHIPTRAP}} = \underbrace{\epsilon_{\mathrm{geom}} \epsilon_{\mathrm{stop}} \epsilon_{\mathrm{extr}}}_{=\epsilon_{\mathrm{cell}}} \epsilon_{\mathrm{bun}} \epsilon_{\mathrm{opt}} \epsilon_{\mathrm{trap}} \epsilon_{\mathrm{det}}, \tag{5.10}$$

consists of multiple contributions as discussed in sections 4.3.1 and 5.1. By comparing the overall efficiencies with respect to, e.g. the recoil energies or the ionization potentials of the EVRs, trends can be evaluated. Therefore, the overall efficiency for the isotopes $^{251,254}No^{2+}$ and $^{254-256}Lr^{2+}$ is analysed. As a starting point, the incoming ion rate

$$\dot{n}_{\mathrm{inc}}(t_0) = 2\dot{\alpha}(t_0)/\mu_{\mathrm{branch}} \tag{5.11}$$

[4]Note that according to the discussion of section 6.5.1, some ions spent an additional accumulation time in the measurement trap prior to their measurement which increases their respective cycle time.

for every isotope is calculated from its measured implanted $\alpha$ rate $\dot{\alpha}$ into the $\alpha$ detector positioned in front of the CGC (at position D1) for a given point in time $t_0$. Since the ions are implanted into the detector surface, a factor of two is accounted in addition to the branching ratio $\mu_{\mathrm{branch}}$ of the measured $\alpha$-decay channel. As the production and thus incoming ion rate depends upon the beam current $I_{\mathrm{beam}}(t)$ which is subject to temporal changes, the rate is normalized to the beam current at this point in time $I_{\mathrm{beam}}(t_0)$. The incoming ion rate at any given time $t$ can then be approximated by

$$\dot{n}_{\mathrm{inc}}(t) = \dot{n}_{\mathrm{inc}}(t_0) \times \frac{I_{\mathrm{beam}}(t)}{I_{\mathrm{beam}}(t_0)}. \tag{5.12}$$

In order to take into account unknown changes in the incoming ion rate, an uncertainty of 20 % is taken for $\dot{n}_{\mathrm{inc}}(t)$. Changes in the incoming ion rate are present due to temporal changes in the transmission efficiency through SHIP or changes in the production rate because of mechanical changes of the target foil. Figure 5.3 shows the measured beam current as well as the incoming ($\dot{n}_{\mathrm{inc}}$) and detected ion rate ($\dot{n}_{\mathrm{det}}$) during the $^{48}Ca^{10+}$ beam time block. The overall efficiency is calculated using equation (5.8). Note the absolute difference in production for different isotopes due to their difference in production cross section. To quantify the off-line efficiency of the SHIPTRAP setup, i.e. on ions originating from the recoil ion source positioned in the buffer-gas volume of the CGC, the detected ion rates of $^{211}Pb^{2+}$ are shown in addition. These rates are normalized to the first obtained value during beam time and corrected for the change in the recoil ion rate due to the half-life of the recoil ion source mother $^{223}$Ra. A drop in the overall efficiency for the EVRs is seen comparing the obtained efficiencies for $^{254}No^{2+}$ at the start and towards the end of the respective beam time blocks. The drop in efficiency is about a factor of two. In the semi-logarithmic plot, a linear trend can be seen throughout the data of all EVRs. An exponential fit to the data translates into a drop in efficiency of 50 % within a time of about 80 h (dashed red line in the overall efficiency plot of figure 5.8). The overall efficiency for $^{251}No^{2+}$ is systematically shifted towards lower efficiencies by about one order of magnitude, which can be attributed to an inefficient stopping due to the higher recoil energy (see section 4.4). In addition, these data points obey a large scattering compared to the others. Both of these circumstances are still being investigated.

The detected $^{211}Pb^{2+}$ rate halves within $\approx 100$ h (see figure 5.8), which is similar to the drop for the EVRs. This is an important information as these ions solely originate from a $^{223}$Ra recoil ion source positioned in the buffer-gas volume of the CGC, which is independent of any stopping efficiency. The detected rate of $^{211}Pb^{2+}$ has been corrected for the loss due to the finite half-life of $^{223}$Ra (see figure 4.2). As both, the overall efficiency on EVRs and the detection rate for $^{211}Pb^{2+}$, decrease at a similar pace it is concluded that this drop does not primarily originate from a change in the stopping efficiency. This is not an obvious point, as the cryogenic temperatures of the entrance window foil freezes out impurities on its surface from both, the cryogenic buffer-gas volume as well as the room-temperature vacuum regime of the separator in front of the CGC. Any deposition of material will ultimately result in an increase of the entrance window foil thickness and thus alters the stopping efficiency. Most importantly the fraction of EVRs stopped inside the entrance window foil, which are lost for any extraction, increases. Figure 5.3 hints to another circumstance that is not clearly visible on the logarithmic scales. The overall efficiencies for the EVRs are isotope-selected presented for different accumulation time ranges. In the case of $^{254}No^{2+}$ the efficiencies for measurements with relatively long accumulation times are systematically lower compared to the ones with relatively short accumulation times by approximately 25 % to 50 %. This trend is not seen in the other EVRs. After their stopping and thermalization, the ions are extracted from the buffer-gas environment of the CGC throughout the extraction RFQ. The time of the ions spent in this environment is independent of the absolute measurement cycle. However, the ions are cooled and stored in the buncher region, waiting for the Penning traps to finish the current measurement cycle. Thus, the storage time of the ions in the buncher does depend upon the accumulation time of choice. Assuming a loss of ions due to charge-exchange

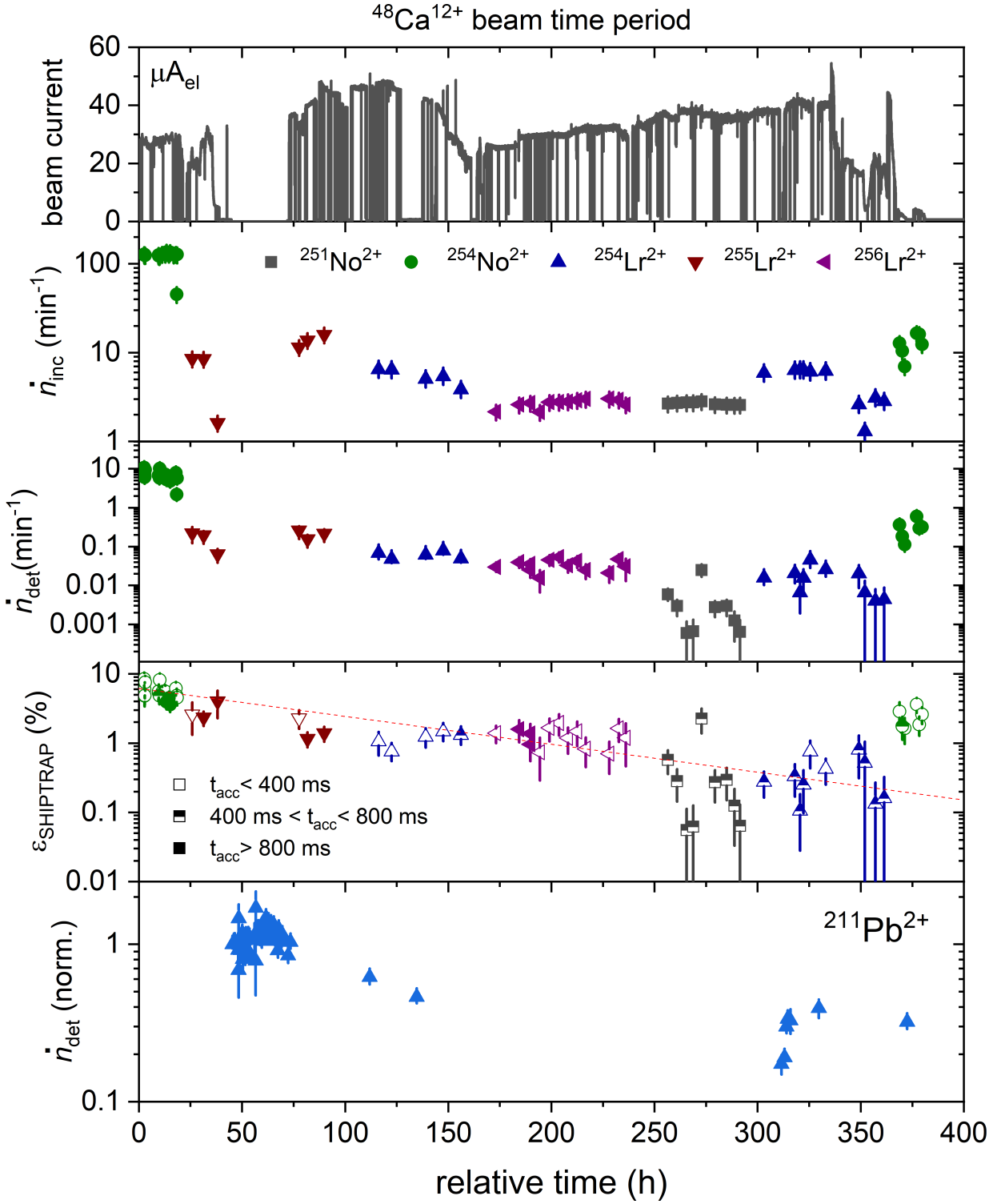


Figure 5.3: Beam current, incoming ion rate $\dot{n}_{\mathrm{inc}}$, detected ion rate $\dot{n}_{\mathrm{det}}$ and the overall efficiency $\epsilon_{\mathrm{SHIPTRAP}}$ for the ground-state mass measurements of $^{251,254}No^{2+}$ and $^{254-256}Lr^{2+}$ during the $^{48}Ca^{10+}$ beam time in 2018. For comparison the detection rate for $^{211}Pb^{2+}$ is shown. As it originated from a $^{223}Ra$ source the rate is normalized to the first obtained value and the half-life of 11.42 d. The overall efficiencies are divided into three categories for measurement cycles in which the accumulation time differs. In all cases the buffer-gas cooling is performed in about 300 ms. Most of the accumulation times range between 40 ms to 100 ms, 500 ms to 600 ms and about 1200 ms. For further details see text.

processes and ion chemistry in the buncher region, respectively, explains the similar trend for the EVRs with respect to $^{211}Pb^{2+}$, as the involved isotopes share similar ionization potentials (see section 4.3.2). This is being investigated in the appendix 10.6.

# Chapter 6

# Data Analysis

## 6.1 Raw Data

To introduce the data analysis procedure an exemplary raw data file obtained for $^{255}Lr^{2+}$ is shown in figure 6.1. In most cases the double-pattern scheme within the PI-ICR technique is used (see section 3.6). The two distinctly measured phase images of the magnetron and modified cyclotron mode show the final phases introduced in equation (3.25). Note the two spatially separated phase spots in the modified cyclotron phase which correspond to the isomeric and ground state of $^{255}Lr^{2+}$. *Raw* in the sense that these phase images define the starting point of the data analysis procedure. These images are already background suppressed by a time-of-flight gate at the corresponding time of flight of the ions of interest.

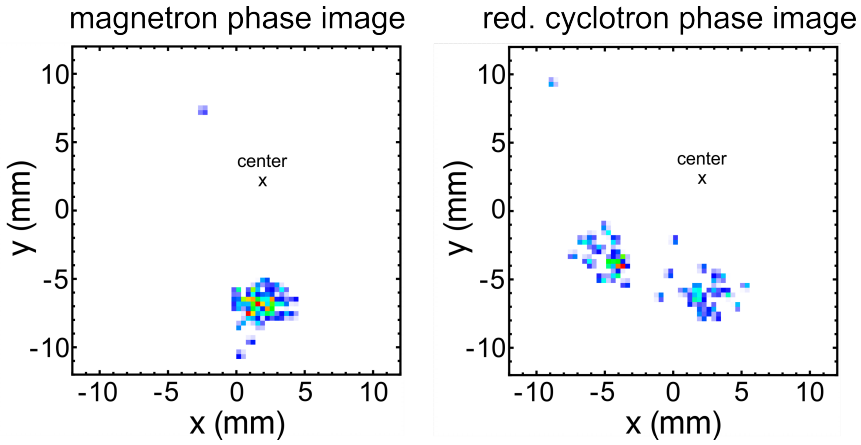


Figure 6.1: Obtained final phase images of a 10 h measurement file for $^{255}Lr^{2+}$ at the delay-line detector positioned at D4. The magnetron (left) and modified cyclotron mode (right) as defined by the double-pattern scheme within the PI-ICR technique are seen. For further details see text.

## 6.2 True Cyclotron Frequency Determination

By making use of the double-pattern scheme of the PI-ICR technique, the true cyclotron frequency of an ion with the charge-to-mass ratio of $q/m$ in the strong magnetic field $B$ is determined by

$$\nu_c = \frac{\omega_c}{2\pi} = \frac{\omega_+ + \omega_-}{2\pi} = \frac{\phi + 2\pi \times (n+m)}{2\pi \times t_{acc}} = \frac{1}{2\pi}\frac{q}{m}B \tag{6.1}$$

where $n$ and $\phi$ are the full ion revolutions and the additional phase difference between the magnetron and the modified cyclotron phase, respectively, obtained in the accumulation time $t_{\mathrm{acc}}$. The uncertainty of the frequency determination is then given by the Gaussian propagation of uncertainty (GPOU)

$$\delta\nu_{\mathrm{c}} = \frac{\delta\phi}{2\pi \times t_{\mathrm{acc}}}, \tag{6.2}$$

where $\delta\phi$ is the uncertainty in the relative phase difference between the magnetron and modified cyclotron phase. There is no error contribution for the amount of ion revolutions $n$ and $m$, as this quantity can only have integer values. In addition, the uncertainty of the accumulation time $t_{\mathrm{acc}}$ can be neglected as it is obtained by the frequency generators, which are locked to a rubidium frequency standard with a relative uncertainty better than $10^{-11}$.

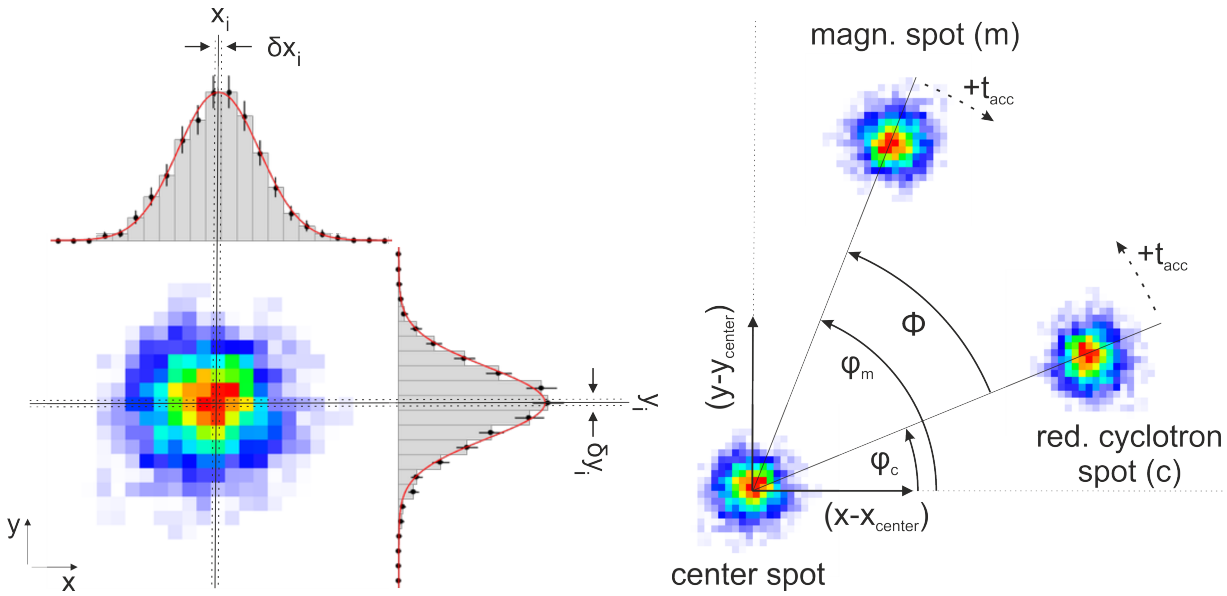


(a) Fit of a phase spot.

(b) Phase spot angles.

Figure 6.2: (a) An obtained phase spot is projected onto the x- and y-axis and fitted to a Gaussian distribution to obtain its center position ($x_{\mathrm{i}} \pm \delta x_{\mathrm{i}}, y_{\mathrm{i}} \pm \delta y_{\mathrm{i}}$). (b) Phase angle determination of the magnetron ($\varphi_{\mathrm{m}}$) and modified cyclotron spot ($\varphi_{\mathrm{c}}$) with respect to a center spot. $\phi$ corresponds to the relative phase difference between both phase spots. The dashed arrows show the spot evolution at the detector with increasing accumulation time $t_{\mathrm{acc}}$. Note the opposing direction of movement as discussed in section 3.6.

The relative phase difference $\phi \pm \delta\phi$ is obtained for every measurement file by fitting the obtained phase spots to a Gaussian distribution (see Fig. 6.2a) resulting in

$$\text{center spot} = (x_{\mathrm{center}} \pm \delta x_{\mathrm{center}}, y_{\mathrm{center}} \pm \delta y_{\mathrm{center}}) \tag{6.3}$$

$$\text{magnetron spot} = (x_{\mathrm{m}} \pm \delta x_{\mathrm{m}}, y_{\mathrm{m}} \pm \delta y_{\mathrm{m}}) \tag{6.4}$$

$$\text{mod. cyclotron spot} = (x_{\mathrm{c}} \pm \delta x_{\mathrm{c}}, y_{\mathrm{c}} \pm \delta y_{\mathrm{c}}) \tag{6.5}$$

where $\delta x_{\mathrm{i}}$ and $\delta y_{\mathrm{i}}$ (i $\in$ [center,m,c]) correspond to the fit uncertainty of the corresponding center or phase spot, respectively (in section 6.5.1 we will address the fact that the center spot positions are subject to temporal changes, resulting in a systematic uncertainty). One has to mention that the center spot is always measured in a separate measurement file, usually using the reference ion (see also Fig. 6.2b). The relative positions are then given by

$$\text{rel. magnetron spot} = (\bar{x}_\mathrm{m} \pm \delta\bar{x}_\mathrm{m}, \bar{y}_\mathrm{m} \pm \delta\bar{y}_\mathrm{m}) \tag{6.6}$$

$$\text{rel. mod. cyclotron spot} = (\bar{x}_\mathrm{c} \pm \delta\bar{x}_\mathrm{c}, \bar{y}_\mathrm{c} \pm \delta\bar{y}_\mathrm{c}) \tag{6.7}$$

where $\bar{x}_\mathrm{i} \equiv (x_\mathrm{i} - x_\mathrm{center})$, $\bar{y}_\mathrm{i} \equiv (y_\mathrm{i} - y_\mathrm{center})$ and $\delta\bar{x}_\mathrm{i} = \sqrt{\delta x_\mathrm{i}^2 + \delta x_\mathrm{center}^2}$, $\delta\bar{y}_\mathrm{i} = \sqrt{\delta y_\mathrm{i}^2 + \delta y_\mathrm{center}^2}$ for i ∈ [m,c].

It makes sense to map the absolute phase angle of the relative magnetron and the relative modified cyclotron phase spot, respectively, in the x-y-plane to [0,2$\pi$[ which if fulfilled for a function satisfying the conditions

$$\varphi_i = \begin{cases} 0 & \text{for } \bar{x}_\mathrm{i} > 0, \bar{y}_\mathrm{i} = 0 \\ \arctan(\bar{y}_\mathrm{i}/\bar{x}_\mathrm{i}) & \text{for } \bar{x}_\mathrm{i} > 0, \bar{y}_\mathrm{i} > 0 \\ \pi/2 & \text{for } \bar{x}_\mathrm{i} = 0, \bar{y}_\mathrm{i} > 0 \\ \pi + \arctan(\bar{y}_\mathrm{i}/\bar{x}_\mathrm{i}) & \text{for } \bar{x}_\mathrm{i} < 0, \bar{y}_\mathrm{i} > 0 \\ \pi & \text{for } \bar{x}_\mathrm{i} < 0, \bar{y}_\mathrm{i} = 0 \\ 3/2\pi - \arctan(\bar{x}_\mathrm{i}/\bar{y}_\mathrm{i}) & \text{for } \bar{x}_\mathrm{i} < 0, \bar{y}_\mathrm{i} < 0 \\ 3/2\pi & \text{for } \bar{x}_\mathrm{i} = 0, \bar{y}_\mathrm{i} < 0 \\ 3/2\pi - \arctan(\bar{x}_\mathrm{i}/\bar{y}_\mathrm{i}) & \text{for } \bar{x}_\mathrm{i} > 0, \bar{y}_\mathrm{i} < 0 \end{cases} \tag{6.8}$$

with an uncertainty (GPOU) of

$$\delta\varphi_\mathrm{i} = \sqrt{\frac{(\bar{x}_\mathrm{i}\delta\bar{y}_\mathrm{i})^2 + (\bar{y}_\mathrm{i}\delta\bar{x}_\mathrm{i})^2}{\bar{x}_\mathrm{i}^2 + \bar{y}_\mathrm{i}^2}} \tag{6.9}$$

for i ∈ [m,c]. A possible realization of the conditions in (6.8) is by making use of the 2-argument-tangents function atan2(y,x) modified in the way that

$$\varphi_i = \mathrm{atan2m}(\bar{y}_\mathrm{i}, \bar{x}_\mathrm{i}) \equiv \begin{cases} \mathrm{atan2}(\bar{y}_\mathrm{i}, \bar{x}_\mathrm{i}) & \text{for } \mathrm{atan2}(\bar{y}_\mathrm{i}, \bar{x}_\mathrm{i}) \geq 0 \\ 2\pi - |\mathrm{atan2}(\bar{y}_\mathrm{i}, \bar{x}_\mathrm{i})| & \text{for } \mathrm{atan2}(\bar{y}_\mathrm{i}, \bar{x}_\mathrm{i}) < 0. \end{cases} \tag{6.10}$$

The phase difference between the magnetron and modified cyclotron phase spot and its attributed uncertainty (GPOU) is then given by

$$\phi = (\varphi_\mathrm{c} - \varphi_\mathrm{m}) \quad \text{and} \quad \delta\phi = \sqrt{(\delta\varphi_\mathrm{m})^2 + (\delta\varphi_\mathrm{c})^2}, \tag{6.11}$$

respectively. Using equations (6.1) and (6.2) the true cyclotron frequency $\nu_\mathrm{c} \pm \delta\nu_\mathrm{c}$ for the corresponding measurement file is obtained.

## 6.3 Frequency Ratio Determination

Suppose successive true cyclotron frequency measurements of the ion of interest $\nu(t_\mathrm{i})$ and the reference ion $\nu_\mathrm{c}^\mathrm{ref}(t_\mathrm{j})$ with the corresponding attributed uncertainties $\delta\nu_\mathrm{c}$ and $\delta\nu_\mathrm{ref}$. Here, $t_\mathrm{i}$ and $t_\mathrm{j}$ are the points

in time where the corresponding measurement was taken, defined as the mid time of the corresponding measurement file.

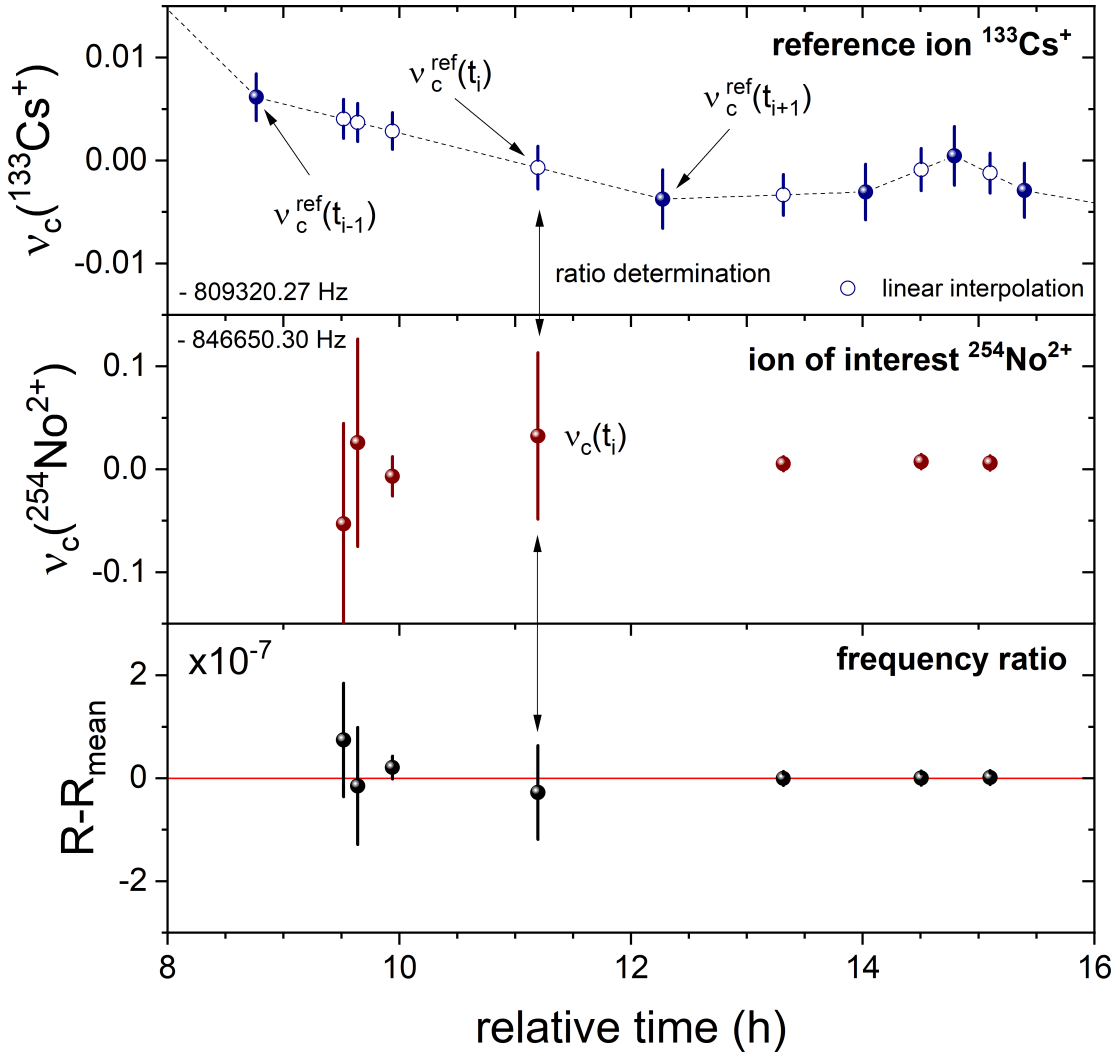


Figure 6.3: Frequency ratio determination during the beam time campaign in 2018. The reference frequency measurements of $^{133}Cs^{+}$ ions (top) are linearly interpolated to the point in time $t_i$ of the frequency measurement of the ion of interest (in this case $^{254}No^{2+}$). The closest reference measurements before and after in time are always used for the linear interpolation. The x-coordinate corresponds to the relative time after the start of the beam time. Note the difference in the frequency scale, the difference in absolute frequency between both species and that occasionally multiple measurements of the ion of interest are performed in between reference ion measurements.

Due to (magnetic) field fluctuations the reference frequency is linearly interpolated to the point in time where the ion of interest was measured (see Fig. 6.3). For two reference measurements obtained at the times $t_{i-1}$ and $t_{i+1}$ the resulting frequency at the time $t_i$ where $t_{i-1} < t_i < t_{i+1}$ is given by

$$\bar{\nu}_{\mathrm{ref}}(t_i) = \bar{t}_i \times (\nu_{\mathrm{ref}}(t_{i+1}) - \nu_{\mathrm{ref}}(t_{i-1})) + \nu_{\mathrm{ref}}(t_{i-1}) \quad \text{with} \quad \bar{t}_i \equiv \frac{t_i - t_{i-1}}{t_{i+1} - t_{i-1}} \tag{6.12}$$

and the uncertainty (GPOU)

$$\delta\bar{\nu}_{\mathrm{ref}}(t_i) = \sqrt{(\bar{t}_i \delta\nu_{\mathrm{ref}}(t_{i+1}))^2 + ((1-\bar{t}_i)\delta\nu_{\mathrm{ref}}(t_{i-1}))^2}. \tag{6.13}$$

Note that for simplicity the subscript c for the true cyclotron frequency is omitted henceforth. In all

cases the reference measurements closest in time are taken for the interpolation (see also Fig. 6.3). The frequency ratio attributed to the measurement file at $t_\mathrm{i}$ is given by

$$r(t_\mathrm{i}) \equiv r_\mathrm{i} \equiv \frac{\bar{\nu}_\mathrm{ref}(t_\mathrm{i})}{\nu(t_\mathrm{i})}. \tag{6.14}$$

Its associated uncertainty is determined by

$$\delta r_\mathrm{i} = \sqrt{\left(\frac{\delta\bar{\nu}_\mathrm{ref}(t_\mathrm{i})}{\nu(t_\mathrm{i})}\right)^2 + \left(\frac{\bar{\nu}_\mathrm{ref}(t_\mathrm{i})\delta\nu(t_\mathrm{i})}{\nu(t_\mathrm{i})^2}\right)^2 + \xi_B^2 r_\mathrm{i}^2 + \xi_D^2 r_\mathrm{i}^2} \tag{6.15}$$

where $\xi_B$ considers a systematic uncertainty originating from time-dependent non-linear magnetic field drifts that is addressed in section 6.5.2. $\xi_D$ considers a systematic uncertainty originating from the distortion of the phase images. For typical operation parameters its contribution is $< 10^{-10}$ [74] and thus can be neglected as typical statistical uncertainties of $> 10^{-9}$ are achieved in this work.

## 6.4 Mean Frequency Ratio Determination

Suppose N single frequency ratio measurements $r_\mathrm{i} \pm \delta r_\mathrm{i}$ for i ∈ [1,...,N]. Then the error-weighted arithmetic mean of the frequency ratio is given by

$$r = \frac{\sum_N w_i r_i}{\sum_N w_i} \quad \text{with the weighting factors} \quad w_i = \frac{1}{\delta r_i^2} \tag{6.16}$$

and the internal and external errors

$$\delta r_\mathrm{int} = \sqrt{\frac{1}{\sum_N w_i}} \tag{6.17}$$

$$\delta r_\mathrm{ext} = \sqrt{\frac{\sum_N w_i (r_i - r)^2}{(N-1)\sum_N w_i}}. \tag{6.18}$$

To obtain the final uncertainty, in addition, a mass-difference-dependent systematic uncertainty $\delta_M$ and a systematic uncertainty of $\delta_\mathrm{syst}$ are quadratically added to obtain the total uncertainty of the frequency ratio

$$\delta r_\mathrm{total} = \sqrt{\delta r_\mathrm{int}^2 + [(\Delta\frac{m}{q})\delta_M r]^2 + (\delta_\mathrm{syst} r)^2}. \tag{6.19}$$

$\delta_M$ is actually a shift, but treated as an uncertainty in e.g. [94]). Here, $(\Delta\frac{m}{q})$ is the mass-to-charge difference between the ion of interest and the reference ion. For the evaluation of $\delta_M$ available off-line data is evaluated in section 6.5.3 which can be neglected within this work. The factor $\delta_\mathrm{syst}$ accounts for additional unknown systematic uncertainties. It is evaluated, e.g., by comparing the inner and outer errors defined in equations (6.17) and (6.18). If the ratio $\delta r_\mathrm{out}/\delta r_\mathrm{int} < 1$, the data scattering is of statistical nature. If not, $\delta_\mathrm{syst}$ accounts for an additional unknown uncertainty as done in e.g. [101]. In most cases,

the evaluated off-line and on-line data in this work show ratios $\delta r_{\mathrm{out}}/\delta r_{\mathrm{int}} \approx 1$ such that no additional unknown systematic is added, i.e. $\delta_{\mathrm{syst}} = 0$.

## 6.5 Systematic Uncertainties

### 6.5.1 Center Spot Scattering

As discussed with respect to equation (6.3) the center spot positions of the magnetron and the modified cyclotron phases are obtained by a Gaussian fit. In addition, as the center spots are subject to temporal changes, the absolute center positions are linear interpolated the same way as for the reference ion measurements (see section 6.3) resulting in

$$\bar{x}_{\mathrm{center}}(t_{\mathrm{i}}) = \bar{t}_{\mathrm{i}} \times (x_{\mathrm{center}}(t_{\mathrm{i+1}}) - x_{\mathrm{center}}(t_{\mathrm{i-1}})) + x_{\mathrm{center}}(t_{\mathrm{i-1}}) \tag{6.20}$$

$$\bar{y}_{\mathrm{center}}(t_{\mathrm{i}}) = \bar{t}_{\mathrm{i}} \times (y_{\mathrm{center}}(t_{\mathrm{i+1}}) - y_{\mathrm{center}}(t_{\mathrm{i-1}})) + y_{\mathrm{center}}(t_{\mathrm{i-1}}), \tag{6.21}$$

where $\bar{t}_{\mathrm{i}}$ is defined as in equation (6.12). Accordingly, $(\bar{x}_{\mathrm{center}}, \bar{y}_{\mathrm{center}})(t_{\mathrm{i-1}})$ and $(\bar{x}_{\mathrm{center}}, \bar{y}_{\mathrm{center}})(t_{\mathrm{i+1}})$ are the center measurements before and after the ion of interest measurement at $t_{\mathrm{i}}$, respectively. This is to be done separately for the magnetron and modified cyclotron phase. In order to account for the scattering of the center spots as seen in figure 6.4, the variance of the center position is evaluated and taken as the uncertainty of the center spot measurements

$$\delta\bar{x}_{\mathrm{center}} \rightarrow \sigma^2(x_{\mathrm{center}}) \tag{6.22}$$

$$\delta\bar{y}_{\mathrm{center}} \rightarrow \sigma^2(y_{\mathrm{center}}). \tag{6.23}$$

The variance $\sigma^2$ is determined individually for the x- and y-position of the magnetron and modified cyclotron center position, respectively. In the case of the x-position for any of the two phases, the variance is calculated by

$$\sigma^2(x_{\mathrm{center}}) = \frac{1}{N}\sum_{i=1}^{N}(x_{i,center} - \mu)^2 \quad \text{with} \quad \mu = \frac{1}{N}\sum_{i=1}^{N} x_{i,center}, \tag{6.24}$$

where $\mu$ corresponds to the mean value. Here, $N$ denotes the total number of individually obtained x-positions of the center spot $x_{\mathrm{i,center}}$. Note that figure 6.24 reveals a sudden change of the center spot positions, especially in the x-direction of both, the magnetron and modified cyclotron phases, around 150 hours and 450 hours into the beam time. This is traced back to the loading of an outdated library file into MM6, a software that controls the time steps of the measurement pattern. This led to the ions spending an additional time in the measurement trap before applying the PI-ICR scheme. Although no physical reason for the change in the center spot position if found, off-line measurements were carried out after the beam time to ensure that this software problem does not affect the mass measurement at the targeted precision. The data is presented in figure 6.5. As one can see, no change in the frequency ratio is caused by the outdated library. In order to obtain the variance from equation (6.24) individual mean values are obtained for the different time periods in which the software issue was present or not. The variance is similar for both the x- and y-direction and for the magnetron and the modified cyclotron phase.

Thus a variance of $\sigma^2 = 0.3\,\mathrm{mm}$ is taken as the uncertainty for any center spot position measurement.

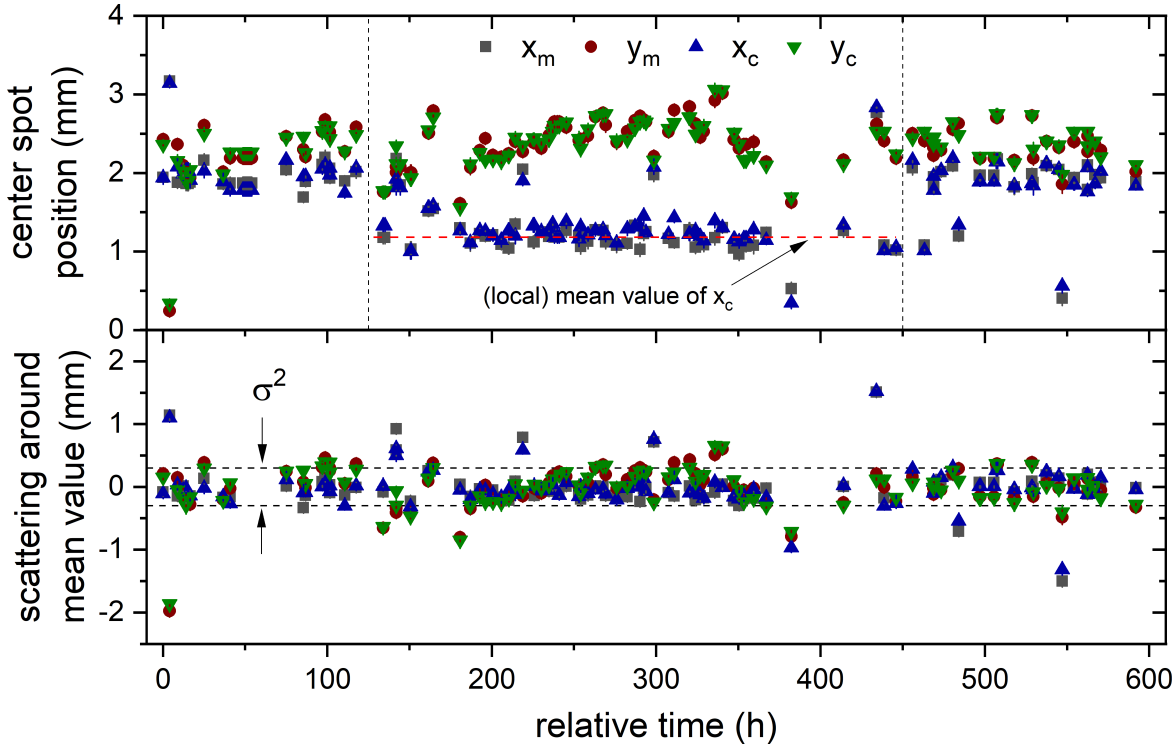


Figure 6.4: (Top figure) Measured magnetron and modified cyclotron center spot positions (x- and y-direction) of the reference ion $^{133}Cs^{+}$ during the beam time. The centers are obtained by a full PI-ICR measurement cycle at an accumulation time of 1200 ms with the excitation amplitudes set to 0 V. A sudden change appears around 150 h and recovers at 450 h. (Bottom figure) The center spot positions are shifted by their corresponding mean value to obtain a general variance of $\sigma^2 = 0.3\,\mathrm{mm}$. For further details see text.

### 6.5.2 Time-Dependent Non-Linear Magnetic Field Drifts

The linear interpolation of the reference ion's frequency to the point in time at which the ion of interest is measured (see section6.3) is only a first-order approximation to the temporal magnetic field evolution. To account for non-linear magnetic field drifts, the standard deviation

$$\sigma((B - B_{\mathrm{lin}})/B)(\Delta T) = \sigma((\nu - \nu_{\mathrm{lin}})/\nu)(\Delta T) = \sqrt{\frac{\sum_N (r_i - \bar{r})^2}{N-1}} \tag{6.25}$$

is evaluated for a set of N adjacent frequency measurements of $^{133}Cs^{+}$, equally spaced in time. This procedure has already been performed in, e.g., [94] and [115]. Here,

$$r_i \equiv \frac{\nu_i - \nu_{\mathrm{lin}}}{\nu_i} = \frac{\nu_i - \bar{t}_i \times (\nu_{i+1} - \nu_{i-1}) + \nu_{i-1}}{\nu_i} \tag{6.26}$$

where $\bar{t}_i$ defined as in equation (6.12). $\Delta T$ then corresponds to the time difference between the measurements of $i-1$ and $i+1$ and the error-weighted arithmetic mean value

$$\bar{r} = \frac{\sum_N \frac{r_i}{\delta r_i^2}}{\sum_N \frac{1}{\delta r_i^2}}. \tag{6.27}$$

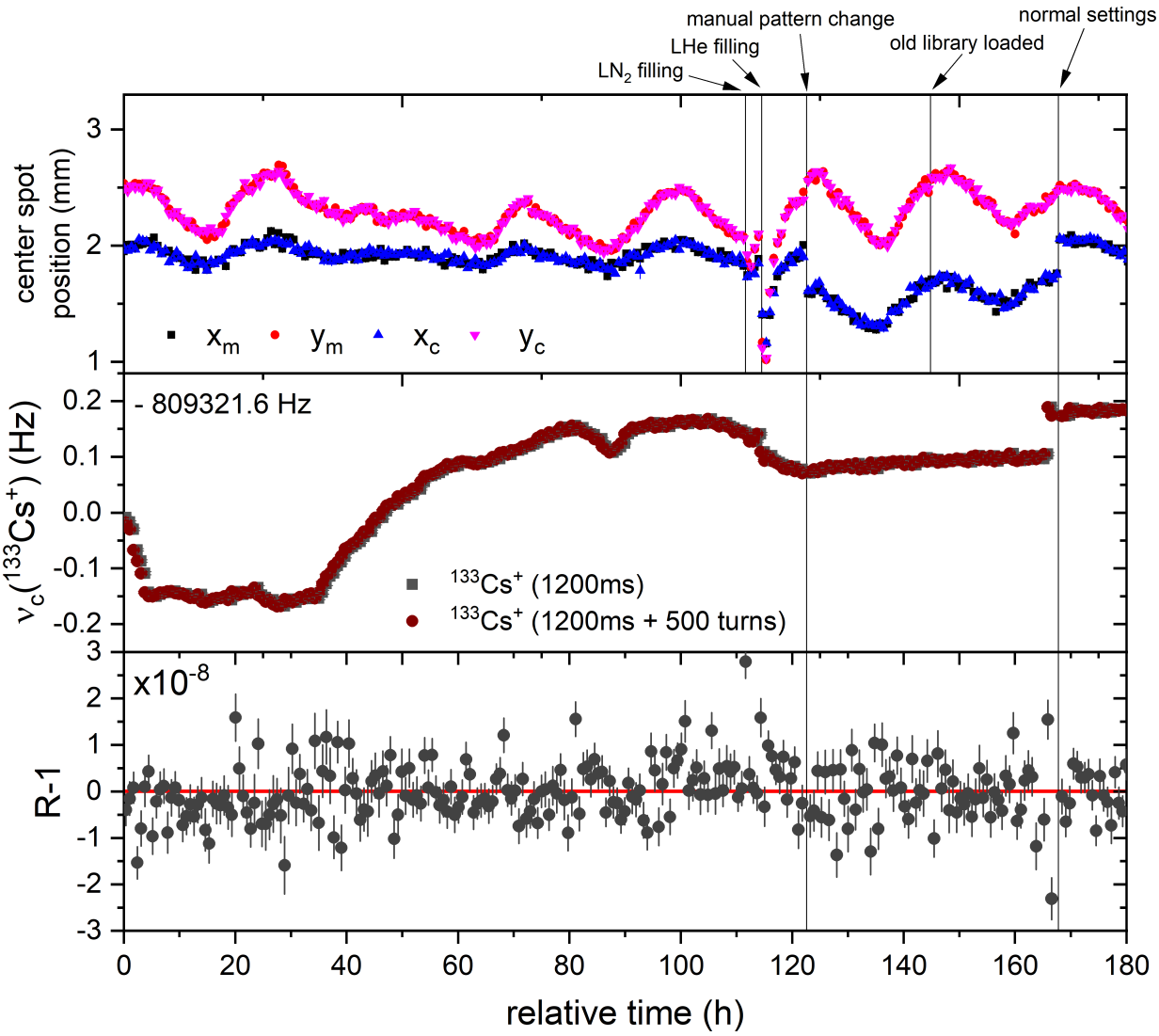


Figure 6.5: Evaluation of successive PI-ICR measurements on $^{133}Cs^+$ ions. The center spot position was measured for 30 min prior to the measurement of $^{133}Cs^+$ ions at 1200 ms accumulation time followed by another measurement of $^{133}Cs^+$ ions 1200 ms plus additional 500 cyclotron periods (both for 5 min). The magnet bore was stabilized to 10 mK at about 309 K. (Top figure) Temporal evolution of the center spot position. Note the sudden change during $LN_2$ and LHe filling. At about 120 h the PI-ICR pattern was manually changed to resemble the software problem during beam time and a sudden change in the x-positions is seen. Switching to the old settings but instead loading the corrupted library file for MM6 at about 140 h has no impact. Switching back to the original library file at 165 h restores the initial change. Note that the y-direction is less affected. (Middle figure) Evolution of the true cyclotron frequency $\nu_c$ for the $^{133}Cs^+$ ions. Note that the sudden change at about 160 h is uncorrelated to changes in the settings. The true cyclotron frequencies are unaffected by the change in settings. (Bottom figure) The frequency ratio between the successive $^{133}Cs^+$ measurements $(R-1) = 1.0(24) \times 10^{-10}$ agrees well with a frequency ratio of one. The changes in settings at 120 h, 140 h and 165 h do not affect the frequency ratio measurement.

is obtained by evaluating the individual uncertainties

$$\delta r_i = \sqrt{(\frac{\partial r_i}{\partial \nu_i}\delta\nu_i)^2 + (\frac{\partial r_i}{\partial \nu_m}\delta\nu_m)^2 + (\frac{\partial r_i}{\partial \nu_n}\delta\nu_n)^2}. \tag{6.28}$$

The resulting $\sigma((B - B_{\mathrm{lin}})/B)(\Delta T)$ plot (see fig. 6.6) is fitted to a linear function

$$\xi_B \equiv \Delta T \times \delta B. \tag{6.29}$$

The obtained slope $\delta_B = 1.3 \times 10^{-9}\,\mathrm{h}^{-1}$ accounts for a time-dependent systematic uncertainty that is added quadratically to the statistical uncertainty of each individually obtained frequency ratio as stated in equation (6.15). The intersection $\Delta B$ from the fit does not contribute to this systematic uncertainty. Generally speaking, the offset re-ensembles the uncertainty of the method neglecting the time drift, which is already covered by the other (systematic) uncertainties in the evaluation.

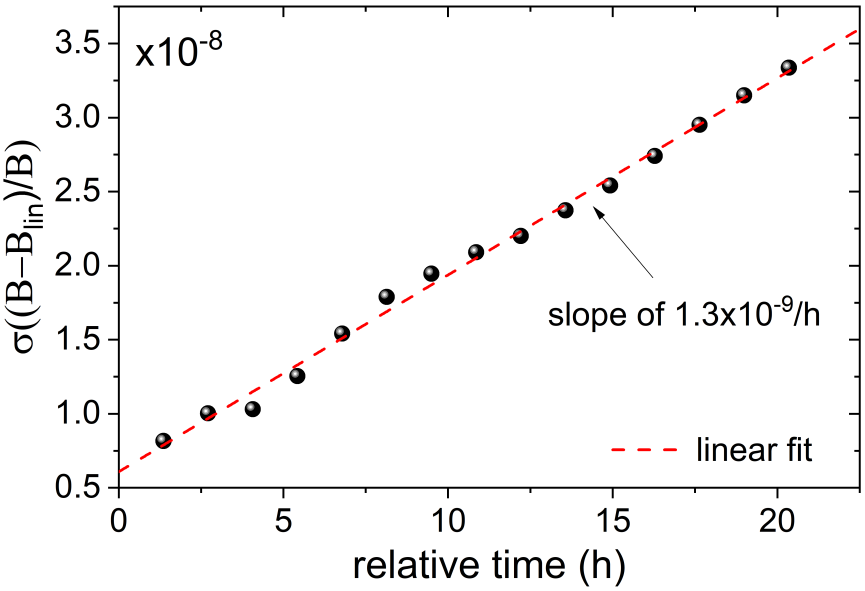


Figure 6.6: Evaluation of the time-dependent non-linear magnetic field systematics using $^{133}Cs^{+}$. For further details see text.

### 6.5.3 Mass-difference dependent Systematic

In high-precision PTMS, the absolute mass difference between the reference ion and the ion of interest leads to a systematic shift in the obtained frequency ratio [94]. This shift is attributed to imperfections of the electric quadrupole field of the Measurement trap or its misalignment with respect to the magnetic-field axis [93, 10]. Note that this systematic uncertainty originates from a difference in the true cyclotron frequency rather than the difference in absolute mass. Thus, the difference in the charge-to-mass ratio is important which is given in units of $u/e$ (atomic mass unit to elementary charge). The measured masses of $^{251,254}No^{2+}$, $^{254,256}Lr^{2+}$ and $^{257}Rf^{2+}$ (including potential isomeric states) differ by $4.5\,u/e$ to $7.5\,u/e$ compared to their reference ion $^{133}Cs^{+}$. To evaluate the systematic shift due to a difference in charge-to-mass ratio, frequency-ratio measurements of $^{119}Sn^{+}$ vs. $^{120}Sn^{+}$, $^{118}Sn^{+}$ vs. $^{124}Sn^{+}$, $^{211}Pb^{2+}$ vs. $^{133}Cs^{+}$ and $^{211}Pb^{2+}$ vs. $^{116}Sn^{+}$ were carried out. A comparison to the literature value results in figure 6.7. A linear fit reveals the absence of any systematic shift on a relative precision below $^{10^{-9}}$ which can be neglected for any of the mass measurements of the nobelium, lawrencium and rutherfordium ions which are measured with relative statistical uncertainties of $10^{-9}$ and higher. Thus, $\delta_M = 0$ in equation (6.19).

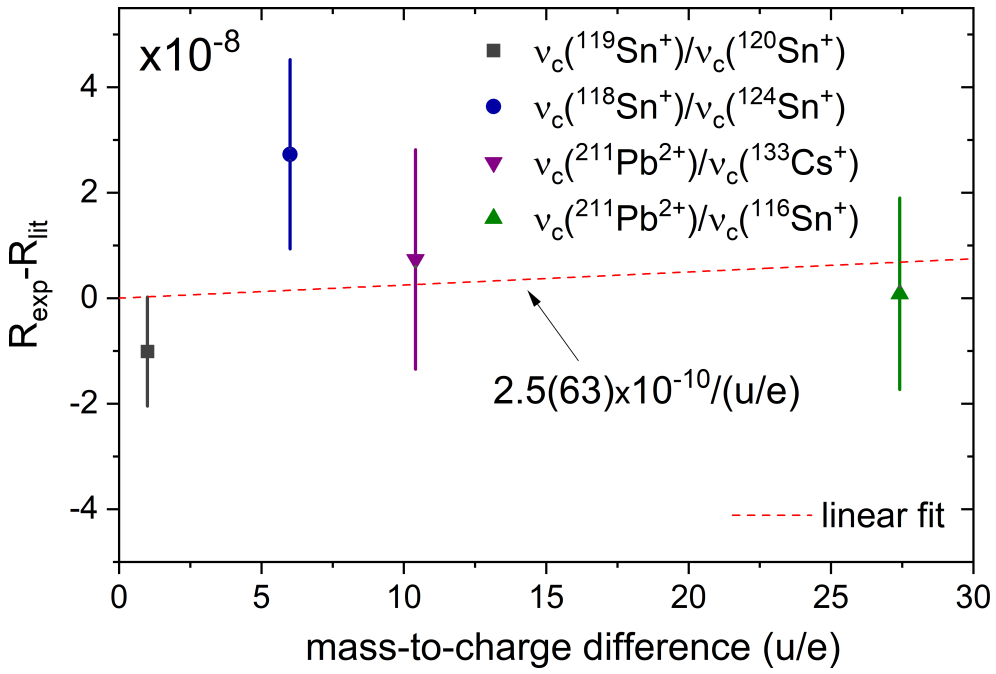


Figure 6.7: Evaluation of mass-difference dependent systematic shifts. The experimentally obtained frequency ratios are compared to literature value. A linear fit yields 0 which excludes the presence of a mass-difference dependent shift for measurements. Note the intercept of the linear fit being fixed to zero as by definition any mass-difference dependent shift vanishes for the absence of any mass difference.

## 6.6 Treatment of Special Cases

### 6.6.1 Single-Ion Files

Due to the low production rate some measurement files from ions of interest contain only single detected ion events. Obviously this single ion cannot be fitted to a Gaussian distribution which is considered for the data analysis as discussed in section 6.2 (see also figure 6.2a). The question arises how these events have to be treated accordingly. The phase spots have a certain standard deviation that resembles the mean scattering distance of the ions from the fitted center position. Thus, single ion events will be assigned an uncertainty that corresponds to the typical scattering distance. Therefore, available data with high statistics is evaluated to obtain the typical scattering distance. Figure 6.8 exemplary shows the standard deviation for the Gaussian fit of the x-position for the magnetron phase spots of $^{133}Cs^{+}$ ions obtained during beam time. As seen, the standard deviation is well described by a mean standard deviation of 1.0(1) mm. This evaluation is repeated for the modified cyclotron phase spot as well as for their y-positions. The same procedure was performed for available off-line data for $^{118-120,124}Sn^{+}$ isotopes and the off-line data for $^{133}Cs^{+}$ obtained directly after beam time. In addition, the on-line data of $^{254}No^{2+}$ is also evaluated. Note that systematically the Gaussian fits for the modified cyclotron phase spots have higher standard deviations. This is explained by a higher sensitivity of the modified cyclotron motion compared to the magnetron motion to e.g. electric and magnetic field fluctuations which results from a distinctly higher frequency. As presented in figure 6.8, the uncertainty of phase spots consisting of a single detected ion is conservatively evaluated as

$$\delta x \text{ and } \delta y \rightarrow 1.2\,\text{mm} \tag{6.30}$$

where $\delta x$ and $\delta y$ are defined in equations (6.4) and (6.5) for the corresponding magnetron and modified cyclotron phase spot, respectively.

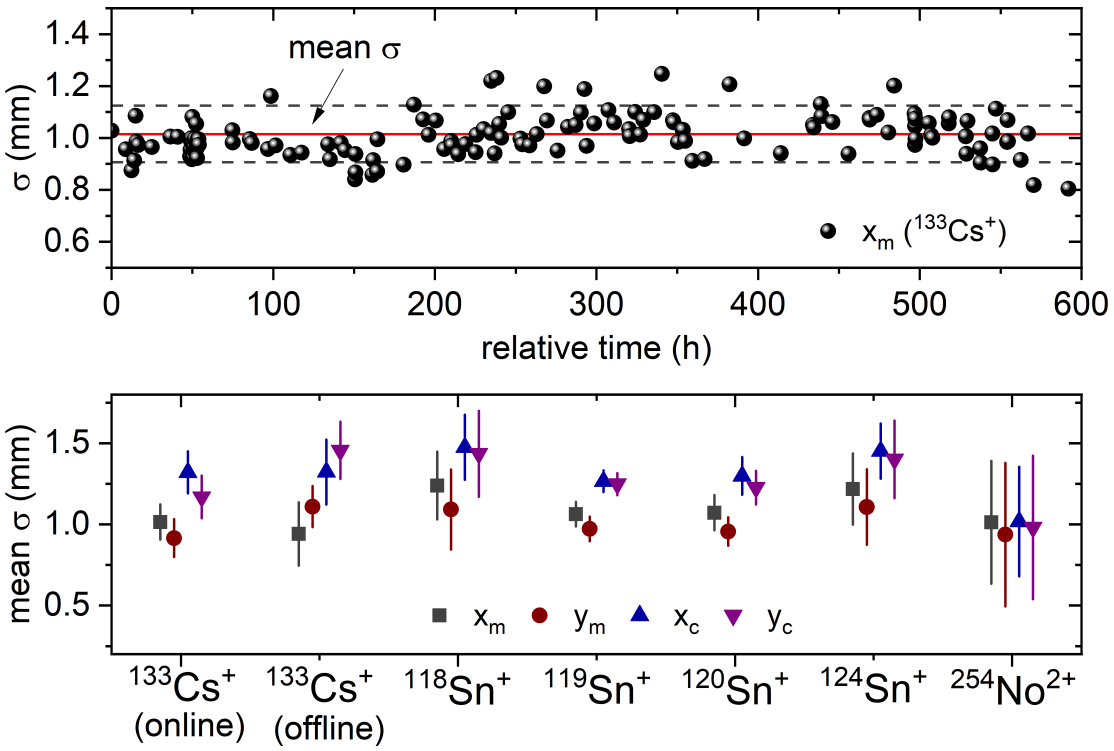


Figure 6.8: (Top figure) Standard deviation from the Gaussian fits for the x-position of the magnetron phase spots for all reference ion ($^{133}Cs^{+}$) measurements performed during beam time. The mean value throughout all measurements in this particular case is given by 1.0(1) mm and corresponds to the first data point in the figure below. (Bottom figure) Mean standard deviations for the Gaussian fits of the x- and y-positions for the magnetron (m) and modified cyclotron phases (c) for various different measurements. All measurements have been carried out with an accumulation time of 1200 ms. For lower accumulation times the standard deviation is assumed to be smaller. Thus, this data reflects an upper limit to the standard deviation present in any of the on-line measurements.

### 6.6.2 Single-Pattern Files

As discussed in 3.6 the *double-pattern* scheme of a PI-ICR measurement requires the final phases of the magnetron motion and modified cyclotron motion to be measured. Due to the low detection rate some measurement files do not contain ion events in both phases and thus do not allow for a cyclotron frequency determination. In this case the measurement file is combined with a the measurement file taken right before or right after provided that the corresponding measurement file contains ion events in the missing phase. Note that this is only feasible if the experimental conditions are identical for the involved measurement files, i.e. identical excitations and accumulation times. As explained in section 6.2, the relative uncertainty of any frequency ratio determination is dominated by the Gaussian fit of the modified cyclotron phase due to its distinctly higher frequency when compared to the magnetron motion. Therefore, for some low-rate measurements, the measurement of the magnetron phase was neglected after sufficient statistics was reached and the PI-ICR measurement pattern was changed into the *single-pattern* scheme in which only the final phase of the modified cyclotron spot was measured. Obviously, for these measurement files the magnetron phase spot does not contain any detected ion events and thus the procedure discussed above is followed.

### 6.6.3 Ambiguous Data Points and Fitting

The position-sensitive delay line detector is subject to noise that occasionally leads to false ion events. As these events are uncorrelated in time with respect to the well-defined time window in which the ions impact into the detector, they are suppressed in statistics by many orders of magnitudes. However, especially for the combination of long measurement times at low incoming ion rates, ambiguous data points may be present in measurement files. It is conceivable that these events are not caused by fake coincidences and reflect real ion events where the ions were subject to e.g. gas collisions and ion-ion interactions within the trap, respectively, although the latter being highly unlikely for sufficiently low incoming particle rates. Figure 6.9 shows the modified cyclotron phase image of a measurement file of $^{255}Lr^{2+}$ in which the isomeric state is resolved from its corresponding ground state. For detected events that differ significantly in phase or radius from a clustered phase spot it is obvious that this event can be rejected from the data analysis. However, three ambiguous data points are found lying in between the ground and isomeric state. For these a distinct assignment to either of those is not obvious. Thus, a quantitative measure if an ambiguous data point has to be considered to be part of a phase spot is inevitable for the data evaluation. Based

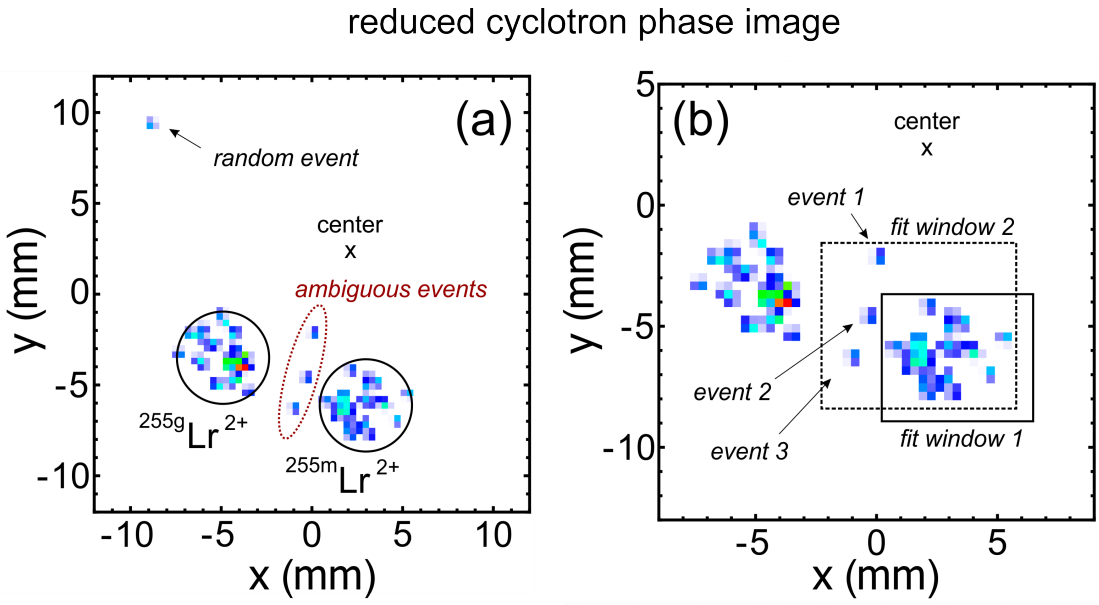


Figure 6.9: (a) Modified cyclotron phase image of a 10 hours measurement file from $^{255}Lr^{2+}$ at an accumulation time of 1200 ms in which the isomeric state is spatially separated from its respective ground state. Three ambiguous data points lie in between the ground and isomeric state. Note the *random event* that can be attributed as background due to its large difference in phase and radius with respect to the clustered phase spot(s). (b) Zoomed version of (a). The question arises which of the fit windows should be used to evaluate the data. As an example two different fit windows are presented, one which contains none of the ambiguous data points (*fit window 1*) and one that contains all of them (*fit window 2*). For further details see text.

on the discussions from section 6.6.1 it is most consistent to evaluate the probability of an ion event at position $(x, y)$ to be part of a measured phase spot represented by a Gaussian distribution with its standard deviation $\sigma$ mm at position $(\mu_x, \mu_y)$. In agreement with section 6.6.1 the standard deviation is assumed to be 1.2 mm for low rate cases in which the standard deviation is much smaller, in particular for the case of phase measurements with only one detected ion. For a given distance $r = \sqrt{(x-\mu_x)^2 + (y-\mu_y)^2}$ of the ion from the centroid of the phase spot

$$P(r, \sigma) = \left(1 - \mathrm{erf}(\frac{r}{\sqrt{2}\sigma})\right) \quad \text{with} \quad \mathrm{erf}(x) \equiv \frac{1}{\sqrt{\pi}} \int_{-x}^{x} e^{-t^2} dt \tag{6.31}$$

resembles to the probability that the ion is part of its Gaussian distribution. Here, $\mathrm{erf}(r, \sigma)$ corresponds to the so-called *error function* (see e.g. [145]). The probability as a function of the distance $r$ for different assumptions of $\sigma$ is shown in figure 6.10. Note that $\mathrm{erf}(\sigma, \sigma) \approx 68\,\%$, $\mathrm{erf}(2\sigma, \sigma) \approx 95\,\%$ and $\mathrm{erf}(3\sigma, \sigma) \approx 99.7\,\%$ as commonly used.

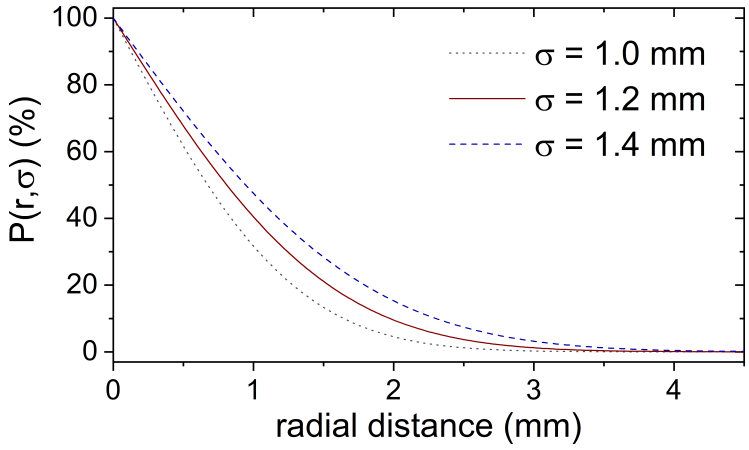


Figure 6.10: Probability that an ion is part of a Gaussian distribution as a function of the ions distance $r = \sqrt{(x-\mu_x)^2 + (y-\mu_y)^2}$ to its centroid position $(\mu_x, \mu_y)$ for three different standard deviations $\sigma$. For further details see text.

The evaluated probabilities for the ambiguous data points shown in figure 6.9 are summarized in table 6.1. Excluding the ambiguous data points the ground-state and isomer phase spots comprise 33 and 26 events in total, respectively. Due to this low statistics a confidence interval of $2\,\sigma$ (95 %) is sufficient to assign data points to their corresponding phase spot. Therefore, all the ambiguous data points are rejected from the data evaluation as their radial difference to the center of either of both phase spots is about $3\,\sigma$ or higher. As a side remark, the impact on the frequency determination is evaluated. If none of the ambiguous data points is taken into consideration a true cyclotron frequency of 843312.7004(73) Hz for the isomeric state of $^{255}Lr^{2+}$ is obtained which is in agreement with the value of 843312.7055(78) Hz in which all of the ambiguous data points were taken into consideration. The impact becomes even smaller when considering the mean frequency ratio obtained for all the available measurement files. The difference in the mean frequency ratio in this case corresponds to $0.11(72) \times 10^{-10}$. Here, only the statistical uncertainties are included. Thus, the overall impact in any case can be neglected. However, whether or not ambiguous data points have to be considered becomes more and more important the lower the overall statistics in the measurements are. In addition, their impact is enhanced for measurements with low accumulation times in which small differences in the fitted phase spots contribute to a higher absolute shift in the determined true cyclotron frequency.

| | ground-state assignment | | | isomer assignment | | |
|---|---|---|---|---|---|---|
| ambiguous data point | $r$ (mm) | $r/\sigma$ | $P(r,\sigma)$ | $r$ (mm) | $r/\sigma$ | $P(r,\sigma)$ |
| *event 1* | 4.5(2) | 3.7(2) | 0.02 % | 5.0(2) | 4.2(2) | 0.003 % |
| *event 2* | 4.0(2) | 3.4(2) | 0.08 % | 3.5(2) | 2.9(2) | 0.33 % |
| *event 3* | 4.3(2) | 3.6(2) | 0.04 % | 3.8(2) | 3.2(2) | 0.15 % |

Table 6.1: Probabilities $P(r, \sigma)$ as defined by equation (6.31) for the three ambiguous data points seen in figure 6.9. The uncertainty in distances originate from the uncertainty in the fitted phase spot positions. The difference is also given in units of the standard deviation $\sigma = 1.2\,\mathrm{mm}$. For further details see text.

# Chapter 7

# Results

## 7.1 Overview

In the beam time period in summer 2018 (see figure 5.1) several nobelium, lawrencium and rutherfordium isotopes have been addressed at SHIPTRAP by means of direct high-precision PTMS. The atomic ground-state masses of the nobelium isotopes $^{251,254}$No and the lawrencium isotopes $^{254-256}$Lr have been measured with relative uncertainties down to $\delta m/m = 10^{-9}$, corresponding to absolute mass uncertainties in the order of keV/c$^2$. These nuclides are of particular interest as they are in the vicinity of the deformed neutron shell closure $N = 152$ and can be accessed with relatively large cross sections via fusion-evaporation reactions. In the cases of $^{251}$No and $^{254}$Lr the atomic masses are determined directly for the first time. So far, their masses have only been extrapolated from $\alpha$-decay spectroscopy [39] and this work improved their uncertainty by about two orders of magnitude. In the cases of $^{254}$No and $^{255,256}$Lr the mass uncertainties were reduced by one order of magnitude compared to literature including previously measured values from SHIPTRAP using ToF-ICR [67, 68, 69]. In addition, the atomic ground-state mass of $^{257}$Rf has been measured using PI-ICR representing the first direct high-precision mass spectrometry of a superheavy element. The fusion-evaporation reactions used to produce the isotopes of interest are presented in table 3.1. In these reactions certain isomeric states are populated with half-lives long enough to be measured directly using PTMS. In this work the excitation energies of the isomeric states $^{251m,254m}$No and $^{254m,255m}$Lr were determined directly for the first time. In sections 7.2 and 7.3 the results for the atomic ground-state masses and the excitation energies of the isomeric states are presented and discussed, respectively.

## 7.2 Atomic Masses of Nobelium, Lawrencium and Rutherfordium Isotopes

### 7.2.1 Atomic Mass Determination

Within the scope of this work the cyclotron frequencies of all ions of interest have been measured for doubly-charged states relative to the cyclotron frequency of $^{133}$Cs$^+$ being the reference ion. Accordingly to equation (3.29) the obtained true cyclotron frequency ratio $R = \nu_{\mathrm{ref}}/\nu$ gives access to the absolute mass of the ion of interest

$$m_{\mathrm{exp}}(^A\mathrm{X}) = 2R(m_{\mathrm{lit}}(^{133}\mathrm{Cs}) - m_{\mathrm{e}}) + 2m_{\mathrm{e}}, \tag{7.1}$$

where $m_{\mathrm{lit}}(^{133}\mathrm{Cs}) = 132.905451961(9)\,\mathrm{u}$ [39] and $m_{\mathrm{e}} = 510.9989461(13)\,\mathrm{keV/c^2}$ [146] correspond to the literature mass of the reference ion and the electron rest mass, respectively. The nuclide is represented by its atomic mass number $A$ and element symbol X. The atomic masses are often expressed in units of the

$$\text{atomic mass unit } u = 931\,494.0954(57)\,\mathrm{keV/c^2} \tag{7.2}$$

which makes use of Einstein's mass-energy equivalence principle [5]. In some cases it is more convenient to express the atomic mass as a *mass excess*

$$ME(^{A}\mathrm{X}) = (m_{\mathrm{exp}}(^{A}\mathrm{X}) - A \times \mathrm{u}). \tag{7.3}$$

In the latter the $Q_{\mathrm{lit}}(\alpha)$ value of an $\alpha$ decay from the ion of interest is typically given. The $Q(\alpha)$ value is defined as the binding energy difference between the $\alpha$-decaying mother and its daughter nucleus. Therefore, the atomic mass of an $\alpha$-emitting nuclide

$$m_{\mathrm{lit}}(^{A}\mathrm{X}) = m_{\mathrm{lit}}(^{A-4}\mathrm{Y}) + m_{\mathrm{lit}}(^{4}\mathrm{He}) + Q_{\mathrm{lit}}(\alpha)/c^2, \tag{7.4}$$

depends upon the atomic mass of the daughter isotope $m_{\mathrm{lit}}(^{A-4}\mathrm{Y})$, the atomic mass of the emitted $\alpha$ particle $m_{\mathrm{lit}}(^{4}\mathrm{He}) = 4.00260325413(6)\,\mathrm{u}$ [39] and the corresponding $Q(\alpha)$ value. Thus, $\alpha$-decay spectroscopy allows measuring atomic masses by means of $Q(\alpha)$ measurements. In general, the absolute mass uncertainty is limited by the uncertainty of the daughter isotope.

In odd-even/even-odd nuclei, $\alpha$ decays often populate excited states in their daughter nucleus which themselves successively decay further into the ground state and granddaughters, respectively. In this case, the $Q(\alpha)$ energy from equation (7.4) is reduced by the excitation energy of the corresponding populated state. However, decay and level schemes are usually needed to derive excitation energies. As they can get complicated an unambiguous determination is often exacerbated, which limits the reliability on derived atomic masses. A challenge that direct mass spectrometry bypasses as it directly measures masses without the necessity of any decay and level schemes.

### 7.2.2 Atomic Mass of $^{251}$No

The first production and identification of the isotope $^{251}$No took place in 1967 and a $Q(\alpha)$ value of 8740(20) keV was obtained [85]. In following experiments [85, 147, 88, 148, 149, 66] the uncertainty of the $Q(\alpha)$ value was reduced down to 4 keV [66], which is the current uncertainty given by the atomic mass evaluation [39]. Even though the $Q(\alpha)$ value is known to a precision of few keV the atomic mass uncertainty of $^{251}$No is two orders of magnitude higher. This is due to the uncertainty of the atomic mass 71670(120) keV [39] of its daughter isotope $^{247}$Fm. This situation did not change over the last 50 years. Currently, the atomic mass of $^{251}$No is evaluated to be 82850(110) keV [39]. In this work, the first direct high-precision PTMS of $^{251}\mathrm{No}^{2+}$ was performed by means of the PI-ICR technique.

Figure 7.1 shows the obtained frequency ratios for $^{251}\mathrm{No}^{2+}$ with respect to the reference ion $^{133}\mathrm{Cs}^{+}$ using PI-ICR. In all cases an accumulation time of ≈500 ms was used. In this work a mean frequency ratio of $R = 0.944614684(9)$ with a relative uncertainty of $\delta R/R = 9.5 \times 10^{-9}$ is obtained. This corresponds to a mass excess of $ME = 82850.6(22)$ keV using equation (7.1) and is in good agreement with the most recent value of 82850(110) keV [39]. This work improves the uncertainty of the literature value by a factor of ≈ 50 from 110 keV down to 2.2 keV.

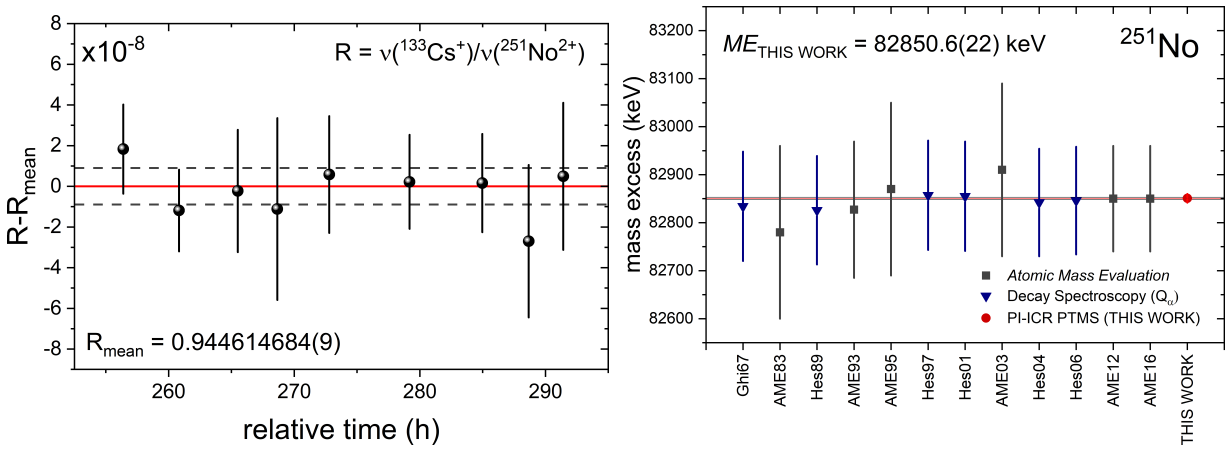


Figure 7.1: (Left figure) Obtained frequency ratios for $^{251}No^{2+}$ with respect to the reference ion $^{133}Cs^{+}$ as a function of the relative time after the start of the beam time. All frequency ratios have been obtained using PI-ICR. (Right figure) Measured mass excesses $ME$ of $^{251}$No from different experiments in historical order (increasing time from left to right). The $Q_\alpha$-values are obtained from decay spectroscopy [85, 147, 88, 148, 149, 66] and evaluated using equation (7.4). For this the atomic mass from the most recent atomic mass evaluation [39] of the daughter isotope $^{247}$Fm is used. This work's value corresponds to the first direct determination of the mass excess. In addition, the atomic mass evaluation [150, 151, 152, 43, 153, 39] is shown. For further details see text.

### 7.2.3 Atomic Mass of $^{254}$No

The first description of $^{254}$No was reported by G. N. Flerov *et al.* in 1958 [154]. About 10 years later its half-life of about 50 s and other decay properties were successfully determined for the first time [155]. Its direct production via the fusion-evaporation reaction $^{208}$Pb($^{48}$Ca,2n) features a relatively high cross section of $\approx 2\,\mu$b compared to other transfermium isotopes. At typical primary beam intensities of 1 p$\mu$A production rates of few ions per second are obtained. Thus, this isotope is often used as a test case and access point for new approaches and experimental techniques in the region of the heaviest elements, e.g. by mass spectrometry at SHIPTRAP in 2010 [67] or by laser spectroscopy at SHIP in 2016 [83].

The binding energy of $^{254}$No is of particular interest as its neutron number $N = 152$ corresponds to the position of a deformed shell closure. Therefore, in previous experiments at SHIPTRAP, its mass has been measured directly with high precision using ToF-ICR [67, 68, 69]. This[1] allowed for the first direct confirmation of the deformed neutron shell closure at $N = 152$ [69]. In this work the atomic mass of $^{254}$No is determined using PI-ICR. In figure 7.2, the result is compared to literature. In addition, the historic evolution of its atomic mass evaluation is shown.

Using PI-ICR a cyclotron frequency ratio of $R = 0.955908551(5)$ is obtained for $^{254}No^{2+}$ with respect to the reference ion $^{133}Cs^{+}$. The relative uncertainty corresponds to $\delta R/R = 4.8 \times 10^{-9}$. The frequency ratio is in agreement with the frequency ratios $R = 0.955908520(60)$ [67, 68] and $R = 0.95590855(40)$ [69] obtained at SHIPTRAP using ToF-ICR. In these measurements the same reference ion $^{133}Cs^{+}$ has been used. In this work using PI-ICR, the obtained relative uncertainties are improved by about one order of magnitude compared to the previous measurements at SHIPTRAP using ToF-ICR. This work's resulting mass excess corresponds to $ME = 84732.8(11)$ keV which is in agreement with the most recent atomic mass evaluation value of 84723(10) keV [39].[2] The improvement compared to the literature value is about one order of magnitude. Recently, in 2018, multireflection time-of-flight mass spectrometry (MR-ToF) suc-

[1] ... in combination with the atomic masses of $^{252}$No and $^{256}$No...
[2] Which is of no surprise as it is dominated by the ToF-ICR measurement at SHIPTRAP.

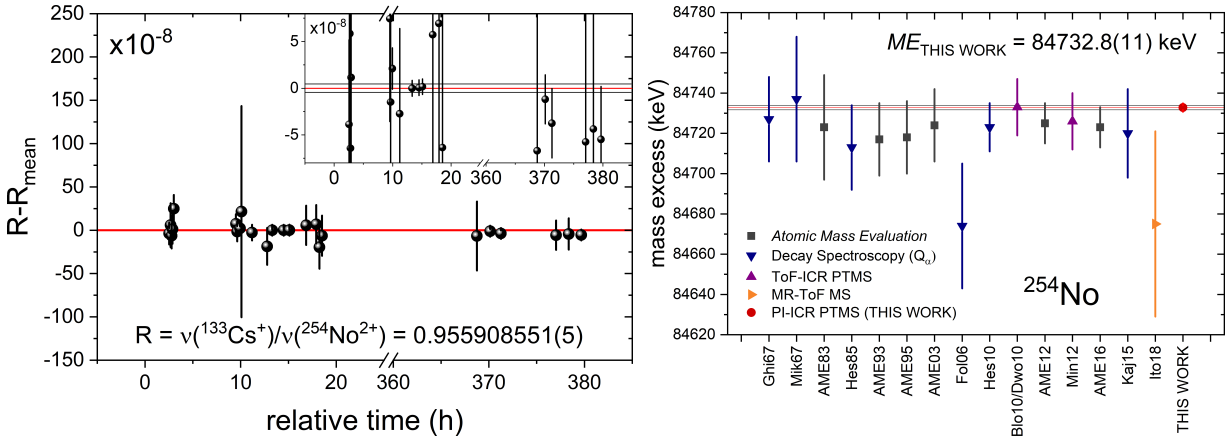


Figure 7.2: (Left figure) Obtained frequency ratios for $^{254}No^{2+}$ with respect to the reference ion $^{133}Cs^{+}$ as a function of the relative time after the start of the beam time. The inlet shows a zoomed-in version to the data. All frequency ratios have been obtained using PI-ICR. (Right figure) Measured mass excesses $ME$ of $^{254}$No from different experiments in historical order (increasing time from left to right). The $Q_\alpha$-values are obtained from decay spectroscopy [85, 156, 157, 158, 104, 159] and evaluated using equation (7.4). In this case the atomic mass from the most recent atomic mass evaluation [39] of the daughter isotope $^{250}$Fm is used. The ToF-ICR measurements were performed at SHIPTRAP [67, 68, 69]. The MR-ToF data is taken from [84]. In addition, the atomic mass evaluation [150, 151, 152, 43, 153, 39] is shown. For further details see text.

cessfully measured the atomic mass of a transfermium element for the first time [84]. The obtained mass excess value for $^{254}$No of $84675(42)_{\text{stat}}(19)_{\text{sys}}$ keV [84] (combined uncertainty of 46 keV) is also presented in figure 7.2 and shows a small discrepancy from this work's value approximately $1.3\,\sigma$. The origin of this deviation is unclear, as no MR-ToF spectra is shown in the corresponding publication and no detailed information concerning the systematic uncertainties is given.

Note that the frequency ratios presented in figure 7.2 differ in uncertainties with respect to each other and that the mean frequency ratio is mainly given by three measurements which are visible in the inserted figure. The different uncertainties originate from different accumulation times. As the isomeric state in $^{254}$No has a relatively short half-life of ≈250 ms [64] the accumulation time has been lowered down to 50 ms. The relatively high excitation energy of $> 1$ MeV requires a lower mass resolving power compared to typically cases where accumulation times of ≈1 s were used. The three frequency ratios presented in the insert, approximately 15 hours after the starting point of the beam time, were measured at an accumulation time of 1.2 s. For the determination of the final frequency ratio all available data is taken into account.

### 7.2.4 Atomic Mass of $^{254}$Lr

The first experiments involving the isotope $^{254}$Lr carried out at SHIP were published in 1985 [157]. Since then its atomic mass has not been improved considerably even though several decay spectroscopy experiments followed [160, 158, 86]. The obtained $Q(\alpha)$ values have uncertainties in the order of ≈20 keV. However, the atomic mass value of $^{254}$Lr has been limited by the imprecise knowledge of its daughter isotope $^{250}$Md with an atomic mass uncertainty of about 300 keV/c$^2$ [39]. Recently, the atomic mass of $^{250}$Md has been measured directly for the first time using MR-ToF mass spectrometry with an mass uncertainty of 140 keV [84].

In this work the atomic mass of $^{254}$Lr was measured directly for the first time using PI-ICR. Accumulation

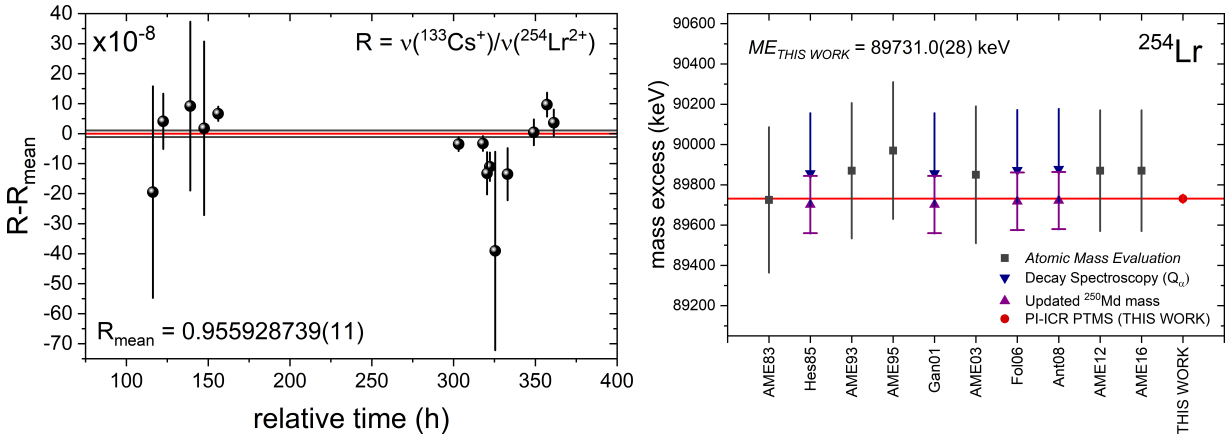


Figure 7.3: (Left figure) Obtained frequency ratios for $^{254}Lr^{2+}$ with respect to the reference ion $^{133}Cs^{+}$ as a function of the relative time after the start of the beam time. All frequency ratios have been obtained using PI-ICR. (Right figure) Measured mass excesses $ME$ of $^{254}$Lr from different experiments in historical order (increasing time from left to right). The $Q(\alpha)$ values are obtained from decay spectroscopy [157, 160, 158, 86] and evaluated using equation (7.4). For this the atomic mass from the most recent atomic mass evaluation [39] of the daughter isotope $^{250}$Md is used. In addition the evaluated values including the recently directly measured atomic mass of $^{250}$Md [84] is shown. This work corresponds to the first direct mass spectrometry of $^{254}$Lr. In addition, the atomic mass evaluation [150, 151, 152, 43, 153, 39] is shown. For further details see text.

times from 50 ms to 600 ms were used. The obtained frequency ratios of $^{254}Lr^{2+}$ with respect to the reference ion $^{133}Cs^{+}$ are presented in figure 7.3. A mean frequency ratio of $R = 0.955928739(11)$ with a relative uncertainty of $1.2 \times 10^{-8}$ is obtained. The corresponding mass excess of $ME = 89731.0(28)$ keV (using equation (7.1) and (7.3)) is in agreement with the most recent estimation of the atomic mass evaluation of 89870(300) keV [39] and corresponds to an improvement of more than two order of magnitude down to 2.8 keV.

### 7.2.5 Atomic Mass of $^{255}$Lr

The isotope $^{255}$Lr was first identified in 1971 by Eskola *et al.* [161]. Its $Q(\alpha)$ value has been measured in a couple of decay spectroscopy experiments [160, 87, 162]. In previous experiments at SHIPTRAP its atomic mass has been determined for the first time directly by means of ToF-ICR and a mass excess of $ME = 89958(16)$ keV was obtained [69].

The obtained frequency ratio of $^{255}Lr^{2+}$ with respect to the reference ion $^{133}Cs^{+}$ is $R_{\mathrm{ToF}} = 0.959691740(60)$ with a relative uncertainty of $6 \times 10^{-8}$. In this work the frequency ratio of $^{255}Lr^{2+}$ with respect to the same reference ion was measured by means of PI-ICR. A value of $R_{\mathrm{mean}} = 0.959691646(7)$ is obtained. The relative uncertainty of $7.3 \times 10^{-9}$ corresponds to an improvement of about one order of magnitude with respect to the previous ToF-ICR measurement. The frequency ratios are presented in figure 7.7. In addition, the obtained mass excess of $ME = 89934.0(17)$ keV is compared to literature values and the atomic mass evaluation.

Note that this work's frequency ratio as well as the mass excess disagrees with the previously measured ToF-ICR values of SHIPTRAP. This can be explained by the presence of the low-lying isomeric state $^{255m}$Lr with an excitation energy of $\approx 30$ keV. A more detailed description on the first direct measurement of the excitation energy of this isomer is presented in section 7.3.4. The frequency ratio of the isomeric state $^{255m}Lr^{2+}$ with respect to $^{133}Cs^{+}$ is $R' = 0.959691778(7)$. Figure 7.5 compares these frequency ratios. As seen, the frequency ratio obtained by means of ToF-ICR lies in between the frequency ratio of the

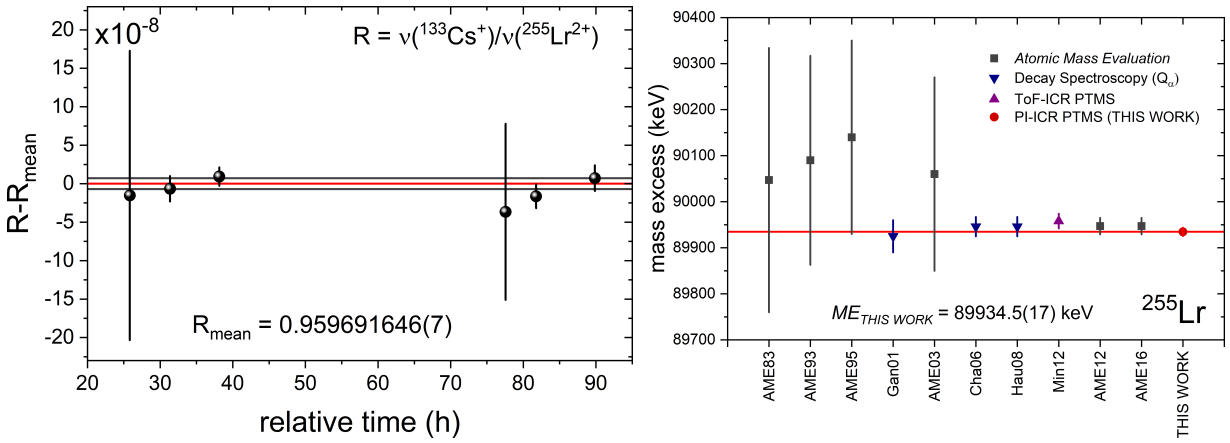


Figure 7.4: (Left figure) Obtained frequency ratios for $^{255}Lr^{2+}$ with respect to the reference ion $^{133}Cs^{+}$ as a function of the relative time after the start of the beam time. All frequency ratios have been obtained using PI-ICR. (Right figure) Measured mass excesses $ME$ of $^{255}$Lr from different experiments in historical order (increasing time from left to right). The $Q_\alpha$-values are obtained from decay spectroscopy [160, 87, 162] and evaluated using equation (7.4). For this the atomic mass from the most recent atomic mass evaluation [39] of the daughter isotope $^{251}$Md is used. The ToF-ICR measurements were performed at SHIPTRAP [69]. In addition, the atomic mass evaluation [150, 151, 152, 43, 153, 39] is shown. For further details see text.

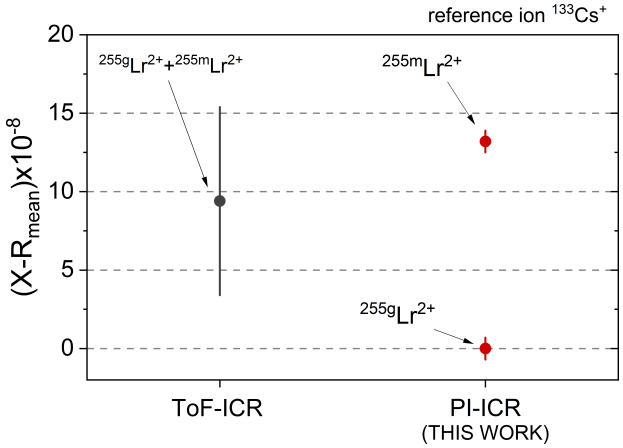


Figure 7.5: Comparison between the obtained mean frequency ratio from Minaya *et al.* [69] with respect to this work. The difference to this work's mean frequency ratio for $^{255g}Lr^{2+}$ is shown. In all cases $^{133}Cs^{+}$ has been used as reference. For further details see text.

ground and isomeric state of this work. It is thus plausible to assume a contribution of the isomeric state in the measurements of Minaya *et al.*. Using the fusion-evaporation reaction $^{209}$Bi($^{48}$Ca,2n) at a primary beam energy of 4.56 MeV/u both, the ground and isomeric state are populated, respectively. The mass difference between the ground and isomeric state corresponds to a frequency difference of $\approx$100 mHz for doubly-charged ions. The mass-resolving power of ToF-ICR, even with excitation times of up to 4 s as used by Minaya *et al.* [69, 163], did not allow disentangling the resonance curves for the ground and isomeric states and thus a contribution of the isomeric state has to be assumed. Whereas the ground state has a half-life of $\approx$31 s, the isomeric state has a half-life of $\approx$2.5 s [87]. The latter is comparable to typical measurement times in both, ToF-ICR and PI-ICR, respectively. Thus, in the work of Minaya *et al.*, several resonances were taken using excitation times from 200 ms to 4 s to evaluate the contribution of the isomeric state [163]. Assuming that the isomeric state is produced in 1/3 of the cases, a contribution of less than 5 % to the overall resonance of the ground state at an excitation time of 4 s has been assumed [163]. Therefore, a contribution of the isomeric state to the atomic mass of $^{255}$Lr published in [69] has been

neglected. However, this work indicates that the production of the isomeric state has been underestimated. At an accumulation time of 1.2 s using PI-ICR the detected ion rate of the ground and isomeric state is about equal. Taking into account the ion preparation, this contributes to an overall measurement time of about 1.5 s. Even at a measurement time of ≈ 4 s the isomeric state will contribute with an intensity of ≈ 30 % to a ToF-ICR[3] resonance.[4] Assuming that the measured frequency ratios from this work and in [69] are correct. Then a contribution of

$$1 - \frac{R_{\mathrm{ToF}} - R'}{R - R'} = 71^{+29}_{-45}\,\% \tag{7.5}$$

from the frequency ratio of the isomeric state of this work $R'$ to the ratio of [69] ($R_{\mathrm{ToF}}$) is obtained ($R$ is the frequency ratio of the ground state). This calculation is valid as the same reference ion has been used. The uncertainty of this calculation is relatively large due to the relative large uncertainty of $R_{\mathrm{ToF}}$ with respect to the absolute difference between $R$ and $R'$. However, it supports the assumption that the contribution of the isomeric state to the ToF-ICR resonance in [69] of $< 5\,\%$ [163] was underestimated. Indeed the contribution agrees with this work's estimation of ≈ 30 % at measurement cycle times of ≈ 4 s as performed by Minaya *et al.*

### 7.2.6 The Performance of ToF-ICR vs. PI-ICR in the Context of $^{255}$Lr

The isotope $^{255}$Lr (the measurement is presented in the previous section 7.2.5) with its low-lying isomer $^{255m}$Lr (presented in section 7.3.4) is a suitable case to compare the performance of PI-ICR and ToF-ICR at SHIPTRAP with respect to the heaviest elements. Up to now, high-precision PTMS of transfermium elements at SHIPTRAP were solely performed applying ToF-ICR. This work proves the feasibility of PI-ICR measurements even for the heaviest elements, facing lowest detection rates, particle integrals and low charge states in combination with large atomic masses[5]. To quantify the performance with respect to ToF-ICR, two measurement files are compared in the following. In this work, the first direct measurement of the excitation energy of the isomeric state $^{255m}$Lr$^{2+}$ is presented (see section 7.3.4). To resolve it from its respective ground state $^{255}$Lr$^{2+}$ (presented in section 7.2.5) a mass resolving power of about 10 million is required which is difficult to achieve using ToF-ICR. About 10 years ago $^{255}$Lr$^{2+}$ was measured directly for the first time by Minaya *et al.* [69]. Figure 7.6 shows one of the obtained measurement ToF-ICR files from 2010 compared to a PI-ICR measurement file from this work. A direct comparison is feasible as excitation time and accumulation time are both on the order of one second. The ToF-ICR technique is based on the measurement of the change of time-of-flight $t_{\mathrm{ToF}}$ of an ejected ion to a detector. The ejection directly follows a conversion pulse in which the slow magnetron mode is converted into the fast modified cyclotron mode. In case the excitation frequency matches the true cyclotron frequency of the ion $\nu_{\mathrm{rf}} = \nu_{\mathrm{c}}$, a full conversion takes place and the time of flight minimizes, as the ions corresponding magnetic moment that results in an acceleration of the ion throughout the magnetic field gradient maximizes. The evaluation of the centroid frequency is given by a fit of the analytically well-known function [164]

$$t_{\mathrm{ToF}}(\nu_{\mathrm{rf}}) = \int_{z_0}^{z_1} \left( \frac{m}{2[E_0 - qV(z) - \mu(\nu_{\mathrm{rf}})B(z)]} \right)^{\frac{1}{2}} dz \tag{7.6}$$

with $E_0$ being the total initial energy of the ion at the axial trap position $z_0$. $V(z)$ and $B(z)$ are the electric and magnetic field along the axial path to the detector at position $z_1$. The ToF-ICR technique

[3] This is of no interest for PI-ICR as the mass-resolving power is high enough to fully resolve both states.

[4] In [69] $^{255}$Lr has been produced using the same fusion-evaporation reaction and the same primary beam energy.

[5] The resulting m/q values are relatively large compared to other Penning-trap experiments. Even though the true cyclotron frequencies can be determined with ≈ 10 mHz uncertainty in the region of the heaviest elements, the achievable relative precision suffers from relatively low true cyclotron frequencies of $< 1$ MHz at a magnetic field strength of 7 T.

is Fourier limited by the excitation time $t_{exc}$ and a mass resolving power of $\approx \nu_c t_{exc}$ can be achieved. A doubly-charged ion with mass number $A = 255$ in the 7 T magnetic field of SHIPTRAP has a true cyclotron frequency of about 840 kHz. Thus, the achievable mass resolving power and frequency resolution for a ToF-ICR measurement with an excitation time $t_{acc} = 1$ s is less than 1 million and 1 Hz, respectively. This is by far insufficient to resolve the isomeric state of $^{255}Lr^{2+}$ from its respective ground state as seen in figure 7.6a.

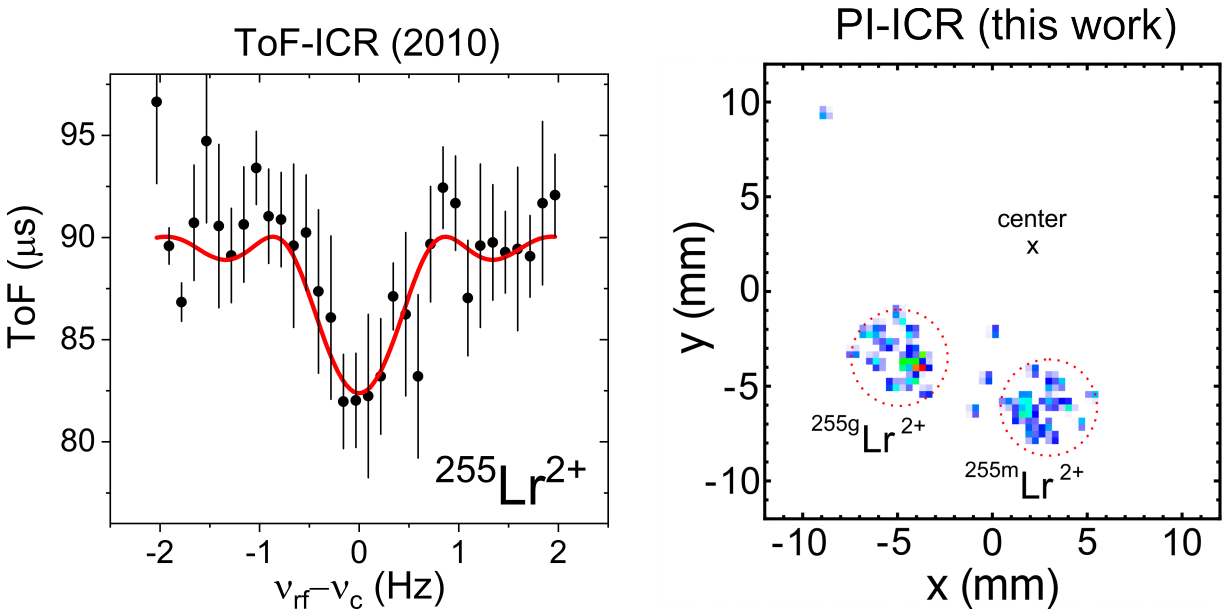


(a) (b)

Figure 7.6: Comparison between a single ToF-ICR resonance from Minaya *et al.* [69] from a beam time in 2010 (a) versus a PI-ICR phase image from this work (b) for $^{255}Lr^{2+}$. In the case of the ToF-ICR resonance 65 ions were detected in 14.5 h (4.5 ions/h). A resonance frequency of 843324.613(85) Hz is obtained with a FWHM of 870 mHz for an excitation time of $t_{exc} = 1$ s. For PI-ICR only the phase spot of the modified cyclotron motion is presented. In total (including the magnetron phase spot) 145 ion events were detected in a measurement time of 10 h (14.5 ions/h) at half the production rate compared to the ToF-ICR file. A spatial separation of the isomeric state $^{255m}Lr^{2+}$ from its respective ground state $^{255g}Lr^{2+}$ is achieved at an accumulation time of $t_{acc} = 1.2$ s. The modified cyclotron phase spots of the ground and isomeric state consist of 34 and 28 detected events, respectively. The true cyclotron frequencies for the ground and isomeric states are 843312.824(7) Hz and 843312.700(7) Hz, respectively. The absolute uncertainties for the determination of the center positions are about 0.15 mm in both cases. Note the absolute change in frequency compared to the ToF-ICR measurement due to a decrease in the absolute magnetic field strength of the SHIPTRAP magnet. Corresponding mass resolving powers for both measurements are ≈970 000 (ToF-ICR) and ≈11 000 000 (PI-ICR). For further details see text.

The difference in the true cyclotron frequency of $^{255m}Lr^{2+}$ and $^{255g}Lr^{2+}$ due to its low excitation energy of about 30 keV is about 100 mHz which requires a mass resolving power of ≈8 million. The mass resolving power of the ToF-ICR technique is not sufficient for the given experimental conditions. PI-ICR on the other hand achieves much higher mass resolving powers of ≈ 10 million for similar experimental conditions to clearly separates both ion species. A spatial resolution of different ion species gets even more important the bigger the difference in statistics between both species is. It is impossible to resolve and measure few isomeric state events with respect to a much more abundant ground-state signal (or the other way around) in the case of ToF-ICR resonances close to each other. In addition, ToF-ICR requires to scan the excitation frequency. The further a measurement is away from the resonance frequency, the less it contributes to the statistical precision of the obtained centroid. In contrast, in PI-ICR every ion carries almost equal phase information and thus also single ion events can be used for mass measurements. This becomes more and more inevitable in the region of the heaviest elements, where production rates and particle integrals

drastically decrease with increasing proton numbers.

In the case of ToF-ICR, an empirical formula for the statistical relative uncertainty of $\delta\nu_c/\nu_c \approx (\nu_c\sqrt{N}T_{\mathrm{exc}})^{-1}$ is found empirically [165], where $N$ corresponds to the total number of detected ions. In the case of figure 7.6a a statistical relative uncertainty of $\approx 1\times10^{-7}$ is achieved by fitting the well-known analytical function of equation (7.6) to the data. PI-ICR, being sensitive to ion phases, achieves a relative statistical uncertainty of about $4.5\times10^{-9}$. The improvement in precision of a factor of 15 is partly due to the increased statistics and is not solely based on using the PI-ICR technique. In this work, overall efficiencies are about a factor of 10 higher compared to the ToF-ICR measurements from 2010. The PI-ICR measurement file in figure 7.6b was obtained in 10 h and comprises 145 ion evens in total (about 50 % in the magnetron phase spot, and 50 % in the modified cyclotron phase spot both sharing about equal events from the isomeric and ground state). Normalizing this performance to the beam current intensity present during the ToF-ICR measurement the detection rate is about 7 times higher compared to 2010. The increase in the overall efficiency can mainly be attributed to the implementation of the CGC into the SHIPTRAP setup [114]. A comparison between the ToF-ICR performance from 2010 with respect to this work's PI-ICR performance as of 2018 is given in table 7.1.

Table 7.1: Comparison between a ToF-ICR measurement from 2010 by Minaya *et al.* [69] with respect to PI-ICR (this work) for $^{255}Lr^{2+}$. Both measurements have been carried out at SHIPTRAP using $^{133}Cs^{+}$ as reference. The corresponding measurement files are presented in figure 7.6. For further details see text.

| | measurement time | mass resolving power | relative precision (statistical) | remarks |
|---|---|---|---|---|
| PI-ICR (this work) | 10 h | $\approx 11\,000\,000$ | $\approx 4\times10^{-9}$ | ground and isomeric state resolved |
| ToF-ICR (2010) | 14.5 h | $\approx 970\,000$ | $\approx 1\times10^{-7}$ | resonance consists of ground and isomeric state |

### 7.2.7 Atomic Mass of $^{256}$Lr

Since 2010 $^{256}$Lr was the heaviest isotope for which its atomic mass has been measured directly [69]. The measurements were carried out at SHIPTRAP by means of the ToF-ICR technique. A frequency ratio of $R_{\mathrm{ToF}} = 0.9634610(3)$ with a relative uncertainty of $3\times10^{-7}$ was obtained using $^{133}Cs^{+}$ as reference [69]. The corresponding mass excess improved the existing value from the atomic mass evaluation by about a factor of 2.5 from 220 keV [43] down to 80 keV [153]. In total, the obtained resonance contained 50 ions accumulated over 4 days. For the last years this experiment defined the limits of direct mass spectrometry in the region of the heaviest elements with respect to its production cross section of 60 nb and the resulting detected ion rate of $< 1$ ion/h.

In this work the atomic mass of $^{256}$Lr is determined using PI-ICR. The evaluated frequency ratios with respect to the reference ion $^{133}Cs^{+}$ are presented in figure 7.7. A mean frequency ratio of $R = 0.963461019(11)$ with a relative uncertainty of $1.2\times10^{-8}$ is obtained. This value is well in agreement with the previously obtained frequency ratio using ToF-ICR. However, the uncertainty is improved by about one order of magnitude. The resulting mass excess $ME = 91737.8(27)$ keV agrees well with the most recent value of the atomic mass evaluation $ME_{\mathrm{AME}} = 91750(80)$. The current stated uncertainty of 2.7 keV is about a factor of 30 smaller compared to the value of the atomic mass evaluation. In this work $^{256}$Lr has been measured at a detection rate of $\approx 2$ ions/h. The primary beam intensity was about a factor of two lower compared to the ToF-ICR experiment in 2010. The increased detection rate is mainly due to the recent implementation of the CGC. As section 7.2.8 presents the first direct mass spectrometry of

the superheavy isotope $^{257}$Rf with a cross section of $\approx 15$ nb, this work represents the current limit with respect to the heaviest directly measured isotope. In addition, it is the isotope with the lowest production cross section that has been measured directly by means of mass spectrometry.

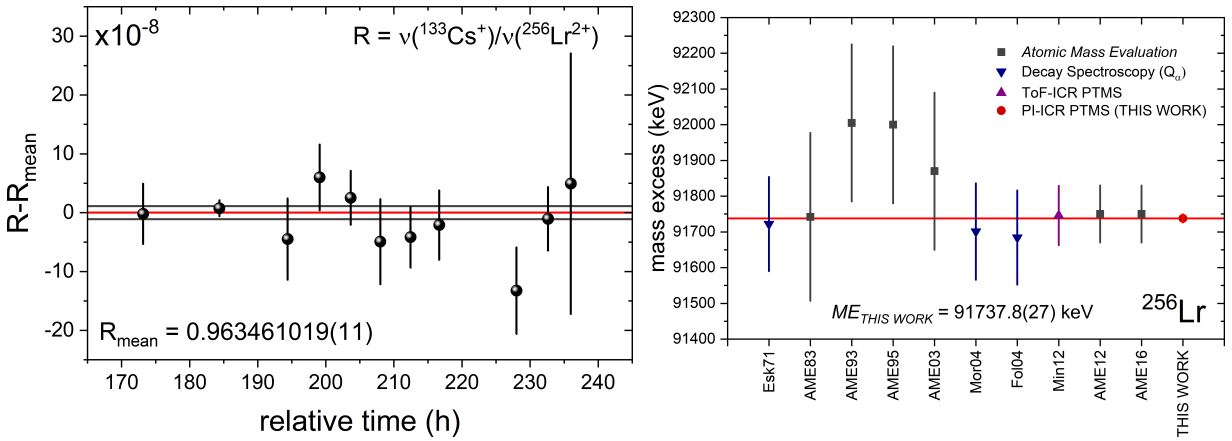


Figure 7.7: (Left figure) Obtained frequency ratios for $^{256}Lr^{2+}$ with respect to the reference ion $^{133}Cs^{+}$ as a function of the relative time after the start of the beam time. All frequency ratios have been obtained using PI-ICR. (Right figure) Measured mass excesses $ME$ of $^{256}$Lr from different experiments in historical order (increasing time from left to right). The $Q_\alpha$-values are obtained from decay spectroscopy [161, 166, 167] and evaluated using equation (7.4). For this the atomic mass from the most recent atomic mass evaluation [39] of the daughter isotope $^{252}$Md is used. The ToF-ICR measurements were performed at SHIPTRAP [69]. In addition, the atomic mass evaluation [150, 151, 152, 43, 153, 39] is shown. For further details see text.

### 7.2.8 First Direct High-Precision Mass Spectrometry of a Superheavy Element ($^{257}$Rf)

This work presents the first direct high-precision mass spectrometry of a superheavy element. During the experimental campaign in summer 2018 the atomic mass of $^{257}$Rf ($Z = 104$) has been measured directly for the first time. This measurement has been particularly challenging compared to the measurements on nobelium and lawrencium isotopes (presented in previous sections). First, the delivered integrated primary beam intensity of the $^{50}$Ti beam from the UNILAC accelerator was about a factor of four lower than expected. For the given primary beam intensity and efficiency of the SHIPTRAP setup with respect to nobelium and lawrencium isotopes the detection rate of $^{257}$Rf has been estimated to be about one detected count every hour. This estimation was based on the experimental production cross sections and corresponding detection rates of nobelium and lawrencium isotopes compared with production cross section of $^{257}$Rf (about 15 nb). The obtained detection rate was only about one detected $^{257}$Rf event per 10 hours and therefore about one order of magnitude lower than estimated. There are several explanations for this reduction. The rutherfordium ions were produced using the fusion-evaporation reaction $^{208}$Pb($^{50}$Ti,1n) at a primary beam energy of 4.65 MeV/u. The recoil energy is $\approx 4$ MeV higher than the recoil energies for the nobelium and lawrencium ions (see table 10.4 in the appendix 10.5). Therefore, a lower stopping efficiency is expected. However, as presented in figure 4.15, the stopping efficiency at a titanium entrance window foil thickness of 3.6 µm at a room-temperature equivalent helium buffer-gas density of 50 mbar only drops from 60 % (in the case of $^{254}$No) to 50 % for $^{257}$Rf. Furthermore, this drop in efficiency was countered by an increased buffer-gas pressure and additional degrader foils during the experiment on $^{257}$Rf. The second possible explanation is a decreased overall efficiency of the SHIPTRAP setup. Indeed, a steady decrease in the overall efficiency has been observed, which is most likely attributed to the decrease in the extraction efficiency of the CGC (this is discussed in section 5.3). Furthermore, an increased impurity level

in the buncher RFQ of the setup (see appendix 10.6) restricted the measurement cycle time, including the ion preparation and the accumulation time, to few hundreds of milliseconds. The ion preparation in the preparation trap takes ≈ 200 ms. Therefore, accumulation times of only ≈ 50 ms have been used in the measurement of $^{257}$Rf. This corresponds to a mass resolving power of about ≈ 500 000 which is insufficient to resolve the isomeric state $^{257m}$Rf at an excitation energy of about ≈85 keV [88] from its respective ground state. Thus, both species contribute to the obtained result of the atomic mass. In addition, probably due to charge-exchange processes in the buncher and the preparation trap, respectively, the obtained phase images of $^{257}$Rf were affected by an enhanced level of background events compared to the measurements on nobelium and lawrencium isotopes. For that reason, two out of nine obtained measurement files for $^{257}$Rf$^{2+}$ have been rejected from the data analysis.

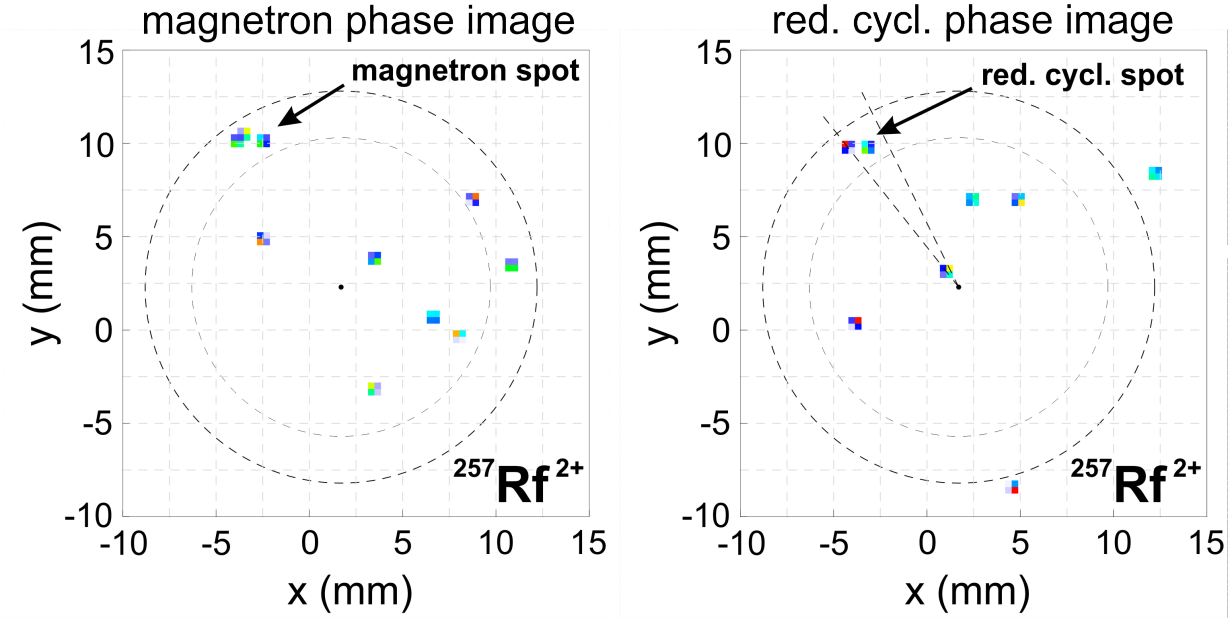


Figure 7.8: Obtained images of the final magnetron and modified cyclotron phases for $^{257}$Rf$^{2+}$ using PI-ICR at an accumulation time of 50 ms. The image is a superposition of 7 measurement files. The dashed circle represent the 99.7 % confidence level in which $^{257}$Rf$^{2+}$ ions should be detected. In addition, the dashed polar lines in the modified cyclotron phase image represent the 99.7 % confidence level in which $^{257}$Rf$^{2+}$ ions should be detected with respect to their magnetron phase. For this the literature value from the most recent atomic mass evaluation [39] of $^{257}$Rf is taken into account. The remaining events are attributed to scattered ions, other ion species and detector noise, respectively. For more details see text.

Despite these challenging conditions and restrictions, the atomic mass of $^{257}$Rf is determined at an absolute precision of about ≈ 120 keV/c$^2$ with only 5 ions in total. Figure 7.8 presents the obtained phase images for the final magnetron and modified cyclotron phase of $^{257}$Rf$^{2+}$, respectively. To select the rutherfordium ions several conditions were applied: besides a time-of-flight gate, two circles are drawn around the center of the trap. These circles correspond to the expected radial position of any true detected ion signal (with a 3$\sigma$ confidence band evaluated using the reference ion). As seen in the magnetron phase image presented in figure 7.8 three detected ion events cluster in the estimated radial distance to the center, which agree with the position of two clustered events in the modified cyclotron phase image. As in any other measurement using PI-ICR, the accumulation time of the reference ion is fine tuned such that its magnetron and modified cyclotron phase spot are spatially overlapping. If the atomic mass of the ion of interest is approximately known, the magnetron and modified cyclotron phase spot also overlaps if the accumulation time is scaled properly with respect to the reference ion. In practice, the atomic masses for heavy elements around this region have been either measured or interpolated with uncertainties in the order of tens to hundreds of keV. In the case of $^{257}$Rf the atomic mass is known with an uncertainty of 11 keV [39]. The literature value of the ion of interest and in particular its uncertainty is used to estimate the expected final modified

cyclotron phase with respect to the magnetron phase. Combining equations (3.28), (3.29) and (3.25) the angle difference between the modified cyclotron and magnetron phase spot is given by

$$\phi = \left(\frac{q}{q_{\mathrm{ref}}}\right)\left(\frac{m_{\mathrm{ref}}}{m}\right) 2\pi\nu_{\mathrm{ref}} t_{\mathrm{acc}} + 2\pi(n+m), \tag{7.7}$$

where the subscript *ref* denotes the quantities of the reference ion. The absolute phase difference between the magnetron and modified cyclotron phase spot $\phi$ is irrelevant in the sense that it corresponds to zero degree if the phase spots of the reference ion are overlapping. Of more interest is the estimated uncertainty of the phase difference with respect to the imprecisely known mass of the ion of interest $m$ and the uncertainty in the magnetic field strength given by the uncertainty in the determined true cyclotron frequency of the reference ion $\nu_{\mathrm{ref}}$. In the case of $^{257}\mathrm{Rf}^{2+}$, using equation (7.7) and the reference ion $^{133}\mathrm{Cs}^{+}$, the uncertainty is given by

$$\delta\phi = (\phi - 2\pi(n+m))\sqrt{\left(\frac{\delta\nu_{\mathrm{ref}}}{\nu_{\mathrm{ref}}}\right)^2 + \left(\frac{\delta m_{\mathrm{ref}}}{m_{\mathrm{ref}}}\right)^2 + \left(\frac{\delta m}{m}\right)^2}, \tag{7.8}$$

where in general the contribution due to the relative uncertainty of the reference ions' atomic mass $\delta m_{\mathrm{ref}}/m_{\mathrm{ref}}$ can be neglected. The atomic mass of $^{257}$Rf is known with an absolute precision of $10\,\mathrm{keV/c^2}$ $\alpha$-decay spectroscopy [39]. At the given experimental conditions, the $1\sigma$ uncertainty in the phase difference between the magnetron and modified cyclotron phase images at an accumulation time of 50 ms is $\pm 2\,^{\circ}$. Figure 7.8 shows the angular uncertainty of $\pm 6\,^{\circ}$ with respect to the measured magnetron phase spot of $^{257}\mathrm{Rf}^{2+}$. This corresponds to a confidence level of 99.7 %. Indeed, the two clustered events in the modified cyclotron image of $^{257}\mathrm{Rf}^{2+}$ have been detected in this region. In addition, they are within the 99.7 % confidence level with respect to their radii. Therefore, they are confirmed as detected $^{257}\mathrm{Rf}^{2+}$ ions.

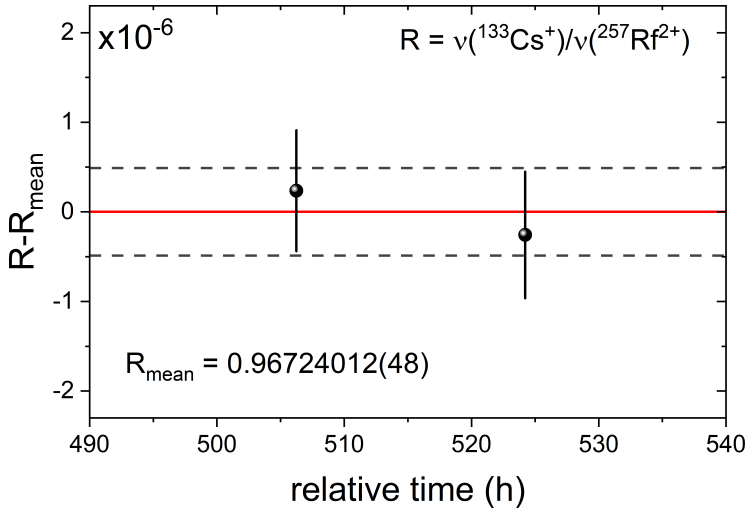


Figure 7.9: Obtained frequency ratios for $^{257}\mathrm{Rf}^{2+}$ with respect to the reference ion $^{133}\mathrm{Cs}^{+}$ as a function of the relative time after the start of the beam time. All frequency ratios have been obtained using PI-ICR.

Figure 7.9 shows the obtained frequency ratios for $^{257}\mathrm{Rf}^{2+}$. A frequency ratio of $R_{\mathrm{mean}} = 0.96724012(48)$ with a relative precision of $5.0 \times 10^{-7}$ and a mass excess of $ME = 95951(120)\,\mathrm{keV}$ is obtained. The achieved mass resolving power of 600 000 did not allow separating the isomeric state $^{257m}$Rf with an excitation energy of $\approx 85\,\mathrm{keV}$ [88] from the respective ground state. During production about 1/3 of the rutherfordium ions are populated in their isomeric state for the given experimental conditions [89]. As the half-life of the isomeric state is comparable with the half-life of its ground state (both $t_{1/2} \approx 4\,\mathrm{s}$ [168]), its contribution to the resonance cannot be neglected. Therefore, as an conservative approach, the excitation energy is quadratically added to the uncertainty of the mass excess value, resulting in a combined

uncertainty of $\sqrt{(120\,\mathrm{keV})^2 + (75\,\mathrm{keV})^2} = 140\,\mathrm{keV}$. The final mass excess value $ME = 95951(140)\,\mathrm{keV}$ is in good agreement with the literature value of 95866(11) keV.

### 7.2.9 The Deformed $N = 152$ Shell Closure

The nuclear shell model has been introduced already more than 60 years ago [169, 170]. The precise determination of atomic masses allows identifying shell closures and quantifying their strength for isotopes and isotones. As discussed in chapter 2, signatures of neutron shell closures are displayed by the two-neutron separation energy (equation (2.4)). In order to enhance the visibility of weak shell closures the two-neutron shell gap parameter

$$\delta_{2n}(N,Z) = S_{2n}(N,Z) - S_{2n}(N+2,Z) \tag{7.9}$$

$$= ME(N-2,Z) - 2ME(N,Z) + ME(N+2,Z) \tag{7.10}$$

is used [171]. In the region of the heaviest elements, this parameter has been derived from masses obtained by high-precision PTMS on nobelium and lawrencium isotopes in the works of Block *et al.* [67], Dworschak *et al.* [68] and Minaya *et al.* [69] at SHIPTRAP. These accurate results allowed quantifying the deformed neutron shell closure at $N = 152$ for the first time based on direct mass measurements. The first direct high-precision mass measurements of $^{251}$No and $^{254}$Lr and the improved atomic masses of $^{254}$No and $^{255,256}$Lr from this work reduce the uncertainties in the respective shell gap parameters. Figures 7.10 and 7.11 show the two-neutron separation energy and two-neutron shell gap parameters, respectively, for the nobelium and lawrencium isotopes around $N = 152$.

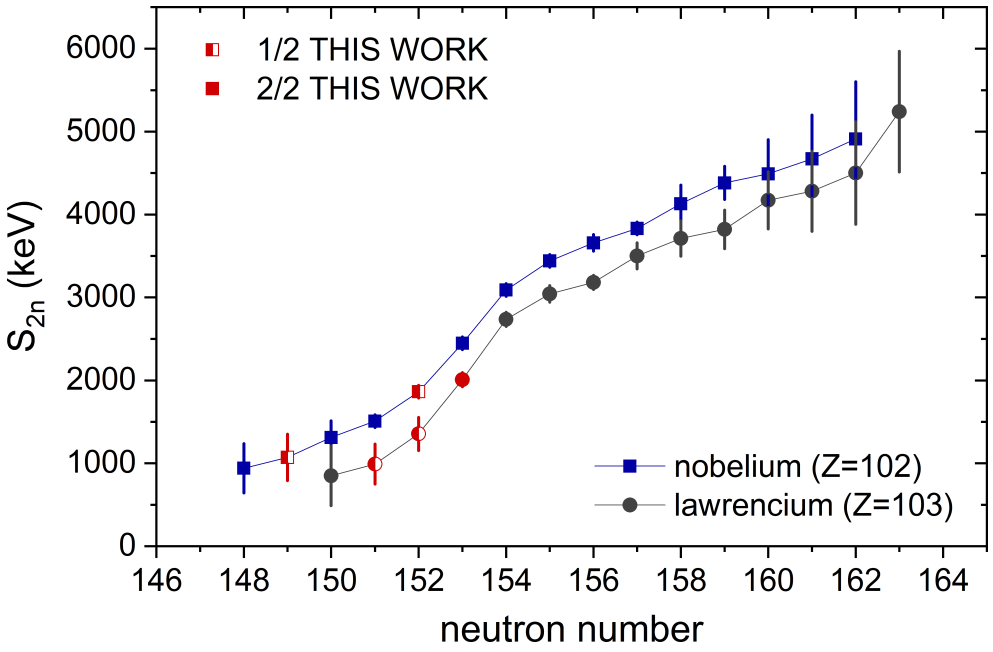


Figure 7.10: Two-neutron separation energies for nobelium and lawrencium isotopes according to equation (2.4). Data points in which one or two mass values from this work contribute are highlighted.

Except for $^{255}$Lr, the obtained atomic masses agree with previous ToF-ICR measurements from SHIPTRAP. Therefore, the general picture of the deformed shell closure at $N = 152$ does not change with respect to the discussions given by Minaya *et al.* [69]. Still, the trend in the two-neutron gap parameter is best described by the macroscopic-microscopic model from Möller *et al.* [16].

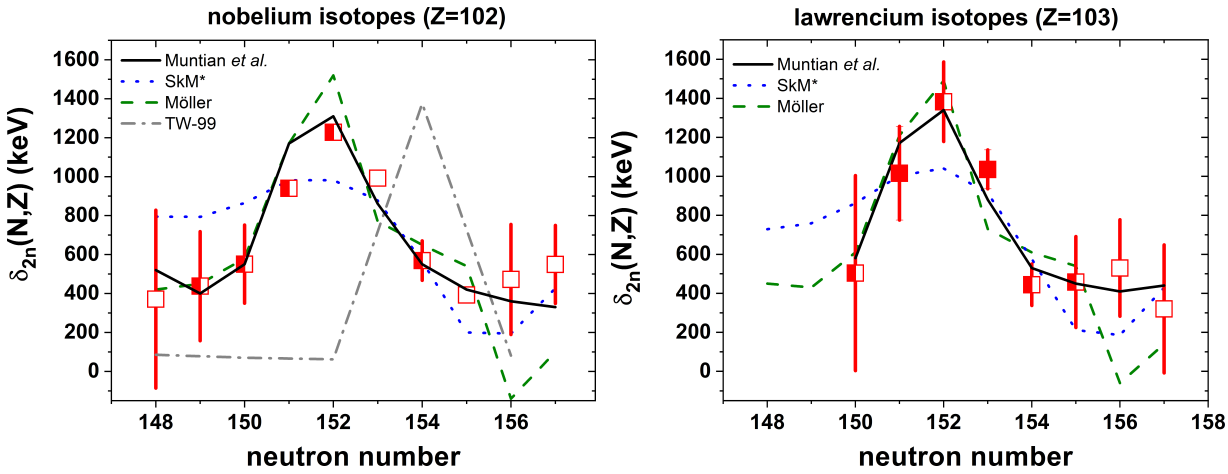


Figure 7.11: Two neutron-shell gap parameter $\delta_{2n}(N, Z)$ for the nobelium (left figure) and lawrencium isotopes (right figure) around the deformed neutron shell closure at $N = 152$. For this, the most recent data of the atomic mass evaluation [39] is used. The data points are shown as empty (no data from this work contributes), semi-filled (one atomic mass from this work contributes) and filled red squares (two atomic masses from this work contribute). In addition, theoretical predictions from [105, 171, 16, 172]. Figure modified from [69]. For further details see text.

### 7.2.10 New Anchor Points to Heavier Elements

Figure 7.12 presents an overview of results from direct high-precision mass spectrometry in the region of the heaviest elements. Due to the achieved uncertainties in the order of few keV/c$^2$ for $^{254}$No and $^{255,256}$Lr with respect to the current atomic mass evaluation [39] and the first ever direct high-precision PTMS of $^{251}$No and $^{254}$Lr at a similar uncertainty, atomic masses of isotopes up to the element darmstadtium ($Z = 110$) will be improved. Of particular interest are very short-lived isotopes, e.g. $^{267}$Ds and $^{268}$Ds, with expected half-lives in the order of microseconds [89], which will most likely never be addressed by direct high-precision PTMS. These nuclides will allow investigating the $N = 162$ shell closure by means of two-neutron separation energies.

### 7.2.11 Summary of Atomic Masses

Figure 7.13 shows the obtained atomic ground-state masses for $^{251,254}$No and $^{254-256}$Lr, respectively. The obtained mean frequency ratios $R_{\mathrm{mean}}$ are summarized in table 7.2 and compared to available literate values.

## 7.3 Isomeric States in Nobelium and Lawrencium Isotopes

### 7.3.1 Excitation Energy Determination

Following Einstein's mass-energy equivalence principle [5] the excitation energy of an isomeric state with respect to its ground state is defined as their difference in total energy

$$E_{\mathrm{exc}} = (m_{\mathrm{isom}} - m_{\mathrm{gs}})c^2 = \Delta m c^2, \tag{7.11}$$

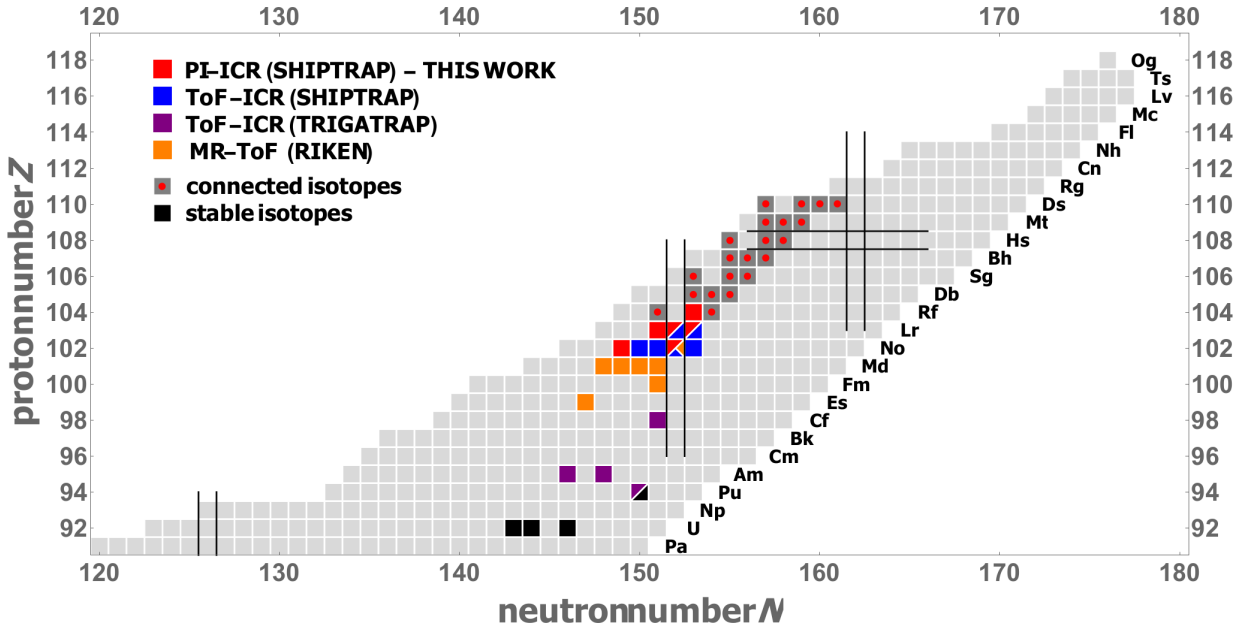


Figure 7.12: Nuclear Chart in the region of the heaviest elements. The color code represents isotopes that have been measured directly by means of PI-ICR (red color), ToF-ICR (blue color) [67, 68, 69] and MR-ToF MS (orange color) [84]. Squares which are solely colored in red represent isotopes for which the atomic mass is determined directly with high-precision for the first time. Red-dotted squares represent heavier isotopes that are connected via $\alpha$ decays to isotopes measured in this work (*connected isotopes*). For more details see text.

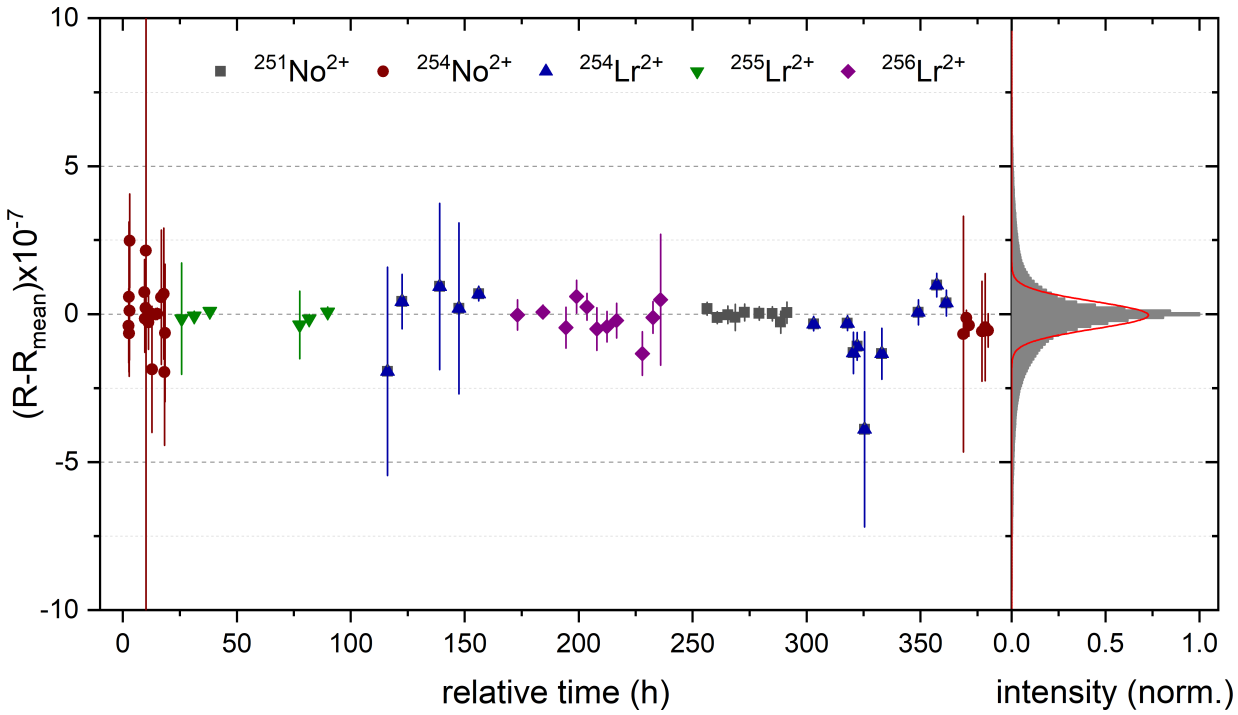


Figure 7.13: Difference between the obtained individual frequency ratios $R = \nu(^{133}Cs^{+})/(^{A}X)$ and the corresponding mean frequency ratio $R_{mean}$ for $^{251,254}No^{2+}$ and $^{254-256}Lr^{2+}$ ions. The frequencies have been measured in this work using PI-ICR at SHIPTRAP. The horizontal axis represents the relative time after the start of the beam time in summer 2018. The error bars correspond to the combined statistical and systematic uncertainty ($1\sigma$). The difference in uncertainty is dominated by different accumulation times $t_{acc}$ in the PI-ICR measurement. Each data point represents a Gaussian distribution. The sum over all data point distributions is presented in the right hand side of the picture. The red curve corresponds to Gaussian least-square fit. For further details see text.

Table 7.2: Summary for the high-precision PTMS on isotopes of the heavy elements nobelium ($Z = 102$) and lawrencium ($Z = 103$) and the superheavy element rutherfordium ($Z = 104$) from this work. All isotopes have been measured as doubly-charged ions using the PI-ICR technique at SHIPTRAP with $^{133}Cs^+$ being the reference ion. If existent, the obtained frequency ratios are compared to previously obtained values from SHIPTRAP [68, 69]. The obtained mass excess $ME$ is compared to the Atomic Mass Evaluation 2016 [39]. † This mass has been measured directly for the first time. ‡ Only an extrapolated value available. ⋆ The combined cross section for the ground and known long-lived isomeric state is given as they are not separated in this work's measurement. For further details see text.

| | | this work | | | literature | | |
|---|---|---|---|---|---|---|---|
| isotope | $\sigma$ | $R$ | $\delta R/R$ | $ME$ (keV) | $R_{\text{lit}}$ | $\delta R_{\text{lit}}/R_{\text{lit}}$ | $ME_{\text{lit}}$ (keV) |
| $^{251}$No† | 15 nb | 0.944614684(9) | 9.5E-9 | 82850.6(22) | | | 82850(110)‡ |
| $^{254}$No | 2 µb | 0.955908551(5) | 4.8E-9 | 84732.8(11) | 0.95590852(6) [68]<br>0.95590855(4) [69] | 6.0E-8<br>3.9E-8 | 84723(10) |
| $^{254}$Lr† | 25 nb | 0.955928767(11) | 1.1E-8 | 89731.0(28) | | | 89870(300)‡ |
| $^{255}$Lr | 250 nb | 0.959691648(7) | 7.3E-9 | 89934.5(17) | 0.95969174(6) [69] | 6.0E-8 | 89947(18) |
| $^{256}$Lr | 60 nb | 0.963461019(11) | 1.2E-8 | 91737.8(27) | 0.9634610(3) [69] | 3.0E-7 | 91750(80) |
| $^{257}$Rf† | 15 nb⋆ | 0.96724012(48) | 5.0E-7 | 95951(140) | | | 95866(11) |

where $m_{\text{isom}}$ and $m_{\text{gs}}$ represent the atomic masses of the isomeric and ground state, respectively. An excited state reduces the nuclear binding energy and therefore increases the nucleus' rest mass in accordance to equation (3.26). Thus, the mass difference $\Delta m \equiv (m_{\text{isom}} - m_{\text{gs}})$ is always positive. The impact of an excited nuclear state on the binding energies of atomic shell electrons can be neglected for absolute uncertainties of about 1 keV the resulting change in the binding energy between both ion species is neglected.[6]

There are two approaches to measure the excitation energy using PTMS. From equation (7.11) it is obvious that the excitation energy is measured by measuring both, the atomic mass of the ground and isomeric state individually and taking their difference. The atomic mass of the ground state is obtained by evaluating its true cyclotron frequency ratio taking $^{133}Cs^+$ as the reference ion $R = \nu_{\text{ref}}/\nu_{\text{gs}}$. The same procedure can be followed for the isomeric state. In this case the true cyclotron frequency ratio $R' = \nu_{\text{ref}}/\nu_{\text{isom}}$ between the isomeric state and $^{133}Cs^+$ is evaluated. Combining equation (7.1) with (7.11) yields the excitation energy

$$E_{\text{exc}} = 2(R' - R) \times m_{\text{lit}}(^{133}\text{Cs})c^2, \tag{7.12}$$

where the assumption is made that the ground and isomeric state are measured as doubly-charged ions. A more direct approach to determine the excitation energy is given by the fact that the ground state itself can act as a reference ion for the isomeric state (or the other way around). Using equation (3.29) the frequency ratio of both states $R^* = \nu_{\text{gs}}/\nu_{\text{isom}}$ yields

$$m_{\text{isom}} = R^*(m_{\text{gs}} - 2m_e) + 2m_e. \tag{7.13}$$

Subtracting $m_{\text{gs}}$ from equation (7.13) in combination with equation (7.11) now gives access to the mass difference and thus the excitation energy

$$E^*_{\text{exc}} = (R^* - 1)(m_{\text{gs}} - 2m_e)c^2. \tag{7.14}$$

Figure 7.14 shows exemplary the evaluation for the excitation energies $E^*_{\text{exc}}$ and $E_{\text{exc}}$ of $^{255m}$Lr. In (a) the measured true cyclotron frequencies $\nu_c$ for $^{255g,255m}Lr^{2+}$ and $^{133}Cs^+$ are presented. The frequencies are evaluated based on the PI-ICR double-pattern scheme using equation 3.25. The most direct evaluation of

[6] This is similar to the discussion about atomic versus ionic masses with respect to the electron binding energy in section 3.7.

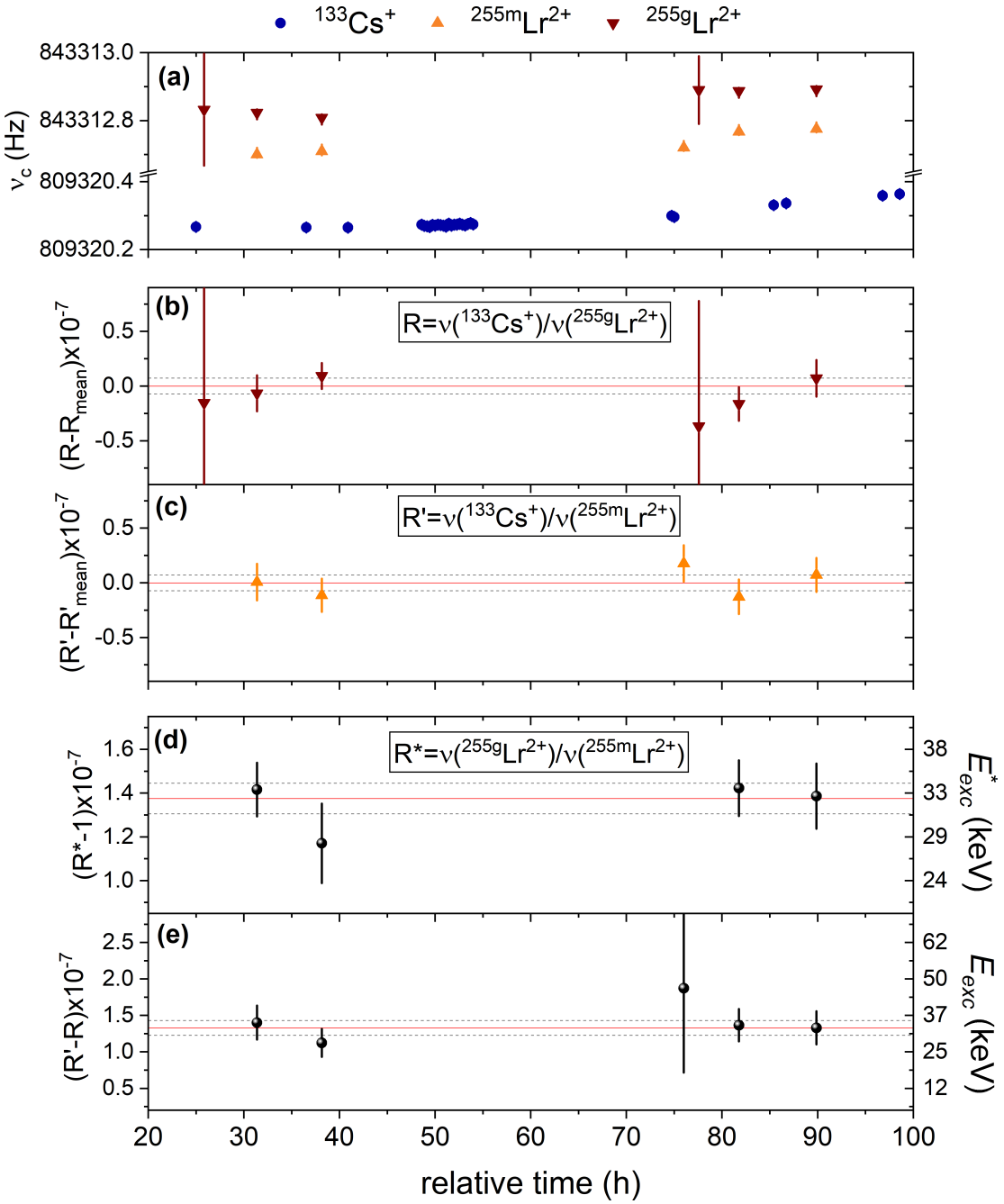


Figure 7.14: (a) Measured true cyclotron frequencies $\nu_c$ for the ground state $^{255g}\mathrm{Lr}^{2+}$, its isomeric state $^{255m}\mathrm{Lr}^{2+}$ and the reference ion $^{133}\mathrm{Cs}^{+}$ during the beam time using PI-ICR. (b) Frequency ratios $R \equiv \nu_c(^{133}\mathrm{Cs}^{+})/\nu_c(^{255g}\mathrm{Lr}^{2+})$ for the ground state with respect to the reference ion. (c) Frequency ratios $R \equiv \nu_c(^{133}\mathrm{Cs}^{+})/\nu_c(^{255m}\mathrm{Lr}^{2+})$ for the isomeric state with respect to the reference ion. (d) Frequency ratios $R \equiv \nu_c(^{255g}\mathrm{Lr}^{2+})/\nu_c(^{255m}\mathrm{Lr}^{2+})$ for the isomeric state with respect to its ground state. (e) Frequency ratio difference between (c) and (b). In all cases the red line represents the obtained mean value and the dashed gray lines its corresponding standard deviation ($1\sigma$). (d) and (e) are used to evaluate the excitation energies $E^*_{\mathrm{exc}}$ and $E_{\mathrm{exc}}$ for the isomeric state. The obtained values are 32(2) keV and 32(3) keV in the case of (d) and (e), respectively. For further details see text.

the excitation energy is followed by determining the true cyclotron frequency ratio of the isomeric state with respect to the ground state. In this case (d) is obtained and the evaluated mean value of $(R^* - 1)$ gives access to the excitation energy $E^*_{\mathrm{exc}}$ using equation (7.11). Using the measured true cyclotron frequency of the reference ion $^{133}\mathrm{Cs}^{+}$, the excitation energy is obtained by first evaluation the frequency ratio with respect to the ground state $^{255g}\mathrm{Lr}^{2+}$ (shown in (b)) and the isomeric state $^{255g}\mathrm{Lr}^{2+}$ (shown in (c)). The mean value of the frequency ratio difference shown in (e) gives access to the excitation energy $E_{\mathrm{exc}}$ using

equation (7.12). The results are summarized in 7.3.

Note that the evaluation in (d) is performed for measurement files in which ground state and isomeric state events are recorded. The evaluation in (e) also makes use of files in which only one of both states has been measured if both states have been measured within a sufficient amount of time. It is worth to mention that the obtained uncertainties usually differ in both evaluations. Since the reference ion is measured with much higher precision, the evaluation in (e) can be more precise with respect to (d) even though the evaluation requires to evaluate the reference ion $^{133}Cs^{+}$ in addition to the ground and isomeric state.

### 7.3.2 The 105 keV Isomer $^{251m}$No

After its first successful production and identification in 1967 [85] the isotope $^{251}$No has been subject to many decay spectroscopy investigations. In [85] the isotope was directly produced via the hot-fusion reaction $^{244}$Cm($^{12}$C,5n) where two $\alpha$ lines at energies of about 8.60 MeV and 8.68 MeV were assigned to the $\alpha$ decay of $^{251}$No into $^{247}$Fm with an attributed half-life of 0.8(2) s. In decay spectroscopy experiments carried out at SHIP $^{251}$No had been produced indirectly via the $\alpha$ decay of $^{255}$Rf [173, 147, 88, 148]. The first $\alpha$ line was reproduced but no indication for the second one was found. In an experiment aimed to study the decays of $^{251}$No and $^{247}$Fm by means of $\alpha$-$\gamma$ spectroscopy performed at SHIP, $^{251}$No was produced directly using the fusion-evaporation reaction $^{206}$Pb($^{48}$Ca,3n). In this case both $\alpha$ lines observed in [85] were reproduced [149]. To further investigate decay properties $\alpha$-$\alpha$ correlations to $\alpha$-decay lines of $^{247}$Fm in combination with correlated $\gamma$ lines in $^{243}$Cf following the $\alpha$ decay of $^{247}$Fm have been analysed. Figure 7.15 shows three correlated $\alpha$ decays in $^{251}$No followed by an $\alpha$ decay in $^{247}$Fm at an energy of about 8172 keV. A corresponding projection to this $\alpha$ line of $^{247}$Fm is also presented. The weak 8562 keV line is interpreted as a decay from $^{251g}$No to $^{247}$Fm [66].

After further investigations a decay scheme of $^{251}$No as part of its $\alpha$ decay chain has been derived [66] (figure 7.16). Note that this decay scheme explains the disappearance of the initially observed 8668 keV line in experiments with indirect production of $^{251}$No. In this case the isomeric state $^{251m}$No, a suggested $1/2^{+}[631]$ Nilsson state, is surpassed by strong E1 transitions into the $7/2^{+}[624]$ ground state and the $9/2^{+}$ member of the ground state rotational band as only the $9/2^{-}[734]$ state is populated by the $\alpha$ decay of $^{255}$Rf. In contrast, a direct production of $^{251}$No via a fusion-evaporation reaction also populates the isomeric state.

As seen in figure 7.16 a derivation of the excitation energy for the isomeric state $^{251m}$No requires the excitation energy of $^{247m}$Fm (as a suggested $1/2^{+}[631]$ Nilsson level) to be known. This, in addition, requires the $\alpha$ decay energy of the ground state to be known, which is not trivial given the fact that no direct $\alpha$ decay of the isomer is observed. The evaluation is based on the discussions in [174] and a value of 45(7) keV is given. Finally, a value of 106(7) keV is obtained for the excitation energy of $^{251m}$No [66]. Due to the required assumptions and no direct observed $\alpha$ line this value has been obtained indirectly.

The isomeric state $^{251m}$No has a half-life of about 1 s [66], which is sufficiently long to apply high-precision PTMS. In this work the excitation energy of the isomeric state $^{251m}$No is determined directly for the first time by means of PI-ICR. The result is presented in figure 7.16. As stated, the ground and isomeric state $^{251g}$No and $^{251m}$No are both populated by the fusion-evaporation reaction $^{206}$Pb($^{48}$Ca,3n) the excitation energy was determined via the frequency ratio between the ground and isomeric state $^{251g}No^{2+}$ and $^{251m}No^{2+}$, respectively, according to equation 7.14. A value of $E^{*}_{\mathrm{exc}} = 109(4)$ keV is obtained. In addition,

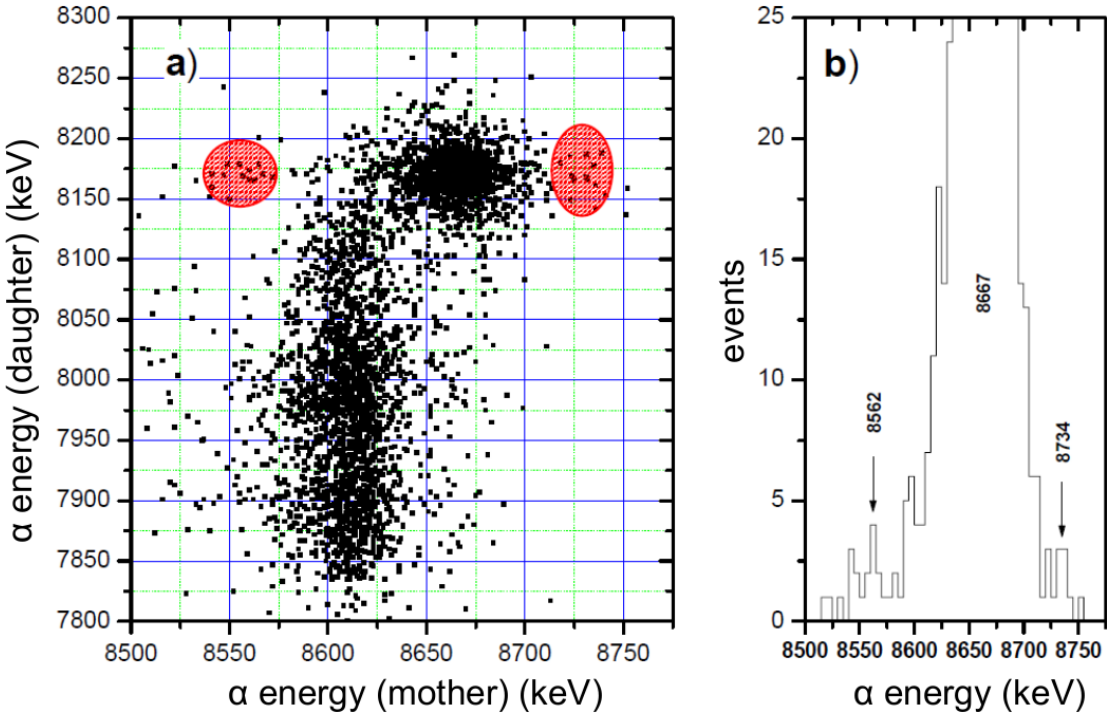


Figure 7.15: (Left figure) $\alpha$-$\alpha$ correlations for $^{251m,251g}$No$\rightarrow^{247m,247g}$Fm. The read areas mark the correlated events of interest from the decay of $^{251m}$No and $^{251g}$No, respectively, followed by a decay from $^{247m}$Fm. (Right figure) Projection of mother energies for daughter energies in the range of 8140 keV to 8200 keV. For further details see text. Both figures provided by [89]. The left figure corresponds to a modified version of the figure presented in [66].

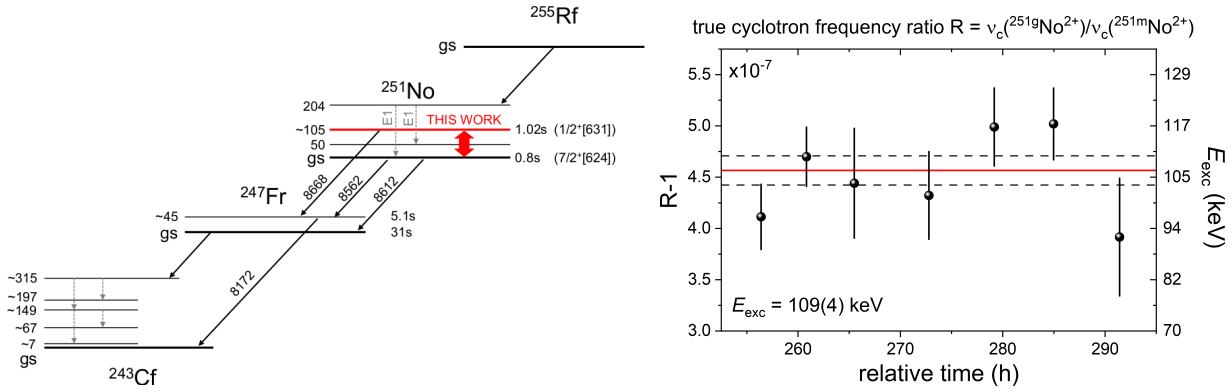


Figure 7.16: (Left figure) Derived decay schemes including $^{251g,251m}$No. $\alpha$ and $\gamma$ transitions are marked with black and gray-dotted arrows, respectively. In this work the excitation energy marked as red arrow is determined directly for the first time using PTMS. Figure based on [66]. (Right figure) The obtained true cyclotron frequency ratios for the isomeric state with respect to its ground state are used to determine the excitation energy $E^*_{\text{ext}} = 109(4)$ keV. The horizontal axis corresponds to the time passed after the beginning of the beam time. For further details see text.

the excitation energy is determined via the frequency ratio between the isomeric state and the reference ion $^{133}Cs^+$ according to equation 7.12. In this case the excitation energy results to $E_{\text{exc}} = 105(3)$ keV. Both values agree well with the indirectly obtained value of 106(7) keV [66] and supports the proposed decay scheme presented in figure 7.16.

### 7.3.3 The 108 keV Isomer $^{254m}$Lr

After the first identification of the isotope $^{254}$Lr via the $\alpha$ dacay of $^{258}$Db [157] in 1985, the obtained $\alpha$ decay spectra did not allow establishing an unambiguous decay nor level scheme. Several decay spectroscopy experiments and three decades later the decay properties of $^{254}$Lr are still not fully understood.

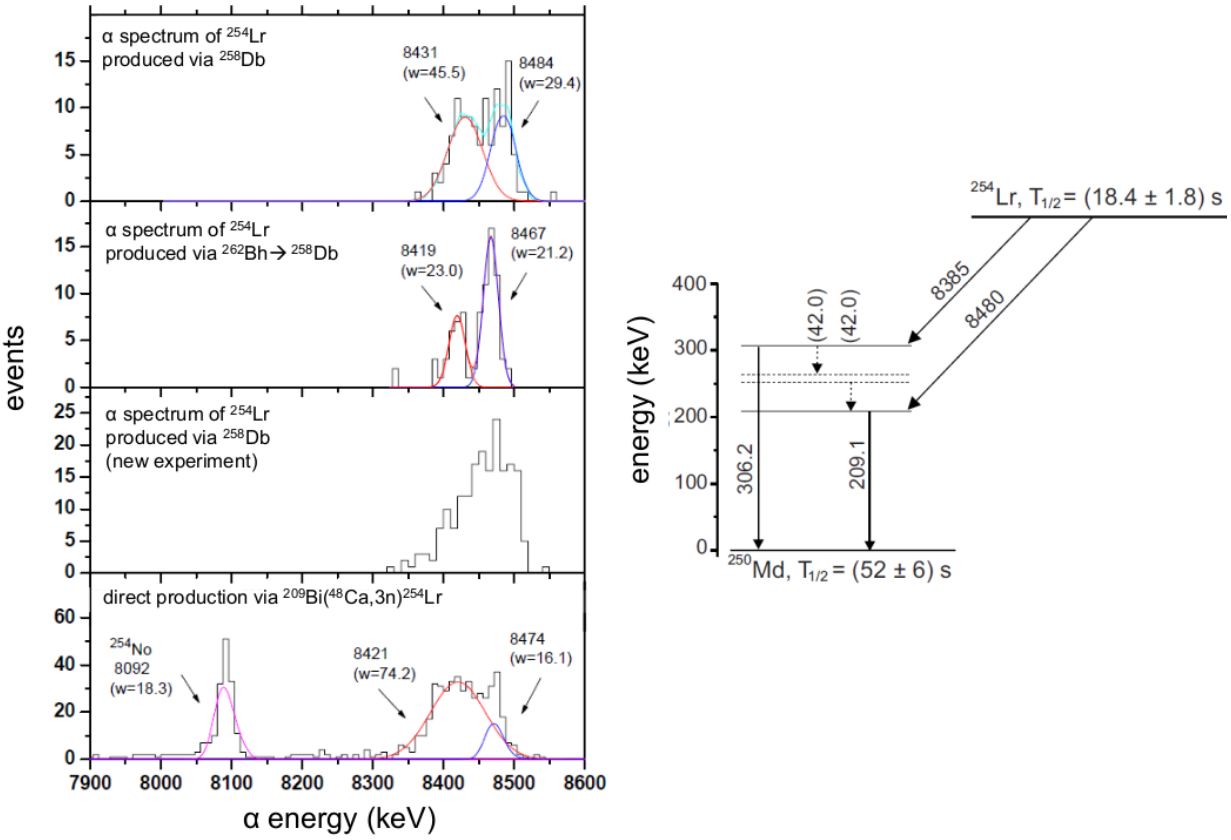


Figure 7.17: (Left figure) Obtained $\alpha$ decay spectra of $^{254}$Lr for different experimental campaigns at SHIP. The red-shaded areas mark the weak observed transitions. Figure provided by [89]. (Right figure) Suggested decay scheme of $^{254g}$Lr. The presence of an isomeric state $^{254m}$Lr alters the obtained decay spectra of $^{254g}$Lr and exacerbates the derivation of a tentative decay scheme. Figure taken from [86].

Figure 7.17 shows $\alpha$ spectra of $^{254}$Lr obtained in different experiments at SHIP. The $\alpha$ decay energies group into two distinct energies around $E_\alpha \approx 8480\,\text{keV}$ and $E_\alpha \approx 8385\,\text{keV}$ which could be attributed to the $\alpha$ decay of the ground-state $^{254g}$Lr into different excited stated in $^{250}$Md [86]. As seen in figure 7.17, the relative intensity between both transitions changes depending upon the production mechanism of $^{254}$Lr. In addition, the spectra show evidence of fine structure which cannot be resolved due to energy summing caused by internal conversion processes. Therefore, at least one low-lying isomeric state was assumed to be present in $^{254}$Lr with a similar half-life as the ground state [89]. Only very recently a tentative level scheme of $^{254}$Lr has been obtained using $\alpha$-$\gamma$ coincidences [175]. Finally, after more than three decades, an isomeric state $^{254m}$Lr with an excitation energy of 108 keV and a half-life of 20(4) s has been derived indirectly from the obtained $\gamma$ spectra. However, the direct $\gamma$ decay into the ground state has not been observed. This is explained by a very weak transition probability due to the suggested spins and parities for both states indicating a $\gamma$ transition of M3 character. The resulting half-life is similar to the half-life of the ground state, which exacerbates the usage of $\alpha$-$\gamma$ correlation studies to disentangle decays from the isomeric and the ground state.

In this work, by using direct PTMS, the existence of the proposed and indirectly determined isomeric

state $^{254m}$Lr is confirmed and its excitation energy is determined directly for the first time. Figure 7.18 shows the obtained frequency ratios of $^{254m}Lr^{2+}$ with respect to its ground state $^{254g}Lr^{2+}$ and $^{133}Cs^{+}$, respectively. Using equation 7.12 the latter results in an excitation energy of $E_{exc} = 110(6)$ keV. In the first more *direct* evaluation an excitation energy of $E^{*}_{exc} = 107(4)$ keV is obtained using equation 7.14. These values agree with the indirectly derived excitation energy of 108 keV [175] and thus supports the derived level scheme presented in figure 7.18.

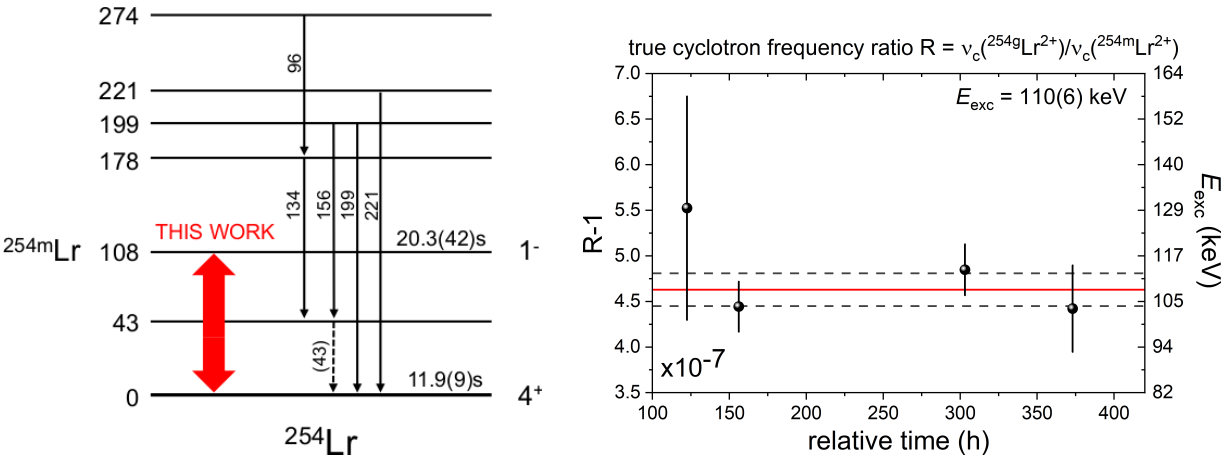


Figure 7.18: (Left figure) Partial, tentative level scheme of $^{254}$Lr. In this work the excitation energy marked as red arrow is determined directly for the first time using PTMS. Figure based on [86]. (Right figure) Direct determination of the excitation energy of $^{254m}$Lr by means of PTMS (this work). The horizontal axis corresponds to the time passed after the beginning of the beam time. For further details see text.

### 7.3.4 The 37 keV Isomer $^{255m}$Lr

In 1971 first $\alpha$ decay data on $^{255}$Lr was published in which one $\alpha$ line at an energy of 8380 keV with a half-life of about 20 s was reported [176] and quickly confirmed [161]. However, in following experiments few years later, two $\alpha$ lines originating from $^{255}$Lr at energies 8429(18) keV and 8370(18) keV were observed [177]. In later experiments, the 8429(18) keV line was not observed but additional $\alpha$ lines were found [178]. Due to differences in the attributed half-lives it was concluded that the transitions originate from either the ground or an isomeric state with a half-life of about 2.5 s [178, 179]. In 2006, A. Chantillon *et al.* suggested a decay scheme of $^{255}$Lr which is shown in figure 7.19. The ground and isomeric state were interpreted as $1/2^{-}[521]$ and $7/2^{-}[514]$ Nilsson states. Using this interpretation an excitation energy of $\approx 37$ keV is derived for the isomeric state $^{255m}$Lr [87]. Based on unpublished data collected at SHIP, an alternative decay scheme is possible (also shown in figure 7.19). In this case the assigned spins are interchanged and the excitation energy of the isomeric state is assumed to be $> 96$ keV. In both cases, expected internal conversions are $7/2^{-} \rightarrow 1/2^{-}$ and $1/2^{-} \rightarrow 7/2^{-}$, respectively, which result in $\gamma$ transition of multipolarity M3 and half-lives in the order of seconds and decay via $\alpha$ transitions are possible [89]. The alternative decay scheme is additionally supported if a ground-state rotational band is assumed to be present. In this case a $3/2^{-}$ state would be present in between the ground and isomeric state which allows the isomeric state to decay into the ground state via two successive E2 transisions $7/2^{-} \rightarrow 3/2^{-} \rightarrow 1/2^{-}$. In this case the $7/2^{-}$ state should not be isomeric [104].

Both level schemes differ in the excitation energy of the isomeric state. In this work, the presence of an isomeric state was confirmed and its excitation energy was measured directly for the first time using PTMS by means of PI-ICR. The obtained data is shown in figure 7.19. Using equations 7.14 and 7.12, respectively, the true cyclotron frequency ratio of $^{255m}Lr^{2+}$ with respect to its ground state $^{255g}Lr^{2+}$ and

to the reference ion $^{133}Cs^{+}$ is evaluated. An excitation energy of $E^{*}_{exc} = 32(2)\,keV$ (using $^{255g}Lr^{2+}$ as reference) and $E_{exc} = 32(3)\,keV$ (using $^{133}Cs^{+}$ as reference) is obtained. The direct determination of the excitation energy is completely independent of any decay scheme assumption and thus confirms the decay scheme presented in [87]. The literature value of $\approx 37\,keV$ is indirectly derived using at least three different $\alpha$ lines with ranging uncertainties of 2 keV to 10 keV [87]. Thus, the result from spectroscopy agrees well with the directly measured values of this work.

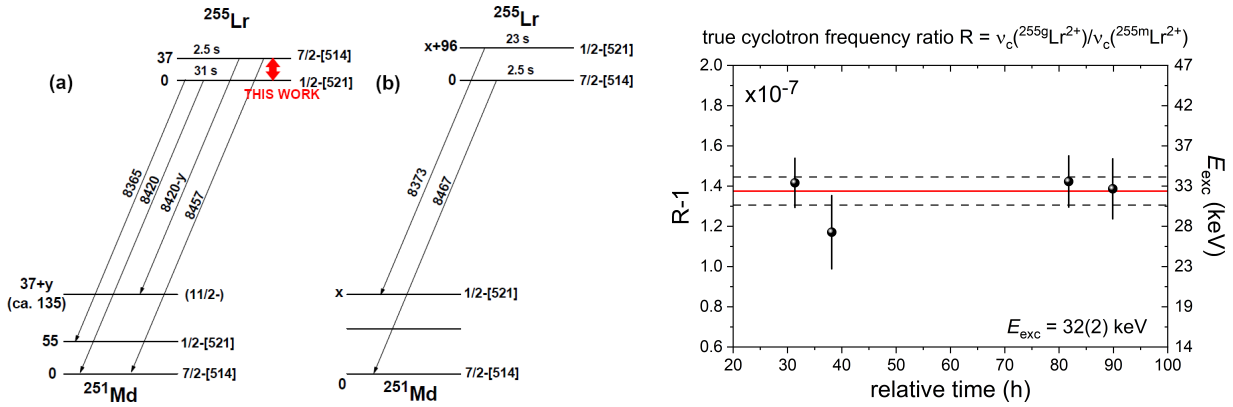


Figure 7.19: (Left figure)(a) Decay scheme of $^{255}Lr$ based on experimental data obtained in $\alpha$ decay spectroscopy. Figure modified from [87]. (b) Alternative decay scheme based on unpublished data obtained at SHIP. Figure provided by [89]. (Right figure) Directly measured excitation energy using PTMS in this work. The horizontal axis corresponds to the time passed after the beginning of the beam time.

### 7.3.5 Summary of Excitation Energies

Table 7.3 summarizes the obtained excitation energies. In all cases the excitation energy is evaluated with respect to the reference ion $^{133}Cs^{+}$ using equation (7.12) and with respect to the ground state using equation (7.14). The analysis procedure is discussed in section 7.3.1 and presented in figure 7.14.

Table 7.3: Obtained excitation energies for the isomeric states $^{251m,254m}No$ and $^{254m,255m}Lr$ using direct high-precision PTMS at SHIPTRAP (this work). In all cases the PI-ICR technique was used. The excitation energies are evaluated with respect to their ground state and by taking $^{133}Cs^{+}$ ions for reference. The data is compared to the literature values $E^{lit}_{exc}$. Note that the at this level of precision the relative uncertainty for the measurements with respect to the ground state can directly be extracted from the uncertainty stated in $(R^{*} - 1)$. For further details see text.

| | vs. ground state | | vs. $^{133}Cs^{+}$ | | | |
|---|---|---|---|---|---|---|
| isomer | $R^{*} - 1$ | $E^{*}_{exc}$ | $R$ | $dR/R$ | $E_{exc}$ | $E^{lit}_{exc}$ |
| $^{251m}No$ | 4.68(16)E-7 | 109(4) keV | 0.944615108(9) | 9.9E-09 | 105(3) keV | 105 keV [66] |
| $^{254m}Lr$ | 4.65(23)E-7 | 110(6) keV | 0.955929198(14) | 1.5E-08 | 107(4) keV | 108 keV [175] |
| $^{255m}Lr$ | 1.36(84)E-7 | 32(2) keV | 0.959691778(7) | 7.5E-09 | 32(3) keV | 37 keV [87] |

# Chapter 8

# Future Perspectives

## 8.1 Direct High-Precision Mass Spectrometry of Superheavy Nuclei

Beside GSI there are several institutes where direct high-precision mass spectrometry of superheavy elements is performed or planned. As an example, the new experimental complex SHEF (superheavy element factory) [180] at the Flerov Laboratory of Nuclear Reaction of the Joint Institute for Nuclear Research in Dubna, Russia, aims at synthesizing and discovering new superheavy nuclides and to study those already synthesized in more detail. Using the DC-280 cyclotron, primary beam intensities of up to 10 pμA for ions with masses of 50-60 u above Coulomb barrier energies will be provided [181]. Direct mass measurements are foreseen but their realization so far remains unclear. Thus, no high-precision direct mass spectrometry results are expected in near future. At the RIKEN Nishina Center in Japan, in addition to fermium (Fm, $Z = 100$) and nobelium isotopes, first direct mass measurements on isotopes of einsteinium (Es, $Z = 99$) and mendelevium (Md, $Z = 101$) have been performed employing a MRTOF mass spectrometry [84]. Its mass resolving power and relative precision are inferior to the performance of PI-ICR at SHIPTRAP. This renders the identification and separation of isomers difficult. First direct measurements of superheavy-element mass numbers of up to moscovium (Mc, $Z = 115$) [182] at the Lawrence Berkeley National Laboratory mainly serve for identification purposes and do only contribute to nuclear structure studies via the observation of correlated decay chains. High-precision mass measurements are not foreseen. In this respect SHIPTRAP will stay unique.

## 8.2 Heavier and more Exotic Nuclei

The successful mass measurement of $^{257}$Rf, despite its low count rate of about one detected ion per day with only 5 detected ions in total, has shown the low-rate capability of the SHIPTRAP setup. Assuming an overall efficiency of 2-5 % of the SHIPTRAP setup as demonstrated for the nobelium and lawrencium isotopes in this work, several heavier and more exotic isotopes, including interesting long-lived isomers, are directly in reach. As an example, one week of primary beam intensity of 1 μpA and a minimum of 5 detected ions in total will allow to perform PTMS of the isotopes and isomers $^{255}$Rf, $^{257m}$Rf,$^{258}$Db and $^{258m}$Db in near future at SHIPTRAP.

To proceed to even heavier and more exotic nuclei, either the overall efficiency of the setup has to be further increased or the amount of required ions to perform a measurement has to be decreased. An overall efficiency of 5 % may indicate a potential gain factor of 20. However, this is not the case as there are certain fundamental limitations in the current system. One of the limiting factors is the detection efficiency of the delay-line detector of about 30 %. In addition, as discussed in section 5.3, the overall efficiency consists of several contributions, e.g. the geometric efficiency of the entrance window and the stopping- and extraction efficiency of the cryogenic gas-stopping cell, buncher and ion optical transmission efficiencies, trap injection efficiency and so forth. Even if all of these contribution on average reach partial efficiencies of 90 %, the resulting overall efficiency in combination with the detector efficiency is on the order of $0.9^6 \times 0.3 \approx 15\,\%$. Furthermore, improvements in certain partial efficiencies are connected to elaborate and costly efforts. As an example, to improve the stopping efficiency of the cryogenic gas-stopping cell from currently about 60% to 90 % will most likely require the design and construction of a next-generation cell. The biggest impact on the overall efficiency is the increase in detection efficiency behind the traps. Exchanging the current delay-line detector with a position-resolving silicon-strip detector (as standard used in decay-spectroscopy experiments at SHIP) could raise the detector efficiency to about 50 % at cost of position resolution. In addition, background events are further suppressed, as the measured $\alpha$ decay from the implanted ion now servers as an additional information. This may also improve the ion sensitivity as now even single ion events can clearly be distinguished from the background. In this case PI-ICR will in principle be capable of measuring an ion species mass with only two detected ions, one in each of the radial eigenmotions, even at lowest detection rates and particle integrals.[1]

A different approach to counter the reduced production rate for heavier and more exotic nuclides is the implementation of the Fourier-Transform Ion-Cyclotron-Resonance (FT-ICR) technique [93] in the form of a second dedicated Penning-trap setup (*SHIPTRAP-2*). In this case, the induced image current from the ion on one of the trap electrodes is picked up and amplified by a resonant circuit close to the traps. For a proper resonant circuit, the detector efficiency is nearly 100 %. In addition, this technique is non-destructive and allows multiple measurements with the same ion which in practice is only limited by either the vacuum condition of the trap volume (collisions resulting in charge-exchange, neutralization or direct loss of the ion) and the particle's half-life. In fact, as presented in figure 8.1, every transfermium element with $Z \leq 113$ has at least one known isotope with a half-life of $> 2\,\mathrm{s}$, which is sufficiently long to be measured by means of FT-ICR. Since cryogenic operation is usually required for the resonant circuits with single-ion sensitivity, vacuum conditions will not impose a limit and - with respect to superheavy elements - only their half-life will be limiting. Furthermore, compared to PI-ICR, mass measurements can be performed with only a single ion. This, in combination with an increase in detection efficiency, will correspond to an increase in sensitivity of about a factor of 15 compared to the performance with PI-ICR in the beam time campaign 2018. However, there are two downsides with respect to the current PI-ICR technique. The detection circuits require quality factors high enough to amplify the tremendously low image currents of single, low-charged and heavy ions in the order of few femtoampere. The geometrical extension of these circuits are in the order of several cm and only allows installing one of them close to the traps. The high quality factor is only available for a small bandwidth of the system and thus limits the acceptance with respect to different masses. From a practical point of view, an easy and reproducible access to the traps is crucial to allow for a fast exchange of the resonant circuits. A cooling power of about 2 W is required to reach about 4 K at the trap and resonant circuit position [183]. This is for example obtained by using powerful two-stage pulse-tube coolers that may introduce vibrations to the systems, which have to be compensated. Reaching the transition temperature at the resonator circuits is more challenging compared to other existing narrow-band FT-ICR experiments, as the externally produced ions

[1] Depending on the half-lives, decay modes and detected rate per pixel of the ions of interest.

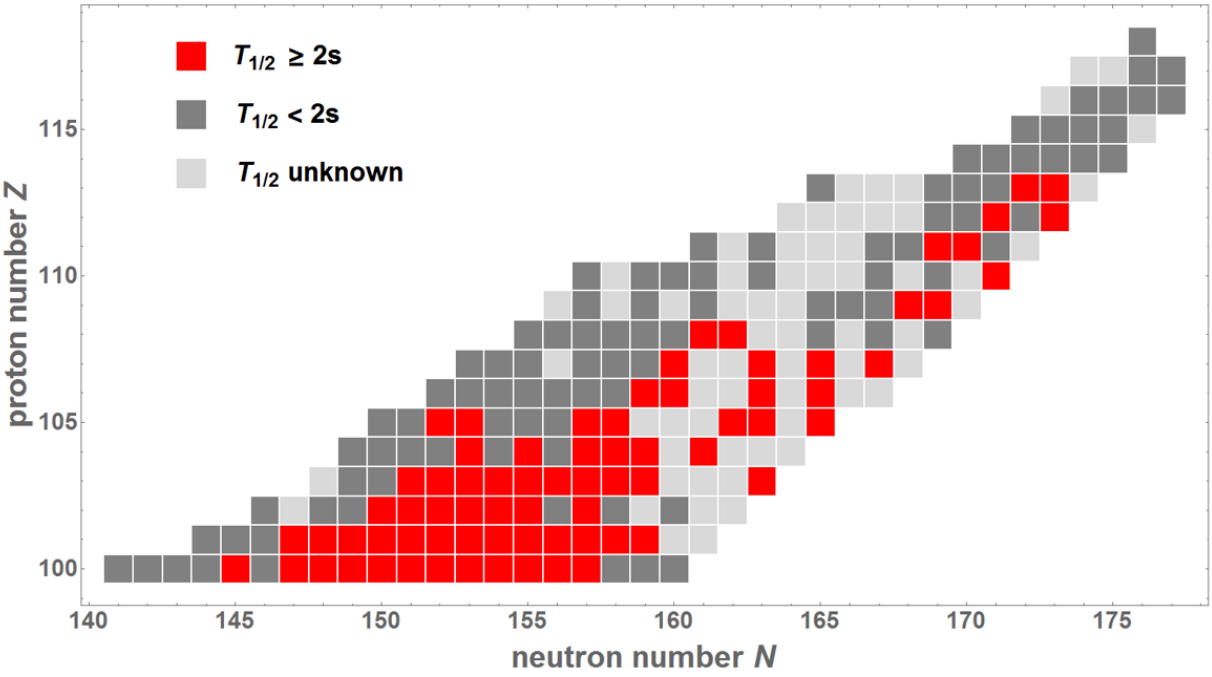


Figure 8.1: Half-lives of isotopes in the region of the heaviest elements.

have to be injected into the traps from a room-temperature environment. Going from PI-ICR to FT-ICR will greatly improve ion sensitivity. However, compared to PI-ICR, FT-ICR is not phase-sensitive at first glance. Thus, the achievable precisions on a single measurement is again, like in the case of the standard ToF-ICR, Fourier-limited. However, for doubly-charged superheavy ions with cyclotron frequencies in the order of about one MHz, an acquisition time of one second results in a precision of $\delta m/m \approx 10^6$, which is still sufficient to study gross nuclear structure phenomena. The reachable precision strongly depends upon the acquisition time, which is limited by the half-lives of the isotopes.[2] Phase-sensitive narrowband FT-ICR signals have already be obtained by means of the so-called PnP- (*pulse and phase*) [184] or PnA-method (*pulse and amplify*) [185], but its feasibility for radioactive, heavy isotopes has to be investigated.

Recently, an FT-ICR setup for single-ion mass measurements was developed and integrated at the existing Low Energy Beam Ion Trap (LEBIT) facility [186], located at the National Superconducting Cyclotron Laboratory (NSCL) in the US. The Single-Ion Penning-Trap (SIPT) is designed for single ion measurements of rare isotopes from projectile fragmentation with detection rates of one per day with the aim of relative precisions in the order of $\delta m/m \leq 10^{-6}$ [183]. Although the scientific focus is on nuclear structure and astrophysics of medium-heavy isotopes, the FT-ICR setup is conceptually similar to SHIPTRAP-2. A first successful FT-ICR commissioning of SIPT was performed with approximately 100 stored ions at an operating temperature of 5.2 K using externally produced $^{84}Kr^+$ ions [183].

Up to now, SHIPTRAP-2 consists of a dedicated 4.7 T superconducting and actively shielded magnet that has been positioned perpendicular to the existing beam line of SHIPTRAP. The magnet was energized and shimmed in 2017. Its magnetic field was recently mapped and first cogitations regarding the ion optics, cooling infrastructure and traps have been made. In parallel, in cooperation with colleagues at TRIGA-TRAP (Mainz) and TRAPSENSOR (Granada, Spain), the feasibility for single-ion FT-ICR sensitivity using a quartz crystal as the inductance of a resonant circuit has been proven [187]. This is of practical importance, as quartz crystals are typically much smaller than the conventionally used coil resonators and

[2] If more than one ion is available, adjacent measurements with an averaging will increase the statistical precision.

do not require superconductivity in order to reach high quality factors. Special emphasis will be taken to reach single-ion sensitivity for superheavy elements at SHIPTRAP-2 in the upcoming years.

# Chapter 9

# Summary

Within the scope of this work, a cryogenic gas-stopping cell was implemented into the existing SHIPTRAP setup. Its performance with respect to efficiency and purity has been investigated by measuring the extracted charge-state distributions from recoil-ion sources positioned inside the active buffer-gas volume. The exchange of a AC/DC mixing board allowed extracting stopped and thermalized nobelium, lawrencium and rutherfordium isotopes as doubly-charged ions. These improvements increased the overall efficiency of the SHIPTRAP setup was improved from less than 0.5 % (in previous measurements at SHIPTRAP using ToF-ICR [68, 67, 69]) to about 5 %. This paves the way for the direct high-precision PTMS of even heavier and more exotic species.

Prior to this work, the heaviest directly measured isotope has been $^{256}$Lr, which at the same time corresponded to the most challenging experiment at SHIPTRAP back in 2010 [67, 69]. For almost 10 years, its production cross section of only 60 nb with a detection rate of 50 ions in 4 days defined the limit for high-precision PTMS. Back then, a relative uncertainty of $\delta m/m = 3 \times 10^{-7}$ was achieved using the conventional ToF-ICR method. In this work, the limits were pushed by an additional factor of four down to 15 nb. Additionally, by making use of high ion sensitivity, superior mass resolving power and high precision of the PI-ICR technique, the uncertainties of the atomic ground-state masses of $^{251,254}$No and $^{254-256}$Lr were reduced by up to two orders of magnitude reaching relative mass uncertainties as low as few $10^{-9}$. For the first time, the mass of a superheavy nuclide, namely $^{257}$Rf, has been determined directly and with high precision at a detection rate of only one detected ion per day with five ions in total. This currently represents the world record on the heaviest directly measured isotope with respect to high-precision PTMS. Mass resolving powers of up to 11 000 000 enabled resolving the isomeric states $^{251m}$No and $^{254m,255m}$Lr with excitation energies of down to 30 keV from their respective ground state. This allowed to directly determine their excitation energies unambiguously for the first time with uncertainties on the order of 1 keV. At the same time, this work in general proves the feasibility of PI-ICR at lowest rates and with a low overall number of detected ions and paves the way for PI-ICR as a complementary tool to decay spectroscopy to investigate nuclear structure of heavier and more exotic nuclides. Moreover, the PI-ICR method can also be applied to nuclides with long half-lives as they are predicted on and close to the island of stability.

# Chapter 10

# Appendices

## 10.1 Basics on Penning Traps

### 10.1.1 Ion Trapping

Spatial confinement of a particle within finite free space requires a three-dimensional potential $V(x, y, z)$ such that the resulting force on the particle

$$\vec{F}(x, y, z) \propto -\vec{\nabla} V(x, y, z) \tag{A10.1}$$

is always directed towards a local minimum. Electromagnetic potentials are suitable for this purpose and allow for the trapping of charged particles. Any local minimum can be approximated using a quadratic function. Therefore, a general electrostatic potential of the form

$$V(x, y, z) = Ax^2 + By^2 + Cz^2 \tag{A10.2}$$

in theory is feasible to create such a potential for coefficients $A > 0$, $B > 0$ and $C > 0$. However, in free space electromagnetic potentials have to satisfy the *Poisson's equation*

$$\Delta V(x, y, z) = 0 \tag{A10.3}$$

which leads to the condition $A + B + C = 0$ and the conclusion that no electrostatic potential possesses a minimum in all three dimensions. This is also known as *Earnshaw's theorem* (see e.g. [188]). Facing this challenge, over the past decades, several types of ion traps have been developed, among which the Paul and the Penning trap are the most common. For a more detailed description of the Paul trap, in particular in the context of mass spectrometry, the reader is referred to e.g. [189]. Paul traps make use of a fast oscillating electric quadrupole field. Depending on the charge-to-mass ratio of the ion, a spatial confinement can be achieved if the amplitude and frequency of the oscillating component is matched properly. Penning traps on the other hand make use of an electrostatic potential in combination with a superimposed strong magnetic field. The ion motion in a Penning trap is well understood and can be manipulated in various ways with highest accuracy, allowing to perform direct high-precision mass spectrometry on single-ion quantities. Penning traps in the context of mass spectrometry are discussed in the following section 10.1.2.

### 10.1.2 Penning Traps

The basics and a general description of Penning traps are found in the publication of Brown and Gabrielse [93]. Applying dc voltages to its electrodes, a Penning trap creates an electrostatic quadrupole field

$$\phi(x, y, z) \propto \left(2z^2 - x^2 - y^2\right). \tag{A10.4}$$

By comparing equation (A10.2) to (A10.4) one can see that $\phi(x, y, z)$ satisfies the conditions $A < 0$, $B < 0$ and $C > 0$. A particle with the electric charge $q$ experiences the electrostatic force $\vec{F}(x, y, z) = -q\vec{\nabla}\phi(x, y, z)$ and therefore a potential minimum in $z$-direction at $z = 0$, and a potential maximum in $x$- and $y$-direction at $x = y = 0$ in the case of $q > 0$. In this case, the charged particle is only confined in $z$-direction. In order to confine it in all three dimensions, the electrostatic quadrupole field is superimposed with a dipolar magnetic field

$$\vec{B} = B_0\vec{e}_z \tag{A10.5}$$

pointing in $z$-direction, where $B_0$ is the magnetic field strength. The *Lorentz force* in combination with the *centrifugal force* in this case ensures a confinement in $x$- and $y$-direction. An electrostatic quadrupole field is created by hyperbolical surfaces which correspond to the surface of equal potential from equation (A10.4). A hyperbolical Penning trap is shown in figure 10.1a. For the sake of simplicity we will define the $z$-direction to be the axial direction and the radial direction $r \equiv \sqrt{x^2 + y^2}$ to be in the $x$-$y$-plane perpendicular to the axial direction. In this case the electrostatic potential of a Penning trap is given by

$$\phi(r, z) = \frac{\tilde{C}_2 U_0}{4d^2}\left(2z^2 - r^2\right) \tag{A10.6}$$

where $d^2 = \frac{1}{2}(z_0^2 + r_0^2/2)$ denotes the characteristic trap dimension and $U_0$ corresponds to the voltage difference between the end-cap and ring electrode. $\tilde{C}_2$ is a dimensionless scaling factor on the order of 0.5 that depends solely upon the trap geometry. Alternatively a cylindrical Penning trap is used to create

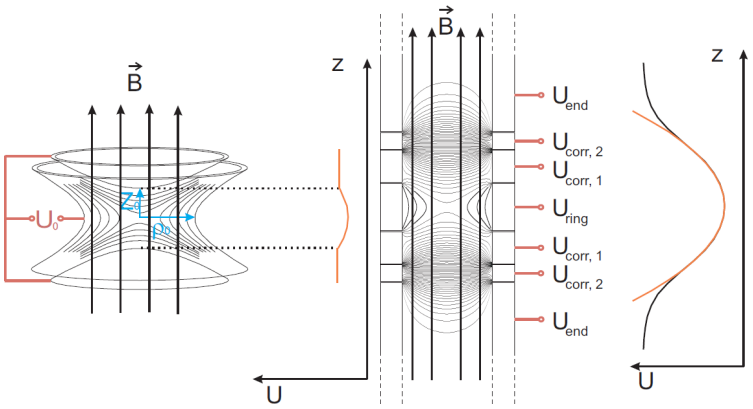


(a) hyperbolic Penning trap (b) cylindrical Penning trap

Figure 10.1: Schematic drawings of a hyperbolic (a) and cylindrical Penning trap (b). The electrostatic quadrupole field in axial direction is also shown. Both types consist of a ring and endcap electrodes. In the case of a cylindrical Penning trap correction electrodes have to be used for correction. Figures taken from [117]. For further details see text.

the required electrostatic quadrupole field (A10.6) (see figure 10.1b). However, in this case, additional correction electrodes are required to compensate for the non-equipotential surfaces of the electrodes. As noted before, the condition

$$qU_0 > 0 \tag{A10.7}$$

has to be fulfilled to trap a charged particle in axial direction. In the case of the cylindrical Penning traps of SHIPTRAP, $z_0 = 0.034\,\text{mm}$ and $r_0 = 0.016\,\text{mm}$ resulting in $d = 0.025\,\text{mm}$.

## 10.2 Recoil-Ion Sources

A suitable recoil-ion source at SHIPTRAP has to fulfil the following conditions:

- The recoil-ion source has to have a sufficient high recoil-ion rate which translates into a sufficient high activity of the mother nucleus. The SHIPTRAP experiment is designed to handle particle rates down to few ions per day. However, in order to ensure its functionality and characterize its performance in a suitable time frame higher ion rates are required. Thus, sources with activities of 100 Bq to 1 kBq are usually used although some characterizations require much higher activities in the order of 10 kBq, e.g. the calibration of some ion-sources themselves (see also section 4.2.1).

- The recoil-ion source has to have a suitable half-life. As these sources have to be produced, transported and inserted into the CGC, the half-life has to exceed at least few days. As an example, reaching cryogenic working conditions at the CGC after the installation of a new recoil-ion source requires about 3 days. In addition, a recoil-ion source is usually installed inside the CGC during on-line experiments to regularly check its performance. Therefore, as beam times can take up to several weeks, half-lives in the order of $> 1$ week are favoured.

- The recoil-ion source should not contain any impurities to not interfere with the high-pure buffer-gas environment of the CGC. This is usually realized by collecting the recoil ion on a sample holder in a clean gas environment. For this an $\alpha$-emitting mother with a suitable long half-life is required.

- The recoiling ion has to be an $\alpha$ emitter itself for the selective and sensitive detection. Only the extracted activity of the first recoiling daughter can be used to determine the extraction efficiency properly. In addition, the half-life of this isotope has to exceed the extraction time of the CGC of $\approx$ tens of milliseconds but at the same time being short enough to allow for fast measurements.

- The decay chain of the recoil ion must not contain any long-lived radioactive isotope. After its installation, the ion source experiences high-vacuum prior to the insertion of helium gas. This is necessary to ensure pure gas conditions at cryogenic temperatures. During the period of high vacuum, the recoiling ions are implanted approximately 20 nm deep[1] into the surrounding electrodes which corresponds to a contamination of the system. In addition, long-lived activity deposited on any of the detectors, especially the position-sensitive detector used for the mass measurements, has to be avoided.

- The $\alpha$ energies of the recoil mother and the recoil ion must not coincide, within statistical resolution, with similar $\alpha$ energies of the daughter nuclei or possible contaminants. Otherwise the source calibration in terms of its activity and the ion identification for efficiency measurements, respectively, are not possible. In addition, any of the $\alpha$ energies must not overlap with the $\alpha$ energies of the isotopes of interest in on-line experiments. To cross check production rates it can be required to identify successfully stopped and extracted EVRs via their characteristic $\alpha$-decay energy.

[1] Simulated using the SRIM code[119] for typical recoiling energies.

## 10.3 Discharges and Recovery Time of the CGC

A discharge inside the gas volume of the CGC will cause the gas volume to become impure as its plasma will ionize the buffer gas, including possible contaminants. In addition, atoms are sputtered off the surfaces at which the discharge happens. In the case of electrical dc fields, the breakdown voltage at which a discharge happens for a given pressure $p$ and gap length $d$ between two flat surfaces is given by the Paschen law [190]

$$V_B = \frac{B\,pd}{\ln(Apd) - \ln[\ln(1+\gamma_{\mathrm{se}}^{-1})]}, \tag{A10.8}$$

where $A$ and $B$ are empirically obtained values that depend upon the gas type and $\gamma_{\mathrm{se}}$ corresponds to a secondary-electron-emission coefficient. Figure 10.2 shows the Paschen curves for helium and argon gas as a function of the pressure and gap length for the case of room temperature and at cryogenic operation. As the breakdown voltage depends upon the gas density, the Paschen curves as a function of the pressure and gap length change depending upon the gas temperature. The values for the coefficients $A$, $B$ and $\gamma_{\mathrm{se}}$ for helium and argon are taken from [191] and [192], respectively. One has to mention that the Paschen law

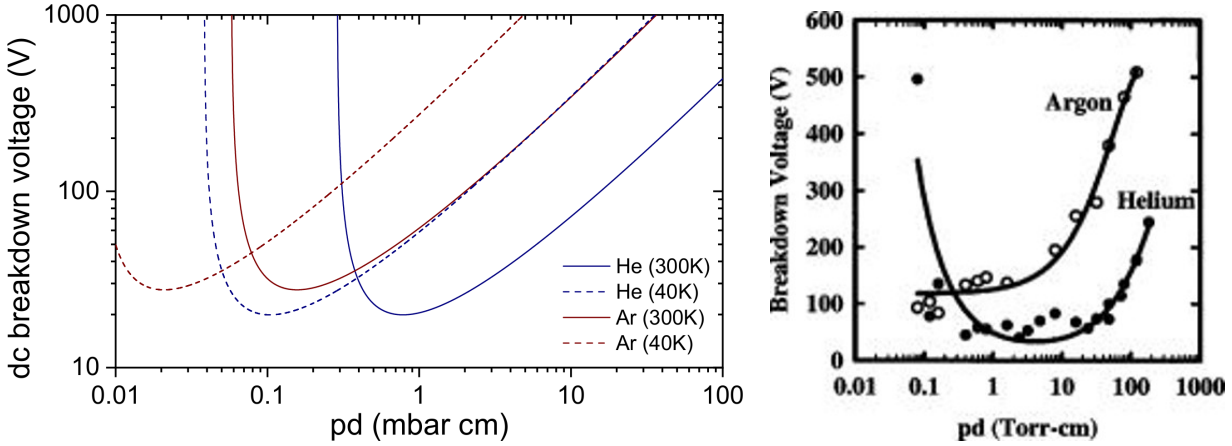


Figure 10.2: (Left figure) Paschen curves for helium and argon gas as a function of the pressure and gap length $pd$ for room temperature and 40 K. The latter was obtained by scaling the pressure according to the ideal gas law. (Right figure) Experimentally obtained data for the rf breakdown voltages for helium and argon gas as a function of the pressure and gap length $pd$ at room temperature. Figure taken from [193]. Note that 1 Torr equals 1.33 mbar.

presented in equation A10.8 only covers dc voltages. For the case of combined dc and rf fields models are thoroughly described in e.g. [194] and [195]. However, these models are not reliable in the pressure and gap length regimes of the CGC. Experimental data on the other hand are scarce and were only found in [193]. The data is shown in figure 10.2 and indicates that the rf voltage breakdown in the interesting pressure and gap length regime of the CGC is approximately a factor of two higher for argon when compared to helium. During operation, voltages have to be changed on a regular bases, e.g. in order to optimize settings. Ramping up or down voltages always increases or decreases the probability for a discharge to occur as one approaches or moves away from the Paschen minimum. Since the extraction efficiency strongly depends upon the purity, extraction efficiency drops close to zero after a discharge. For practical reasons it is therefore of great importance to quantize the recovery time, e.g. the time it takes for the CGC to go back to its initial purity and extraction efficiency. Thus, a discharge was created by applying a too high rf voltage to the funnel structure and the extraction efficiency was monitored. Figure 10.3 shows the obtained extraction efficiency as a function of the time passed after the discharge. At room temperature, approximately 80 min are required after a discharge at the funnel region to recover the nominal extraction efficiency of the GCG.

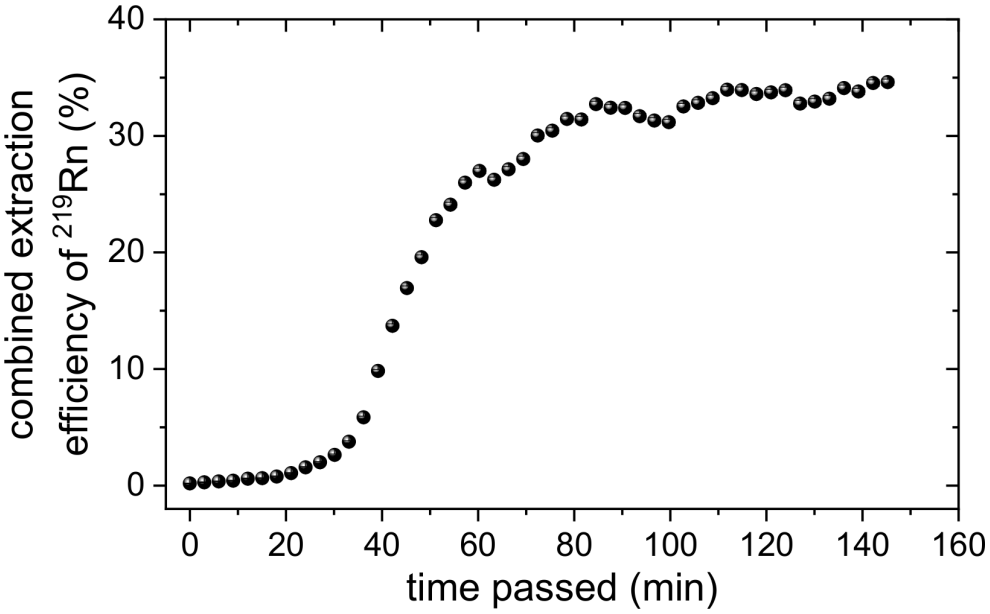


Figure 10.3: Combined extracted efficiency of $^{219}$Rn at the detector position D2 as a funtion of the time passed after a initialized discharge at the funnel electrodes. The discharge was caused by a rf funnel amplitude of approximately 120 $V_{pp}$ at room temperature. The exact position of the discharge within the funnel structure is unknown. The $^{223}$Ra ion source has an activity of 14 kBq and is positioned about 10 cm in front of the funnel rf structure. The statistical error bars are covered by the data points.

## 10.4 Stopping Efficiency Simulations

### 10.4.1 Stopping of Ions in Matter

The interaction of moving ions through matter is complex as it depends upon the atomic number, the charge state (distribution), the electron configuration (the electron cloud), polarizabilities and the relative velocity of the involved atoms and ions. In addition, these parameters are a function of the relative velocity itself and constantly change throughout the penetration as the ion constantly looses energy in collision processes [196, 119]. It is reasonable to divide the energy loss of an ion in matter into the losses to the heavy target nuclei (*nuclear stopping*), and to the target electrons (*electronic stopping*). The nuclear and electronic stopping forces (or stopping powers) NSTF($E$) and ESTF($E$), respectively, correspond to the energy loss of an ion penetrating a target per unit length -d$E$/d$x$. A detailed presentation on the theory of nuclear and electronic stopping forces is waived as it is not necessary for the upcoming discussions. For more details and an historic overview of the progress on these theories the interested reader is referred to, e.g., [196].

#### Nuclear Stopping

The theoretical description of the nuclear stopping is based on the Coulomb interaction between two charged point-particles (the incoming ion nucleus and the target atom nucleus) which are screened by their electron cloud. For this, various *interatomic potentials* can be proposed. In a simplified picture, an interatomic potential has the form

$$V = V_{\mathrm{nn}} + V_{\mathrm{en}} + V_{\mathrm{ee}} + V_{\mathrm{k}} + V_{\mathrm{a}}, \tag{A10.9}$$

where $V_{\mathrm{nn}}$ and $V_{\mathrm{ee}}$ correspond to the repulsive Coulomb potential between the two involved nuclei and electron clouds, respectively. The attractive potential $V_{\mathrm{en}}$ corresponds to an energy increase if the incoming ion nucleus penetrates into the electron cloud of the target atom. The two remaining contributions are due to quantum mechanics. $V_{\mathrm{k}}$ is the increase in kinetic energy of the electrons in the region of overlapping electron clouds due to the Pauli principle that forbids fermions to share the same quantum numbers (*Pauli excitation*). The *exchange energy* $V_{\mathrm{a}}$ arises because of a decrease in electron density for electrons sharing the same spin orientation (for a more detailed description see e.g. [196]). The nuclear stopping power is more dominant the lower the kinetic energy of the incident particle.

**Electronic Stopping**

The energy loss of an ion due to its interaction with the electrons of the penetrated material is complex since both the ion's and the target's electron configuration constantly change during the passage of the ion. The charge state of the penetrating ion continually changes depending on its velocity and the electron density of the target. The target electrons polarize in the vicinity of the ion which changes the electron density of the target electrons and the shape of the ion's electron cloud. As the Pauli principle forbids fermions to share the same set of quantum numbers, electrons are excited to higher energy levels when the electron clouds of the ion and the target atom merge. This effect is also known as *Pauli excitation*. In addition, band-gap effects of semiconductors give additional constraints on the available energy levels. Following this discussion, the complexity naturally increases for heavier ions as the number of electrons and electronic configurations increase.

**Total Stopping Force**

The total stopping power STF is given as the sum of the nuclear (NSTF) and the electronic stopping force (ESTF). Instead of the unit length, it is often more convenient to use the material type specific unit of areal density (mg/cm$^2$) which equals the unit of a length (m) but comprises the material type, e.g. its atomic number and its state of matter (i.e. gaseous or solid). The total stopping force in an arbitrary direction x

$$\mathrm{STF}(E) = -\frac{dE}{dx} = \mathrm{NSTF}(E) + \mathrm{ESTF}(E) \tag{A10.10}$$

equals the sum of both contributions. The total range of an ion in matter can thus be calculated by

$$R_{\mathrm{tot}} = \int_0^{E_0} \mathrm{STF}(E) dE, \tag{A10.11}$$

where $E_0$ correspond to the initial kinetic energy of the ion. Since the nature of such interactions is statistical, the number of collisions required to bring an incoming ion to rest will vary. This results into a variation of the total depth (stopping range) of the ion in matter, known as *straggling*. In addition, a lateral straggling also occurs due to momentum transfers in perpendicular direction with respect to the direction of the incoming ion.

In the non-relativistic limit the stopping force for an ion with kinetic energy $E$, mass $m$ and charge $Z_1$ can be estimated using the Bethe formula which is given by (see e.g. [42])

$$\mathrm{STF}(E) = \frac{2\pi n_e Z_1^2 m}{m_e E} \left(\frac{e^2}{4\pi\epsilon_0}\right)^2 \ln\left(\frac{4m_e E}{mI}\right). \tag{A10.12}$$

Here, $n_e \propto Z_2\rho_2/A_2$ equals the electron number density of the target material and $\epsilon_0 =$ corresponds to the

vacuum permittivity [146]. Note that this parameter is proportional to the atomic to mass number ratio $Z_2/A_2$ and the density $\rho_2$ of the target material for any value of $E$. The mean ionization potential of the material can be estimated by $I = (10\,\mathrm{eV}) \times Z_2$ for target materials with $Z_2 > 20$ [42].

Figure 10.4 shows the stopping powers as a function of the incident ion's kinetic energy for different ion and target elements. For $^{238}$U into C and PbS and kinetic energies above 25 MeV its stopping force STF($E$) is inverse proportional to its kinetic energy $E$. Equation (A10.13) implies an anti-proportional behaviour with respect to the target material density $\rho_2$. Thus, the assumption for can be approximated. Typical incident kinetic energies of the primary beam particles correspond to about 225 MeV to 250 MeV. EVRs have kinetic energies in the order of 30 MeV to 45 MeV. Thus,

$$\mathrm{STF}(E) \propto \frac{\rho_2}{E} \tag{A10.13}$$

is a good assumption and is used in section 10.4.4 to scale the stopping powers to elements heavier than uranium.

In the case of fusion-evaporation reactions, the incoming mid-heavy particle beam, typically $A \approx 50$ and $Z \approx 22$, has kinetic energies in the range of 4.5 MeV/u to 5.0 MeV/u which correspond to about 225 MeV to 250 MeV. At this energy, the ion stopping is entirely dominated by the electronic stopping power as seen in figure 10.4. For the case of the EVRs, the recoiling energies are on the order of 30 MeV to 50 MeV. At this energy, the electronic stopping power still dominates but as the ion is slowed down by the entrance window foil it transitions into an energy region where the nuclear stopping power takes over. Since there is no equivalent concept to extrapolate the nuclear stopping power to heavier elements than $Z > 92$, the nuclear stopping power in particular will be not well reflected by the SRIM simulation. Indeed, this was seen by D. Wittwer et al. [143] by comparing experimental stopping powers of nobelium ($Z = 102$) ions in a Mylar foil and argon gas with SRIM simulation applying the concept of effective charge. The simulated STF for nobelium in mylar of 26.89(58) MeV/(mg cm$^{-2}$) agrees well with the measured value of 24.83(35) MeV/(mg cm$^{-2}$) (about 5 % deviation), whereas the STF in argon gas is overestimated by 70 % (simulated STF of 17.7(18) MeV/(mg cm$^{-2}$) compared to a measured STF of 10.1(16) MeV/(mg cm$^{-2}$)). This is congruent with practical experience when designing gas-stopping cells for (super-)heavy ions in this energy range. In this occasions, the active gas volume of gas stopping cells is increased by about 50 % with respect to the SRIM simulation estimates. This compensates for the overestimation of SRIM simulation on stopping powers in gaseous materials. Thus, all the following simulations are run with gas pressures of 30 mbar to 70 mbar (room-temperature equivalent densities) which, taking this overestimation into account, corresponds to about 50 mbar to 100 mbar of operational pressure.

### 10.4.2 SRIM Software

SRIM is a software package dedicated to the Stopping and Range of Ions in Matter [119]. It includes a semi-empirical Monte Carlo code based on a binary collision model which was parametrized using experimental data. It adopts an effective charge for the projectile and calculates the average charge state in matter using the Ziegler-Biersack-Littmar model [197]. After several improvements over the last decades, SRIM is able to reproduce the stopping powers of about 25 000 experimental data points with an overall accuracy of better than 4 %. An overview of different models and programs is found in [198].

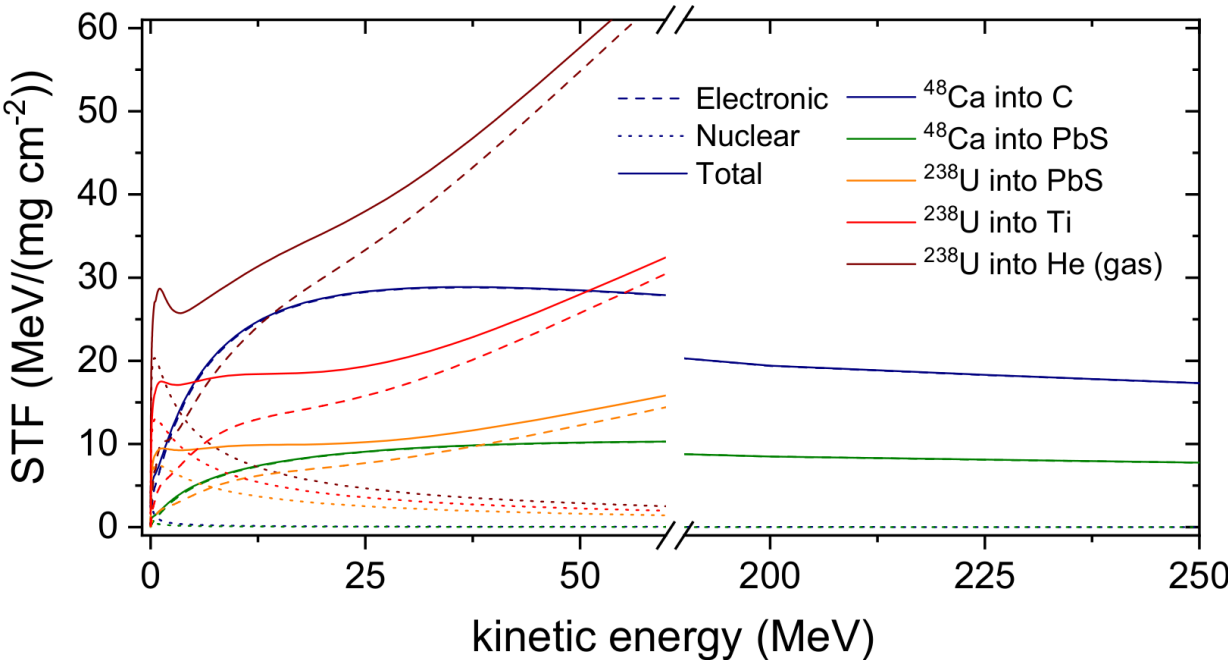


Figure 10.4: Electronic, nuclear and total stopping powers as a function of the penetrating ion's kinetic energy. Shown are values for $^{48}$Ca and $^{238}$U ions penetrating through various target materials. Data taken from SRIM [119].

SRIM does not deal with atomic species above uranium ($Z = 92$) because no experimental data are available in this region and therefore theoretical models cannot be tested. In addition, the relatively broad ion charge distribution, peaked around 22+ [89], for these heavy elements reflects *uncharted territory* when it comes to simulations using SRIM [199]. Nonetheless SRIM offers a great opportunity to estimate and optimize the entrance window foil material, its thickness and the buffer gas type and its density for a variety of EVRs if projectile parameters are adjusted accordingly to represent the stopping of heavier ions. Furthermore, it has been proven that these simulations are consistent with experimentally obtained stopping efficiencies from previous experiments [118].

Within the scope of this work thousands of individual simulations have been performed with a total of millions of single ions. Such large number of simulated events has been produced running the SRIM code in *batch mode* using a POWERSHELL script. The latter allows to iterate the SRIM simulations progressively, over a given range of parameters, e.g. ion energies, entrance window thicknesses and buffer-gas densities. An exemplary script is presented in Appendix 10.5.

### 10.4.3 General Procedure

A similar evaluation of the obtained stopping efficiencies is already presented by the author's work in [118]. SRIM outputs the three-dimensional position of every stopped ion which we denote in the following as $\vec{r}_{\mathrm{ion}} = (x_{\mathrm{ion}}, y_{\mathrm{ion}}, z_{\mathrm{ion}})$. With no loss of generality the x-direction is set as the depth or axial position of the ion whereas the y- and z-direction represent the lateral direction. The position $x = 0$ correspond to the beginning of the first target layer, in this case the entrance window foil. By superimposing the geometry of the CGC the number of ions that were stopped in different regimes is evaluated, e.g. inside the entrance window foil or the active gas volume to obtain the stopping efficiency. The geometrical extension of the CGC is presented in table 10.2. In the case of $x_{\mathrm{ion}} \leq d_{\mathrm{foil}}$ the ion was stopped inside the entrance window

foil and is lost for any extraction. For the case of

$$d_{\text{foil}} < x_{\text{ion}} \leq (d_{\text{foil}} + d_{\text{cage}} + d_{\text{gap}}) \text{ with } \sqrt{y_{\text{ion}}^2 + z_{\text{ion}}^2} \leq r_{\text{cage}} \tag{A10.14}$$

the ion is considered to be stopped inside the active gas volume of the dc cage. Note that the volume corresponding to the gap region is also accounted for this. For

$$(d_{\text{foil}} + d_{\text{cage}} + d_{\text{gap}}) < x_{\text{ion}} \leq (d_{\text{foil}} + d_{\text{cage}} + d_{\text{gap}} + d_{\text{funnel}}) \tag{A10.15}$$

with

$$\sqrt{y_{\text{ion}}^2 + z_{\text{ion}}^2} \leq (r_{\text{funnel}}^{\text{min}} - r_{\text{funnel}}^{\text{max}})(x_{\text{ion}} - (d_{\text{foil}} - d_{\text{cage}} - d_{\text{gap}}))d_{\text{funnel}}^{-1} + r_{\text{funnel}}^{\text{max}} \tag{A10.16}$$

the ion is stopped inside the active gas volume of the funnel rf region. The total number of successfully stopped ions, i.e. inside the active volume of the CGC, is the sum of the ions for which equation (A10.14) and (A10.15) (together with (A10.16)) holds, respectively. This number divided by the total amount of simulated ions gives the simulated stopping efficiency for the given set of parameters.

The simulated stopping efficiencies are a function of the entrance window foil's type, i.e. atomic number ($Z_{\text{foil}}$), and its thickness $t_{\text{foil}}$ as well as the buffer-gas element ($Z_{\text{gas}}$) and its density $\rho_{\text{gas}}^{\text{RTE}}$. Note that the CGC operates at cryogenic temperatures and that the following densities are always given as room-temperature equivalent (RTE). For a given set of the parameters for the CGC, a SRIM simulation with 1000 ions is performed for three incident ion energies $E_{\text{kin}}$ to represent the kinetic energy distribution of the ions (see 10.5). This is mandatory due to the energy loss of the primary beam particle and the EVR, respectively, in the target material (this will be discussed in more detail in section 10.4.5). For simplicity we summarize these parameters

$$\epsilon_{\text{stop}}^{\text{SRIM}}(E_{\text{kin}}, Z_{\text{foi}}, t_{\text{foil}}, Z_{\text{gas}}, \rho_{\text{gas}}^{\text{RTE}}) \equiv \epsilon_{\text{stop}}^{\text{SRIM}}(E_{\text{kin}}, set). \tag{A10.17}$$

For any *set* of parameters, the three obtained extraction efficiencies are fitted using a quadratic function (figure 10.5). The simulated mean stopping efficiency is then given by the mean of the fitted function

$$\bar{\epsilon}_{\text{stop}}^{\text{SRIM}}(set) = (E_{\text{max}} - E_{\text{min}})^{-1} \int_{E_{\text{min}}}^{E_{\text{max}}} (a_2 x^2 + a_1 x + a_0)\, dx, \tag{A10.18}$$

where $a_0$, $a_1$ and $a_2$ correspond to the fit parameters and $E_{\text{min}}$ and $E_{\text{max}}$ denote the lowest and highest energy value that was used for the simulation of this set of parameters. This procedure is exemplary shown in figure 10.5. It makes sense to directly implement the incident energy distribution of the incoming ion into the batch-mode script. However, changing the incident particle's kinetic energy requires to restart the SRIM software which significantly increases the simulation time and thus is impractical.

### 10.4.4 Simulation and Ion Parameters

#### Suitable Number of Ions

One of the first issues that has to be addressed when Monte Carlo methods are applied, is the choice of the minimum number of iterations needed for a particular simulation to get a sufficient confidence level. In the case of SRIM this is translated to the question, how many events (ions) should be simulated for a given set of parameters (window foil type and thickness and buffer gas type and density) to ensure a valid

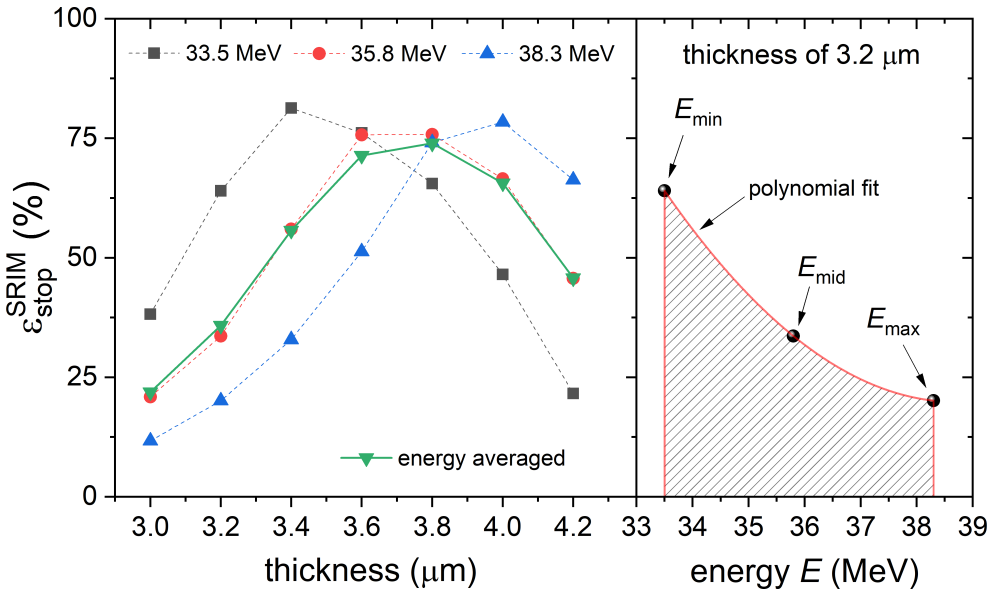


Figure 10.5: (Left figure) Simulated stopping efficiencies of $^{238}$U as a function of the titanium entrance window foil thickness for the incident kinetic energies 33.5 MeV ($E_{\mathrm{min}}$), 35.8 MeV ($E_{\mathrm{mid}}$) and 38.3 MeV ($E_{\mathrm{max}}$) at a room-temperature equivalent buffer-gas density of 50 mbar. The energies correspond to the *uncorrected* recoil energies for $^{254}$No produced at the beginning, in the mid and at the end of the target, respectively. In addition, the energy-averaged stopping efficiency is shown which is obtained by the areal mean of the polynomial fitted distribution. This is exemplary shown for the case of a foil thickness of 3.2 μm (right figure). For further details see text.

representation of the stopping distribution and thus the stopping efficiency for this particular set of data. As computing time is limited and hundreds of different parameter sets have to be simulated, one wants to choose the lowest number possible. Depending on the set of parameters, a simulation with 10 000 ions usually takes 1.5 to 3 hours on an Intel(R) Core(TM) i5-3320M CPU with 2.60 GHz running on one core. However, multiple SRIM simulations can be run in parallel on different cores.

Figure 10.6 shows the evaluation of 200 successive simulations for two different sets of parameters. It is well seen that the simulated efficiencies are normally distributed around their peak value. Thus, we can evaluate the standard deviation

$$\sigma(N) = \sqrt{(n-1)^{-1}\sum_{i=1}^{n}(x_i - \bar{x})^2} = \frac{\mathrm{FWHM}}{2\sqrt{2\ln 2}} \quad \text{where} \quad \bar{x} = n^{-1}\sum_{i=1}^{n} x_i, \tag{A10.19}$$

as a function of the number of ions $N$ to probe the accuracy in the representation of the stopping efficiency for a given set of parameters. Here, $x_i$ represents the simulated stopping efficiency of the $i^{\mathrm{th}}$ simulation with $n$ simulations in total. Figure 10.6 shows the obtained stopping efficiencies for three different sets of parameters. In this case, the simulations were performed at a helium gas pressure of 50 mbar with a kinetic energy of the uranium ions of 37 MeV. The entrance window foil (titanium) was changed to reflect the different regimes of the simulations where ions are predominantly stopped at the end of the active gas volume (entrance window foil thickness of 3.0 μm), close after the entrance window foil (3.6 μm) and inside the entrance window foil (4.2 μm), respectively. As the ion number $N$ increases, the scattering of the data points converge into a standard deviation of less than 1 % for ≥ 1000 ions. A good compromise between computation time and accuracy are simulations with about 1000 ions. Here, the 99.7 % confidence band ($3\sigma$-deviation) as well as the maximum deviation is well below 5 % (absolute) with respect to the obtained stopping efficiency.

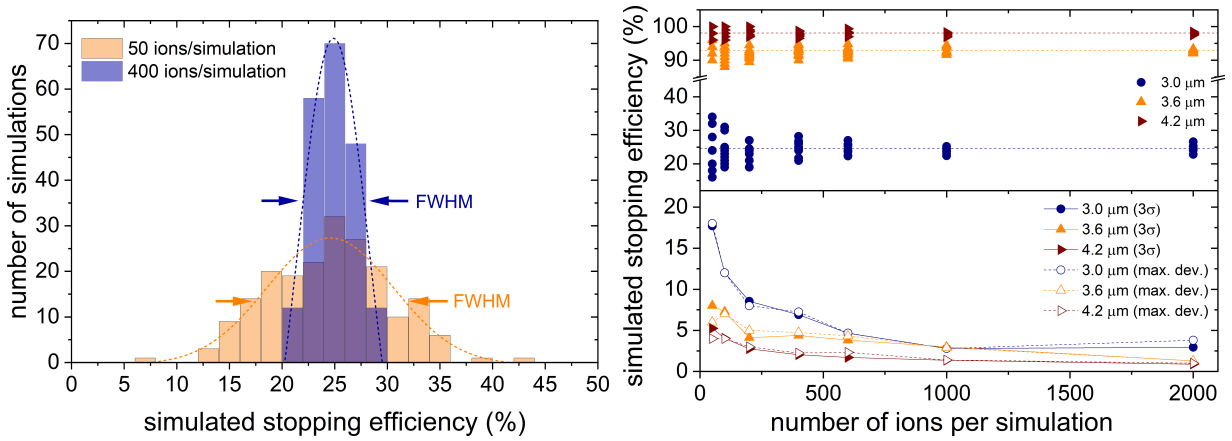


Figure 10.6: (Left figure) Distribution of 200 simulated stopping efficiencies using SRIM for a fixed set of parameters for 50 and 400 ions per simulation, respectively. The data is well described by a Gaussian distribution (dotted lines). The FWHM of the distribution decreases for an increased number of simulated ions.(Right figure) Evaluation of the 99.7 %-confidence level ($3\sigma$) and the maximum deviation (max.dev.) between single simulations as a function of ions per simulation. 10 simulations per data point are used and the number of ions per simulation is varied from 50 to 2000. In addition, the evaluation is performed for three entrance window foil thicknesses. For further details see text.

**Simulations with $Z > 92$**

The highest atomic number available for SRIM is 92, uranium. Hence, to be able to simulate heavier elements it is necessary to choose an ion with properties such that it resembles the supposed behaviour of heavier elements in the energy region and material of interest. However, as discussed in section 10.4.1, there is no theory that can describe the stopping of ions on a fundamental level. Present theories have semi-empirical parameters that were benchmarked on available experimental data which is almost non-existing for elements heavier than uranium. In addition, the typical recoil ion energies of the heavy elements are usually in the range where both, electronic and nuclear stopping, becomes equally strong which adds difficulty to a representative description. Thus, even rough estimations on stopping powers for ions with $Z > 92$ have to be worked out with care. One concept to model the stopping powers for heavy ions was introduced by L. C. Northcliffe [200] by introducing an effective charge

$$(\gamma Z_1)^2 = \frac{\mathrm{STF}(E, Z_1, Z_2)}{\mathrm{STF}(E, 1, Z_2)}, \tag{A10.20}$$

of the penetrating ion with atomic number $Z_1$, where $\mathrm{STF}(E, Z_1, Z_2)$ corresponds to its stopping power at the kinetic energy $E$ in a material with atomic number $Z_2$. It is normalized to the stopping power of a proton ($Z_1 = 1$) penetrating the same material at the same kinetic energy. This concept emerged from the idea that the $Z_1^2$-term in the Bethe theory (see equation A10.12) can simply be replaced by an effective charge $(\gamma Z_1)^2$ reflecting a screened point charge in its so-called *charge equilibrium* [200, 201]. Based on a relation given by J. F. Ziegler et al. [197], in the work of D. Wittwer et al. [143] the effective charge fraction was instead normalized to the stopping power of uranium:

$$\mathrm{STF}(E, Z_1, Z_2) = \left( \frac{q_{\mathrm{eff}}^{\mathrm{EVR}}}{q_{\mathrm{eff}}^{\mathrm{U-238}}} \right)^2 \times \mathrm{STF}(E, 92, Z_2). \tag{A10.21}$$

Here, $q_{\mathrm{eff}}^{\mathrm{EVR}}$ and $q_{\mathrm{eff}}^{\mathrm{U}}$ are the effective charges of the penetrating ion and uranium, respectively. In the non-relativistic case they can be calculated using

$$q_{\mathrm{eff}} = \sqrt{1 - \exp(-v_1/v_{\mathrm{TF}})} Z_1 e \tag{A10.22}$$

with the so-called *Thomas-Fermi velocity* $v_{\mathrm{TF}} = Z_1^{2/3} \alpha_{\mathrm{fs}} c_0$ [202]. Here, $v_1 = \sqrt{2E/m}$ correspond to the non-relativistic kinetic velocity of the incident particle. In more convenient units, the effective charge in units of the elementary charge $e$ can be calculated using

$$q_{\mathrm{eff}}[e] = \left(1 - \exp\left(-6.35 \times \sqrt{E[\mathrm{MeV}]/m[\mathrm{u}]/Z_1^{2/3}}\right)\right)^{0.5} \times Z_1 \tag{A10.23}$$

where the vacuum speed of light $c_0 = 299792458$ m/s and the fine-structure constant $a_{\mathrm{fs}} = 1/137$ were used, respectively. The effective charges for uranium and the EVRs of interest are shown in figure 10.7 as a function of the kinetic energy. In addition, the square of the effective charge ratio from equation (A10.21) is shown. Table 10.1 summarizes the values that are used in the simulations. In SRIM stopping powers

Table 10.1: Squares of the effective charge ratios for the EVRs of interest with respect to uranium.

| | $^{251}$No | $^{254}$No | $^{254}$Lr | $^{255}$Lr | $^{256}$Lr | $^{257}$Rf | $^{258}$Db |
|---|---|---|---|---|---|---|---|
| $(q_{\mathrm{eff}}^{\mathrm{EVR}}/q_{\mathrm{eff}}^{\mathrm{U-238}})^2$ | 1.12 | 1.11 | 1.12 | 1.12 | 1.12 | 1.14 | 1.15 |

cannot be modified. There are two options to scale the stopping powers of the EVRs according to equation A10.21. As a first-order approximation for low kinetic energies, the stopping power is both, proportional to the target density and inverse proportional to the ion's kinetic energy (see equation (A10.13)). Thus, the density can be scaled with $(q_{\mathrm{eff}}^{\mathrm{EVR}}/q_{\mathrm{eff}}^{\mathrm{U-238}})^2$ and the energy with its inverse to resemble the stopping of the corresponding EVR.

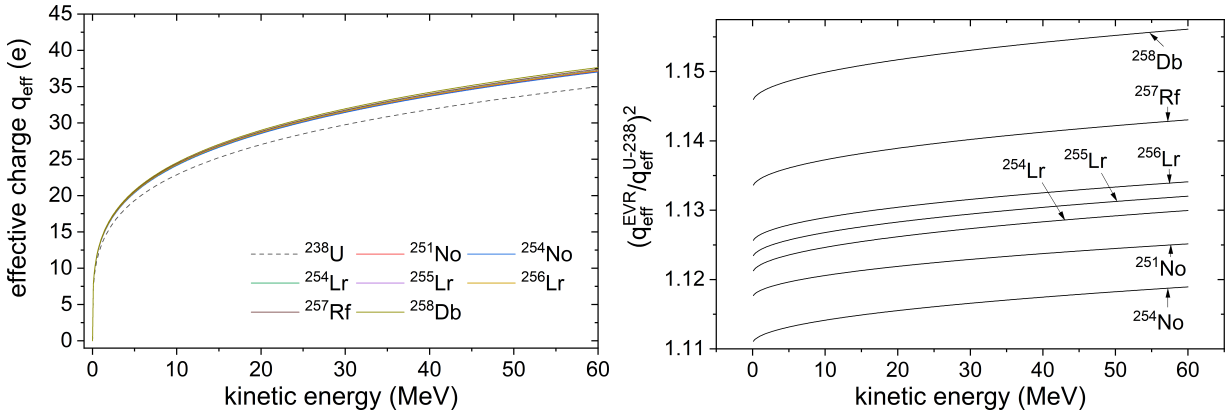


Figure 10.7: (Left figure) Effective charge of the isotopes of interest as a function of its kinetic energy as given by equations (A10.22) and (A10.23), respectively. (Right figure) Square of the effective charge ratio of the ion of interest with respect to $^{238}$U. This parameter is used as a scaling factor according to equation (A10.21).

### Realistic Beam Profiles

SRIM does not allow for a spatial distribution of the incoming particles. All ions enter the material axially or with a fixed incoming angle. However, simulations have shown that spatial distributions (as presented in the work of F. Lautenschläger *et al.* [144]) for typical beam profiles at SHIP can be neglected with respect to simulations for the CGC.

### 10.4.5 Input Parameters

#### Geometry of the CGC

The geometry of the CGC has been presented elsewhere, for instance in the work of O.,Kaleja [118]. However, the values used in this work differ slightly. They are summarized in table 10.2.

Table 10.2: Geometric dimensions of the CGC that define the active volume of the buffer-gas volume from which ions can be extracted. The dimensions are taken from technical drawings of the CGC and thus vary slightly from the ones used in [118].

| | $d_{\text{foil}}$ | $d_{\text{cage}}$ | $r_{\text{cage}}$ | $d_{\text{gap}}$ | $d_{\text{funnel}}$ | $r_{\text{funnel}}^{\text{max}}$ | $r_{\text{funnel}}^{\text{min}}$ |
|---|---|---|---|---|---|---|---|
| dimension (mm) | variable | 212 | 140 | 38 | 130.5 | 133.5 | 2.75 |

#### Recoil Energy of the EVRs

The kinetic recoil energy of the EVRs can be calculated using energy and momentum conservation. For complete-fusion reactions at Coulomb barrier energies, non-relativistic calculations are sufficient. For a target at rest, the recoil energy of an EVR is given by

$$E_{\text{EVR}} = \left(\frac{E_{\text{CN}}}{m_{\text{CN}}}\right) \times m_{\text{EVR}} \quad \text{with} \quad \frac{E_{\text{CN}}}{m_{\text{CN}}} = \left(\frac{m_{\text{proj}}}{m_{\text{proj}} + m_{\text{target}}}\right)^2 \times \left(\frac{E_{\text{proj}}}{m_{\text{proj}}}\right), \tag{A10.24}$$

where $m_{\text{EVR}}$, $m_{\text{CN}}$, $m_{\text{proj}}$ and $m_{\text{target}}$ are the EVRs, the compound nucleus', the projectile and target mass, respectively. The incoming kinetic energy of the projectile is given by $E_{\text{proj}}$. The neutron evaporation is assumed to be isotropic. Since $m_{\text{CN}} \approx m_{\text{proj}} + m_{\text{target}}$ equation (A10.24) can be approximated by

$$E_{\text{EVR}} \approx \frac{m_{\text{proj}} m_{\text{EVR}}}{m_{\text{CN}}^2} \times E_{\text{proj}}. \tag{A10.25}$$

As an example, $^{254}$No from the $^{208}$Pb($^{48}$Ca,2n)-reaction at a primary beam energy of 4.55 MeV/u has a kinetic recoil energy of 40.6 MeV behind the target production wheel. According to section 10.4.3 the primary beam particle as well as the EVR experiences an energy loss due to the target foil material. This has to be taken into account and is discussed in the following section.

#### Energy Loss through the Production Target

The target materials used in the fusion-evaporation reactions at SHIP are typically supported by additional thin carbon foils, both on the front and rear faces of the target, to increase its mechanical stability. Additionally, a charge-exchange foil is placed about 15 cm behind the production target. The latter is used to compensate for any changes in the charge state of the EVRs by radiation, e.g. internal transitions. SHIP is a velocity filter and its separation capability thus does not depend upon the charge state. However, the ion optics required to focus the EVRs through SHIP are charge-dependent. Charge states that are too far away from the *nominal* charge-state distribution will have a decreased transmission efficiency through SHIP. Table 10.3 presents the target compositions used at SHIP to produce the isotopes of interest $^{251,254}$No, $^{254-256}$Lr and $^{257}$Rf. In addition, the target composition for the production of $^{258}$Db is shown. The fusion-evaporation reactions occur within the PbS and $Bi_2O_3$ layer, respectively.

Since the stopping power depends upon the mass and atomic number of the moving ion (see equation (A10.12)), the energy loss through the target changes according to the position where the fusion-

Table 10.3: Target compositions used to produce the fusion-evaporation reaction products $^{251,254}$No, $^{254-256}$Lr and $^{257}$Rf. The same PbS target is used to produce $^{254}$No and $^{257}$Rf. The same applies to the $Bi_2O_3$ target used for the production of $^{254-256}$Lr and $^{258}$Db. Changing the isotope of interest in these cases requires to change the primary beam energy and particle type, respectively. For further details see text.

| | target composition | | | | charge exchange foil |
|---|---|---|---|---|---|
| fusion-evaporation reaction | C | PbS | $Bi_2O_3$ | C | C |
| | $\mu g/cm^2$ | | | | |
| $^{206}$Pb($^{48}$Ca,3n)$^{251}$No | 38 | 396 | | 10 | |
| $^{208}$Pb($^{48}$Ca,2n)$^{254}$No | 42 | 478 | | 10 | |
| $^{209}$Bi($^{48}$Ca,3n)$^{254}$Lr | | | | | |
| $^{209}$Bi($^{48}$Ca,2n)$^{255}$Lr | 44 | | 463 | 10 | 30 |
| $^{209}$Bi($^{48}$Ca,1n)$^{256}$Lr | | | | | |
| $^{208}$Pb($^{50}$Ti,1n)$^{257}$Rf | 42 | 478 | | 10 | |
| $^{209}$Bi($^{50}$Ti,1n)$^{258}$Db | 44 | | 463 | 10 | |

evaporation reaction takes place. As an example, if the $^{208}$Pb($^{48}$Ca,2n)$^{254}$No reaction takes place right at the beginning of the target material layer (PbS), the calcium ion only experienced an energy loss throughout the first carbon foil. The resulting nobelium ion will then have to pass through all the remaining foil depths. In contrast, if the reaction occurs at the end, the nobelium ion only has to penetrate through the remaining two carbon foils. Since the stopping powers of calcium and nobelium in the material differ, the resulting recoil energy of the nobelium is different in both examples. For the simulation the cases of a reaction at the beginning, half the depth and the end of the target material is considered. Thus, three different simulations are performed. The energy difference is at most on the order of 5-7 MeV between these cases which changes the simulated stopping efficiency tremendously as presented in figure 10.5. Therefore, as discussed in section 10.4.3, an averaged stopping efficiency is obtained by taking all three cases into account. As discussed in section 10.4.4, the stopping power of $^{238}$U is taken and scaled according to equation (A10.21) to evaluate the energy loss of the heavy ions. In the case of the primary beam particle, the tabulated values from the SRIM software [119] are used. The stopping powers for any ion in the molecular compound material PbS and $Bi_2O_3$ in unkown. Thus the density-weighted stopping powers of the compounds are used for calculation. Table 10.4 summarizes the recoil energies used for the SRIM simulations. For comparison reasons the simulation are performed in three different manners. As discussed in section 10.4.4 the EVRs are represented as $^{238}$U ions. The kinetic energies are always calculated using the kinematics from equation (A10.25), taking the mass numbers of the EVRs into account. In so-called *uncorrected* simulations, the stopping powers of $^{238}$U ions in the target material are used. As the stopping powers for heavier elements tend to be higher, these kinetic energies are overestimated and thus the stopping in the CGC will be underestimated. Thus, in the case of *density corrected* simulations, the stopping power of $^{238}$U in the target foil material is scaled using the effective charge ratios from table 10.1. Here, the densities of the titanium entrance window foil as well as the buffer-gas is scaled. As discussed with respect to equation (A10.13), for the incident energies of interest, the energy can be scaled instead of the target material density. Thus, the simulations are run without any density scaling and instead the incident particle energy is scaled up by the effective charge ratio. For the evaluation of the optimal entrance window foil thickness the *density corrected* and *energy corrected* simulations will be taken into account.

The production cross section of any fusion-evaporation reaction depends upon the primary beam energy and thus changes as a function of target depth. However, the energy loss is on the order of few MeV (compared to an overall kinetic energy of about 230 MeV) throughout the target such that the production cross section can be assumed to be constant throughout the target (as an example, the excitation function for $^{253-255}$No are shown in figure 3.1). In addition, the stopping power is a function of the particles energy

Table 10.4: Calculated recoil energies of EVRs for a fusion-evaporation reaction taking place at the beginning ($E_{\mathrm{min}}$), the mid ($E_{\mathrm{mid}}$) and at the end of the target material layer ($E_{\mathrm{max}}$). In all cases the energy loss of the primary particle was calculated using the tabulated stopping powers of SRIM. In addition, in all cases, the kinematics are calculated using equation (A10.25). The *uncorrected* values are obtained by taking into account the stopping power of $^{238}$U in the target material. The *density corrected* values scale the energy loss of $^{238}$U in the target using the effective charge ratio for the corresponding isotope from table 10.1. The *energy corrected* values are obtained by scaling the *uncorrected* values using the effective charge ratio. For details see text.

| EVR | primary beam energy (MeV/u) | recoil energy (MeV) uncorrected | | | density corrected | | | energy corrected | | |
|---|---|---|---|---|---|---|---|---|---|---|
| | | $E_{\mathrm{min}}$ | $E_{\mathrm{mid}}$ | $E_{\mathrm{max}}$ | $E_{\mathrm{min}}$ | $E_{\mathrm{mid}}$ | $E_{\mathrm{max}}$ | $E_{\mathrm{min}}$ | $E_{\mathrm{mid}}$ | $E_{\mathrm{max}}$ |
| $^{251}$No | 4.8 | 36.40 | 38.47 | 40.67 | 35.42 | 37.76 | 40.23 | 31.53 | 33.61 | 35.80 |
| $^{254}$No | 4.56 | 33.47 | 35.81 | 38.29 | 32.67 | 35.29 | 38.04 | 29.40 | 31.76 | 34.23 |
| $^{254}$Lr | 4.81 | 35.52 | 37.77 | 40.16 | 34.65 | 37.19 | 39.88 | 30.84 | 33.10 | 35.49 |
| $^{255}$Lr | 4.56 | 33.69 | 35.85 | 38.14 | 32.84 | 35.28 | 37.86 | 29.23 | 31.40 | 33.70 |
| $^{256}$Lr | 4.5 | 33.38 | 35.50 | 37.77 | 32.53 | 34.94 | 37.49 | 28.96 | 31.10 | 33.37 |
| $^{257}$Rf | 4.65 | 37.20 | 39.70 | 42.35 | 36.15 | 39.02 | 42.02 | 31.81 | 34.34 | 36.98 |
| $^{258}$Db | 4.72 | 38.08 | 40.42 | 42.85 | 36.99 | 39.70 | 42.50 | 32.18 | 34.54 | 36.97 |

and thus also varies throughout the target material. However, also the stopping power can be assumed to be constant throughout the target (see also figure 10.4). For a fixed projectile energy both assumptions will result in a uniform energy distribution of the EVRs behind the target that will be taken into account in the simulation in section 10.4.3.

## 10.5 SRIM Script

SRIM-BATCH is an exemplary POWERSHELL script which executes SRIM in the so-called *batch mode* by changing the parameters defined in SRIM-TEMPLATE. In this particular example $^{238}$U ions penetrate two subsequent target material layers. The first layer is composed of $^{22}$Ti and has an attributed thickness ranging from 3.0 µm to 4.8 µm in steps of 0.2 µm. The subsequent layer consists of helium gas at room-temperature equivalent pressures of 30, 50 and 70 mbar (the layer is set arbitrary large to stop any incoming ion). The incident kinetic energy of the $^{238}$U ions range from 37200 keV to 42350 keV. A total of 1000 ions are simulated for each set of parameters and their positions after stopping are recorded. The evaluation of the stopping efficiency is performed in a separate step using a different software.

### SRIM-BATCH

```
#Set-ExecutionPolicy Bypass -Scope Process
#Set-ExecutionPolicy remotesigned

#INPUT VALUES
$N = 1000 #number of ions to simulate
$Energies = 37200, 39700, 42350, 31810, 34340, 36980, 38080, 40420, 42850, 32180, 34540, 36970
$Thicknesses = 3.0, 3.2, 3.4, 3.6, 3.8, 4.0, 4.2, 4.4, 4.6, 4.8 #foil thickness (micro-m)
$Pressures = 30, 50, 70 #gas pressures (mbar
#$Energies = 32500, 33500, 34500, 35500, 36500, 37500 #incoming particle energy (keV)
#$Thicknesses = 3.0, 3.1, 3.2, 3.3, 3.4, 3.5, 3.6, 3.7, 3.8, 3.9, 4.0, 4.1, 4.2 #foil thickness (micro-m)
#$Pressures = 30, 35, 40, 45, 50, 55, 60, 65, 70, 75, 80, 85, 90, 95 #gas pressures (mbar)
function Gas-Density{
param([double]$pressure)
[double]$pressure*0.0001787*0.001 #claculate from atmospheric gas density
}

#DEFINING WORKING PATH AS PATH OF CURRENT SCRIPT FILE
```

```
function Get-ScriptDirectory {
    if ($psise) {Split-Path $psise.CurrentFile.FullPath}
    else {$global:PSScriptRoot}
}
$currentPath = Get-ScriptDirectory
cd $currentPath
write-host $currentPath

#PROVIDE INFORMATION ABOUT SIMULATION
$nbr_simulations = $Energies.Length*$Thicknesses.Length*$Pressures.Length #how many simulations in total
$current_nbr = 1

#LOOP STARTS HERE
foreach($Energy in $Energies){
    foreach($Thickness in $Thicknesses){
        foreach($Pressure in $Pressures){

write-host "... running simulation number $current_nbr ($nbr_simulations in total)."
$current_nbr = $current_nbr+1

#LOAD TEMPLATE FILE AND MODIFY CONTENT
$inputData = Get-Content .\TRIM_template_TiHe.txt
$inputData[2] = "92 238.051 $Energy 0 $N 1 $N" #change line 2 to current values
$random_seed = get-random -minimum 0 -maximum 999999999
$inputData[4] = "1 $random_seed 0" #change line 4 (random number seed)
$Tconv=$Thickness*10000 #foil thickness in Angstrom
$inputData[16] = "1 ""Foil"" $Tconv 4.5189 1 0" #change line 16 to current values
[double]$Density = Gas-Density -pressure $Pressure #gas density calculation
$DensityConv = '{0:f10}' -f $Density | foreach {$_.replace(",",".") } #gas density formatting
$inputData[17] = "2 ""Gas"" 20000000000 $DensityConv 0 1" #change line 17 to current values

#WRITE TRIM.IN FILE
Set-Content .\'TRIM.IN' -Value $inputData

#RUN TRIM.exe
.\TRIM.exe | Out-Null

#COPY OUTPUT/OTHER FILES AND RENAME
Copy-Item .\'SRIM Outputs'\RANGE_3D.txt -Destination .\'_MY OUTPUTS' {Recurse #THIS IS WHAT YOU ANALYZE
Copy-Item .\TRIM.IN -Destination .\'_MY OUTPUTS'\'INPUT FILES' {Recurse #to retrace simulation
$ThicknessString = $Thickness.ToString("0.0") | foreach {$_.replace(",",".") } #format foil thickness
$PressureString = $Pressure.ToString("000") #format pressure
Rename-Item .\'_MY OUTPUTS'\RANGE_3D.txt -NewName $Energy'keV'$ThicknessString'um'$PressureString'mbar'$N'ions.txt' -Force
Rename-Item .\'_MY OUTPUTS'\'INPUT FILES'\TRIM.IN -NewName $Energy'keV'$ThicknessString'um'$PressureString'mbar'$N'ions.IN' -Force

        }
    }
}
write-host "DONE!"
```

# SRIM-TEMPLATE

```
==> SRIM-2013.00 This file controls TRIM Calculations.
Ion: Z1 ,  M1,  Energy (keV), Angle,Number,Bragg Corr,AutoSave Number.
    92 238.051       38000       0      10        1        5
Cascades(1=No;2=Full;3=Sputt;4-5=Ions;6-7=Neutrons), Random Number Seed, Reminders
                     1                                    0       0
Diskfiles (0=no,1=yes): Ranges, Backscatt, Transmit, Sputtered, Collisions(1=Ion;2=Ion+Recoils), Special EXYZ.txt file
                          1       0           0       0               0                                0
Target material : Number of Elements & Layers
"U (38000) into Foil+Gas                 "       2               2
PlotType (0-5); Plot Depths: Xmin, Xmax(Ang.) [=0 0 for Viewing Full Target]
       5                         0    2.000003E+10
Target Elements:    Z   Mass(amu)
Atom 1 = Ti =       22    47.9
Atom 2 = He =        2   4.003
Layer   Layer Name /               Width Density    Ti(22)   He(2)
Numb.   Description                (Ang) (g/cm3)    Stoich  Stoich
 1      "Foil"           37999.9995231628  4.5189       1       0
```

```
 2      "Gas"           20000000000  .00000894       0       1
0  Target layer phases (0=Solid, 1=Gas)
0 1
Target Compound Corrections (Bragg)
 1   1
Individual target atom displacement energies (eV)
      25       5
Individual target atom lattice binding energies (eV)
       3       1
Individual target atom surface binding energies (eV)
    4.89       2
Stopping Power Version (1=2011, 0=2011)
 0
```

## 10.6 Buncher Impurities

In section 5.3 the detected ion rate of isotopes seem to depend upon the overall measurement cycle time of the PI-ICR measurement, which defines the time of the ions spent in the buncher RFQ. To quantify the ion losses in the bunching process, the detected ratios of the recoil ions $^{211}Pb^{2+}$ and $^{219}Rn^{2+}$ are evaluated as a function of the buncher storage time. Typical buncher storage times are in the order of 400 ms to 2000 ms depending upon the desired mass resolving power and precision of the mass measurements, respectively. The obtained data is shown in figure 10.8. Note that $^{219}Rn$ has a half-life of about 4 s [103] which contributes to a certain amount of loss due to the natural decay. Suppose an additional loss mechanism in the buncher with an attributed decay constant $\lambda_{\mathrm{bun}}$. In this case, the probability for an ion to be lost in the buncher is given by $e^{-\lambda_{\mathrm{bun}}t}$. Due to the finite half-life of the involved isotopes, the combined probability that an ion is found after a given time t is calculated as

$$p(t) = e^{-\lambda_{\mathrm{bun}}t} \times e^{-\lambda t} = e^{-(\lambda_{\mathrm{bun}}+\lambda)t}, \tag{A10.26}$$

where $\lambda$ corresponds to the natural decay constant of the isotope. As the recoil ion source continuously emits ions the extracted ion rate after a buncher storage time $T$ is expressed as

$$\dot{n}_{\mathrm{bun}}(T) = \frac{A_0}{T}\int_0^T p(t)dt = T^{-1}\frac{A_0}{\lambda_{\mathrm{bun}}+\lambda}\left(1 - e^{-(\lambda_{\mathrm{bun}}+\lambda)T}\right), \tag{A10.27}$$

where equation (A10.26) has been used. $A_0$ is a proportionality factor. For half-lives much longer than the buncher storage time $\lambda T \ll 1$ and $(\lambda_{\mathrm{bun}} + \lambda) \approx \lambda_{\mathrm{bun}}$, then equation (A10.27) reduces to

$$\dot{n}_{\mathrm{bun}}(T) = T^{-1}\frac{A_0}{\lambda_{\mathrm{bun}}}\left(1 - e^{-\lambda_{\mathrm{bun}}T}\right). \tag{A10.28}$$

In this case the loss of extracted ion rate is solely given by the loss mechanism in the buncher. Equations (A10.27) and (A10.28) are now fitted to the data points presented in figure 10.8. In this way, the loss mechanism with its attributed decay constant $\lambda_{\mathrm{bun}}$ can be evaluated independently of any finite half-life.

The more intuitive value $\tau = \ln(2)/\lambda_{\mathrm{bun}}$, which corresponds to the time in which half the ion rate is lost due do the loss mechanism in the buncher, is evaluated. As seen in figure 10.8, the obtained values for $^{211}Pb^{2+}$ and $^{219}Rn^{2+}$ are $\tau = 390(40)$ ms and $\tau = 91(10)$ ms, respectively. The difference between both ion species arise from the difference in their ionization potential and thus implies a loss due to charge-transfer and ion chemistry, respectively. It explains the difference in the obtained ion rates for $^{254}No^{2+}$ with respect to different measurement cycle times. In section 5.3 a loss of about 25 % to 50 % is seen for a change in the accumulation time from below 100 ms to 1200 ms. This corresponds to buncher storage times of 400 ms and 1500 ms, respectively. In the case of $^{211}Pb^{2+}$ (which has a similar second ionization potential as $^{254}No^{2+}$) a drop in the extracted ion rate of about 50 % is seen.

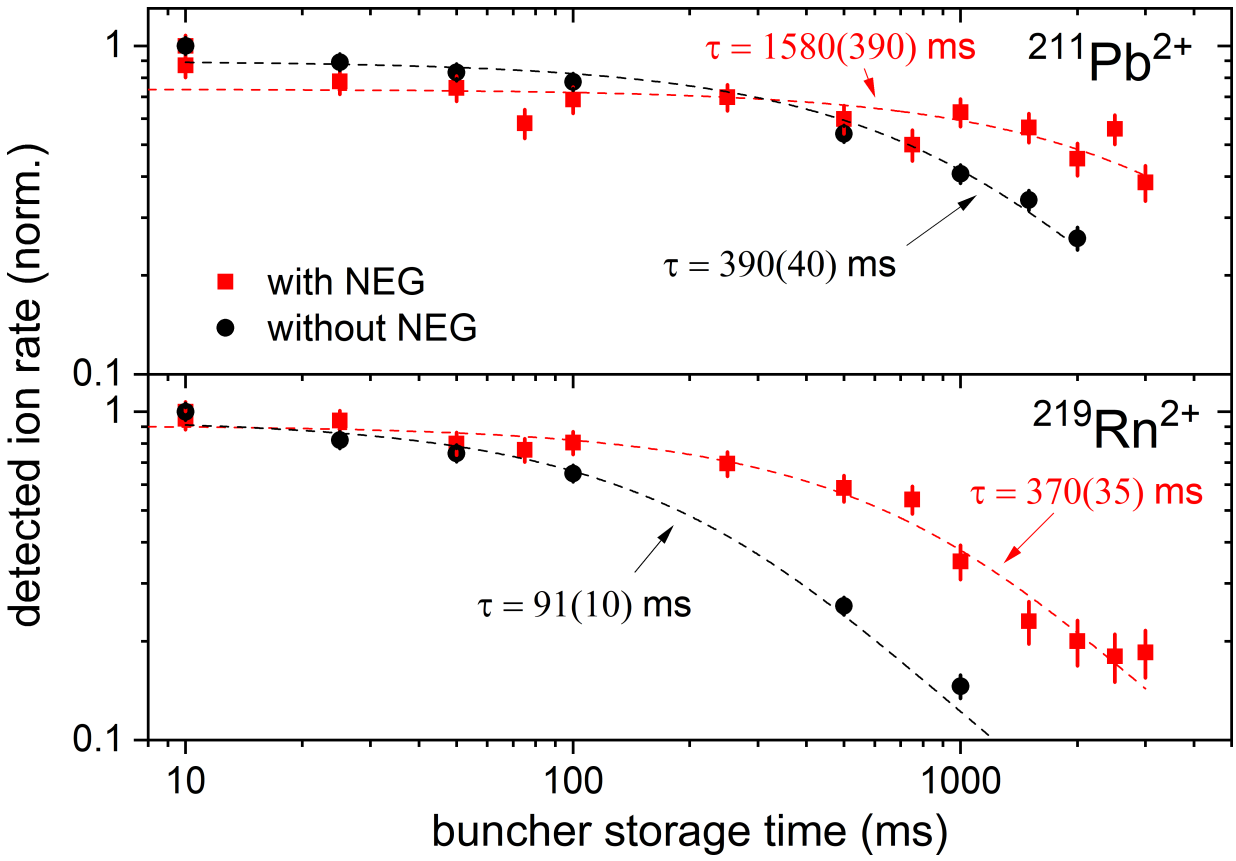


Figure 10.8: Detected ion rates at the time-of-flight detector positioned at D3 for $^{211}Pb^{2+}$ and $^{219}Rn^{2+}$ ions as a function of the buncher storage time. The buncher operated at a helium buffer-gas pressure of $1.25 \times 10^{-3}$ mbar at an amplitude of 100 $V_{pp}$. The fit curves are given by equation (A10.27. For further details see text.

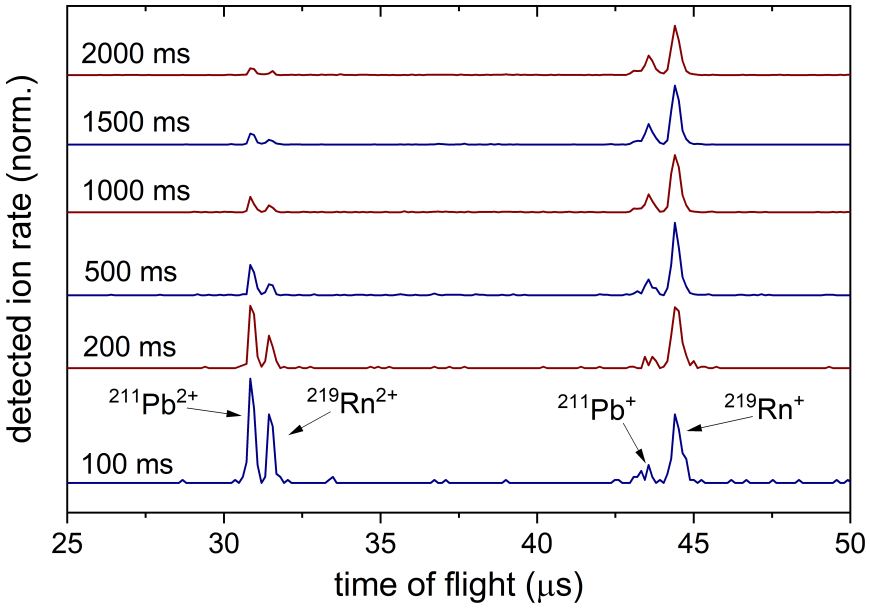


Figure 10.9: Extracted time-of-flight spectra from a $^{223}Ra$ recoil ion source positioned inside the buffer-gas volume of the CGC on-axis about 10 cm in front of the funnel structure for different buncher storage times. The helium gas pressure and temperature of the CGC are 7 mbar and 40 K, respectively. The parameters for the buncher are identical to the ones stated in figure 10.8 (without NEG pump). For details see text.

The question remains what kind of loss mechanism the ions experience during bunching. To answer qualitatively the entire time-of-flight spectra for different bunching storage times is evaluated in figure

10.9. Here, ion loss for the doubly-charged state distributions is clearly visible for an increasing buncher storage time. No molecular formation is seen and only a minor potion of the doubly-charges states are transferred into single-charged states. Thus it is assumed that the ions neutralize entirely due to collisions with contaminants in the buffer-gas environment. The buncher typically operates at helium buffer-gas pressures of about $1 \times 10^{-3}$ mbar at room temperature. Possible contaminations in the buffer-gas are argon (Ar), nitrogen ($N_2$) and hydrogen ($H_2$). Thus a non-evaporable getter (NEG) pump has been installed at the buncher section recently. After its installation the detected ion rate of $^{211}Pb^{2+}$ and $^{219}Rn^{2+}$ were re-evaluated and are in addition shown in figure 10.8. Indeed, a severe reduction in the ion loss rate is observed. The $^{211}Pb^{2+}$ ions now survive approximately 4 times longer.

# Bibliography


[1] Yu. Ts. Oganessian, V. K. Utyonkov, Yu. V. Lobanov, F. Sh. Abdullin, A. N. Polyakov, R. N. Sagaidak, I. V. Shirokovsky, Yu. S. Tsyganov, A. A. Voinov, G. G. Gulbekian, S. L. Bogomolov, B. N. Gikal, A. N. Mezentsev, S. Iliev, V. G. Subbotin, A. M. Sukhov, K. Subotic, V. I. Zagrebaev, G. K. Vostokin, M. G. Itkis, K. J. Moody, J. B. Patin, D. A. Shaughnessy, M. A. Stoyer, N. J. Stoyer, P. A. Wilk, J. M. Kenneally, J. H. Landrum, J. F. Wild, and R. W. Lougheed. Synthesis of the isotopes of elements 118 and 116 in the $^{249}$Cf and $^{245}$Cm+$^{48}$Ca fusion reactions. *Physical Review C*, 74(4), oct 2006.

[2] R. V. Gentry, T. A. Cahill, N. R. Fletcher, H. C. Kaufmann, L. R. Medsker, J. W. Nelson, and R. G. Flocchini. Evidence for Primordial Superheavy Elements. *Physical Review Letters*, 37(1):11–15, jul 1976.

[3] W. Wolfli, J. Lang, G. Bonani, M. Suter, Ch. Stoller, and H.-U. Nissen. Evidence for primordial superheavy elements? *Journal of Physics G: Nuclear Physics*, 3(2):L33–L37, feb 1977.

[4] S. Hofmann, F. P. Heßberger, D. Ackermann, S. Antalic, P. Cagarda, S. Ćwiok, B. Kindler, J. Kojouharova, B. Lommel, R. Mann, G. Münzenberg, A. G. Popeko, S. Saro, H. J. Schött, and A. V. Yeremin. The new isotope $^{270}$110 and its decay products $^{266}$Hs and $^{262}$Sg. *The European Physical Journal A*, 10(1):5–10, feb 2001.

[5] A. Einstein. Ist die Trägheit eines Körpers von seinem Energieinhalt abhängig? *Annalen der Physik*, 18(639), 1905.

[6] M. Block. Direct mass measurements of the heaviest elements with Penning traps. *International Journal of Mass Spectrometry*, 349–350:94 – 101, 2013. 100 years of Mass Spectrometry.

[7] M. Block. Direct mass measurements of the heaviest elements with Penning traps. *Nuclear Physics A*, 944:471–491, dec 2015.

[8] S. Eliseev, K. Blaum, M. Block, C. Droese, M. Goncharov, E. Minaya Ramirez, D. A. Nesterenko, Yu. N. Novikov, and L. Schweikhard. Phase-Imaging Ion-Cyclotron-Resonance Measurements for Short-Lived Nuclides. *Physical Review Letters*, 110(8), feb 2013.

[9] S. Eliseev, K. Blaum, M. Block, A. Dörr, C. Droese, T. Eronen, M. Goncharov, M. Höcker, J. Ketter, E. Minaya Ramirez, D. A. Nesterenko, Yu. N. Novikov, and L. Schweikhard. A phase-imaging technique for cyclotron-frequency measurements. *Applied Physics B*, 114(1-2):107–128, sep 2013.

[10] G. Bollen, S. Becker, H.-J. Kluge, M. König, R. B. Moore, T. Otto, H. Raimbault-Hartmann, G. Savard, L. Schweikhard, and H. Stolzenberg. ISOLTRAP: a tandem Penning trap system for accurate on-line mass determination of short-lived isotopes. *Nuclear Instruments and Methods in Physics Research Section A: Accelerators, Spectrometers, Detectors and Associated Equipment*, 368(3):675–697, jan 1996.

[11] International Energy Agency. Steep decline in nuclear power would threaten energy security and climate goals. 2019-05-28. Retrieved 2019-07-08.

[12] P. M. Walker and G. Dracoulis. Energy traps in atomic nuclei. *Nature*, 399(6731):35–40, may 1999.

[13] L. von der Wense, B. Seiferle, M. Laatiaoui, J. B. Neumayr, H.-J. Maier, H.-F. Wirth, C. Mokry, J. Runke, K. Eberhardt, Ch. E. Düllmann, N. G. Trautmann, and P. G. Thirolf. Direct detection of the $^{229}$Th nuclear clock transition. *Nature*, 533(7601):47–51, may 2016.

[14] S. Goriely, N. Chamel, and J. M. Pearson. Further explorations of Skyrme-Hartree-Fock-Bogoliubov mass formulas. XII. Stiffness and stability of neutron-star matter. *Physical Review C*, 82(3), sep 2010.

[15] S. Goriely, S. Hilaire, M. Girod, and S. Péru. First Gogny-Hartree-Fock-Bogoliubov Nuclear Mass Model. *Physical Review Letters*, 102(24), jun 2009.

[16] P. Moller, J. R. Nix, W. D. Myers, and W. J. Swiatecki. Nuclear Ground-State Masses and Deformations. *Atomic Data and Nuclear Data Tables*, 59(2):185–381, mar 1995.

[17] W. D. Myers and W. J. Swiatecki. Nuclear properties according to the Thomas-Fermi model. *Nuclear Physics A*, 601(2):141–167, may 1996.

[18] K. Pomorski and J. Dudek. Nuclear liquid-drop model and surface-curvature effects. *Physical Review C*, 67(4), apr 2003.

[19] J. K. L. MacDonald. Successive Approximations by the Rayleigh-Ritz Variation Method. *Physical Review*, 43(10):830–833, may 1933.

[20] J. Duflo and A. P. Zuker. Microscopic mass formulas. *Physical Review C*, 52(1):R23–R27, jul 1995.

[21] H. Koura, T. Tachibana, M. Uno, and M. Yamada. Nuclidic Mass Formula on a Spherical Basis with an Improved Even-Odd Term. *Progress of Theoretical Physics*, 113(2):305–325, feb 2005.

[22] N. Wang, Z. Liang, M. Liu, and X. Wu. Mirror nuclei constraint in nuclear mass formula. *Physical Review C*, 82(4), oct 2010.

[23] N. Wang, M. Liu, X. Wu, and J. Meng. Surface diffuseness correction in global mass formula. *Physics Letters B*, 734:215–219, jun 2014.

[24] M. Liu, N. Wang, Y. Deng, and X. Wu. Further improvements on a global nuclear mass model. *Physical Review C*, 84(1), jul 2011.

[25] A Sobiczewski and Yu. A. Litvinov. Quality of theoretical masses in various regions of the nuclear chart. *Physica Scripta*, T154:014001, may 2013.

[26] A. Sobiczewski and Yu. A. Litvinov. Accuracy of theoretical descriptions of nuclear masses. *Physical Review C*, 89(2), feb 2014.

[27] S. Liran, A. Marinov, and N. Zeldes. Semiempirical shell model masses with magic number $Z = 126$ for superheavy elements. *Physical Review C*, 62(4), sep 2000.

[28] A. Sobiczewski and K. Pomorski. Description of structure and properties of superheavy nuclei. *Progress in Particle and Nuclear Physics*, 58(1):292–349, jan 2007.

[29] F. W. Aston. Bakerian Lecture. A New Mass-Spectrograph and the Whole Number Rule. *Proceedings of the Royal Society A: Mathematical, Physical and Engineering Sciences*, 115(772):487–514, aug 1927.

[30] F. W. Aston. A second-order focusing mass spectrograph and isotopic weights by the doublet method. *Proceedings of the Royal Society of London. Series A - Mathematical and Physical Sciences*, 163(914):391–404, dec 1937.

[31] A. S. Eddington. The Internal Constitution of the Stars. *Nature*, 106(2653):14–20, sep 1920.

[32] D. Mendeleev. Ueber die Beziehung der Eigenschaften zu den Atomgewichten der Elemente. *Zeitschrift fuer Chemie*, 12:405, 1986.

[33] J. Erler, N. Birge, M. Kortelainen, W. Nazarewicz, E. Olsen, A. M. Perhac, and M. Stoitsov. The limits of the nuclear landscape. *Nature*, 486(7404):509–512, jun 2012.

[34] F. W. Aston. XLIV. the constitution of atmospheric neon. *The London, Edinburgh, and Dublin Philosophical Magazine and Journal of Science*, 39(232):449–455, apr 1920.

[35] J. Chadwick. The Existence of a Neutron. *Proceedings of the Royal Society A: Mathematical, Physical and Engineering Sciences*, 136(830):692–708, jun 1932.

[36] B. Fricke, W. Greiner, and J. T. Waber. The continuation of the periodic table up to $Z = 172$. The chemistry of superheavy elements. *Theoretica Chimica Acta*, 21(3):235–260, sep 1971.

[37] P. Pyykkö. A suggested periodic table up to $Z \leq 172$, based on Dirac–Fock calculations on atoms and ions. *Phys. Chem. Chem. Phys.*, 13(1):161–168, 2011.

[38] P. Indelicato, J. Bieroń, and P. Jönsson. Are MCDF calculations 101% correct in the super-heavy elements range? *Theoretical Chemistry Accounts*, 129(3-5):495–505, jan 2011.

[39] M. Wang, G. Audi, F. G. Kondev, W. J. Huang, S. Naimi, and X. Xu. The AME2016 atomic mass evaluation (II). tables, graphs and references. *Chinese Physics C*, 41(3):030003, mar 2017.

[40] C. F. v. Weizsäcker. Zur Theorie der Kernmassen. *Zeitschrift fuer Physik*, 96(7-8):431–458, jul 1935.

[41] A. H. Wapstra. Atomic Masses of Nuclides. In *Encyclopedia of Physics / Handbuch der Physik*, pages 1–37. Springer Berlin Heidelberg, 1958.

[42] T. Mayer Kuckuk. *Kernphysik*, volume 6. Teubner Verlag, 1994.

[43] G. Audi, O. Bersillon, J. Blachot, and A. H. Wapstra. The Nubase evaluation of nuclear and decay properties. *Nuclear Physics A*, 729(1):3–128, dec 2003.

[44] M. Dworschak. *First direct mass measurements on nobelium and lawrencium with the Penning trap mass spectrometer SHIPTRAP*. PhD thesis, Johannes Gutenberg-Universität Mainz, 2009.

[45] M. G. Mayer. On Closed Shells in Nuclei. II. *Physical Review*, 75(12):1969–1970, jun 1949.

[46] O. Haxel, J. Hans D. Jensen, and H. E. Suess. On the "Magic Numbers" in Nuclear Structure. *Physical Review*, 75(11):1766–1766, jun 1949.

[47] The Nobel Prize in Physics 1963. NobelPrize.org. Nobel Media AB 2019. Tue. 6 Aug 2019.

[48] R. D. Woods and D. S. Saxon. Diffuse Surface Optical Model for Nucleon-Nuclei Scattering. *Physical Review*, 95(2):577–578, jul 1954.

[49] K. S. Krane and D. Halliday. *Introductory Nuclear Physics. Second Edition.* JohnWiley & Sons, 1987.

[50] H. Schüler and Th. Schmidt. über Abweichungen des Atomkerns von der Kugelsymmetrie. *Zeitschrift für Physik*, 94(7-8):457–468, jul 1935.

[51] Y. Shi, J. Dobaczewski, and P. T. Greenlees. Rotational properties of nuclei around $^{254}$No investigated using a spectroscopic-quality Skyrme energy density functional. *Physical Review C*, 89(3), mar 2014.

[52] W. D. Myers and W. J. Swiatecki. Nuclear masses and deformations. *Nuclear Physics*, 81(1):1–60, jun 1966.

[53] V. M. Strutinsky. Shell effects in nuclear masses and deformation energies. *Nuclear Physics A*, 95(2):420–442, apr 1967.

[54] V. M. Strutinsky. "shells" in deformed nuclei. *Nuclear Physics A*, 122(1):1–33, dec 1968.

[55] T. H. R. Skyrme. The effective nuclear potential. *Nuclear Physics*, 9(4):615–634, jan 1958.

[56] D. Vautherin and D. M. Brink. Hartree-Fock Calculations with Skyrme Interaction. I. Spherical Nuclei. *Physical Review C*, 5(3):626–647, mar 1972.

[57] D. Vautherin. Hartree-Fock Calculations with Skyrme Interaction. II. Axially Deformed Nuclei. *Physical Review C*, 7(1):296–316, jan 1973.

[58] M. Bender, W. Nazarewicz, and P.-G. Reinhard. Shell stabilization of super- and hyperheavy nuclei without magic gaps. *Physics Letters B*, 515(1-2):42–48, aug 2001.

[59] J. Dobaczewski, H. Flocard, and J. Treiner. *Nucl. Phys.*, A422(103), 1984.

[60] E. Chabanat, P. Bonche, P. Haensel, J. Meyer, and R. Schaeffer. *Nucl. Phys.*, A643(441(E)), 1998.

[61] P.-G. Reinhard and H. Flocard. Nuclear effective forces and isotope shifts. *Nuclear Physics A*, 584(3):467–488, feb 1995.

[62] G. A. Lalazissis, J. König, and P. Ring. New parametrization for the Lagrangian density of relativistic mean field theory. *Physical Review C*, 55(1):540–543, jan 1997.

[63] M. Bender, K. Rutz, P.-G. Reinhard, J. A. Maruhn, and W. Greiner. Shell structure of superheavy nuclei in self-consistent mean-field models. *Physical Review C*, 60(3), aug 1999.

[64] R.-D. Herzberg, P. T. Greenlees, P. A. Butler, G. D. Jones, M. Venhart, I. G. Darby, S. Eeckhaudt, K. Eskola, T. Grahn, C. Gray-Jones, F. P. Hessberger, P. Jones, R. Julin, S. Juutinen, S. Ketelhut, W. Korten, M. Leino, A.-P. Leppänen, S. Moon, M. Nyman, R. D. Page, J. Pakarinen, A. Pritchard, P. Rahkila, J. Sarén, C. Scholey, A. Steer, Y. Sun, Ch. Theisen, and J. Uusitalo. Nuclear isomers in superheavy elements as stepping stones towards the island of stability. *Nature*, 442(7105):896–899, aug 2006.

[65] M. Hult, J. S. E. Wieslander, G. Marissens, J. Gasparro, U. Wätjen, and M. Misiaszek. Search for the radioactivity of $^{180m}$Ta using an underground HPGe sandwich spectrometer. *Applied Radiation and Isotopes*, 67(5):918–921, may 2009.

[66] F. P. Heßberger, S. Hofmann, D. Ackermann, S. Antalic, B. Kindler, I. Kojouharov, P. Kuusiniemi, M. Leino, B. Lommel, R. Mann, K. Nishio, A. G. Popeko, B. Sulignano, S. Saro, B. Streicher, M. Venhart, and A. V. Yeremin. Alpha-gamma decay studies of $^{255}$Rf, $^{251}$No and $^{247}$Fm. *The European Physical Journal A*, 30(3):561–569, dec 2006.

[67] M. Block, D. Ackermann, K. Blaum, C. Droese, M. Dworschak, S. Eliseev, T. Fleckenstein, E. Haettner, F. Herfurth, F. P. Heßberger, S. Hofmann, J. Ketelaer, J. Ketter, H.-J. Kluge, G. Marx, M. Mazzocco, Yu. N. Novikov, W. R. Plaß, A. Popeko, S. Rahaman, D. Rodríguez, C. Scheidenberger, L. Schweikhard, P. G. Thirolf, G. K. Vorobyev, and C. Weber. Direct mass measurements above uranium bridge the gap to the island of stability. *Nature*, 463(7282):785–788, feb 2010.

[68] M. Dworschak, M. Block, D. Ackermann, G. Audi, K. Blaum, C. Droese, S. Eliseev, T. Fleckenstein, E. Haettner, F. Herfurth, F. P. Heßberger, S. Hofmann, J. Ketelaer, J. Ketter, H.-J. Kluge, G. Marx, M. Mazzocco, Yu. N. Novikov, W. R. Plaß, A. Popeko, S. Rahaman, D. Rodríguez, C. Scheidenberger, L. Schweikhard, P. G. Thirolf, G. K. Vorobyev, M. Wang, and C. Weber. Penning trap mass measurements on nobelium isotopes. *Physical Review C*, 81(6), jun 2010.

[69] E. M. Ramirez, D. Ackermann, K. Blaum, M. Block, C. Droese, C. E. Dullmann, M. Dworschak, M. Eibach, S. Eliseev, E. Haettner, F. Herfurth, F. P. Hessberger, S. Hofmann, J. Ketelaer, G. Marx, M. Mazzocco, D. Nesterenko, Y. N. Novikov, W. R. Plass, D. Rodriguez, C. Scheidenberger, L. Schweikhard, P. G. Thirolf, and C. Weber. Direct Mapping of Nuclear Shell Effects in the Heaviest Elements. *Science*, 337(6099):1207–1210, aug 2012.

[70] G. Münzenberg, W. Faust, S. Hofmann, P. Armbruster, K. Güttner, and H. Ewald. The velocity filter SHIP, a separator of unslowed heavy ion fusion products. *Nuclear Instruments and Methods*, 161(1):65–82, apr 1979.

[71] W. Barth, W. Bayer, L. Dahl, L. Groening, S. Richter, and S. Yaramyshev. Upgrade program of the high current heavy ion UNILAC as an injector for FAIR. *Nuclear Instruments and Methods in Physics Research Section A: Accelerators, Spectrometers, Detectors and Associated Equipment*, 577(1-2):211–214, jul 2007.

[72] S. Eliseev, K. Blaum, M. Block, S. Chenmarev, H. Dorrer, Ch. E. Düllmann, C. Enss, P. E. Filianin, L. Gastaldo, M. Goncharov, U. Köster, F. Lautenschläger, Yu. N. Novikov, A. Rischka, R. X. Schüssler, L. Schweikhard, and A. Türler. Direct measurement of the mass difference of $^{163}$Ho and $^{163}$Dy solves the $Q$-value puzzle for the neutrino mass determination. *Physical Review Letters*, 115(6), aug 2015.

[73] E. Minaya Ramirez. An investigation of the Accuracy of the PI-ICR Technique at SHIPTRAP by a Measurement of the Mass Difference between $^{132}$Xe and $^{131}$Xe. In *Proceedings of the Conference on Advances in Radioactive Isotope Science (ARIS2014)*. Journal of the Physical Society of Japan, jun 2015.

[74] P. Filianin, S. Schmidt, K. Blaum, M. Block, S. Eliseev, F. Giacoppo, M. Goncharov, F. Lautenschlaeger, Yu. Novikov, and K. Takahashi. The decay energy of the pure s-process nuclide $^{123}$Te. *Physics Letters B*, 758:407–411, jul 2016.

[75] R. Orford, J.A. Clark, G. Savard, A. Aprahamian, F. Buchinger, M.T. Burkey, D.A. Gorelov, J.W. Klimes, G.E. Morgan, A. Nystrom, W.S. Porter, D. Ray, and K.S. Sharma. Improving the measurement sensitivity of the Canadian Penning Trap mass spectrometer through PI-ICR. *Nuclear Instruments and Methods in Physics Research Section B: Beam Interactions with Materials and Atoms*, 463:491–495, jan 2020.

[76] J. Karthein. *Precision mass measurements using the Phase-Imaging Ion-Cyclotron-Resonance detection technique*. PhD thesis, University of Heidelberg, 2017.

[77] D. A. Nesterenko, T. Eronen, A. Kankainen, L. Canete, A. Jokinen, I. D. Moore, H. Penttilä, S. Rinta-Antila, A. de Roubin, and M. Vilen. Phase-Imaging Ion-Cyclotron-Resonance technique at the JYFLTRAP double Penning trap mass spectrometer. *The European Physical Journal A*, 54(9), sep 2018.

[78] M. Vilén, A. Kankainen, P. Baczyk, L. Canete, J. Dobaczewski, T. Eronen, S. Geldhof, A. Jokinen, M. Konieczka, J. Kostensalo, I. D. Moore, D. A. Nesterenko, H. Penttilä, I. Pohjalainen, M. Reponen, S. Rinta-Antila, A. de Roubin, W. Satuła, and J. Suhonen. High-precision mass measurements and

production of neutron-deficient isotopes using heavy-ion beams at IGISOL. *Physical Review C*, 100(5), nov 2019.

[79] V. Manea, J. Karthein, D. Atanasov, M. Bender, K. Blaum, T. E. Cocolios, S. Eliseev, A. Herlert, J. D. Holt, W. J. Huang, Yu. A. Litvinov, D. Lunney, J. Menéndez, M. Mougeot, D. Neidherr, L. Schweikhard, A. Schwenk, J. Simonis, A. Welker, F. Wienholtz, and K. Zuber. First glimpse of the $N = 82$ shell closure below $Z = 50$ from masses of neutron-rich cadmium isotopes and isomers, 2020.

[80] H. W. Gäggeler, D. T. Jost, A. Türler, P. Armbruster, W. Brüchle, H. Folger, F. P. Heßberger, S. Hofmann, G. Münzenberg, V. Ninov, W. Reisdorf, M. Schädel, K. Sümmerer, J. V. Kratz, U. Scherer, and M. E. Leino. Cold fusion reactions with $^{48}$Ca. *Nuclear Physics A*, 502:561–570, oct 1989.

[81] W. Reisdorf. Analysis of fissionability data at high excitation energies. *Zeitschrift fuer Physik A: Atoms and Nuclei*, 300(2-3):227–238, jun 1981.

[82] W. Reisdorf and M. Schädel. How well do we understand the synthesis of heavy elements by heavy-ion induced fusion? *Zeitschrift fuer Physik A Hadrons and Nuclei*, 343(1):47–57, mar 1992.

[83] M. Laatiaoui, W. Lauth, H. Backe, M. Block, D. Ackermann, B. Cheal, P. Chhetri, Ch. E. Düllmann, P. van Duppen, J. Even, R. Ferrer, F. Giacoppo, S. Götz, F. P. Heßberger, M. Huyse, O. Kaleja, J. Khuyagbaatar, P. Kunz, F. Lautenschläger, A. K. Mistry, S. Raeder, E. Minaya Ramirez, T. Walther, C. Wraith, and A. Yakushev. Atom-at-a-time laser resonance ionization spectroscopy of nobelium. *Nature*, 538(7626):495–498, sep 2016.

[84] Y. Ito, P. Schury, M. Wada, F. Arai, H. Haba, Y. Hirayama, S. Ishizawa, D. Kaji, S. Kimura, H. Koura, M. MacCormick, H. Miyatake, J. Y. Moon, K. Morimoto, K. Morita, M. Mukai, I. Murray, T. Niwase, K. Okada, A. Ozawa, M. Rosenbusch, A. Takamine, T. Tanaka, Y. X. Watanabe, H. Wollnik, and S. Yamaki. First Direct Mass Measurements of Nuclides around $Z = 100$ with a Multireflection Time-of-Flight Mass Spectrograph. *Physical Review Letters*, 120(15), apr 2018.

[85] A. Ghiorso, T. Sikkeland, and M. J. Nurmia. Isotopes of Element 102 with Mass 251 to 258. *Physical Review Letters*, 18(11):401–404, mar 1967.

[86] S. Antalic, F.P. Heßberger, S. Hofmann, D. Ackermann, S. Heinz, B. Kindler, I. Kojouharov, P. Kuusiniemi, M. Leino, B. Lommel, R. Mann, K. Nishio, Š. Šáro, B. Streicher, B. Sulignano, and M. Venhart. Decay studies of neutron-deficient lawrencium isotopes. *The European Physical Journal A*, 38(2):219–226, Nov 2008.

[87] A. Chatillon, Ch. Theisen, P. T. Greenlees, G. Auger, J. E. Bastin, E. Bouchez, B. Bouriquet, J. M. Casandjian, R. Cee, E. Clément, R. Dayras, G. de France, R. de Toureil, S. Eeckhaudt, A. Görgen, T. Grahn, S. Grévy, K. Hauschild, R. D. Herzberg, P. J. C. Ikin, G. D. Jones, P. Jones, R. Julin, S. Juutinen, H. Kettunen, A. Korichi, W. Korten, Y. Le Coz, M. Leino, A. Lopez-Martens, S. M. Lukyanov, Yu. E. Penionzhkevich, J. Perkowski, A. Pritchard, P. Rahkila, M. Rejmund, J. Saren, C. Scholey, S. Siem, M. G. Saint-Laurent, C. Simenel, Yu. G. Sobolev, Ch. Stodel, J. Uusitalo, A. Villari, M. Bender, P. Bonche, and P. H. Heenen. Spectroscopy and single-particle structure of the odd-$Z$ heavy elements $^{255}$Lr, $^{251}$Md and $^{247}$Es. *The European Physical Journal A*, 30(2):397–411, nov 2006.

[88] F. P. Heßberger, S. Hofmann, V. Ninov, P. Armbruster, H. Folger, G. Münzenberg, H. J. Schött, A. G. Popeko, A. V. Yeremin, A. N. Andreyev, and S. Saro. Spontaneous fission and alpha-decay properties of neutron deficient isotopes $^{257-253}$104 and $^{258}$106. *Zeitschrift fuer Physik A Hadrons and Nuclei*, 359(4):415–425, Dec 1997.

[89] F. P. Heßberger. Private Communication, 2019.

[90] Separator for Heavy Ion Reaction Products (ship). `https://www.gsi.de/work/forschung/nustarenna/nustarenna_divisions/she_physik/experimental_setup/ship.htm`. Accessed: 2019-09-15.

[91] C. Droese, S. Eliseev, K. Blaum, M. Block, F. Herfurth, M. Laatiaoui, F. Lautenschläger, E. Minaya Ramirez, L. Schweikhard, V. V. Simon, and P. G. Thirolf. The cryogenic gas stopping cell of SHIPTRAP. *Nuclear Instruments and Methods in Physics Research Section B: Beam Interactions with Materials and Atoms*, 338:126–138, nov 2014.

[92] M. Kretzschmar. Particle motion in a Penning trap. *European Journal of Physics*, 12(5):240–246, sep 1991.

[93] L. S. Brown and G. Gabrielse. Geonium theory: Physics of a single electron or ion in a Penning trap. *Reviews of Modern Physics*, 58(1):233–311, jan 1986.

[94] A. Kellerbauer, K. Blaum, G. Bollen, F. Herfurth, H.-J. Kluge, M. Kuckein, E. Sauvan, C. Scheidenberger, and L. Schweikhard. From direct to absolute mass measurements: A study of the accuracy of ISOLTRAP. *The European Physical Journal D - Atomic, Molecular and Optical Physics*, 22(1):53–64, jan 2003.

[95] M. Kretzschmar. The Ramsey method in high-precision mass spectrometry with Penning traps: Theoretical foundations. *International Journal of Mass Spectrometry*, 264(2-3):122–145, jul 2007.

[96] M. Kretzschmar. Calculating damping effects for the ion motion in a Penning trap. *The European Physical Journal D*, 48(3):313–319, jun 2008.

[97] K. Blaum, G. Bollen, F. Herfurth, A. Kellerbauer, H.-J. Kluge, M. Kuckein, S. Heinz, P. Schmidt, and L. Schweikhard. Recent developments at ISOLTRAP: towards a relative mass accuracy of exotic nuclei below $10^{-8}$. *Journal of Physics B: Atomic, Molecular and Optical Physics*, 36(5):921–930, feb 2003.

[98] G. Savard, St. Becker, G. Bollen, H.-J. Kluge, R. B. Moore, Th. Otto, L. Schweikhard, H. Stolzenberg, and U. Wiess. A new cooling technique for heavy ions in a Penning trap. *Physics Letters A*, 158(5):247–252, sep 1991.

[99] C. Weber. *Konzeption eines kryogenen Penningfallenaufbaus für SHIPTRAP und Massenbestimmungen von Radionukliden um den $Z = 82$-Schalenabschluss an ISOLTRAP*. PhD thesis, Ruprecht-Karls-Universität Heidelberg, 2004.

[100] G. Eitel, M. Block, A. Czasch, M. Dworschak, S. George, O. Jagutzki, J. Ketelaer, J. Ketter, Sz. Nagy, D. Rodríguez, C. Smorra, and K. Blaum. Position-sensitive ion detection in precision Penning trap mass spectrometry. *Nuclear Instruments and Methods in Physics Research Section A: Accelerators, Spectrometers, Detectors and Associated Equipment*, 606(3):475–483, jul 2009.

[101] A. Chaudhuri, M. Block, S. Eliseev, R. Ferrer, F. Herfurth, A. Martín, G. Marx, M. Mukherjee, C. Rauth, L. Schweikhard, and G. Vorobjev. Carbon-cluster mass calibration at SHIPTRAP. *The European Physical Journal D*, 45(1):47–53, jan 2007.

[102] M. Lindinger, St. Becker, G. Bollen, K. Dasgupta, R. Jertz, H.-J. Kluge, L. Schweikhard, M. Vogel, and K. Lützenkischen. Cluster isobars for high-precision mass spectrometry. *Zeitschrift fuer Physik D Atoms, Molecules and Clusters*, 20(1-4):441–443, mar 1991.

[103] Brookhaven National Laboratory National Nuclear Data Center. NuDat (Nuclear Structure and Decay Data), March 18, 2008 2008.

[104] F. P. Heßberger, S. Antalic, B. Sulignano, D. Ackermann, S. Heinz, S. Hofmann, B. Kindler, J. Khuyagbaatar, I. Kojouharov, P. Kuusiniemi, M. Leino, B. Lommel, R. Mann, K. Nishio, A. G. Popeko, Š. Šáro, B. Streicher, J. Uusitalo, M. Venhart, and A. V. Yeremin. Decay studies of $k$ isomers in $^{254}$No. *The European Physical Journal A*, 43(1), dec 2009.

[105] I. Muntian, S. Hofmann, Z. Patyk, and A. Sobiczewski. Properties of Heaviest Nuclei. *Acta Physica Polonica B*, 34(4):2073, Apr 2003.

[106] J. Ärje, J. Äystö, H. Hyvönen, P. Taskinen, V. Koponen, J. Honkanen, A. Hautojärvi, and K. Vierinen. Submillisecond On-Line Mass Separation of Nonvolatile Radioactive Elements: An Application of Charge Exchange and Thermalization Processes of Primary Recoil Ions in Helium. *Physical Review Letters*, 54(2):99–101, jan 1985.

[107] W. R. Plaß, T. Dickel, S. Purushothaman, P. Dendooven, H. Geissel, J. Ebert, E. Haettner, C. Jesch, M. Ranjan, M. P. Reiter, H. Weick, F. Amjad, S. Ayet, M. Diwisch, A. Estrade, F. Farinon, F. Greiner, N. Kalantar-Nayestanaki, R. Knöbel, J. Kurcewicz, J. Lang, I. Moore, I. Mukha, C. Nociforo, M. Petrick, M. Pfützner, S. Pietri, A. Prochazka, A.-K. Rink, S. Rinta-Antila, D. Schäfer, C. Scheidenberger, M. Takechi, Y. K. Tanaka, J. S. Winfield, and M. I. Yavor. The FRS Ion Catcher - A facility for high-precision experiments with stopped projectile and fission fragments. *Nuclear Instruments and Methods in Physics Research Section B: Beam Interactions with Materials and Atoms*, 317:457–462, dec 2013.

[108] M. Wada, Y. Ishida, T. Nakamura, Y. Yamazaki, T. Kambara, H. Ohyama, Y. Kanai, T. M. Kojima, Y. Nakai, N. Ohshima, A. Yoshida, T. Kubo, Y. Matsuo, Y. Fukuyama, K. Okada, T. Sonoda, S. Ohtani, K. Noda, H. Kawakami, and I. Katayama. Slow RI-beams from projectile fragment separators. *Nuclear Instruments and Methods in Physics Research Section B: Beam Interactions with Materials and Atoms*, 204:570–581, may 2003.

[109] S. Schwarz, G. Bollen, D. Lawton, P. Lofy, D. J. Morrissey, J. Ottarson, R. Ringle, P. Schury, T. Sun, V. Varentsov, and L. Weissman. The low-energy-beam and ion-trap facility at NSCL/MSU. *Nuclear Instruments and Methods in Physics Research Section B: Beam Interactions with Materials and Atoms*, 204:507–511, may 2003.

[110] G. Savard, J. Clark, C. Boudreau, F. Buchinger, J.E. Crawford, H. Geissel, J. P. Greene, S. Gulick, A. Heinz, J. K. P. Lee, A. Levand, M. Maier, G. Münzenberg, C. Scheidenberger, D. Seweryniak, K. S. Sharma, G. Sprouse, J. Vaz, J. C. Wang, B. J. Zabransky, and Z. Zhou. Development and operation of gas catchers to thermalize fusion–evaporation and fragmentation products. *Nuclear Instruments and Methods in Physics Research Section B: Beam Interactions with Materials and Atoms*, 204:582–586, may 2003.

[111] J. B. Neumayr, L. Beck, D. Habs, S. Heinz, J. Szerypo, P. G. Thirolf, V. Varentsov, F. Voit, D. Ackermann, D. Beck, M. Block, Z. Di, S. Eliseev, H. Geissel, F. Herfurth, F. P. Heßberger, S. Hofmann, H.-J. Kluge, M. Mukherjee, G. Münzenberg, M. Petrick, W. Quint, S. Rahaman, C. Rauth, D. Rodríguez, C. Scheidenberger, G. Sikler, Z. Wang, C. Weber, W. R. Plaß, M. Breitenfeldt, A. Chaudhuri, G. Marx, L. Schweikhard, A. F. Dodonov, Y. Novikov, and M. Suhonen. The ion-catcher device for SHIPTRAP. *Nuclear Instruments and Methods in Physics Research Section B: Beam Interactions with Materials and Atoms*, 244(2):489–500, mar 2006.

[112] S. Eliseev, M. Block, A. Chaudhuri, Z. Di, D. Habs, F. Herfurth, H.-J. Kluge, J. B. Neumayr, W. R. Plaß, C. Rauth, P. G. Thirolf, G. Vorobjev, and Z. Wang. Extraction efficiency and extraction time

of the SHIPTRAP gas-filled stopping cell. *Nuclear Instruments and Methods in Physics Research Section B: Beam Interactions with Materials and Atoms*, 258(2):479–484, may 2007.

[113] S. Eliseev, M. Block, M. Dworschak, F. Herfurth, H.-J. Kluge, A. Martin, C. Rauth, and G. Vorobjev. A new cryogenic gas-filled stopping chamber for SHIPTRAP. *Nuclear Instruments and Methods in Physics Research Section B: Beam Interactions with Materials and Atoms*, 266(19-20):4475–4477, oct 2008.

[114] O. Kaleja, B. Andjelić, K. Blaum, M. Block, P. Chhetri, C. Droese, Ch. E. Düllmann, M. Eibach, S. Eliseev, J. Even, S. Götz, F. Giacoppo, N. Kalantar-Nayestanaki, A. Mistry, T. Murböck, S. Raeder, and L. Schweikhard. The performance of the cryogenic buffer-gas stopping cell of SHIPTRAP. *Nuclear Instruments and Methods in Physics Research Section B: Beam Interactions with Materials and Atoms*, 2019.

[115] M. Block, D. Ackermann, K. Blaum, A. Chaudhuri, Z. Di, S. Eliseev, R. Ferrer, D. Habs, F. Herfurth, F. P. Heßberger, S. Hofmann, H.-J. Kluge, G. Maero, A. Martín, G. Marx, M. Mazzocco, M. Mukherjee, J. B. Neumayr, W. R. Plaß, W. Quint, S. Rahaman, C. Rauth, D. Rodríguez, C. Scheidenberger, L. Schweikhard, P. G. Thirolf, G. Vorobjev, and C. Weber. Towards direct mass measurements of nobelium at SHIPTRAP. *The European Physical Journal D*, 45(1):39–45, jun 2007.

[116] F. Giacoppo, K. Blaum, M. Block, P. Chhetri, Ch. E. Düllmann, C. Droese, S. Eliseev, P. Filianin, S. Götz, Y. Gusev, F. Herfurth, F. P. Hessberger, O. Kaleja, J. Khuyagbaatar, M. Laatiaoui, F. Lautenschläger, C. Lorenz, G. Marx, E. Minaya Ramirez, A. Mistry, Yu. N. Novikov, W. R. Plass, S. Raeder, D. Rodríguez, D. Rudolph, L.G. Sarmiento, C. Scheidenberger, L. Schweikhard, P. Thirolf, and A. Yakushev. Recent upgrades of the SHIPTRAP Setup: On the Finish Line Towards Direct Mass Spectroscopy of Superheavy Elements. *Acta Physica Polonica B*, 48(3):423, 2017.

[117] C. Droese. *The masses of nobelium and lawrencium isotopes, the mass difference between* $^{180}W$ *and* $^{180}Hf$*, and a characterization of the future cryogenic stopping cell of the online massspectrometer SHIPTRAP*. PhD thesis, Ernst-Moritz-Arndt-Universität Greifswald, 2014.

[118] O. Kaleja, K. Blaum, M. Block, P. Chhetri, S. Eliseev, F. Giacoppo, F.-P. Heßberger, M. Laatiaoui, F. Lautenschläger, E. Minaya-Ramirez, A. Mistry, S. Raeder, L. Schweikhard, and P. Thirolf. GSI Scientific Report 2015. 2016, DOI 10.15120/gr-2016-1.

[119] J. F. Ziegler, M. D. Ziegler, and J. P. Biersack. SRIM - The Stopping and Range of Ions in Matter (2010). *Nuclear Instruments and Methods in Physics Research Section B: Beam Interactions with Materials and Atoms*, 268(11-12):1818–1823, jun 2010.

[120] N. Trautmann and H. Folger. Preparation of actinide targets by electrodeposition. *Nuclear Instruments and Methods in Physics Research Section A: Accelerators, Spectrometers, Detectors and Associated Equipment*, 282(1):102–106, oct 1989.

[121] J. Runke, Ch E. Düllmann, K. Eberhardt, P. A. Ellison, K. E. Gregorich, S. Hofmann, E. Jäger, B. Kindler, J. V. Kratz, J. Krier, B. Lommel, C. Mokry, H. Nitsche, J. B. Roberto, K. P. Rykaczewski, M. Schädel, P. Thörle-Pospiech, N. Trautmann, and A. Yakushev. Preparation of actinide targets for the synthesis of the heaviest elements. *Journal of Radioanalytical and Nuclear Chemistry*, 299(2):1081–1084, jul 2013.

[122] A. Vascon, N. Wiehl, T. Reich, J. Drebert, K. Eberhardt, and Ch. E. Düllmann. The performance of thin layers produced by molecular plating as $\alpha$-particle sources. *Nuclear Instruments and Methods in Physics Research Section A: Accelerators, Spectrometers, Detectors and Associated Equipment*, 721:35–44, sep 2013.

[123] P. Schwamb. *Entwicklung eines Detektors zum direkten massenselektiven Ionennachweis nach Resonanzionisationsspektroskopie in einer Puffergaszelle.* PhD thesis, Institutfür Physik, Universität Mainz, 1996.

[124] H. Bateman. The solution of a system of differential equations occurring in the theory of radio-active transformations. *Proc. Cambridge Phil. Soc., 1908*, 15:423–427, 1908.

[125] P. Schury, G. Bollen, M. Block, D. J. Morrissey, R. Ringle, A. Prinke, J. Savory, S. Schwarz, and T. Sun. Beam purification techniques for low energy rare isotope beams from a gas cell. *Hyperfine Interactions*, 173(1-3):165–170, nov 2006.

[126] F. Muntean and P. B. Armentrout. Guided ion beam study of collision-induced dissociation dynamics: integral and differential cross sections. *The Journal of Chemical Physics*, 115(3):1213–1228, jul 2001.

[127] A. Jacobs. *Collision Induced Dissociation and Mass Spectrometry with the TITAN Multiple-Reflection Time-of-Flight Mass-Spectrometer.* M.sc. thesis, University of British Columbia, 2019.

[128] A. Kramida, Yu. Ralchenko, J. Reader, and NIST ASD Team. NIST Atomic Spectra Database (ver. 5.6.1), [Online]. Available: `https://physics.nist.gov/asd` [2018, December 13]. National Institute of Standards and Technology, Gaithersburg, MD., 2018.

[129] Y. N. Joshi and M. Mazzoni. The $6s_26p_23P_0$-$6s_26p$ nd $^3D_1$ series in photoabsorption of Bi II. *Physics Letters A*, 118(5):237–238, oct 1986.

[130] M. E. Hanni, J. A. Keele, S. R. Lundeen, C. W. Fehrenbach, and W. G. Sturrus. Polarizabilities of $Pb^{2+}$ and $Pb^{4+}$ and ionization energies of $Pb^+$ and $Pb^{3+}$ from spectroscopy of high-L Rydberg states of $Pb^+$ and $Pb^{3+}$. *Physical Review A*, 81(4), apr 2010.

[131] W. Finkelnburg and W. Humbach. Ionisierungsenergien von Atomen und Atomionen. *Die Naturwissenschaften*, 42(2):35–37, 1955.

[132] I. Velchev, W. Hogervorst, and W. Ubachs. Precision VUV spectroscopy of Ar I at 105 nm. *Journal of Physics B: Atomic, Molecular and Optical Physics*, 32(17):L511–L516, aug 1999.

[133] T. Trickl, E. F. Cromwell, Y. T. Lee, and A. H. Kung. State-selective ionization of nitrogen in the $x2 = 0$ and $v = 1$ states by two-color $(1 + 1)$ photon excitation near threshold. *The Journal of Chemical Physics*, 91(10):6006–6012, 1989.

[134] D. Shiner, J. M. Gilligan, B. M. Cook, and W. Lichten. $H_2$,$D_2$, and HD ionization potentials by accurate calibration of several iodine lines. *Physical Review A*, 47(5):4042–4045, may 1993.

[135] V. L. Varentsov and D. Habs. "fair-wind gas cell" - a new concept of a buffer gas cell design. *Nuclear Instruments and Methods in Physics Research Section A: Accelerators, Spectrometers, Detectors and Associated Equipment*, 496(2-3):286–292, jan 2003.

[136] J. D. Anderson Jr. *Modern Compressible Flow: with Historical Perspective.* McGraw-Hill, New York, 1990.

[137] A. Krönig. Grundzüge einer Theorie der Gase. *Annalen der Physik und Chemie*, 175(10):315–322, 1856.

[138] R. Cumeras, E. Figueras, C. E. Davis, J. I. Baumbach, and I. Gràcia. Review on Ion Mobility Spectrometry. Part 1: current instrumentation. *The Analyst*, 140(5):1376–1390, 2015.

[139] L. A. Viehland. Zero-field mobilities in helium: highly accurate values for use in ion mobility spectrometry. *International Journal for Ion Mobility Spectrometry*, 15(1):21–29, oct 2011.

[140] T.-C. Jen, L. Pan, L. Li, Q. Chen, and W. Cui. The acceleration of charged nano-particles in gas stream of supersonic de-Laval-type nozzle coupled with static electric field. *Applied Thermal Engineering*, 26(5-6):613–621, apr 2006.

[141] W. Paul. Electromagnetic traps for charged and neutral particles. *Reviews of Modern Physics*, 62(3):531–540, jul 1990.

[142] J. D. Prestage, A. Williams, L. Maleki, M. J. Djomehri, and E. Harabetian. Dynamics of charged particles in a Paul radio-frequency quadrupole trap. *Physical Review Letters*, 66(23):2964–2967, jun 1991.

[143] D. Wittwer, F. Sh. Abdullin, N. V. Aksenov, Yu. V. Albin, G. A. Bozhikov, S. N. Dmitriev, R. Dressler, R. Eichler, H. W. Gäggeler, R. A. Henderson, S. Hübener, J. M. Kenneally, V. Ya. Lebedev, Yu. V. Lobanov, K. J. Moody, Yu. Ts. Oganessian, O. V. Petrushkin, A. N. Polyakov, D. Piguet, P. Rasmussen, R. N. Sagaidak, A. Serov, I. V. Shirokovsky, D. A. Shaughnessy, S. V. Shishkin, A. M. Sukhov, M. A. Stoyer, N. J. Stoyer, E. E. Tereshatov, Yu. S. Tsyganov, V. K. Utyonkov, G. K. Vostokin, M. Wegrzecki, and P. A. Wilk. Gas phase chemical studies of superheavy elements using the Dubna gas-filled recoil separator - Stopping range determination. *Nuclear Instruments and Methods in Physics Research Section B: Beam Interactions with Materials and Atoms*, 268(1):28–35, jan 2010.

[144] F. Lautenschläger, P. Chhetri, D. Ackermann, H. Backe, M. Block, B. Cheal, A. Clark, C. Droese, R. Ferrer, F. Giacoppo, S. Götz, F.P. Heßberger, O. Kaleja, J. Khuyagbaatar, P. Kunz, A.K. Mistry, M. Laatiaoui, W. Lauth, S. Raeder, Th. Walther, and C. Wraith. Developments for resonance ionization laser spectroscopy of the heaviest elements at SHIP. *Nuclear Instruments and Methods in Physics Research Section B: Beam Interactions with Materials and Atoms*, 383:115–122, sep 2016.

[145] W. Bryc. *The Normal Distribution*. Springer New York, 1995.

[146] A. Kramida, Yu. Ralchenko, J. Reader, and NIST ASD Team. NIST Atomic Spectra Database (version 5.6.1). Online, 2018. Available at https://physics.nist.gov/asd, accessed 14.12.2018.

[147] F. P. Hessberger, S. Hofmann, G. Muenzenberg, K.-H. Schmidt, P. Armbruster, and R. Hingmann. Influence of energy summing of $\alpha$-particles and conversion electrons on the shapes of $\alpha$-spectra in the region of the heaviest nuclei. *Nuclear Instruments and Methods in Physics Research Section A: Accelerators, Spectrometers, Detectors and Associated Equipment*, 274(3):522 – 527, 1989.

[148] F. P. Heßberger, S. Hofmann, D. Ackermann, V. Ninov, M. Leino, G. Münzenberg, S. Saro, A. Lavrentev, A. G. Popeko, A. V. Yeremin, and Ch. Stodel. Decay properties of neutron-deficient isotopes $^{256,257}$Db, $^{255}$Rf, $^{252,253}$Lr. *Eur. Phys. J. A*, 12(1):57–67, 2001.

[149] F. P. Heßberger, S. Hofmann, D. Ackermann, P. Cagarda, R.-D. Herzberg, I. Kojouharov, P. Kuusiniemi, M. Leino, and R. Mann. Alpha-gamma decay studies of $^{251,253}$No and their daughter products $^{247,249}$Fm. *The European Physical Journal A*, 22(3):417–427, nov 2004.

[150] A. H. Wapstra and G. Audi. The 1983 atomic mass evaluation. *Nuclear Physics A*, 432(1):1–54, jan 1985.

[151] G. Audi and A. H. Wapstra. The 1993 atomic mass evaluation. *Nuclear Physics A*, 565(1):1–65, dec 1993.

[152] G. Audi and A. H. Wapstra. The 1995 update to the atomic mass evaluation. *Nuclear Physics A*, 595(4):409–480, dec 1995.

[153] M. Wang, G. Audi, A. H. Wapstra, F. G. Kondev, M. MacCormick, X. Xu, and B. Pfeiffer. The AME2012 atomic mass evaluation. *Chinese Physics C*, 36(12):1603–2014, dec 2012.

[154] G. N. Flerov, S. M. Polikano, and et al. Experiments on the production of the element 102. *Doklady Akad. Nauk S.S.S.R.*, 120, 5 1958.

[155] E. D. Donets, V. A. Shchegolev, and V. A. Ermakov. The properties of the isotope $^{254}$102. *Soviet Atomic Energy*, 20(3):257–263, mar 1966.

[156] V. L. Mikheev, V. I. Ilyushchenko, M. B. Miller, S. M. Polikanov, G. N. Flerov, and Yu. P. Kharitonov. Synthesis of isotopes of element 102 with mass numbers 254, 253, and 252. *Soviet Atomic Energy*, 22(2):93–100, feb 1967.

[157] F. P. Heßberger, G. Münzenberg, S. Hofmann, Y. K. Agarwal, K. Poppensieker, W. Reisdorf, K.-H. Schmidt, J. R. H. Schneider, W. F. W. Schneider, H. J. Schött, P. Armbruster, B. Thuma, C.-C. Sahm, and D. Vermeulen. The new isotopes $^{258}$105, $^{257}$105, $^{254}$Lr and $^{253}$Lr. *Zeitschrift fuer Physik A Atoms and Nuclei*, 322(4):557–566, Dec 1985.

[158] C. M. Folden, S. L. Nelson, Ch. E. Düllmann, J. M. Schwantes, R. Sudowe, P. M. Zielinski, K. E. Gregorich, H. Nitsche, and D. C. Hoffman. Excitation function for the production of $^{262}$Bh ($Z = 107$) in the odd-Z-projectile reaction $^{208}$Pb($^{55}$Mn,n). *Physical Review C*, 73(1), jan 2006.

[159] D. Kaji, K. Morimoto, Y. Wakabayashi, M. Takeyama, and M. Asai. First $\alpha$-$\gamma$ Spectroscopy Using Si–Ge Detector Array Installed at Focal Plane of GARIS. In *Proceedings of the Conference on Advances in Radioactive Isotope Science (ARIS2014)*. Journal of the Physical Society of Japan, jun 2015.

[160] Z. G. Gan, Z. Qin, H. M. Fan, X. G. Lei, Y. B. Xu, J. J. He, H. Y. Liu, X. L. Wu, J. S. Guo, X. H. Zhou, S. G. Yuan, and G. M. Jin. A new $\alpha$-particle-emitting isotope $^{259}$Db. *The European Physical Journal A*, 10(1):21–25, feb 2001.

[161] K. Eskola, P. Eskola, M. Nurmia, and A. Ghiorso. Studies of Lawrencium Isotopes with Mass Numbers 255 Through 260. *Physical Review C*, 4(2):632–642, aug 1971.

[162] K. Hauschild, A. Lopez-Martens, A. V. Yeremin, O. Dorvaux, S. Antalic, A. V. Belozerov, Ch. Briançon, M. L. Chelnokov, V. I. Chepigin, D. Curien, B. Gall, A. Görgen, V. A. Gorshkov, M. Guttormsen, F. Hanappe, A. P. Kabachenko, F. Khalfallah, A. C. Larsen, O. N. Malyshev, A. Minkova, A. G. Popeko, M. Rousseau, N. Rowley, S. Saro, A. V. Shutov, S. Siem, L. Stuttgè, A. I. Svirikhin, N. U. H. Syed, Ch. Theisen, and M. Venhart. High-K $t_{1/2}$=1.4(1)ms, isomeric state $^{255}$Lr. *Physical Review C*, 78(2), aug 2008.

[163] E. Minaya Ramirez. Private Communication, 2019.

[164] M. König, G. Bollen, H.-J. Kluge, T. Otto, and J. Szerypo. Quadrupole excitation of stored ion motion at the true cyclotron frequency. *International Journal of Mass Spectrometry and Ion Processes*, 142(1-2):95–116, mar 1995.

[165] G. Bollen. Mass measurements of short-lived nuclides with ion traps. *Nuclear Physics A*, 693(1-2):3–18, oct 2001.

[166] K. Morita, K. Morimoto, D. Kaji, H. Haba, E. Ideguchi, J. C. Peter, R. Kanungo, K. Katori, H. Koura, H. Kudo, T. Ohnishi, A. Ozawa, T. Suda, K. Sueki, I. Tanihata, H. Xu, A. V. Yeremin, A. Yoneda, A. Yoshida, Y.-L. Zhao, T. Zheng, S. Goto, and F. Tokanai. Production and Decay Properties of $^{272}$111 and its Daughter Nuclei. *Journal of the Physical Society of Japan*, 73(7):1738–1744, jul 2004.

[167] C. M. Folden, K. E. Gregorich, Ch. E. Düllmann, H. Mahmud, G. K. Pang, J. M. Schwantes, R. Sudowe, P. M. Zielinski, H. Nitsche, and D. C. Hoffman. Development of an Odd-Z-Projectile Reaction for Heavy Element Synthesis: $^{208}$Pb($^{64}$Ni,n)$^{271}$Ds and $^{208}$Pb($^{65}$Cu,n)$^{272}$111. *Physical Review Letters*, 93(21), nov 2004.

[168] I. Dragojević, K. E. Gregorich, Ch. E. Düllmann, M. A. Garcia, J. M. Gates, S. L. Nelson, L. Stavsetra, R. Sudowe, and H. Nitsche. Influence of projectile neutron number in the $^{208}$Pb($^{48}$Ti, n)$^{255}$Rf and $^{208}$Pb($^{50}$Ti, n)$^{257}$Rf reactions. *Physical Review C*, 78(2), aug 2008.

[169] M. G. Mayer. On Closed Shells in Nuclei. *Physical Review*, 74(3):235–239, aug 1948.

[170] M. G. Mayer and J. H. D. Jensen. *Elementary theory of nuclear shell structure*. Wiley, New York, NY, 1955.

[171] K. Rutz, M. Bender, T. Bürvenich, T. Schilling, P.-G. Reinhard, J. A. Maruhn, and W. Greiner. Superheavy nuclei in self-consistent nuclear calculations. *Physical Review C*, 56(1):238–243, jul 1997.

[172] W. Zhang, J. Meng, S. Q. Zhang, L. S. Geng, and H. Toki. Magic numbers for superheavy nuclei in relativistic continuum Hartree-Bogoliubov theory. *Nuclear Physics A*, 753(1-2):106–135, may 2005.

[173] F. P. Hessberger, G. Muenzenberg, S. Hofmann, W. Reisdorf, K. H. Schmidt, H. J. Schoett, P. Armbruster, R. Hingmann, B. Thuma, and D. Vermeulen. Study of evaporation residues produced in reactions of $^{207,208}$Pb with$^{50}$Ti. *Zeitschrift fuer Physik A Atoms and Nuclei*, 321(2):317–327, jun 1985.

[174] F. P. Heßberger, S. Hofmann, D. Ackermann, S. Antalic, B. Kindler, I. Kojouharov, P. Kuusiniemi, M. Leino, B. Lommel, R. Mann, K. Nishio, A. G. Popeko, B. Sulignano, S. Saro, B. Streicher, M. Venhart, and A. V. Yeremin. Alpha-gamma decay studies of $^{255}$No. *The European Physical Journal A*, 29(2):165–173, aug 2006.

[175] M. Vostinar, F. P. Heßberger, D. Ackermann, B. Andel, S. Antalic, M. Block, C. Droese, J. Even, S. Heinz, Z. Kalaninova, I. Kojouharov, M. Laatiaoui, A. K. Mistry, J. Piot, and H. Savajols. Alpha-gamma decay studies of $^{258}$Db and its (grand)daughter nuclei $^{254}$Lr and $^{250}$Md. *The European Physical Journal A*, 55(2), feb 2019.

[176] V. A. Druin. *Yadern. Fiz.*, 12(268), 1970.

[177] et al. C.E. Bemis CE. ORNL-5137, p. 73, 1976.

[178] M. Leino and F. P. Heßberger. The nuclear structure of heavy-actinide and trans-actinide nuclei. *Annual Review of Nuclear and Particle Science*, 54(1):175–215, dec 2004.

[179] S. Antalic. *Synthesis and properties of neutron decient isotopes of elements around $Z = 100$*. PhD thesis, Comenius University, Bratislava, 2005.

[180] S. Dmitriev, M. Itkis, and Yu. Oganessian. Status and perspectives of the Dubna superheavy element factory. *EPJ Web of Conferences*, 131:08001, 2016.

[181] G. G. Gulbekian, S. N. Dmitriev, Yu. Ts. Oganessian, B. N. Gikal, I. V. Kalagin, V. A. Semin, S. L. Bogomolov, I. A. Ivanenko, N. Yu. Kazarinov, G. N. Ivanov, and N. F. Osipov. The New DC-280 Cyclotron. Status and Road Map. *Physics of Particles and Nuclei Letters*, 15(7):809–813, dec 2018.

[182] J. M. Gates, G. K. Pang, J. L. Pore, K. E. Gregorich, J. T. Kwarsick, G. Savard, N. E. Esker, M. Kireeff Covo, M. J. Mogannam, J. C. Batchelder, D. L. Bleuel, R. M. Clark, H. L. Crawford, P. Fallon, K. K. Hubbard, A. M. Hurst, I. T. Kolaja, A. O. Macchiavelli, C. Morse, R. Orford, L. Phair, and M. A. Stoyer. First Direct Measurements of Superheavy-Element Mass Numbers. *Physical Review Letters*, 121(22), nov 2018.

[183] A. Hamaker, G. Bollen, M. Eibach, C. Izzo, D. Puentes, M. Redshaw, R. Ringle, R. Sandler, S. Schwarz, and I. Yandow. SIPT - an ultrasensitive mass spectrometer for rare isotopes. *Hyperfine Interactions*, 240(1), apr 2019.

[184] E. A. Cornell, R. M. Weisskoff, K. R. Boyce, R. W. Flanagan, G. P. Lafyatis, and D. E. Pritchard. Single-ion cyclotron resonance measurement of $M(CO^+)/M(N_2^+)$. *Physical Review Letters*, 63(16):1674–1677, oct 1989.

[185] S. Sturm, A. Wagner, B. Schabinger, and K. Blaum. Phase-Sensitive Cyclotron Frequency Measurements at Ultralow Energies. *Physical Review Letters*, 107(14), sep 2011.

[186] R. Ringle, S. Schwarz, and G. Bollen. Penning trap mass spectrometry of rare isotopes produced via projectile fragmentation at the LEBIT facility. *International Journal of Mass Spectrometry*, 349-350:87–93, sep 2013.

[187] S. Lohse, J. Berrocal, M. Block, S. Chenmarev, J. M. Cornejo, J. G. Ramírez, and D. Rodríguez. A quartz amplifier for high-sensitivity Fourier-transform ion-cyclotron-resonance measurements with trapped ions. *Review of Scientific Instruments*, 90(6):063202, jun 2019.

[188] R. Weinstock. On a fallacious proof of Earnshaw's theorem. *American Journal of Physics*, 44(4):392–393, apr 1976.

[189] R. E. March and R. J. Hughes. *Quadrupole storage mass spectrometry*. Chem. Anal. Wiley, New York, NY, 1989.

[190] F. Paschen. Ueber die zum Funkenuebergang in Luft, Wasserstoff und Kohlensaeure bei verschiedenen Drucken erforderliche Potentialdifferenz. *Annalen der Physik*, 273(5):69–96, 1889.

[191] Electrical Breakdown in Gases. In *Foundations of Pulsed Power Technology*, pages 369–438. John Wiley & Sons, Inc., jul 2017.

[192] E. Oyarzabal, A. B. Martin-Rojo, and F. L. Tabarés. Electron-induced secondary electron emission coefficient of lithium, tungsten and stainless steel surfaces exposed to low-pressure plasmas. *Journal of Nuclear Materials*, 452(1-3):37–40, sep 2014.

[193] M. Moravej, X. Yang, G. R. Nowling, J. P. Chang, R. F. Hicks, and S. E. Babayan. Physics of high-pressure helium and argon radio-frequency plasmas. *Journal of Applied Physics*, 96(12):7011–7017, dec 2004.

[194] V. A. Lisovsky and V. D. Yegorenkov. Low-pressure gas breakdown in combined fields. *Journal of Physics D: Applied Physics*, 27(11):2340–2348, nov 1994.

[195] V. A. Lisovskiy and V. D. Yegorenkov. Rf breakdown of low-pressure gas and a novel method for determination of electron-drift velocities in gases. *Journal of Physics D: Applied Physics*, 31(23):3349–3357, dec 1998.

[196] J. Ziegler and et al. *SRIM - The Stopping and Range of Ions in Matter*. Not Stated, 2008.

[197] J. F. Ziegler and J. P. Biersack. The Stopping and Range of Ions in Matter. In *Treatise on Heavy-Ion Science*, pages 93–129. Springer US, 1985.

[198] H. Paul and A. Schinner. Judging the reliability of stopping power tables and programs for heavy ions. *Nuclear Instruments and Methods in Physics Research Section B: Beam Interactions with Materials and Atoms*, 209:252–258, aug 2003.

[199] J. F. Ziegler. Private Communication, 2019.

[200] L. C. Northcliffe. Energy Loss and Effective Charge of Heavy Ions in Aluminum. *Physical Review*, 120(5):1744–1757, dec 1960.

[201] P. Sigmund and A. Schinner. Effective charge and related/unrelated quantities in heavy-ion stopping. *Nuclear Instruments and Methods in Physics Research Section B: Beam Interactions with Materials and Atoms*, 174(4):535–540, may 2001.

[202] P. Sigmund. Charge-dependent electronic stopping of swift nonrelativistic heavy ions. *Physical Review A*, 56(5):3781–3793, nov 1997.